

Evaluation of Multilayer Silicon Carbide Composite Cladding Under Loss of Coolant Accident Conditions

By

Gregory Welch Daines
B.S. Mechanical Engineering (2014)
The University of Maryland at College Park

SUBMITTED TO THE DEPARTMENT OF NUCLEAR SCIENCE AND ENGINEERING IN PARTIAL
FULFILLMENT OF THE REQUIREMENTS FOR THE DEGREE OF

MASTER OF SCIENCE IN NUCLEAR SCIENCE AND ENGINEERING
AT THE
MASSACHUSETTS INSTITUTE OF TECHNOLOGY

February 2016

© 2016 Massachusetts Institute of Technology. All rights reserved.

Signature of Author: _____
Gregory Welch Daines
Department of Nuclear Science and Engineering
December 17, 2015

Certified by: _____
Michael P. Short, Ph.D.
Assistant Professor of Nuclear Science and Engineering
Thesis Supervisor

Certified by: _____
Thomas J. McKrell, Ph.D.
Research Scientist
Thesis Reader

Accepted by: _____
Ju Li, Ph.D.
Battelle Energy Alliance Professor of Nuclear Science and Engineering
And Professor of Materials Science and Engineering
Chairman, Department Committee on Graduate Students

THIS PAGE INTENTIONALLY LEFT BLANK

Evaluation of Multilayer Silicon Carbide Composite Cladding Under Loss of Coolant Accident Conditions

by

Gregory Welch Daines

Submitted to the Department of Nuclear Science and Engineering
on December 17, 2015 in Partial Fulfillment of the
Requirements for the Degree of Master of Science

Abstract

Silicon carbide (SiC) has been proposed as an alternative to zirconium alloys used in current light water reactor (LWR) fuel cladding because it exhibits superior corrosion characteristics, high-temperature strength, and a 1000°C higher melting temperature, all of which are important during a loss of coolant accident (LOCA). To improve the performance of SiC cladding, a multilayered architecture consisting of layers of monolithic SiC (mSiC) and SiC/SiC ceramic matrix composite (CMC) has been proposed.

In this work, the mechanical performance of both the tubing and the endplug joint of two-layer SiC cladding is investigated under conditions associated with the LOCA. Specifically, SiC cladding mechanical performance is investigated after exposure to 1,400°C steam and after quenching from 1,200°C into either 100°C or 90°C atmospheric-pressure water. The samples consist of two-layer SiC, with an inner SiC/SiC CMC layer and an outer monolith SiC layer. The relationship between mechanical performance and sample architecture is investigated through ceramography and internal void characterization.

The two-layered SiC cladding design offered an as-received failure hoop stress of about 600 MPa, with little strength reduction due to thermal shock, and the tube failure hoop stress remained above 200 MPa after 48 hour high-temperature steam oxidation. The cladding showed pseudo-ductile behavior and failed in a non-frangible manner. The designs investigated for joint strength offered as-received burst strength above 30 MPa, although the impact of thermal shock and oxidation showed possible dependence on architecture. Overall, the cladding showed promising accident-tolerant performance.

Because the implementation of SiC is complicated by the need for an open gap and low plenum pressure, thorium-based mixed oxides (MOX) are a promising fuel for SiC cladding because they have higher thermal conductivity and lower fission gas release (FGR). Previous efforts at MIT have modified the FRAPCON code to include thorium MOX fuel. In this work, the fission gas release and thermal conductivity models of FRAPCON-3.4-MIT are validated against published data. The results of this validation indicate a need to update the FGR model, which was accomplished in this work.

Thesis Supervisor: Michael P. Short, Ph.D.

Title: Assistant Professor of Nuclear Science and Engineering

Thesis Reader: Thomas J. McKrell, Ph.D.

Title: Research Scientist

THIS PAGE INTENTIONALLY LEFT BLANK

Acknowledgments

This work was supported under the United States Department of Energy award number DE-NE0000566 where MIT acted as a subcontractor to Westinghouse Electric. The samples investigated in this work were manufactured and provided by General Atomics.

I would like to extend my gratitude to the late Professor Mujid Kazimi, who recruited me to this topic and supervised my research until his death. He provided me with valuable direction, feedback, and encouragement on my research. I also wish to express my gratitude to Professor Michael Short, who assumed the role of my thesis supervisor upon Professor Kazimi's death, and to Professor Jacopo Buongiorno and Dr. Koroush Shirvan, who assumed leadership roles of the CANES group after Professor Kazimi's death and provided feedback and guidance on my research.

I would also like to thank Dr. Thomas McKrell, who provided invaluable guidance and support on the experimental aspects of my research. His experience in experimentation immeasurably helped my research and experimental skills, and his supervision and feedback during my frequent contact with the project clients enhanced my communication skills. Furthermore, I appreciate Professor Ron Ballinger and Peter Stahle for allowing me to use the load frame in the H. H. Uhlig corrosion laboratory. I also recognize Dr. Christian Deck, Dr. George Jacobsen, and Dr. Hesham Khalifa of General Atomics and Dr. Ed Lahoda and Dr. Peng Xu of Westinghouse Electric for providing feedback and suggestions for my research. Their input helped direct the conduct of my research, and they provided feedback on the results of my investigation.

I thank Pierre Guenoun with whom I worked closely and I also thank Yongsoo Park, whose concern for lab safety went above-and-beyond expectations. Finally, I thank my family for their support and assistance while I have been at MIT.

Table of Contents

Abstract.....	3
Acknowledgments.....	5
List of Figures	10
List of Tables	15
Nomenclature	17
1. Introduction	18
1.1. Motivation.....	18
1.2. Overview of Current LWR Cladding	19
1.2.1. LWR Cladding Overview	19
1.2.2. Limitations of Current PWR Cladding	19
1.3. Accident Tolerant Fuels.....	20
1.3.1. Motivation and Description of Accident Tolerant Fuels	20
1.3.2. Silicon Carbide for Nuclear Applications.....	21
1.4. Objectives and Scope	22
1.5. Thesis Organization.....	23
2. Performance Modeling of Thorium-Based Fuels	25
2.1. Motivation.....	25
2.2. Fission Gas Release Mechanism.....	25
2.3. FRAPCON Fission Gas Release Model	26
2.3.1. Forsberg-Masih Model	26
2.4. FRAPCON Modifications.....	28
2.4.1. Thermal Conductivity Models	28
2.4.2. Fission Gas Release Models	34
2.5. Discussion.....	42
2.5.1. Densification Uncertainty	42
2.5.2. Comparison to Published Data	42
2.5.3. Implications for Fuel Performance.....	45
2.5.4. Implications for Silicon Carbide	46
3. Silicon Carbide Cladding.....	51
3.1. Uses of Silicon Carbide	51
3.2. Previous Silicon Carbide LWR Cladding Research	51

3.3.	Manufacturing of Silicon Carbide Cladding.....	53
3.3.1.	Monolith SiC.....	53
3.3.2.	SiC/SiC Composites	53
3.3.3.	Endplug	55
3.4.	Silicon Carbide Cladding Options	56
4.	Experimental Methodology	59
4.1.	Overview of Specimens.....	59
4.1.1.	Open-Ended Specimens	61
4.1.2.	Close-Ended Specimens	61
4.2.	Strength Test Facilities	62
4.2.1.	Pressurization Test Facility.....	63
4.2.2.	Joint Strength Test Facility	70
4.3.	Thermal Shock Facility	73
4.4.	Oxidation Facility.....	74
5.	XCT Analysis of Cladding Specimens	77
5.1.	Motivation.....	77
5.2.	Void Analysis Methodology	77
5.2.1.	Void Analysis Facility	77
5.2.2.	Image Processing	77
5.3.	Void Analysis of CMC	81
5.3.1.	CMC Void Data	82
5.3.2.	CMC Void Discussion.....	87
5.3.3.	CMC Void Implications.....	89
5.4.	Void Analysis of Endplug Joint	91
5.4.1.	Endplug Joint Void Data	91
5.4.2.	Endplug Joint Void Discussion.....	93
5.4.3.	Endplug Joint Void Implications	94
5.5.	Conclusion.....	95
6.	Experimental Results	97
6.1.	Analysis of SiC Cladding Mechanical Performance As-Received.....	97
6.1.1.	Motivation.....	97
6.1.2.	Hoop Testing of As-Received Open-Ended Samples.....	97

6.1.3.	Joint Testing of As-Received Close-Ended Samples	98
6.1.4.	Failure Observations	99
6.2.	Analysis of SiC Cladding Performance after Thermal-Shock.....	101
6.2.1.	Motivation.....	101
6.2.2.	Hoop Testing of Thermal-Shock Open-Ended Samples	101
6.2.3.	Joint Testing of Thermal-Shock Close-Ended Samples.....	103
6.2.4.	Failure Observations	104
6.3.	Analysis of SiC Cladding Performance after Steam Oxidation	107
6.3.1.	Motivation.....	107
6.3.2.	Oxidation Data	107
6.3.3.	Hoop Testing Evaluation	109
6.3.4.	Joint Testing Evaluation	111
6.3.5.	Failure Observations	113
6.4.	Summary of Results	116
6.4.1.	As-Received Results	116
6.4.2.	Thermal-Shock Results.....	116
6.4.3.	High-Temperature Steam Oxidation Results	117
7.	Discussion of Results.....	119
7.1.	As-Received Discussion	119
7.1.1.	Hoop Test	119
7.1.2.	Joint Test	121
7.1.3.	Microstructural Analysis	122
7.2.	Thermal-Shock Discussion	125
7.2.1.	Hoop Test	125
7.2.2.	Joint Test	127
7.2.3.	Microstructural Analysis	129
7.3.	Oxidation Discussion.....	132
7.3.1.	Oxidation Microstructural Analysis.....	132
7.3.2.	Hoop Test	141
7.3.3.	Joint Test	143
7.3.4.	Microstructural Analysis	146
8.	Conclusions and Recommendations for Future Work.....	151

8.1. Summary of Results	151
8.2. Conclusions of As-Received Testing.....	152
8.3. Conclusions of Thermal-Shock Testing	154
8.4. Conclusions of High-Temperature Steam Oxidation Testing.....	155
8.5. Recommendations for Future Work	156
Works Cited.....	160

List of Figures

Figure 1: Diffusivity for UO_2 implemented in FRAPCON Massih model.....	28
Figure 2: Thermal conductivity comparison for urania.....	30
Figure 3: Urania thermal conductivity versus temperature comparison	30
Figure 4: Comparison of FRAPCON urania thermal conductivity models.....	31
Figure 5: Thermal conductivity comparison for thoria-urania.....	32
Figure 6: Thoria-urania thermal conductivity versus temperature comparison	32
Figure 7: Thermal conductivity comparison for thoria-plutonia	33
Figure 8: Thoria-plutonia thermal conductivity versus temperature comparison	34
Figure 9: Vicious cycle of fuel temperature increase.....	36
Figure 10: FGR versus peak calculated historic thoria-urania fuel temperature.....	37
Figure 11: Results of FGR modeling for thoria-urania rods	37
Figure 12: Diffusivity for UO_2 and modified thoria-urania model	38
Figure 13: Bruce-type 37-element bundle showing test rod locations (adapted from Karam (Karam, et al., 2008)).....	39
Figure 14: FGR versus calculated peak historic thoria-plutonia fuel temperature (#1 rods only)	40
Figure 15: Results of FGR modeling for thoria-plutonia rods	41
Figure 16: Diffusivity for UO_2 and modified thoria-plutonia model	41
Figure 17: Comparison of modified FRAPCON thoria-urania diffusivity and published data (burnup indicated)	43
Figure 18: Comparison of FRACON UO_2 diffusivity and published data (burnup indicated)	44
Figure 19: Comparison of calculated FGR LWBR fuel with and without thoria	45
Figure 20: Comparison of calculated peak temperature for LWBR fuel with and without thoria.....	45
Figure 21: Comparison of calculated FGR for AECL fuel with and without urania	46
Figure 22: Comparison of calculated peak fuel temperature for AECL fuel with and without urania	46
Figure 23: Comparison of fuel temperature for simulated rods	48
Figure 24: Comparison of FGR for simulated rods.....	48
Figure 25: Comparison of plenum pressure for simulated rods.....	49
Figure 26: Temperature comparison between diffusivity models.....	50
Figure 27: FGR comparison between diffusivity models	50
Figure 28: EOL plenum pressure comparison between diffusivity models	50
Figure 29: Schematic of TRISO fuel particle.....	52
Figure 30: Production of Hi-Nicalon fibers (Ishikawa, 1994)	54
Figure 31: Comparison of failure behavior for monolith (left) and multilayer composite (right) tubing (Carpenter, 2010).....	56
Figure 32: Cross-sectional SEM views of three-layer (left) and two-layer (right) samples.....	57
Figure 33: Graphic of sample architectural and geometric terminology.....	60
Figure 34: Overview of the three architectures investigated	60
Figure 35: Cross-sectional SEM view showing two-layer architecture	60
Figure 36: Typical GAOE sample and SEM close-up.....	61
Figure 37: Typical GACE-A sample (left) and GACE-B sample (right) with SEM close-ups.....	62

Figure 38: Schematic of the internal pressurization test facility	64
Figure 39: Photograph of strain gage (ruler increments 1/16 inch)	65
Figure 40: Diagram of half-bridge used for strain gage measurement.....	65
Figure 41: Strain gage curing jig with brass sample.....	66
Figure 42: Strain gage validation setup.....	67
Figure 43: Strain gage validation data	68
Figure 44: Pressurization test validation data	69
Figure 45: Photograph of GAOE sample undergoing pressurization test	70
Figure 46: Endplug joint strength test facility.....	71
Figure 47: Failure characteristics of valid dummy tests	72
Figure 48: Diagram of thermal-shock facility.....	73
Figure 49: Diagrammatic representation of the high-temperature steam oxidation facility.....	75
Figure 50: Oxidation regime for SiC (Lee Y. , McKrell, Yue, & Kazimi, 2013)	76
Figure 51: XCT images of typical GAOE sample (left), GACE-A sample (middle), and endplug region (right)	77
Figure 52: Comparison of original grayscale image (left) with threshold processed (middle) and moving average processed (right) Boolean images.....	78
Figure 53: Void fraction algorithm flowchart	79
Figure 54: Original grayscale image (left) and joint scan region with joint voids (right).....	80
Figure 55: Endplug joint void fraction algorithm flowchart.....	80
Figure 56: Sample density algorithm flowchart.....	80
Figure 57: Void height algorithm flowchart.....	81
Figure 58: XCT image distortion due to strain gage on bottom left	81
Figure 59: Axial variation of void fraction for GAOE series.....	83
Figure 60: Axial variation of void fraction for GACE-A series.....	84
Figure 61: Axial variation of void fraction for GACE-B series.....	84
Figure 62: Histogram of void heights for GAOE series.....	85
Figure 63: Histogram of void heights for GACE-A series.....	86
Figure 64: Histogram of void heights for GACE-B series.....	86
Figure 65: Comparison of void morphology and sample architecture	88
Figure 66: Observed dependence of CMC void fraction on interlace angle.....	88
Figure 67: Bimodal void height distribution for GACE-B series	89
Figure 68: Thermal conductivity for 2-D Nicalon CG/SiC composites (Fenici, Rebelo, Jones, Kohyama, & Snead, 1998)	90
Figure 69: SEM cross-sectional view of GAOE 4 showing entrances to the CMC void network at the cut surfaces	91
Figure 70: Axial distribution of joint void fraction for GACE samples.....	92
Figure 71: Axial distribution of joint thickness for GACE samples	92
Figure 72: Comparison of joint voids for GACE 5 (left) and GACE 4 (right)	93
Figure 73: Comparison of joint thickness for GACE 7 (left) and GACE 3 (right).....	94
Figure 74: Comparison of joint length for GACE 8 (left) and GACE 6 (right)	94
Figure 75: Approximated relative joint strengths of GACE samples from XCT analysis	96

Figure 76: Stress-strain behavior for GAOE 2	98
Figure 77: Pushrod load versus displacement curves for as-received GACE samples	99
Figure 78: Cross-sectional view of GAOE 2 and fragment after pressurization testing.....	100
Figure 79: GAOE 2 sample before (left) and after (right) pressurization testing.....	100
Figure 80: Endplug post-pushout characteristics for GACE 2 (A, left) and GACE 6 (B, right)	100
Figure 81: XCT analysis of GACE 2 showing location of tube fracture (red line)	101
Figure 82: Stress-strain comparison between thermal-shock and as-received GAOE samples	102
Figure 83: Pushrod load versus displacement comparison between thermal-shock and as-received GACE-A samples	103
Figure 84: Pushrod load versus displacement comparison between thermal-shock and as-received GACE-B samples	104
Figure 85: Lateral view of failure characteristics of GAOE 5 (left) and GAOE 6 (right).....	105
Figure 86: Cross-sectional view of the failure characteristics for GAOE 5 (left) and GAOE 6 (right).....	105
Figure 87: Endplug failure characteristics for GACE 1 (left), GACE 5 (middle), and GACE 8 (right).....	106
Figure 88: XCT analysis of GACE 1 (left), GACE 5 (middle), and GACE 8 (right) showing location of tube fracture (red line).....	106
Figure 89: Comparison of as-received cross-section for GACE 4 (left) and GAOE 4 (right)	109
Figure 90: Stress-strain comparison between oxidized and as-received GAOE samples	110
Figure 91: Comparison of weight change and failure stress for oxidized GAOE samples	111
Figure 92: Pushrod load versus displacement comparison between oxidized and as-received GACE-A samples	112
Figure 93: Pushrod load versus displacement comparison of oxidized and as-received GACE-B samples	113
Figure 94: Lateral photographs of GAOE 3 (left), GAOE 4 (middle), and GAOE 1 (right) after testing	114
Figure 95: Cross-sectional photographs of GAOE 3 (left), GAOE 4 (middle), and GAOE 1 (right) after testing	114
Figure 96: Endplug failure characteristics for GACE 3 (A, left) and GACE 4 (B, right).....	115
Figure 97: Photographs of the failed CMC surface in the tube (left) and on the endplug (right) for GACE 4	115
Figure 98: XCT analysis of GACE 3 showing location of tube fracture (red line)	115
Figure 99: Comparison of as-received and thermal-shock results for all series.....	117
Figure 100: Comparison of as-received and oxidized results for all series.....	118
Figure 101: Unique regimes of stress-strain behavior for GAOE 2	119
Figure 102: SEM view of failure location for GAOE 2 showing freed fibers	120
Figure 103: SEM view of fragmented intra-tow matrix for GAOE 2	121
Figure 104: Joint comparison between GACE 2 (A, left) and GACE 6 (B, right)	122
Figure 105: SEM view of CMC region of GAOE sample showing fragmented matrix among exposed fibers	122
Figure 106: Cross-sectional SEM image of GAOE 2 showing exposed fibers.....	123
Figure 107: Lateral SEM image of GAOE 2 showing exposed fibers	123
Figure 108: Lateral SEM image of GAOE 2 showing cracked EBC	123
Figure 109: Cross-sectional SEM view of GACE 2 endplug joint showing large void	124

Figure 110: Cross sectional SEM view of GACE 2 endplug joint showing voids.....	124
Figure 111: Cross-sectional SEM view of CMC region still attached to endplug	124
Figure 112: SEM view of joint inside tubing for GAOE 6 showing voids	125
Figure 113: Lateral SEM view comparison of post-thermal-shock sample (left) with as-received sample (right)	126
Figure 114: Cross-sectional SEM view comparison of post-thermal-shock sample (left) with as-received sample (right).....	126
Figure 115: SEM view of failure location in thermal-shock sample showing fiber pullout	127
Figure 116: XCT comparison of joints for GACE 1 (left) and GACE 2 (right).....	128
Figure 117: XCT comparison of joints for GACE 5 (left) and GACE 6 (right).....	128
Figure 118: SEM views of failure location for GAOE 5 (left) and GAOE 6 (right) showing exposed fibers.....	129
Figure 119: SEM views of failure location for GAOE 5 (left) and GAOE 6 (right) showing fragmented matrix.....	130
Figure 120: Lateral SEM view of failure location for GAOE 5	130
Figure 121: Cross-sectional SEM view of failure location for GAOE 6	131
Figure 122: Cross-sectional SEM view of endplug joint for GACE 1 showing void	131
Figure 123: Cross-sectional SEM view of endplug joint for GACE 5 showing void	131
Figure 124: Cross-sectional SEM view of CMC remaining attached to endplug for GACE 5	132
Figure 125: Comparison of a GAOE sample before (left) and after (right) oxidation.....	133
Figure 126: Lateral SEM view of GAOE 4 before (left) and after (right) oxidation	133
Figure 127: Cross-sectional SEM view of GACE 3 endplug showing faceted oxide morphology.....	134
Figure 128: Crystalline silica morphology (Costello & Tressler, 1986).....	134
Figure 129: Lateral SEM view of GACE 4 endplug showing textured and smooth oxide.....	135
Figure 130: Lateral SEM view of GACE 3 showing textured oxide morphology	136
Figure 131: Lateral SEM view of GACE 3 showing smooth and textured oxide.....	136
Figure 132: Lateral SEM view of GACE 4 showing cracked oxide coating	136
Figure 133: Lateral SEM view of endplug for GACE 4 showing cracks in silica	136
Figure 134: Lateral SEM view of GACE 4 endplug showing silica plate structure.....	137
Figure 135: Cross-sectional SEM views of oxidized GAOE 3 (left) and GAOE 4 (right) showing oxide formation in CMC voids	137
Figure 136: SEM view of silica formation filling GAOE 1 interior CMC void	138
Figure 137: SEM view investigating oxidation penetration at GAOE 1 interior CMC void	139
Figure 138: EDS analysis of GAOE 1 oxidation penetration from CMC voids into surrounding SiC.....	140
Figure 139: Illustration of stress-strain regimes important for oxidation behavior	142
Figure 140: Illustration of evolution of brittle failure for oxidized samples	143
Figure 141: Comparison of XCT images for GACE 3 (left) and GACE 2 (right).....	143
Figure 142: Comparison of XCT images for GACE 4 (left) and GACE 6 (right).....	144
Figure 143: Cross-sectional post-pushout SEM views of GACE 4 (left) and GACE 3 (right).....	145
Figure 144: Lateral SEM view of endplug joint region post-pushout for GACE 4	145
Figure 145: Lateral SEM view of failure location for GAOE 3 (left) and GAOE 4 (right)	146
Figure 146: Cross-sectional SEM view of failure location for GAOE 3 (left) and GAOE 4 (right)	147
Figure 147: Lateral SEM view of fiber pullout observed in GAOE 4.....	147

Figure 148: Lateral SEM view of failure location for GAOE 1	148
Figure 149: Steam flow path (left) and SEM view of top surface of GACE 3 endplug (right)	148
Figure 150: Cross-sectional SEM view of endplug joint (Area 2) and CMC (Area 3) for GACE 3	149
Figure 151: Lateral SEM view of endplug lapped surface for GACE 3	150
Figure 152: Comparison of results for all samples.....	151
Figure 153: Comparison of approximated and measured joint strengths for GACE samples	152

List of Tables

Table 1: Experimental testing performed in this work	22
Table 2: Thoria-urania test rods investigated in this work	35
Table 3: Thoria-plutonia test rods investigated in this work	39
Table 4: Typical parameters for 37-element bundle (adapted from Page (Page, 1976))	39
Table 5: Transport parameters for modified FRAPCON thoria-urania system and published data	43
Table 6: Transport parameters for FRAPCON urania system and published data.....	44
Table 7: Westinghouse PWR rods simulated in this work	47
Table 8: Comparison of results between different diffusivity models	49
Table 9: Properties of SiC fibers (Takeda, Sakamoto, Saeki, & Ichikawa, 1996).....	54
Table 10: Overview of architecture and geometry of samples.....	59
Table 11: Test matrix for GAOE samples	61
Table 12: Test matrix of GACE-A and GACE-B samples.....	62
Table 13: Strain gage validation results	67
Table 14: Pressurization test validation results	69
Table 15: Results of joint strength testing with dummy samples.....	72
Table 16: Test matrix for thermal-shock samples.....	73
Table 17: Oxidation test matrix for all samples	76
Table 18: Table showing XCT analysis test matrix with reasons for omitted tests.....	82
Table 19: Results of CMC XCT analysis for all samples	87
Table 20: Results of CMC XCT analysis for all series	87
Table 21: Results of endplug XCT analysis for GACE samples.....	93
Table 22: Strength test results for GAOE 2	98
Table 23: Joint strength test results for as-received GACE samples.....	99
Table 24: Strength test results for thermal-shock and as-received GAOE samples	103
Table 25: Pushout test results for thermal-shock and as-received GACE-A samples.....	104
Table 26: Pushout test results for thermal-shock and as-received GACE-B samples	104
Table 27: Oxidation weight change measurements for all series.....	108
Table 28: Strength test results for the oxidized and as-received GAOE samples.....	111
Table 29: Pushout test results for oxidized and as-received GACE-A samples.....	112
Table 30: Pushout test results for oxidized and as-received GACE-B samples.....	113
Table 31: EDS results for lateral view of GAOE 4.....	133
Table 32: EDS results for cross-sectional view of GACE 3 endplug.....	134
Table 33: EDS results for lateral view of GACE 4 endplug	135
Table 34: EDS results for lateral view of GACE 4 endplug plate structure.....	137
Table 35: EDS results for GAOE 1 oxidized interior void.....	138
Table 36: EDS results for oxidation penetration behavior in GAOE 1.....	139
Table 37: EDS results for lateral post-pushout GACE 4 endplug	145
Table 38: EDS results for cross-sectional view of top surface of GACE 3 endplug	148
Table 39: EDS results for view of endplug joint and CMC for GACE 3	149
Table 40: EDS results for endplug lapped surface of GACE 3	150

Table 41: Summary of results for all samples	151
Table 42: Summary of as-received properties for all series	153
Table 43: As-received GACE endplug joint properties	154
Table 44: Summary of post-thermal-shock properties for all series	155
Table 45: Summary of post-oxidation properties of all series.....	156

Nomenclature

AECL	atomic energy of Canada limited	kN	kilonewton(s)
°C	degrees Celsius	LOCA	loss of coolant accident
CMC	ceramic matrix composite	LWBR	light water breeder reactor
CVD	chemical vapor deposition	MIT	Massachusetts Institute of Technology
CVI	chemical vapor infiltration	mm	millimeter(s)
DAS	data acquisition system	MPa	megapascal(s)
DPA	displacements per atom	mSiC	monolithic Silicon Carbide
EDS	energy dispersive spectroscopy	NRC	Nuclear Regulatory Commission
EOL	end of life	PWR	pressurized water reactor
g/min	grams per minute	SEM	scanning electron microscope
GA	General Atomics	SiC	silicon carbide
GACE	General Atomics Close-Ended	TEP	transient eutectic phase
GAOE	General Atomics Open-Ended	VDC	volt(s), direct current
GPa	gigapascal(s)	XCT	x-ray computed tomography

1. Introduction

1.1. Motivation

Nuclear fuel cladding plays an essential role in preventing the release of radioactivity and conducting heat from the fuel into the coolant in a nuclear reactor, and cladding performance is critical during accident conditions to prevent radioactive release into the environment. One of the most important accident scenarios of a nuclear plant is the loss-of-coolant accident (LOCA). During a LOCA the cladding temperature rises to levels far higher than those seen during normal operation due to the lack of coolant available to remove the fuel's decay heat. Furthermore, the cladding can also be exposed to high-temperature steam due to the boiling of the coolant. This is especially important for a LOCA coupled with a prolonged station electrical blackout.

The cladding material used in today's light-water reactors (LWRs) is Zircaloy 4, which was developed as a replacement for stainless steel due to the steel's excessive stress-corrosion cracking (Locke, 1975). Additionally, Zircaloy also offers the advantages of lower neutron absorption cross-section and less corrosion in hot water and steam during normal operating conditions compared to stainless steel (Stehle, Kaden, & Manzel, 1975). The Zircaloy-4 used in modern reactors is composed of zirconium alloyed with tin, iron, chromium, and nickel to improve workability and reduce corrosion and hydrogen pickup (Stehle, Kaden, & Manzel, 1975). However, Zircaloy has several crucial limitations during normal and accident conditions. Because of hydrogen pickup and hydride formation, the Zircaloy embrittles and consequently limits peak allowable fuel burnup. Also, Zircaloy experiences exothermic oxidation above 1200°C and liberates hydrogen gas, thus causing a hydrogen explosion danger as was observed in the Fukushima nuclear accident.

Silicon Carbide (SiC) has been proposed as an alternate cladding material with potentially higher accident tolerance when compared to Zircaloy. Key parameters of accident tolerant fuel cladding are:

1. High melting temperature
2. Mechanical performance at high temperatures
3. High-temperature corrosion resistance
4. Maintain coolable fuel geometry
5. Satisfactory performance at normal operating conditions

SiC has a melting temperature nearly 1000°C higher than that of Zircaloy and retains much of its mechanical strength up to 1500°C (Snead, et al., 2007). Furthermore, SiC has been shown to be 1000 times less reactive with steam than Zircaloy during LOCA conditions (Lee, McKrell, & Kazimi, 2014). Despite the high-temperature and corrosion benefits of SiC, the accident tolerance of SiC cladding is severely limited by its lack of ductility. To combine the pseudo-ductile behavior of composite SiC and corrosion resistance of monolith SiC, multilayer SiC cladding has been investigated for its ability to serve as an effective cladding both during normal operation and during accident conditions. To date there is very little published data concerning the use of multilayer SiC composite cladding. Therefore this investigation is also motivated by the desire to expand the current knowledge base of SiC cladding.

1.2.Overview of Current LWR Cladding

It is important to understand the role of cladding in an LWR to assess cladding options and evaluate the viability of advanced cladding materials. Proposed cladding designs must still be mindful of the design space of LWR cladding, and performance during normal and off-normal conditions must be evaluated to determine the overall feasibility of any proposed LWR cladding.

1.2.1. LWR Cladding Overview

The purpose of the cladding in a nuclear reactor is to contain the radioactive fission products and fission gases, transfer heat from the fuel to the coolant, and maintain a coolable geometry for the reactor's fuel. In fulfilling these performance goals, the cladding must withstand challenging conditions. One of the most important challenges for the cladding is the ability to withstand corrosion and degradation during its residency in the core. To this end, the cladding must be able to operate in an aqueous environment at elevated temperatures for several years without failure. Furthermore, the cladding must be able to withstand mechanical loads such as flow-induced vibrations and thermomechanical stresses. However, due to the radiation field present in the core, the cladding must have good resistance to radiation and have limited neutron interaction. To this end, the cladding must have limited neutron-induced radiation damage and low transmutation, and the neutron absorption cross-section must be low to minimize the neutronic penalty of the cladding. All of these factors must be considered when assessing LWR cladding.

1.2.2. Limitations of Current PWR Cladding

Zirconium has entered into extensive use as nuclear fuel cladding and the industry has developed significant experience with its use and manufacturing. However the Zircaloy material used as today's LWR cladding has several shortcomings that lead to poor performance both during high-burnup steady-state operation and during accident scenarios.

Firstly, Zircaloy has key limitations during normal operation. Zircaloy embrittles during its residency in the core due to radiation damage, oxidation, and hydride formation (Yang, 2006). The embrittlement of Zircaloy leads to an increased risk of failure at high burnup and has resulted in the NRC imposing a maximum allowable burnup of 62 MWd/kgU (Nuclear Regulatory Commission). As modern reactors have the capacity to achieve burnup in excess of 62 MWd/kgU, this effectively limits the overall productivity and efficiency of the nuclear plant (Carpenter, 2010). An additional concern with Zircaloy cladding is that it can react with the fuel pellets and result in extreme corrosion of the wall thickness of the cladding (Carpenter, 2010).

Secondly, Zircaloy also has important deficiencies during accident conditions, with especially poor behavior during LOCA scenarios. Oxidation growth on Zircaloy cladding has been observed to increase exponentially as the cladding temperature rises above 300°C (Carpenter, 2010). Furthermore, if the Zircaloy temperature surpasses 1200°C it can experience an exothermic oxidation reaction with steam to produce volatile hydrogen gas, leading not only to severe corrosion of Zircaloy but also an explosion hazard. This condition has resulted in the imposition of strict guidelines for the emergency systems of nuclear power plants to prevent excessive Zircaloy temperatures (Nuclear Regulatory Commission). Although emergency core cooling systems (ECCS) are designed to limit the Zircaloy temperature to

below the 1200°C threshold, it is nonetheless possible that a severe accident could cripple the ECCS and reduce its capacity to maintain a Zircaloy temperature below 1200°C. The 2011 Fukushima-Daiichi incident illustrates this possibility, whereby the reaction between high-temperature Zircaloy cladding and water produced enough hydrogen gas to cause multiple hydrogen explosions in the reactor containment buildings. Finally, Zircaloy loses strength at high temperatures, leading to an increased risk of failure especially during accident scenarios during which the high-temperature cladding strength is most critical.

1.3. Accident Tolerant Fuels

The limitations of Zircaloy cladding during nuclear accident scenarios resulted in interest in advanced fuel rod materials that will have improved accident performance. Accident tolerant fuel (ATF) research has two primary arenas: improved fuel materials and improved cladding materials. Ultimately, ATF efforts are aimed at developing materials that will enhance the safety margin of the fuel during normal operating conditions and reduce the consequences of a nuclear accident.

1.3.1. Motivation and Description of Accident Tolerant Fuels

Research efforts in the ATF field strive to achieve nuclear fuel (both the fueled and unfueled components) with a higher safety margin and improved resistance to nuclear accident conditions. The first area of ATF research is in developing fueled materials that have improved performance over the UO₂ used in the reactors of today. To this end, numerous fueled materials have been researched, including UN and UO₂ with BeO additive. The first of these options, UN, presents a number of advantages over UO₂, including high density, high melting temperature, and high thermal conductivity (Ross, El-Genk, & Matthews, 1988), the latter two of which are the reasons for its attraction as an accident tolerant fuel. Because of the high thermal conductivity and melting point of UN, it would present a greater safety margin to melting during normal operating conditions, and would be more resistant to melting during accident conditions. Furthermore, the high density adds the benefit of greater heavy metal loading and consequently potentially longer fuel cycles. However, UN has not been implemented in commercial fuel due to its susceptibility to being dissolved by water and steam (Sunder & Miller, 1998), such as may occur after cladding failure. Another fueled material option is the use of UO₂ with BeO matrix. A BeO matrix would have a very high thermal conductivity and high melting point while exhibiting low neutron absorption and resistance to radiation (Sarma, Fourcade, Lee, & Solomon, 2006). The BeO would help channel heat from the interior of the fuel pellet to the surface, thereby reducing the centerline temperature and increasing the safety margin to fuel melting. However, implementation of BeO is hindered by its anisotropic crystal growth under irradiation and its production of helium during neutron irradiation (Sarma, Fourcade, Lee, & Solomon, 2006).

Another approach in the ATF field is the development of cladding materials that have improved accident performance over Zircaloy. Among the options that have been investigated are coated Zircaloy, new metallic alloys, and SiC cladding. The coated cladding philosophy is to use coatings consisting of FeCrAl alloys or ceramic particles with the goal of reducing hydrogen pickup and increasing cladding lifespan during accident conditions (Bragg-Sitton, 2014). Efforts have shown the FeCrAl coatings can delay Zircaloy oxidation during accident conditions by up to 180 minutes, and work is underway to assess the oxidation performance of ceramic coatings (Bragg-Sitton, 2014). However, whereas the coated cladding

efforts still retain Zircaloy as the primary cladding material and are only designed to delay cladding failure during accident conditions, the SiC ATF efforts are aimed at altogether replacing Zircaloy in favor of a cladding that has much greater accident tolerance and has a much larger margin to failure during accident scenarios. SiC cladding has the benefit of high corrosion resistance and a high melting temperature, in addition to good stability in a nuclear environment. Furthermore, to enhance the mechanical behavior of the SiC cladding, composites were developed which exhibit improved mechanical properties. The SiC composite allows for pseudo-plastic behavior, during which cracking within the composite allows the bulk to behave in a plastic manner despite the absence of any true plastic deformation. Furthermore, the composite experiences non-frangible failure behavior because the fibers help prevent catastrophic fragmentation after failure by helping to maintain the original geometry of the specimen.

1.3.2. Silicon Carbide for Nuclear Applications

In this work, SiC composites are investigated for use as LWR cladding. The SiC composites have been developed to capitalize on the corrosion resistance of SiC and the mechanical performance associated with composite architecture. However, the performance of the SiC composites depends on the manufacturing techniques and purity of the final product. It is important to understand the relationship between SiC fabrication and performance in a nuclear environment to assess the adequacy of SiC for use as LWR cladding.

The radiation resistance of SiC has been observed to be dependent on manufacturing techniques. Although SiC inherently has low activation and dimensional stability at high temperatures, the response of SiC to radiation is dependent on impurities (Fenici, Rebelo, Jones, Kohyama, & Snead, 1998). SiC with higher impurity content is significantly more susceptible to radiation than purer SiC and consequently somewhat incompatible with a nuclear environment. Furthermore, research has shown that SiC fibers containing impurities have significant strength degradation during irradiation, but fibers with greater crystallinity and less oxygen content show improved stability during irradiation (Bloom, 1998). Overall, the key to radiation performance of the SiC composites is the stability of the SiC fibers (Fenici, Rebelo, Jones, Kohyama, & Snead, 1998). Therefore, nuclear-grade SiC must be manufactured to minimize impurities in order to enhance radiation resistance.

The thermomechanical performance of SiC is also dependent on manufacturing. The room-temperature thermal-conductivity of SiC strongly depends on defects and impurities and can vary from 1 W/mK for nano-crystalline fibers up to 490 W/mK for high-purity single crystal SiC. The thermal-conductivity for industrial SiC composites is about 12 W/mK; the lower conductivity for composites is attributable to the as-manufactured matrix porosity, micro-cracks, and the grain size (Fenici, Rebelo, Jones, Kohyama, & Snead, 1998). Indeed, voids in the CMC are almost inevitable due to the difficulty of chemical vapor infiltration (CVI) at filling all inter-tow regions (Bloom, 1998). Because of the impurities and defects associated with the CVI SiC, the theoretical thermal conductivity of CVI SiC is only 40 W/mK whereas the thermal conductivity of chemical vapor deposition (CVD) SiC is 300 W/mK. (Fenici, Rebelo, Jones, Kohyama, & Snead, 1998). The thermal conductivity of SiC composites also has a strong dependence on radiation, with a substantial decrease between doses of 0-1 dpa (Fenici, Rebelo, Jones, Kohyama, & Snead, 1998). In comparison, Zircaloy cladding has a temperature-dependent thermal conductivity

which ranges from 13 W/mK at 300 K to 41 W/mK at 1800 K. Ultimately, the low thermal conductivity of SiC composites is a primary concern with the use of SiC as nuclear cladding. The manufacturing of SiC cladding must minimize voids, defects, and impurities to improve thermomechanical performance.

Overall, silicon carbide shows promise for nuclear applications when manufactured to minimize flaws and impurities. Although the SiC shows radiation resistance and as-received (non-irradiated) thermal conductivity that is somewhat comparable to that of Zircaloy, these properties are very sensitive to its fabrication. The manufacturing techniques employed in the fabrication of the samples investigated in this work are described in Section 3.3 below. Ultimately, because SiC shows promising performance as a cladding material, its macro-scale implementation as cladding must be evaluated for LWR performance.

1.4.Objectives and Scope

This work investigates the effect of thermal-shock and high-temperature steam oxidation conditions associated with LOCA scenarios on corrosion kinetics, microstructure, and mechanical performance of SiC cladding samples. Additionally, this work analyzes the as-received characteristics of the cladding specimens to evaluate their performance during normal reactor operating conditions. The cladding samples investigated in this work consist of 14 different specimens within three unique architectures and were provided by General Atomics (GA). The three architectures differ in weave pattern, displaying either two-tow or three-tow architecture and have different interlace angles and tow spacing. One series, termed GAOE, consists of 6 cladding specimens open on both ends and was used for investigation of the tube strength. The other two series, termed GACE-A and GACE-B, consist of respectively three and five cladding specimens open on one end and endplug-sealed on the other end. Architectural details of the samples investigated in this work are provided below in Section 4.1. An overview of the testing performed in this work is presented in Table 1.

Table 1: Experimental testing performed in this work

Test	Purpose
As-received strength testing	Evaluate mechanical properties of control sample not exposed to LOCA conditions
High-temperature quench followed by strength testing	Evaluate mechanical degradation of sample quenched after restoration of coolant flow following LOCA
High-temperature steam oxidation followed by strength testing	Evaluate mechanical degradation of sample exposed to high-temperature steam during LOCA

The objective of the tests outlined in Table 1 is to determine the mechanical degradation, the corrosion kinetics, the weakening mechanisms, and the failure modes of the SiC cladding samples at different LOCA conditions. Firstly, a sample is strength-tested as-received to obtain the baseline mechanical properties for the rest of the samples of that series. Secondly, samples undergo high-temperature thermal-shock tests followed by strength testing to evaluate the mechanical degradation when the cladding is quenched by the restoration of coolant flow after the LOCA. Finally, samples undergo high-temperature steam oxidation tests followed by a strength tests to evaluate the mechanical degradation when the cladding is exposed to steam during a LOCA. By comparing the test results among samples within one series, the mechanical degradation and corrosion behavior of the SiC cladding during a LOCA

can be better understood. Furthermore, by comparing the results between series, the influence of architecture on mechanical properties and corrosion behavior can be better understood.

This work also investigated the sample architecture using X-ray computed tomography (XCT). The XCT allowed for non-destructive examination of the sample architecture and enabled quantification of the void morphology within the CMC and joint regions of the samples as well as quantitative comparison of the endplug joint quality among the GACE samples. The XCT analysis was performed to provide better understanding of the void characteristics within the samples and allow for comparison of void morphology between architectures.

In summary, the objectives of this investigation are:

1. Improve the modelling ability for thorium-based fuels viable for use with SiC cladding
2. Simulate the effects of LOCA conditions on SiC cladding samples
3. Perform tests on SiC cladding samples to evaluate as-received performance
4. Evaluate mechanical degradation, corrosion kinetics, weakening mechanism, and failure modes of SiC samples due to LOCA conditions
5. Evaluate influence of sample architecture on cladding performance
6. Investigate internal void behavior of SiC samples
7. Provide data for realization of commercial SiC cladding
8. Identify areas of improvement for future research efforts

1.5. Thesis Organization

This thesis is divided into chapters as summarized below:

Chapter 2: Performance Modeling of Thorium-Based Fuels

This section presents Thorium-Uranium and Thorium-Plutonium mixed oxide fuels as two candidates for high-burnup fuels to be used with SiC cladding. The section updates and validates the fission gas release model for a fuel performance code against published experimental results for the fuels under consideration.

Chapter 3: Silicon Carbide Cladding

This chapter presents a discussion of the previous uses and research efforts associated with SiC and SiC composites. It outlines the motivation for SiC's use as an accident tolerant fuel material, and proceeds to describe the samples investigated in this work, including manufacturing methods.

Chapter 4: Experimental Methodology

This section discusses the samples that are investigated in this work and introduces the experimental facilities used in this work. Specifically, the internal pressurization test facility, joint strength test facility, thermal-shock test facility, and high-temperature steam oxidation facility are discussed as well.

Chapter 5: XCT Analysis of Cladding Specimens

The XCT analysis of the cladding samples investigated in this work is presented and discussed in this chapter. Of interest is the void fraction and void morphology in the CMC layer and in the endplug joint.

The results of the XCT analysis are discussed in relation to the expected consequences on the strength of the samples and in the oxidation mechanisms.

Chapter 6: Experimental Results

The results of the experimental testing of the cladding specimens as-received, after thermal-shock, and after high-temperature steam oxidation are discussed in this section. Furthermore, the failure modes observed for the samples is discussed, and the implications of the failure modes are analyzed.

Chapter 7: Discussion of Results

This chapter analyzes the experimental results for the as-received, thermal-shock, and high-temperature steam oxidation tests. The results are used to gain insight into the microstructural behavior of the cladding specimens and evaluate their accident tolerance and mechanical behavior.

Chapter 8: Conclusions and Recommendations for Future Work

In this chapter, the conclusions and results of this work are presented and the practicality of SiC cladding is assessed for the conditions investigated in this work. Additionally, topics for future research efforts that will expand upon this work are identified.

2. Performance Modeling of Thorium-Based Fuels

2.1. Motivation

The use of thoria (ThO_2) in place of urania (UO_2) as the fuel matrix is motivated by numerous advantages of thoria over urania. Thorium is more abundant than uranium, produces fewer transuranic elements, and can allow for higher burnup (Lombardi, Luzzi, Padovani, & Vettraino, 2008) (Karam, et al., 2008). Furthermore, when compared to urania-based fuels, thoria-oxide based fuels are also appealing for the 340°C higher melting point, 50% higher thermal conductivity, and greater inertness (Karam, et al., 2008), as well as the lower fission gas release (FGR). Additionally, thoria has been investigated as a fuel matrix for burning plutonium resulting from weapons manufacture in reactors similar to the current LWRs (Andrews, Sukjai, Pilat, Shirvan, & Kazimi, 2014). Using a thoria fuel matrix in place of a urania matrix can allow a PWR to be loaded with more plutonium and maintain negative void reactivity coefficients while producing minimal plutonium (Lombardi, Luzzi, Padovani, & Vettraino, 2008). Thus, thoria-urania and thoria-plutonia mixed oxide (MOX) fuels have several distinct advantages that have motivated investigation into their implementation in LWRs.

The benefits of thoria-based fuels cannot be fully exploited using current Zircaloy cladding due Zircaloy's limitations. As discussed above, the maximum burnup in current Zircaloy cladding is restricted to 62 MWd/kgU due to corrosion and embrittlement in LWR conditions; thus SiC has been investigated as a cladding that can better utilize thoria fuels due to enhanced performance at high burnup. However, there are key issues that must be addressed before successful implementation of SiC-clad thoria fuels. Firstly, because of the high strength of SiC cladding, the cladding does not creep down onto the fuel, thus resulting in a large fuel-cladding gap that increases the fuel temperature (Andrews, Sukjai, Pilat, Shirvan, & Kazimi, 2014). Secondly, the inherently lower thermal conductivity of SiC cladding upon irradiation would further increase the fuel temperature during normal operation. Finally, the high temperature of the fuel would result in increased FGR due to the dependence of FGR on fuel temperature, resulting in higher EOL fuel pressures for the SiC-clad thoria fuel.

To successfully implement thoria fuels in SiC cladding, it is essential to be able to effectively predict the FGR of thoria fuels to minimize the risk of cladding failure at EOL conditions. As discussed in Section 3.2, the best way to minimize the SiC cladding's swelling-induced EOL failure risk is to make the cladding thin (Ben-Belgacem, Richet, Terrani, Katoh, & Snead, 2014). In order to prevent the thin cladding from rupturing due to excessive internal pressure, the accurate prediction of thoria fuel FGR is essential. This section attempts to update the FRAPCON-3.4-MIT code to more accurately predict the FGR from thoria fuels to allow for better modeling of the EOL plenum pressure for SiC-clad thoria LWR fuel rods.

2.2. Fission Gas Release Mechanism

The general FGR mechanism is described by Long (Long, 2002) and consists of several steps, beginning with the production of the gas atoms, and culminating in the release of the fission gases to the free volume of the plenum.

The first important step in FGR involves the transport of the fission gases from within the grain to the grain boundary. First, the fission produces insoluble gas atoms, consisting primarily of xenon and

krypton, which coalesce within the grain to form fission gas bubbles. The bubbles then migrate from within the grain to the grain boundary by a diffusion process and are eventually released into the grain boundary. However, the diffusion of the gas bubbles to the grain boundary is influenced by imperfections within the fuel lattice such as vacancy clusters or dislocation loops produced by fission fragments which trap the gas bubbles either temporarily or permanently (Matzke, 1980). Because of this mechanism, the gas bubble apparent diffusion decreases substantially with increasing burnup due to the increased radiation damage within the matrix.

Once the fission gas bubbles have diffused through the matrix into the grain boundary, the bubbles can be destroyed by fission fragments or radiation and the bubbles can dissolve back into the fuel matrix via the re-resolution mechanism due to trapping by lattice imperfections. However, the gas bubbles also coalesce in the grain boundary, forming larger bubbles and resulting in larger gas concentrations within the grain boundary. Eventually, after enough gas bubble coalescence within the grain boundary, a critical concentration is achieved after which the gas bubble is released into the free volume of the fuel.

Once the fission gasses are released from the fuel, they can collect in the central void of the pellet (if such a void exists), in the plenum, in the gap, and in the inherent porosity of the fuel. Fission gas release results in an increased plenum pressure, and it also reduces the fuel-clad gap conductance due to the poor thermal conductivity of the fission gasses relative to the helium fill-gas. Thus, fission gas release has deleterious consequences on the thermomechanical performance of the fuel because, all else being constant, it increases both the temperature and plenum pressure of the fuel.

2.3. FRAPCON Fission Gas Release Model

The FRAPCON code is used to calculate the thermomechanical parameters of LWR fuel rods during steady-state operation and long-term burnup (Geelhood & Luscher, 2014). The code calculates the temperature, pressure, and mechanical deformation of the fuel rod based on the power history and coolant conditions by modeling heat conduction, cladding deformation, fuel-cladding interaction, fission gas release, and cladding oxidation (Geelhood & Luscher, 2014). Although FRAPCON implements several FGR models, this investigation only focuses on the Forsberg-Massih model because the Massih model is recommended by the developers of the code.

2.3.1. Forsberg-Massih Model

The Forsberg-Massih model (Forsberg & Massih, 1985) begins with a solution to gas diffusion for constant production and properties within a spherical grain. However, the model's analysis is complicated by the treatment of partial resolution of the gasses at the grain boundary into the grain. Therefore, the model solves the gas diffusion equation for the case where there is resolution of the gas on the grain surface. Forsberg and Massih solved the integro-differential equation for the gas particle density to determine the time-dependent accumulation of the gasses at the grain boundary.

Forsberg and Massih then imposed a saturation criterion for gas release from the grain boundary to the free volume of the fuel. Essentially, after a critical concentration of fission gasses have accumulated at the grain boundary, the gas is released to the fuel via the formation of tunnels through the fuel. After

gas release from the grain boundary, the tunnels close due to deformation of the fuel, and the process repeats.

The FRAPCON code modified the original Massih model by adjusting the fission gas re-resolution parameter implemented in the model. In the FRAPCON Massih model, the fission gasses transferred to the grain boundary are determined without regard to gas resolution. Then, the gasses in the grain boundary are partitioned into accumulated and resolved gasses using an adjustable parameter. The modification was implemented because the gas resolution treatment implemented in the original Massih model did not appear to give realistic resolution results.

The mathematics of the Forsberg-Massih model implemented in FRAPCON can be found elsewhere (Geelhood & Luscher, 2014) and therefore will not be reproduced here. However, integral in the model's determination of the fission gas release is the accurate implementation of a temperature-dependent diffusion coefficient for modeling the fission gas diffusion through the grain. The FRAPCON Massih model uses a low-temperature and a high-temperature relationship to determine the diffusion coefficient. However, because FRAPCON is designed primarily to simulate UO_2 , the diffusion coefficients determined by the model do not necessarily accurately model thorium-based fuels. For UO_2 , the high-temperature diffusion coefficient relationship (where T is temperature in degrees Kelvin) is given as:

$$D_{UO_2} = 2.14 \times 10^{-13} e^{\frac{-22884 \times 1.15}{T}}$$

However, the diffusion coefficient is not permitted to fall below the low-temperature diffusion coefficient. The low-temperature diffusion coefficient relationship (where T is temperature in degrees Kelvin) is given as:

$$D_{UO_2} = 1.51 \times 10^{-17} e^{\frac{-9508}{T}}$$

Thus, the diffusion coefficient relationship used by the FRAPCON Massih model is either the high-temperature or low-temperature diffusion coefficient relationship, depending on which is greater. The diffusion coefficient for UO_2 plotted as a function of temperature is shown in Figure 1. In the figure, it can be observed that the diffusivity model changes at a temperature of approximately 1750 K, corresponding to the point when the diffusivity model changes from the low-temperature to the high-temperature model.

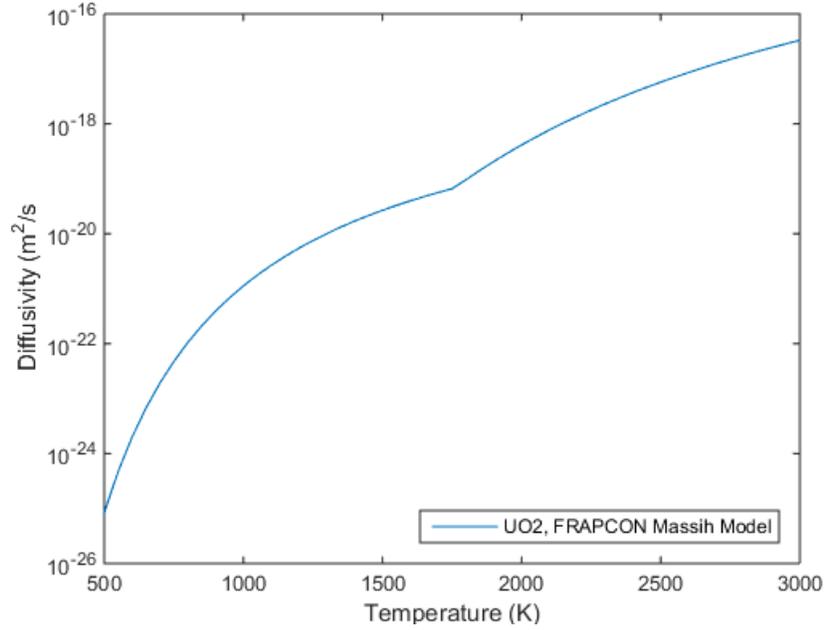


Figure 1: Diffusivity for UO₂ implemented in FRAPCON Massih model

2.4. FRAPCON Modifications

Because FRAPCON was not designed to model thoria-based fuels, modifications must be made to the code to allow for performance analysis of thoria fuels. The modifications have been an ongoing effort at MIT, starting with those modifications made by Long to FRAPCON-3.2 (Long, 2002). Although Long modified the diffusion coefficients in the FRAPCON-3.2 Massih model to more accurately predict the FGR for thoria-urania fuels, it was discovered that Long's modifications to the FRAPCON Massih model did not give accurate FGR results in FRAPCON-3.4-MIT (the version used in this work) due to various changes made in the code between FRAPCON-3.2 and FRAPCON-3.4. Therefore, this work intends to update the FRAPCON-3.4-MIT Massih model to more accurately predict the FGR of thoria-urania fuel.

In addition to modeling thoria-urania fuel, it was desired to model thoria-plutonia fuel because of its advantages in plutonium burning over traditional urania-plutonia MOX. Therefore, this work also intends to suggest modifications to the FRAPCON-3.4-MIT Massih model to allow for more accurate calculation of the FGR from thoria-plutonia fuel.

2.4.1. Thermal Conductivity Models

One of the most important factors influencing FGR is the fuel temperature, as higher fuel temperatures lead to significantly increased FGR. Therefore, it is important to verify the accuracy of the FRAPCON-3.4-MIT thermal conductivity models prior to investigating the FGR models. The FRAPCON-3.4-MIT thermal conductivity model begins by calculating the phonon transport thermal conductivity for pure urania, thoria, and plutonia (where T is temperature in degrees Kelvin):

$$k_{phonon, UO_2, 95\%TD} = \frac{1}{4.52E - 2 + 2.46E - 4 * T}$$

$$k_{phonon, ThO_2, 95\%TD} = \frac{1}{4.2E - 4 + 2.25E - 4 * T}$$

$$k_{phonon, ThO_2, 97\%TD} = \frac{1}{4.6E - 3 + 2.83E - 4 * T}$$

The equations are then corrected to 100% theoretical density (where %TD is the percentage theoretical density used in the original phonon transport thermal conductivity relation):

$$k_{phonon, 100\%TD} = \frac{k_{phonon} \left(1 + \frac{1 + \%TD}{2}\right)}{\%TD}$$

If the fuel material is a pure substance, then the corresponding phonon transport relation is used. However, if the fuel is a mixture (for example, (Th-U)O₂), then the Abeles mixing method (Abeles, 1963) is used to obtain an effective phonon transport thermal conductivity for the mixture. Once the phonon thermal conductivity of the fuel material has been determined, the electron transport thermal conductivity is determined:

$$k_{electron} = \frac{3.5E9}{T^2} * e^{\frac{-E}{k_b T}}$$

Where T is temperature in degrees Kelvin, k_b is the Boltzmann constant, and E is the activation energy of the fuel material. The effective thermal conductivity of the fuel is the sum of the phonon transport conductivity and the electron transport conductivity:

$$k_{total} = k_{phonon} + k_{electron}$$

The FRAPCON-3.4-MIT thermal conductivity models were compared against published experimental thermal conductivity for urania, thoria-urania, and thoria-plutonia MOX. Although there have been numerous publications concerning the thermal conductivity of oxide fuels, there is significant spread in the experimentally-obtained thermal conductivity values among different authors. Ronchi (Ronchi, Sheindlin, Musella, & Hyland, 1999) noted that the literature concerning urania has a 15% spread in the experimentally-obtained thermal diffusivity and a 30% spread in the heat capacity. Ronchi noted that the extreme spread in experimental data of urania is attributable in part to measurement precision and in part due to uncontrolled physical differences in the samples, such as variation in oxygen content and specimen microstructure. Ronchi was of the opinion that the physical differences among the samples were the more important source of uncertainty in the experimental results.

2.4.1.1. Urania Thermal Conductivity

To ensure that the FRAPCON-3.4-MIT urania thermal conductivity model was accurate, it was tested against the experimental results of Ronchi (Ronchi, Sheindlin, Musella, & Hyland, 1999) and Bates (Bates, 1970) for urania fuels from approximately 500-3000 K. Both the Ronchi and the Bates results were obtained using laser-flash techniques. The results of the comparison between the experimental results and FRAPCON-3.4-MIT are presented in Figure 2 and Figure 3. In the figures, it can be observed that the Ronchi results agree very well with the FRAPCON-3.4-MIT model (2% mean error magnitude),

whereas FRAPCON-3.4-MIT appears to under predict the Bates results (6% mean error magnitude). Overall, the Ronchi results are likely more accurate than the Bates results owing to the comparatively small spread of the Ronchi results and the fact that, because of technological advances in the 30 years between the Bates and Ronchi studies, Ronchi was able to obtain the results via the simultaneous measurement of thermal diffusivity and heat capacity on the same sample. Because of the good correspondence between the FRAPCON-3.4-MIT urania thermal conductivity mode and the Ronchi results, the FRAPCON-MIT urania model is considered to be accurate at modeling the thermal conductivity of urania fuel.

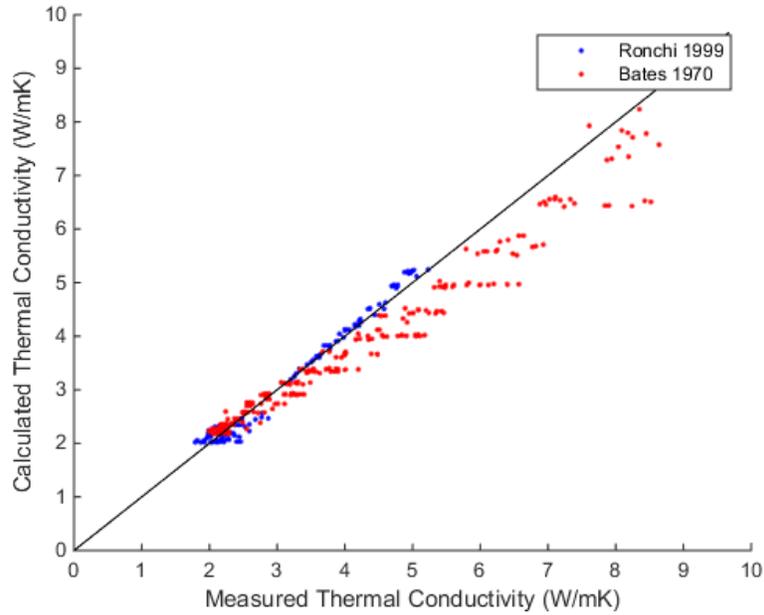


Figure 2: Thermal conductivity comparison for urania

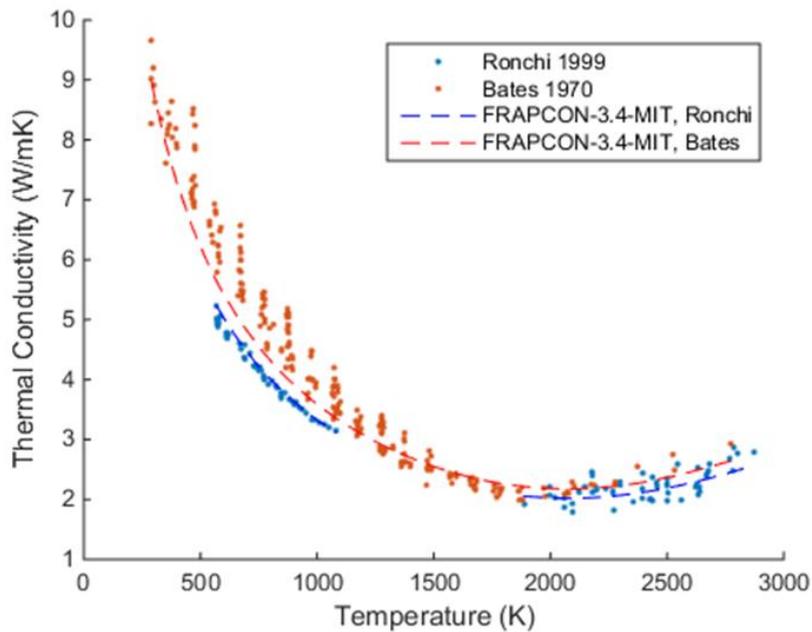


Figure 3: Urania thermal conductivity versus temperature comparison

The UO_2 phonon transport model used in FRAPCON-3.4-MIT is based on the Nuclear Fuels Industries (NFI) model (Ohira & Itagaki, 1997), except that the FRAPCON-3.4-MIT model includes the influence of electron thermal transport. The effect of the electron transport model can be seen in Figure 4, where the FRAPCON-3.4-MIT model and the NFI model diverge at temperatures above 1500 K because of electron-transport's contribution to heat conduction. Long also implemented a high-temperature heat transfer addition to the NFI model in his work and argued that radiative heat transfer should cause an increase in thermal conductivity at high temperatures (Long, 2002). Figure 4 shows a comparison between Long's results and the FRAPCON-3.4-MIT model, where both models produce almost identical results for UO_2 . Although Long implemented a radiative heat transfer relationship instead of electron transport, he nevertheless identified the need for a high-temperature addition to the standard NFI model to more accurately model UO_2 's thermal conductivity at high temperatures, and his work supports the FRAPCON-3.4-MIT UO_2 thermal conductivity model.

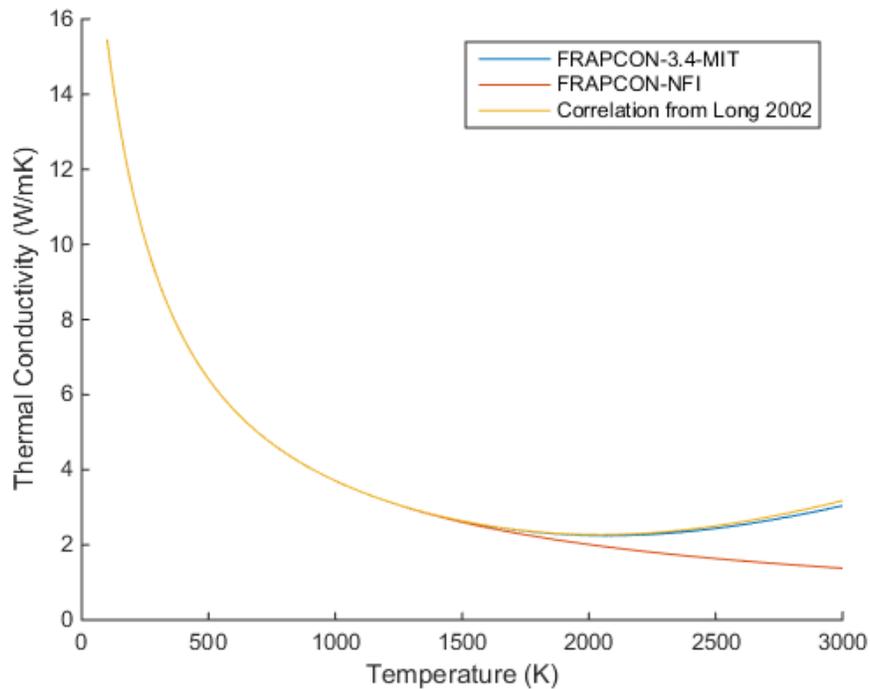


Figure 4: Comparison of FRAPCON urania thermal conductivity models

2.4.1.2. *Thoria-Urania Thermal Conductivity*

The FRAPCON-3.4-MIT thoria-urania thermal conductivity model was compared against the experimental results of Belle (Belle & Berman, 1984), Basak (Basak, Sengupta, & Ganguly, 1989), Murabayashi (Murabayashi, 1970), Pillai (Pillai & Raj, 2000), TECDOC-1496 (IAEA, 2006), and Springer (Springer, Eldridge, Goodyear, Wright, & Langedrost, 1968). The comparison between the experimental results and the FRAPCON-3.4-MIT results are presented in Figure 5 and Figure 6.

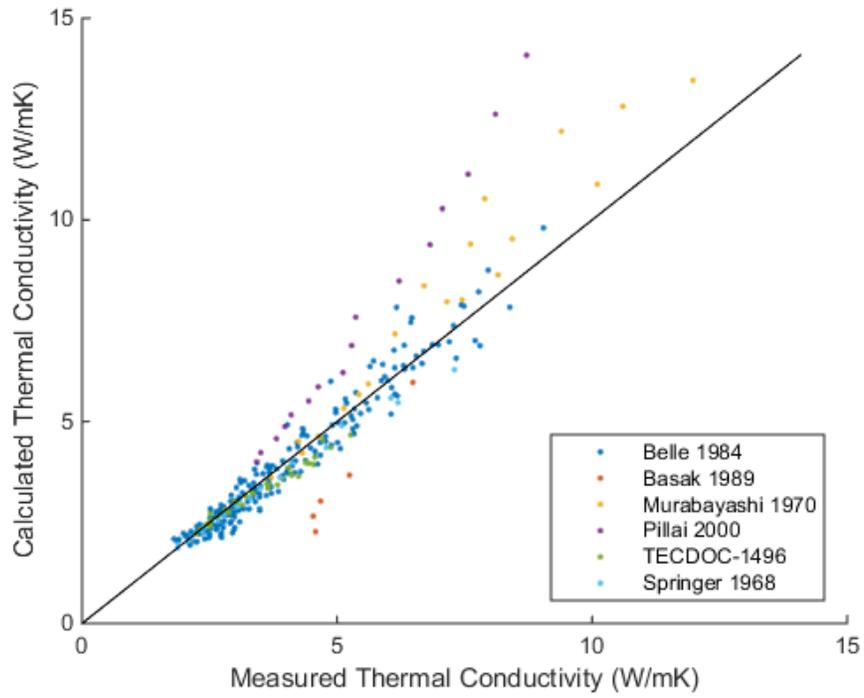


Figure 5: Thermal conductivity comparison for thoria-urania

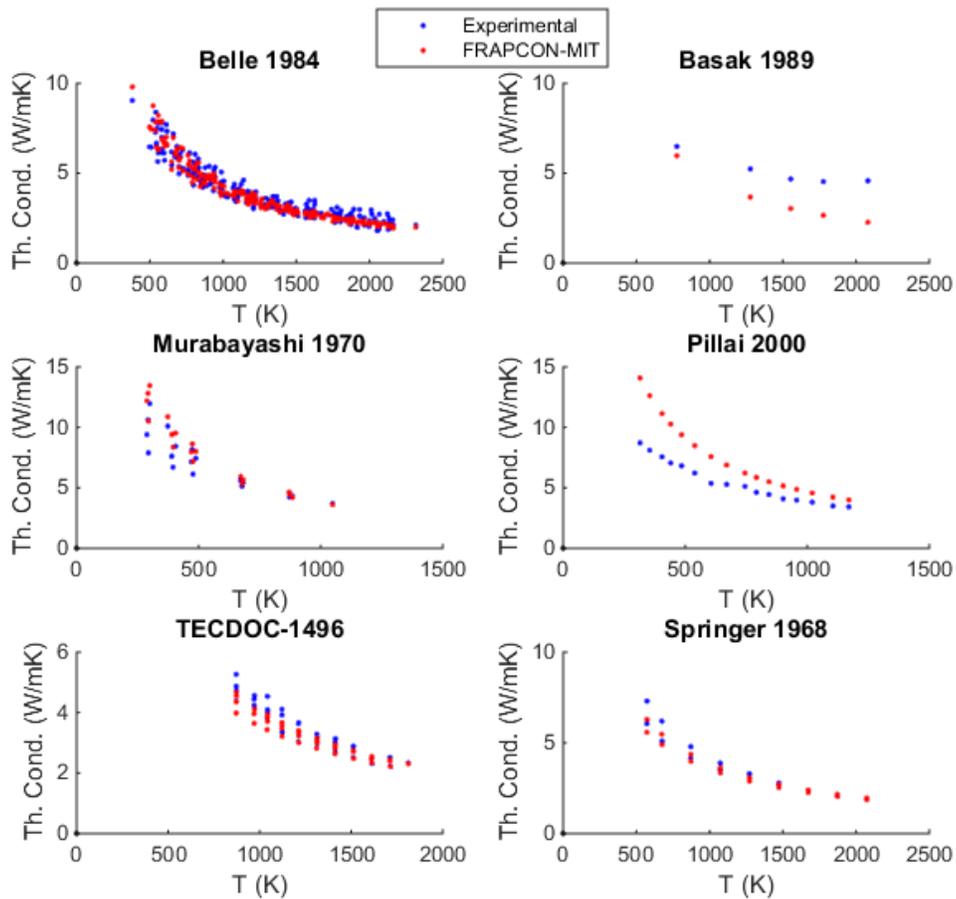


Figure 6: Thoria-urania thermal conductivity versus temperature comparison

Similar to the data for urania, the data for thoria-urania had significant spread among the various studies. The FRAPCON-3.4-MIT thoria-urania model best matches the Belle (7% mean error magnitude), TECDOC (5% mean error), and Springer (5% mean error magnitude) data, while it under predicts the Basak data (33% mean error) and over predicts the Murabayashi (12% mean error magnitude) and Pillai (33% mean error magnitude) data. Much of the spread in the thoria-urania data must be attributable to impurities and inhomogeneity among the different samples investigated. Additionally, experimental differences among the different investigations (most authors used the laser flash technique, but Pillai used a steady state axial heat flow apparatus) possibly led to additional spread in the data. Overall, the FRAPCON-3.4-MIT model fairly accurately predicts much of the experimental data.

2.4.1.3. *Thoria-Plutonia Thermal Conductivity*

The FRAPCON-3.4-MIT thoria-plutonia model was compared to the experimental results of Cozzo (Cozzo, Staicu, Somers, Fernandez, & Konings, 2011). The experimental results were obtained using a laser-flash technique similar to that used in the urania and thoria-urania cases outlined above. The comparison between Cozzo’s results and the FRAPCON-3.4-MIT model is presented in Figure 7 and Figure 8.

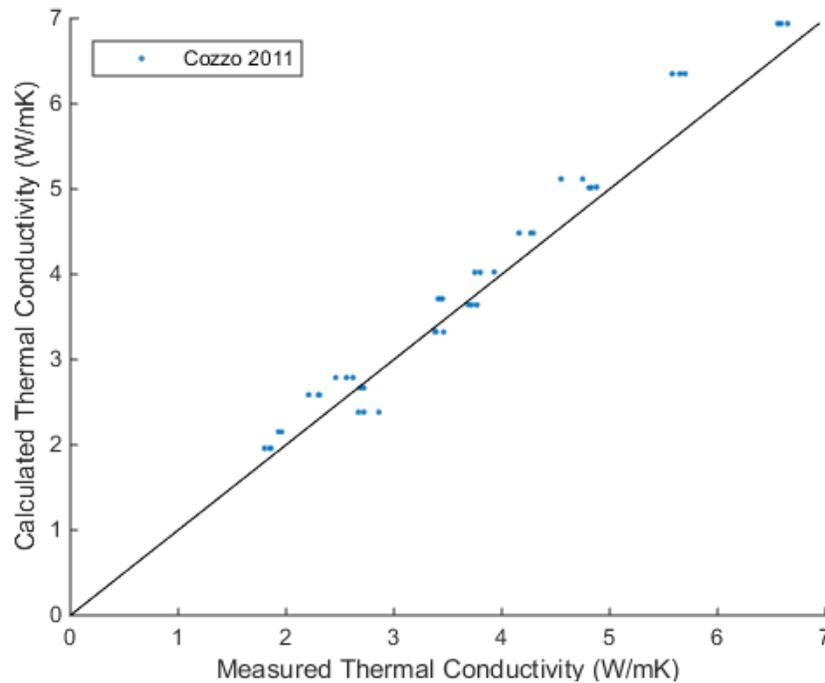


Figure 7: Thermal conductivity comparison for thoria-plutonia

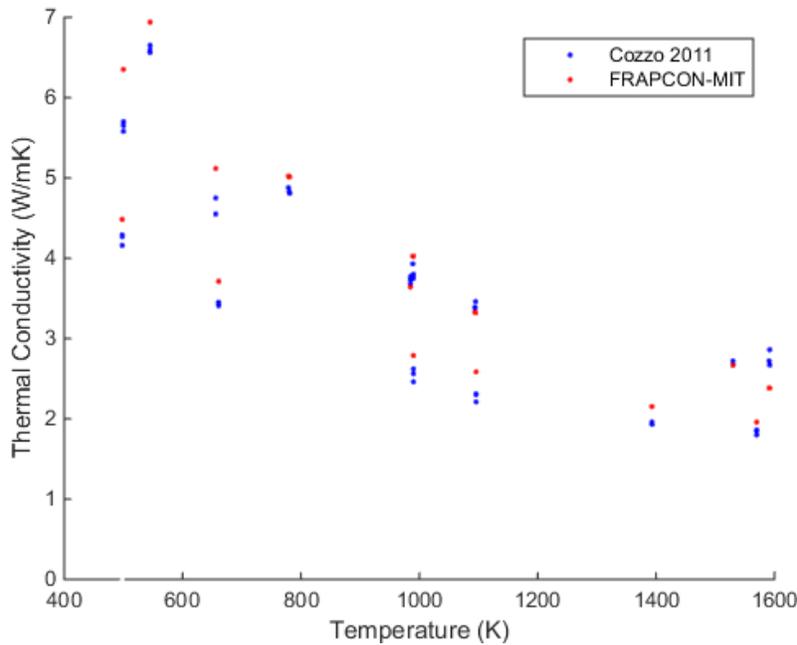


Figure 8: Thoria-plutonia thermal conductivity versus temperature comparison

The validation of the thoria-plutonia FRAPCON-3.4-MIT model is encumbered by the paucity of data concerning thoria-plutonia thermal conductivity. Because significant variation was observed in the thermal conductivity data for the urania and the thoria-urania experimental cases, it can be expected that there would be similar variation in thoria-plutonia cases. Therefore, more studies of thoria-urania thermal conductivity would be required to more definitively evaluate the FRAPCON-3.4-MIT thoria-plutonia model. Nevertheless, the model predicts the Cozzo data well (7% mean error magnitude).

2.4.2. Fission Gas Release Models

2.4.2.1. Methodology

In order to evaluate the FRAPCON-3.4-MIT FGR models for thoria-urania and thoria-plutonia fuel, test rods were simulated in FRAPCON-3.4-MIT and the calculated FGR was compared to the experimentally-measured fission gas release. The low-temperature and high-temperature diffusion coefficients were adjusted in FRAPCON-3.4-MIT until the calculated FGR best predicted the experimental FGR. However, this analysis is hindered by the limited number of test rod results available in the literature.

Fitting the FRAPCON-3.4-MIT FGR model to experimental test rods is necessary because the existing experimental diffusivity relations have significant spread and don't reflect the diffusivity that works best in FRAPCON (see Section 2.5.2). FGR must be empirically fitted in FRAPCON-3.4-MIT because FGR, thermal conductivity, relocation, and swelling are all coupled phenomena empirically fitted in FRAPCON.

2.4.2.2. Thorium-Uranium Mixed Oxides

To evaluate and update the FRAPCON-3.4-MIT Massih model for more accurate FGR calculation of thoria-urania fuel, thoria-urania test rods were simulated in FRAPCON-3.4-MIT, and the calculated FGR was compared to the experimentally-measured FGR. The data for the rods investigated in this work originated from the light water breeder reactor (LWBR) program, which irradiated numerous thoria and

thoria-urania test rods as discussed in Goldberg (Goldberg, et al., 1978). Sufficient data (including geometry and power history) for seven test rods was available in the literature to allow for simulation in FRAPCON. Parameters of the test rods investigated in this work are presented in Table 2.

Table 2: Thoria-urania test rods investigated in this work

	79-442	79-506	79-349	79-375	79-405	79-481	79-576
Wt% Thoria	93.4	82.9	80	70	80	91.5	96.9
Fuel %TD	96	95.3	95	92	94	98	97.5
Pellet Diameter (mm)	5.3	11.7	16.6	16.4	16.5	5.2	13.8
Cladding Diameter (mm)	6.5	13.4	18.2	18.2	18.2	6.4	15.6
Diametric Gap (mm)	0.18	0.18	0.10	0.30	0.15	0.20	0.10
Peak Linear Power (kW/m)	34.0	47.5	73.7	63.5	72.7	27.1	45.5
Peak Burnup (MWd/kgHM)	45.3	21.1	9.7	10.0	11.3	49.9	28.2
Axial Peaking Factor	1.43	1.41	1.33	1.33	1.33	1.00	1.32
Measured FGR %	0.5	2	1.9	8.4	15	2.8	0.4

Although many properties for the rods are given in the literature, the densification of the rods is a critical parameter that is not available for the rods of interest. For the rods investigated here, FRAPCON-3.4-MIT FGR has a high sensitivity to densification because densification increases fuel-clad gap size, thus increasing temperature, which increases FGR, which itself lowers the gap conductance and resultantly increases fuel temperature. Furthermore, as fuel temperature increases, its thermal conductivity decreases and FGR increases, both of which have the deleterious effect of increasing fuel temperature. The circular dependence of fuel temperature, thermal conductivity, and FGR results in a vicious cycle of fuel temperature increases, as shown in Figure 9. The relatively minor influence of densification on gap size can have significant cascading effects on fuel temperature and FGR. However, this effect is more pronounced for the small-diameter rods 79-442 and 79-481 than the larger diameter rods because of the relatively low clad creep-down of the smaller rods (due to higher clad strength). Indeed, for the larger rods densification was observed to lower the FGR because, although densification initially increases the gap size, the cladding creeps down onto the pellet and closes the gap, thus resulting in lower fuel temperatures with higher densification because of a smaller pellet diameter and increased density (as was observed for rod 79-576).

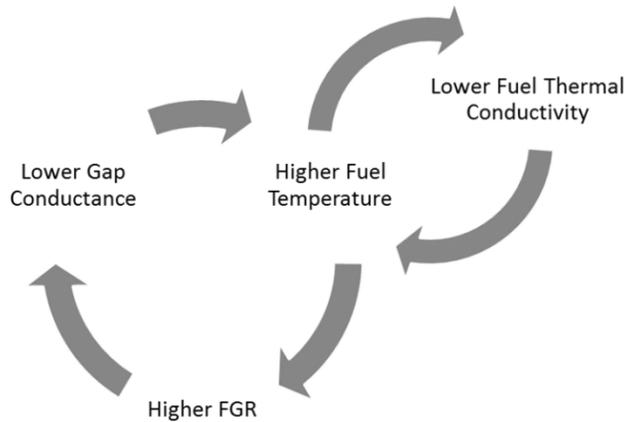


Figure 9: Vicious cycle of fuel temperature increase

When Long analyzed the FGR of the LWBR rods (Long, 2002), he assumed that rods 79-442, 79-506, 79-349, and 79-405 all densified to 98% TD. However, he observed that the FGR results for 79-375 were very high when densified to 98% TD, and therefore Long assumed that this rod did not fully densify owing to its low original density. When similar methodology was applied to the rods in FRAPCON-3.4, it was discovered that the FGR was excessively high when the aforementioned rods were densified to 98% TD, and therefore this analysis assumed that the rods are arbitrarily densified to 96% TD. Rods 79-481 and 79-576 were not analyzed in Long’s work, and those rods have a higher initial density (above 97%) than the other five rods. Therefore, this analysis arbitrarily assumes that rods 79-481 and 79-576 are densified to 98%, because any higher densification leads to excessively high FGR. One possible reason why the two sets of rods could realistically densify differently is the different initial densities of the two sets. However, densification of the thorium-uranium rods is a crucial parameter that must be determined in the future to allow for more accurate modeling. Currently, there is no experimental data concerning densification of thorium-uranium rods; therefore the treatment of thorium-uranium densification is unknown to date (Bjork & Kekkonen, 2015).

The LWBR test rods were simulated in FRAPCON-3.4-MIT, and the calculated FGR was compared to the experimentally reported FGR. It was observed that using the original UO₂ diffusion coefficients to simulate the thorium-uranium rods resulted in a general over prediction of FGR for the lower temperature rods and a general under prediction of FGR for the higher temperature rods. This result suggests that the low-temperature diffusion coefficient should be lowered, while the high-temperature diffusion coefficient should be increased, for the thorium-uranium system. Figure 10 presents the observed correlation between peak historic fuel temperature and FGR error.

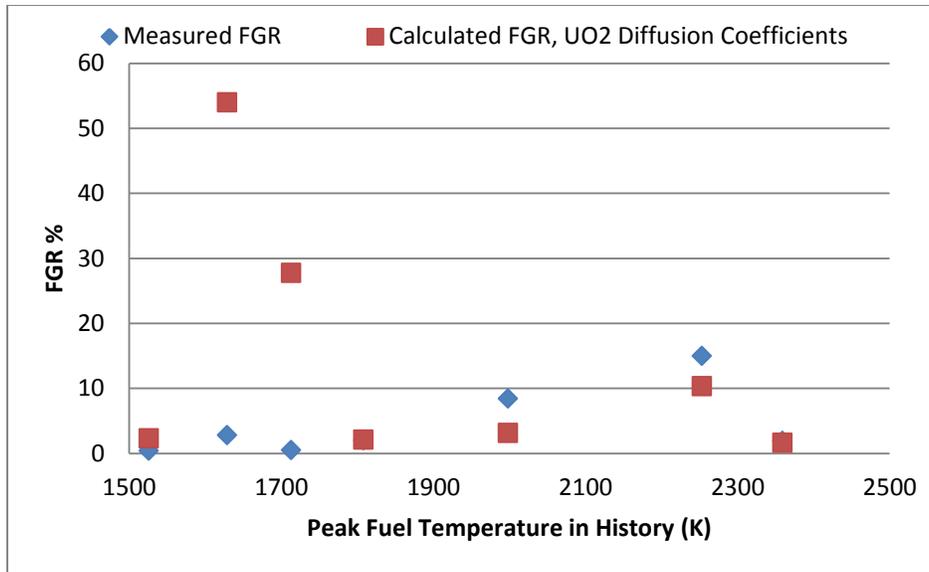


Figure 10: FGR versus peak calculated historic thorium-uranium fuel temperature

The high- and low-temperature diffusion coefficients were adjusted until the calculated FGR most closely matched the experimentally measured FGR. According to the result presented in Figure 10, and through trial and error, it was determined that the diffusion coefficients that allowed FRAPCON-3.4-MIT to best predict the experimental results were:

$$D_{(Th-U)O_2 \text{ Low Temp}} = 0.65 * D_{UO_2 \text{ Low Temp}}$$

$$D_{(Th-U)O_2 \text{ High Temp}} = 4 * D_{UO_2 \text{ High Temp}}$$

The resulting comparison between the UO_2 diffusion coefficients and the modified diffusion coefficients is presented in Figure 11. From the figure, it can be observed that the modified coefficients better predict the experimental results than the UO_2 coefficients.

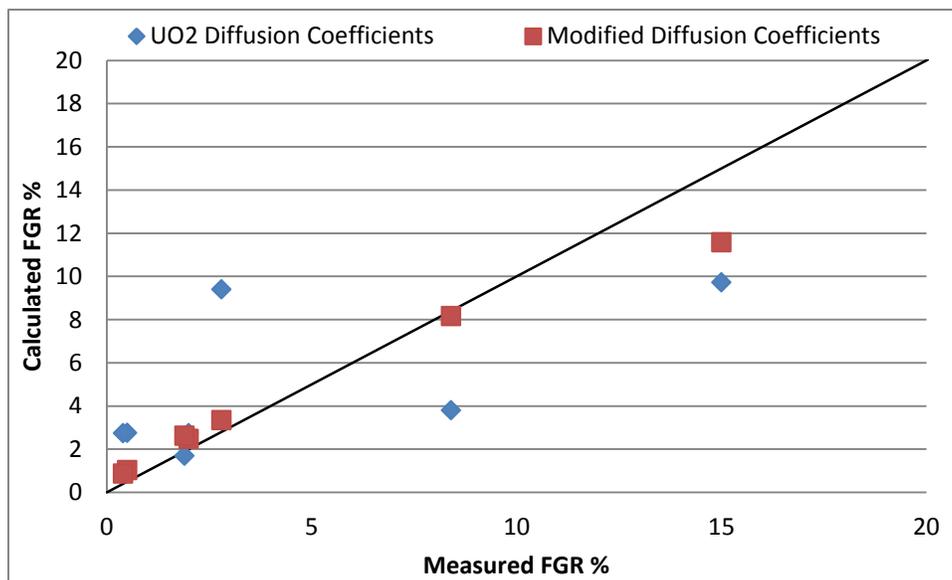


Figure 11: Results of FGR modeling for thorium-uranium rods

The comparison between the UO_2 diffusion coefficients and the modified diffusion coefficients are presented in Figure 12. From the figure it can be observed that the modified thoria-urania diffusivity is slightly lower than the UO_2 diffusivity at low temperatures, and significantly higher than the UO_2 diffusivity at high temperatures. This implies that, unlike what is commonly found in the literature, thoria-urania fuel at high temperature will have higher fission gas diffusion than urania fuel.

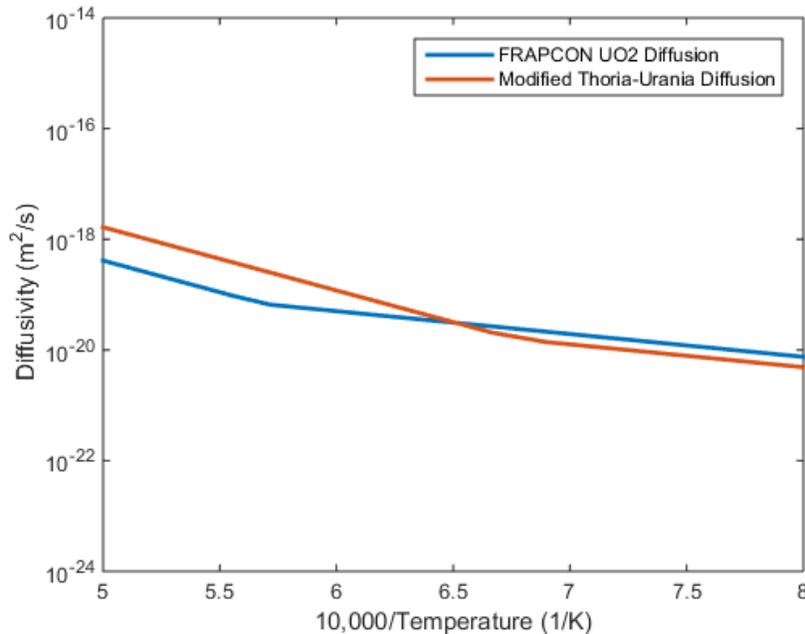


Figure 12: Diffusivity for UO_2 and modified thoria-urania model

2.4.2.3. Thorium-Plutonium Mixed Oxides

It was also desired to evaluate and update the FRAPCON-MIT Massih model for thoria-plutonia rods to allow for accurate prediction of thoria-plutonia FGR. Therefore, thoria-plutonia test rods were simulated in FRAPCON-MIT-3.4, and the calculated FGR was compared to the experimentally determined FGR. The test rods analyzed in this work were from the Atomic Energy of Canada Limited (AECL) CANDU thoria-plutonia irradiation campaign detailed by Karam (Karam, et al., 2008). The test rods originated from six Bruce-type 37-element bundles fueled with thoria-plutonia pellets. Three of the test rods originated from the outer ring of the bundle (ADC-1, ADE-1, and ADF-1), and three of the test rods originated from the intermediate ring of the bundle (ADC-19, ADE-19, ADF-19). Figure 13 shows a diagram of a fuel bundle and shows the locations of the rods. Table 3 presents parameters of the test rods investigated in this work. Table 4 presents parameters of a typical Bruce-type 37-element bundle such as what was used to irradiate the thoria-plutonia test pellets in the AECL work.

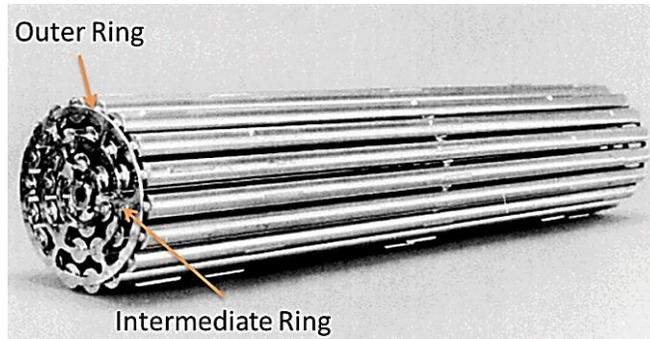


Figure 13: Bruce-type 37-element bundle showing test rod locations (adapted from Karam (Karam, et al., 2008)).

Table 3: Thoria-plutonia test rods investigated in this work

	ADC-1	ADC-19	ADE-1	ADE-19	ADF-1	ADF-19
Wt% Thoria	98	98	98	98	98	98
Fuel %TD	94.4	94.4	94.4	94.4	94.4	94.4
Peak Linear Power (kW/m)	67	22	64	32	52	37
Peak Burnup (MWd/kgHM)	18.8	11.9	24.9	14.8	35.7	20.7
Measured FGR %	5.3	0.3	1.2	0.1	2.8	0.2

Table 4: Typical parameters for 37-element bundle (adapted from Page (Page, 1976))

	Typical Bundle
Pellet Diameter (mm)	12.3
Cladding Diameter (mm)	13.1
Diametric Gap (mm)	0.06

There were several parameters that were not available in the literature concerning the AECL thoria-plutonia test rods. The axial power profile for the test rods was not specified, and therefore it was estimated that the test rods were placed centrally in the CANDU reactor. The axial power profile for the entire CANDU reactor was assumed to be a chopped cosine shape with an axial peaking factor of 1.3, and because there are 12 bundles stacked end-to-end in each fuel channel, the assumed axial power profile for the test bundles was the central one-twelfth of the total core power profile. Additionally, the densification for thoria-plutonia rods was not available in the literature, and therefore the rods were assumed to densify to 96% to be consistent with the assumed behavior of the thoria-urania rods. It is essential that future efforts determine the true densification behavior of thoria-plutonia rods to allow for more realistic modeling.

Additionally, although the power histories were provided for the #1 rods, the histories of the #19 rods were not provided. Therefore, it was assumed that the power history for each #19 rod was of similar

shape to the history for its corresponding #1 rod, and the power history for the #1 rod was shifted according to the peak power and burnup reported for the #19 rod.

The AECL test rods were simulated in FRAPCON-3.4-MIT, and the calculated FGR was compared to the experimentally reported FGR. It was observed that the FGR for the ADC-19, ADE-19, and ADF-19 rods was entirely unaffected by reasonable adjustments in the diffusion coefficients. The reason for the observed FGR insensitivity of the #19 rods is that their grain boundaries never reached the saturation condition for FGR due to the low temperature and low burnup of the rods. Therefore, these rods could not be used in the calibration of the diffusion model for thoria-plutonia, and only the #1 rods were used.

It was observed that using the original UO_2 diffusion coefficients to simulate the thoria-plutonia rods resulted in a large over prediction of FGR for the lower temperature #1 rods, while the UO_2 diffusion coefficients accurately predicted the FGR for the high temperature #1 rod. This result suggested that the low-temperature diffusion coefficient should be lowered substantially, and the high temperature coefficient should remain similar to the UO_2 coefficient. Figure 14 presents the observed correlation between peak historic fuel temperature and FGR error.

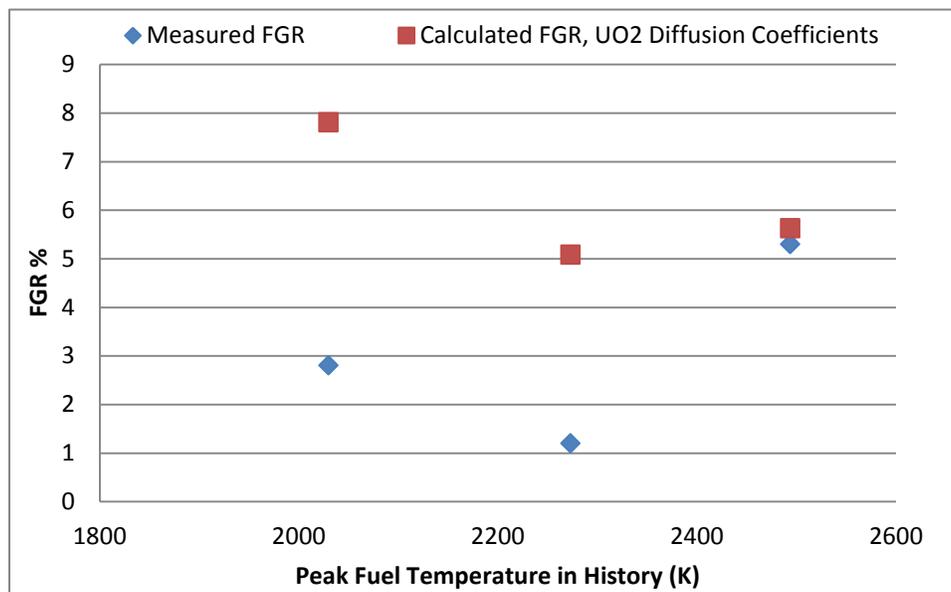


Figure 14: FGR versus calculated peak historic thoria-plutonia fuel temperature (#1 rods only)

Similar to the process used in updating the thoria-urania models, the high- and low-temperature diffusion coefficients for thoria-plutonia were adjusted until the calculated FGR most closely matched the experimentally measured FGR. According to the result presented in Figure 14, and through trial and error, it was determined that the diffusion coefficients that allowed FRAPCON-3.4-MIT to best predict the experimental results were:

$$D_{(Th-U)O_2 \text{ Low Temp}} = 0.1 * D_{UO_2 \text{ Low Temp}}$$

$$D_{(Th-U)O_2 \text{ High Temp}} = D_{UO_2 \text{ High Temp}}$$

The resulting comparison between the UO_2 diffusion coefficients and the modified diffusion coefficients is presented in Figure 15. From the figure, it can be observed that the modified coefficients better predict the experimental results than the UO_2 coefficients. Furthermore, the figure illustrates how the #19 rods (clustered at low FGR) did not show any FGR sensitivity to the change in diffusion coefficients.

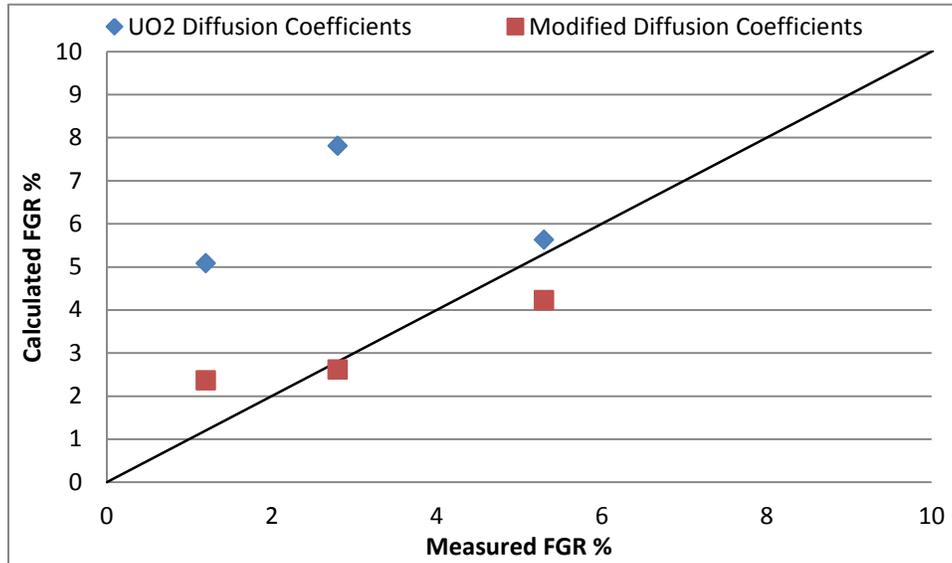


Figure 15: Results of FGR modeling for thoria-plutonia rods

The comparison between the UO_2 diffusion coefficients and the modified thoria-plutonia diffusion coefficients is presented in Figure 16. From the figure, it can be observed that the high-temperature thoria-plutonia diffusivity is identical to that of UO_2 , but the low-temperature diffusivity is much lower for thoria-plutonia.

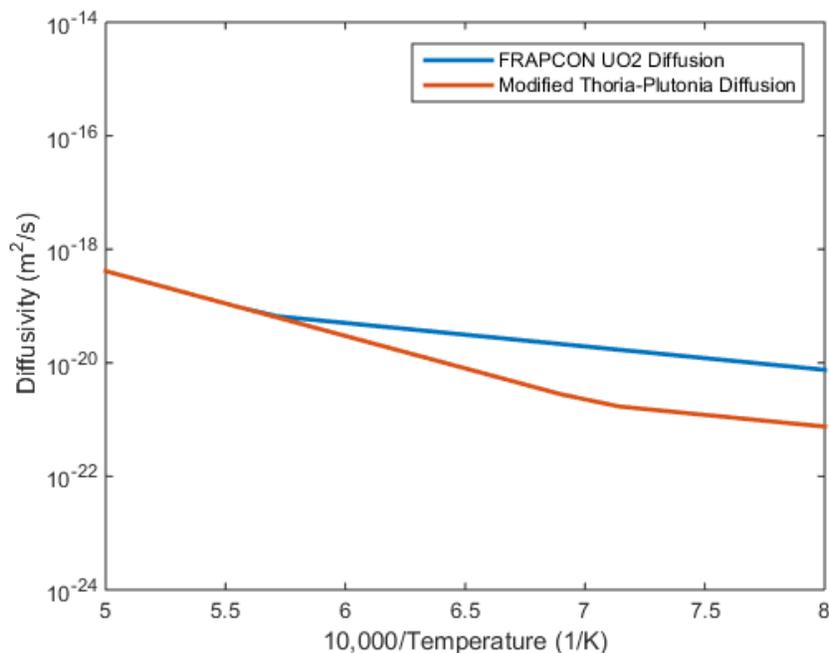


Figure 16: Diffusivity for UO_2 and modified thoria-plutonia model

2.5. Discussion

2.5.1. Densification Uncertainty

Although there were several sources of uncertainty that possibly influenced the results of the fuel performance modeling, perhaps the most crucial source of uncertainty is the densification behavior of the rods. The modeling showed that the FGR of the rods 79-442 and 79-481 (smallest diameter rods, listed in Table 2) was very sensitive to densification, and that any significant densification for those rods resulted in excessive calculated FGR. Therefore, those two rods were modeled with essentially zero densification and motivated the densification limits assumed in this analysis (96% for 79-442, 79-506, 79-349, 79-375, and 79-405, and 98% for 79-481 and 79-576). For the AECL rods, densification influenced the calculated FGR, but because the rods showed less sensitivity than the 79-442 and 79-481 rods, the results of the AECL rods are likely less sensitive to uncertainty in the densification behavior than the results of the LWBR rods.

All thoria-plutonia test rods had the same initial density, which means the assumption that they all densify to the same value is likely valid. In contrast, the thoria-urania rods had different initial densities, suggesting that the assumption that they densify to the same value is probably unrealistic. However, the assumption that all rods densify to the same value was used in Long's analysis of the LWBR rods (Long, 2002). In any event, if the true densification behavior was different than what was assumed in this work, then the FGR results would likely be different for both the thoria-urania and thoria-plutonia cases.

2.5.2. Comparison to Published Data

This analysis determined the diffusivity of thoria-urania and thoria-plutonia that gave the best correspondence between the FGR calculated with FRAPCON-3.4-MIT and the experimental data. It was desired to compare the results of this analysis to data obtained experimentally concerning fission gas diffusivity in fuel materials. The experiments solve for the transport parameters of the diffusivity equation, which is of the form:

$$D = D_0 * e^{\frac{-Q_0}{RT}}$$

Where D is the diffusivity at the temperature of interest, D_0 is the frequency factor, Q_0 is the activation energy, R is the gas constant, and T is the temperature. Although previous studies concerning thoria-plutonia fuel are lacking, studies by Naik (Naik, 1992), Shiba (Shiba, 1992), and Basu (Basu, Mishra, Bharadwaj, & Das, 2010) have attempted to experimentally determine the diffusivity of thoria-urania fuel. The comparison between the experimentally-derived diffusivity and the diffusivity implemented in FRAPCON-3.4-MIT in this work is presented in Figure 17 and Table 5. It can be noted that the sudden change in slope of the FRAPCON model is attributable to the change from the low-temperature diffusivity to the high-temperature diffusivity model.

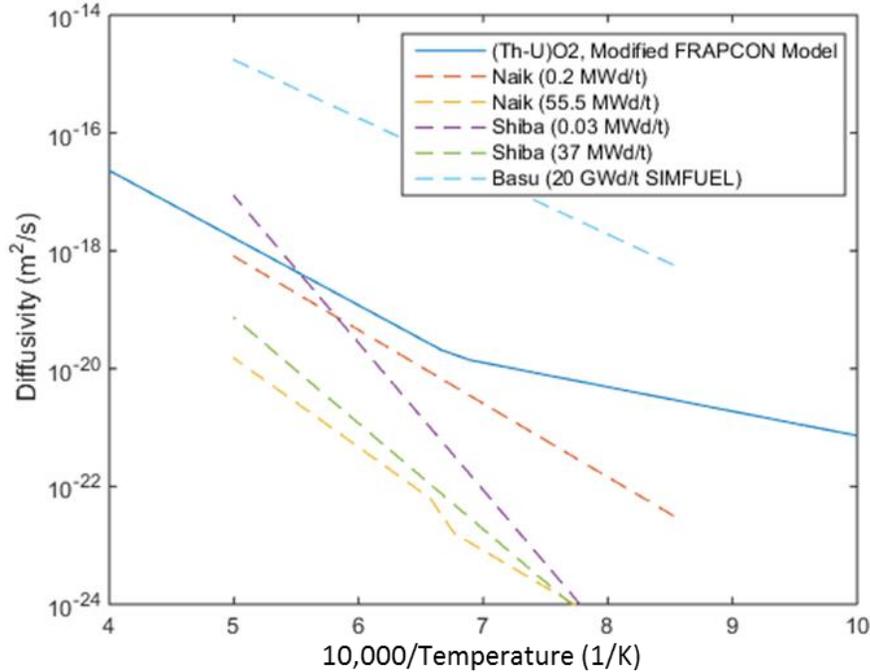


Figure 17: Comparison of modified FRAPCON thoria-urania diffusivity and published data (burnup indicated)

Table 5: Transport parameters for modified FRAPCON thoria-urania system and published data

Study	D_0 ($m^2 s^{-1}$)	Q_0 ($kJ mol^{-1}$)
FRAPCON-3.4-MIT	$8.6E-13$, $T > 1500$ K	219 , $T > 1500$ K
	$9.8E-18$, $T < 1500$ K	79 , $T < 1500$ K
Naik (0.2 MWd/t)	$1.4E-12$	239
Naik (55.5 MWd/t)	$5.3E-13$, $T > 1500$ K	289 , $T > 1500$ K
	$4.5E-15$, $T < 1500$ K	239 , $T < 1500$ K
Shiba (0.03 MWd/t)	$2.6E-5$	478
Shiba (37 MWd/t)	$7.1E-11$	344
Basu (20 GWd/t SIMFUEL)	$1.5E-10$	189

Clearly, there is significant spread in the experimental results for the thoria-urania system, and there is little to be concluded from the comparison of the modified thoria-urania FRAPCON model to the published data other than that the modified FRAPCON model appears to over predict the diffusivity. The Naik and Shiba studies have good high burnup diffusivity correspondence, but the studies have a large divergence for the low burnup measurements. Furthermore, the Basu study obtained a diffusivity approximately six orders of magnitude higher than the Naik and Shiba studies. The discrepancy between the Basu study and the Naik and Shiba studies is attributable to the SIMFUEL used by Basu. Although the SIMFUEL was intended to simulate high burnup by introducing fission products in the sintering powder prior to pellet manufacture, the evaporation of the doped MgO, BaO, and SrO during the long sintering time resulted in tri-vacancies that led to a high frequency factor for the diffusion.

The Naik, Shiba, and Basu studies all identified different mechanisms of gas diffusion through the thoria-urania matrix. Naik's study determined that the diffusion was by the interstitial mechanism, Shiba's study identified that the diffusion was by the tetra-vacancy diffusion where the tetra-vacancy consists of

a missing XO_2 molecule plus a missing O from a neighboring XO_2 molecule (where X is either Th or U), and Basu's study determined that the diffusion was via tri-vacancy diffusion, where the tri-vacancy consists of a missing XO_2 molecule.

Because of the large spread in diffusivity and diffusion mechanisms observed among the different thoria-urania studies, more studies are needed before substantial conclusions can be obtained concerning the accuracy of the modified FRAPCON-3.4-MIT thoria-urania diffusivity model. Furthermore, it is possible that none of the experimentally-derived diffusivity relationships can accurately model FGR in FRAPCON. To illustrate this point, the original FRAPCON-3.4 UO_2 diffusivity model was compared to the experimental results of Naik (Naik, 1992), Une (Une, Tanabe, & Oguma, 1987), Cornell (Cornell, 1968), and Davies and Long (Davies & Long, 1963). The comparison between the experimentally-derived diffusivity and the urania diffusivity implemented in FRAPCON-3.4 is presented in Figure 18 and Table 6. It can be noted that the sudden change in slope of the FRAPCON model is attributable in the change from the low-temperature diffusivity to the high-temperature diffusivity model.

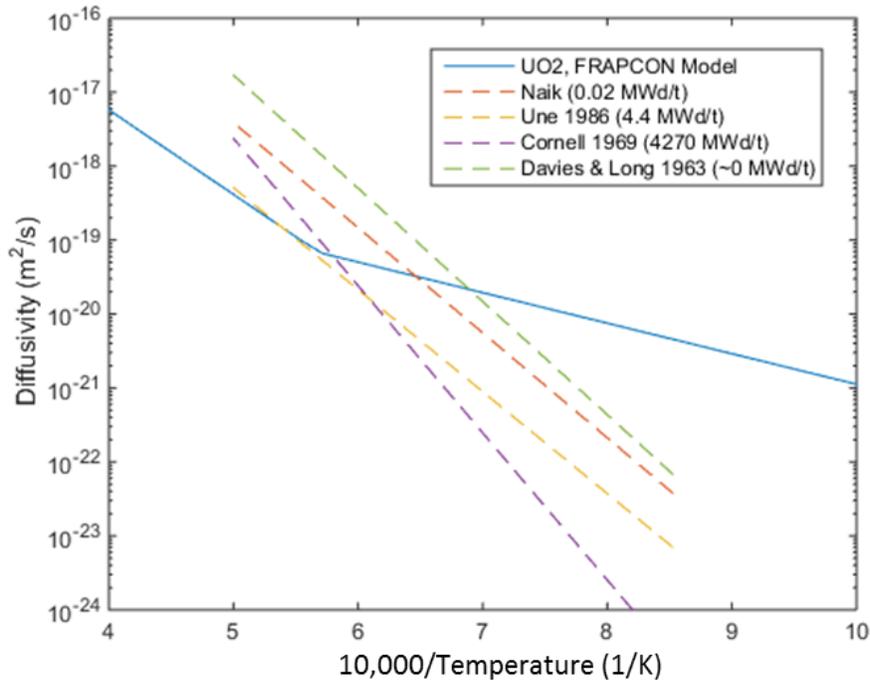


Figure 18: Comparison of FRACON UO_2 diffusivity and published data (burnup indicated)

Table 6: Transport parameters for FRAPCON urania system and published data

Study	D_0 ($m^2 s^{-1}$)	Q_0 ($kJ mol^{-1}$)
FRAPCON-3.4	$2.1E-13$, $T > 1800$ K	219 , $T > 1800$ K
	$1.5E-17$, $T < 1800$ K	79 , $T < 1800$ K
Naik (0.02 MWd/t)	$4.9E-11$	272
Une (4.4 MWd/t)	$4.0E-12$	264
Cornell (4270 MWd/t)	$2.1E-8$	381
Davies, Long (0 MWd/t)	$7.6E-10$	293

From Figure 18 and Table 6, it is clear that none of the experimental results match the FRAPCON UO₂ diffusivity model. This demonstrates that FRAPCON’s UO₂ diffusivity model does not necessarily reflect the diffusivity obtained by experimentation. Indeed, thermal conductivity, FGR, relocation, and swelling are all coupled phenomena that are empirically fitted in FRAPCON. Ultimately, the diffusivity models that give the most accurate FGR results in FRAPCON will not necessarily correspond with experimental data, and any comparison between the two should be taken with caution.

2.5.3. Implications for Fuel Performance

To evaluate the influence of using thoria-urania fuel over conventional urania fuel, the LWBR test rods were simulated in FRAPCON-3.4-MIT using thoria-urania fuel models as well as assuming the fuel is pure urania and using the standard FRAPCON urania fuel models. This was done to see the thermomechanical advantages of using thoria-based fuel. The calculated FGR and calculated peak fuel temperature (for the entire history) were compared between thoria-urania and urania cases. The results of the FGR comparison are shown in Figure 19, and the results of the temperature comparison are shown in Figure 20. It can be observed that the urania-fueled rods have consistently higher FGR (except for 79-375). Similarly, the fuel temperature is much higher for the urania-fueled rods (except for 79-375), which is attributable to the lower thermal conductivity of urania compared to thoria. The higher temperature of the urania rods is a significant contributor to the higher FGR seen in the urania rods.

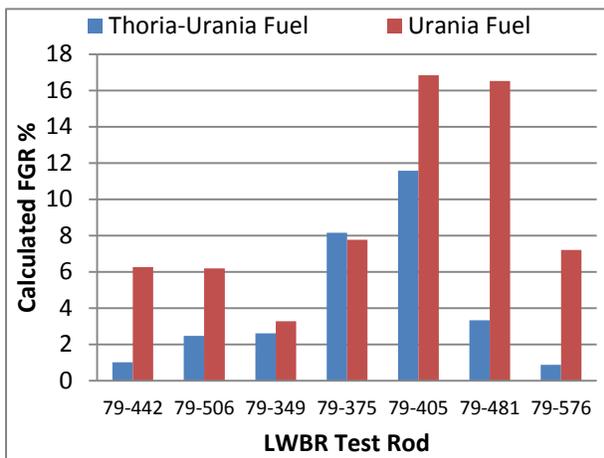


Figure 19: Comparison of calculated FGR LWBR fuel with and without thoria

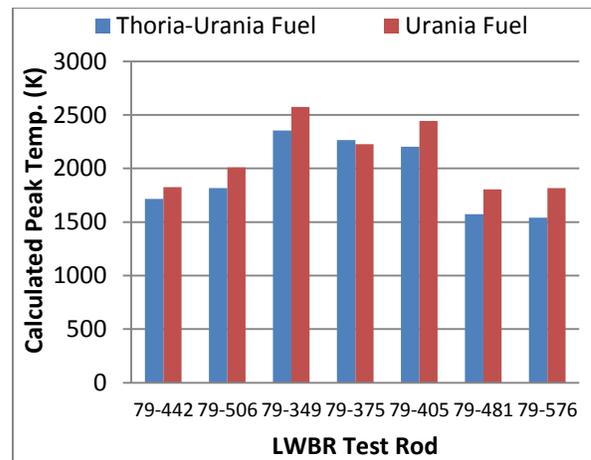


Figure 20: Comparison of calculated peak temperature for LWBR fuel with and without thoria

Similar analysis was performed on the thoria-plutonia AECL rods. The #19 rods showed little FGR sensitivity to fuel composition because the fuel’s grain boundaries do not achieve saturated conditions before end of life (EOL), and therefore the #19 rods are neglected here. Although it was desired to simulate the #1 AECL rods with complete substitution of thoria with urania, rods ADC-1 and ADE-1 could not be simulated with total thoria replacement due to excessive temperatures, so their simulations were run with the highest urania content that still allowed for permissible temperatures in FRAPCON-3.4-MIT. To this end, ADC-1 was simulated with 77% thoria -- 21% urania – 2% plutonia, and ADE-1 was simulated with 67% thoria – 31% urania – 2% plutonia. ADF-1 was simulated with 98% urania – 2% plutonia.

The results of the simulations for FGR and peak historic fuel temperature are presented in Figure 21 and Figure 22 respectively. From the analysis, it can be seen that the addition of 21% urania to ADC-1, 31% urania to ADE-1, and 98% urania to ADC-1 (with an equivalent decrease in the thorium content when compared to the original AECL rods) resulted in substantially higher FGR and peak fuel temperature. The increased fuel temperature likely contributes to the increased FGR.

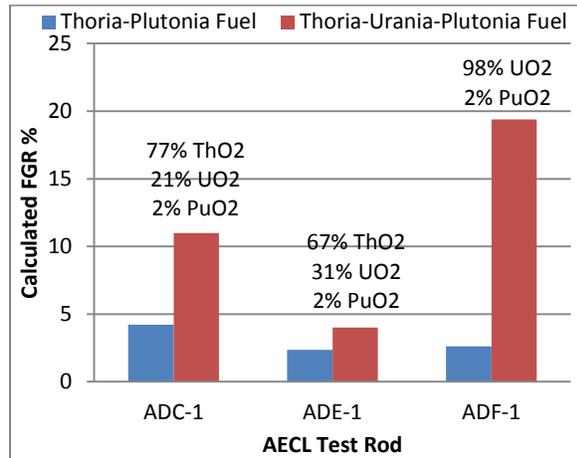


Figure 21: Comparison of calculated FGR for AECL fuel with and without urania

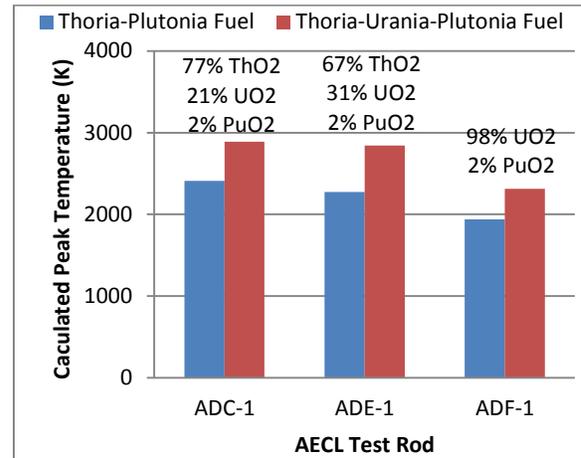


Figure 22: Comparison of calculated peak fuel temperature for AECL fuel with and without urania

2.5.4. Implications for Silicon Carbide

The use of thorium-based fuels in SiC cladding has two primary motivations: lower fuel temperature and lower FGR. The lower fuel temperature of thorium-based fuels is important for implementation in SiC cladding because SiC cladding must maintain an open gap due to the inability of the SiC to strain to accommodate fuel swelling. Furthermore, the swelling strain of SiC cladding causes the gap to grow larger, resulting in even higher fuel temperature. Because of the open gap, fuel temperature is inherently increased with SiC cladding, and therefore the higher thermal conductivity of thorium-based fuels would help mitigate the temperature rise. Furthermore, the higher melting temperature of thorium compared to urania allows for higher fuel temperatures and/or safety margins.

Thorium-based fuels are also attractive for use with SiC cladding because of lower FGR. As discussed in further detail in Section 3.2, Ben-Belgacem (Ben-Belgacem, Richet, Terrani, Katoh, & Snead, 2014) determined that the EOL failure risk of SiC cladding can be reduced by making the cladding thin, although the thin cladding requires lower plenum pressures to reduce stress. Because increased FGR causes increased plenum pressure, the lower FGR of thorium-based fuels will lower the plenum pressure of SiC cladding and allow for higher burnup to be achieved than urania fuel with SiC cladding.

To evaluate the benefit of using thorium-based fuels with SiC cladding, a typical Westinghouse PWR fuel rod (such as what would be found at Seabrook) was simulated in FRAPCON-3.4-MIT using the new modifications to the diffusivity model. Although a more detailed description of the rods can be found in Andrews (Andrews, Sukjai, Pilat, Shirvan, & Kazimi, 2014), some parameters of the rods are detailed in Table 7 and approximate what would be used to burn plutonium (either urania-plutonia or thorium-plutonia). The table shows that the use of thorium-plutonia in lieu of traditional thorium-urania MOX

reduces the FGR, peak temperature, and EOL plenum pressure of the rods. Additionally, by virtue of the lower density of thorium, the thorium-based rods achieve higher burnup than the uranium-based rods.

Table 7: Westinghouse PWR rods simulated in this work

	Zircaloy-4 (U-Pu)O₂	Zircaloy-4 (Th-Pu)O₂	SiC (U-Pu)O₂	SiC (Th-Pu)O₂
Wt% Plutonia	7.51	7.71	7.51	7.92
Fuel %TD	95	95	95	95
Pellet Diameter (mm)	8.19	8.19	7.81	7.81
Cladding Diameter (mm)	9.5	9.5	9.5	9.5
Cladding Thickness (mm)	0.571	0.571	0.762	0.762
Peak Linear Power (kW/m)	26.93	26.93	26.93	26.93
Peak Burnup (MWd/kgHM)	66.57	72.39	73.23	79.59
Calculated FGR %	16.4	8.5	28.3	27.5
Calculated Peak Temperature (K)	1837	1654	2092	2061
Calculated EOL Plenum Pressure (MPa)	19.6	15.9	29.5	27.9

From this analysis, it was seen that using the thorium-plutonium fuel substantially reduced the temperature, FGR, and plenum pressure for the fuel clad in Zircaloy-4. However, the SiC-clad fuel was much less influenced by the use of thorium. Because of the lower thermal conductivity of irradiated SiC cladding and its open gap, the SiC-clad fuel temperature is higher than its Zircaloy-clad counterpart. Therefore, the SiC-clad fuel operates in the high-temperature region of the new diffusivity model which, as discussed in Section 2.4.2.3, is identical to the high-temperature diffusivity model of uranium. However, the higher thermal conductivity of thorium does reduce the fuel temperature slightly and results in slightly less FGR and plenum pressure for the thorium-plutonium rod than for the uranium-plutonium rod. Figure 23, Figure 24, and Figure 25 present comparisons of the fuel temperature, FGR, and plenum pressure for the Zircaloy- and SiC-clad rods.

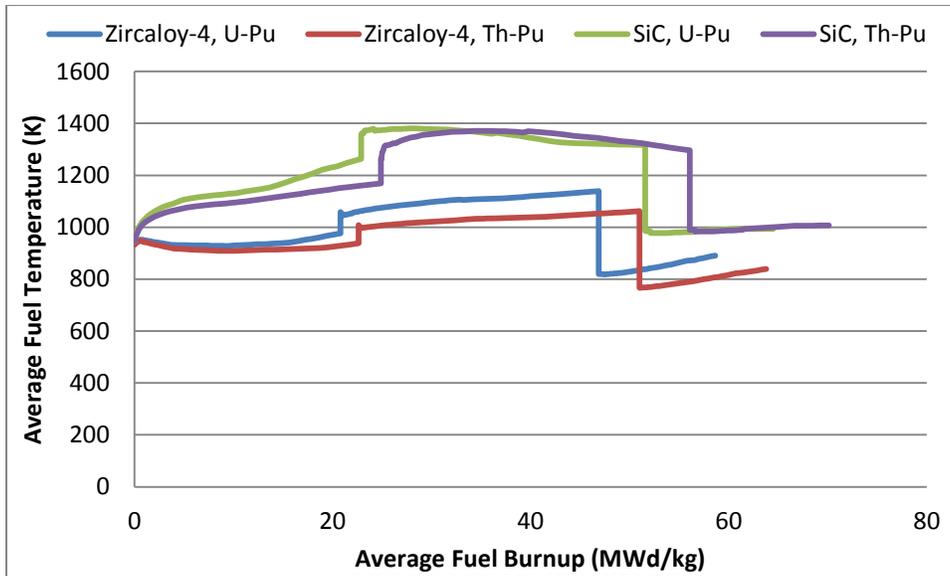


Figure 23: Comparison of fuel temperature for simulated rods

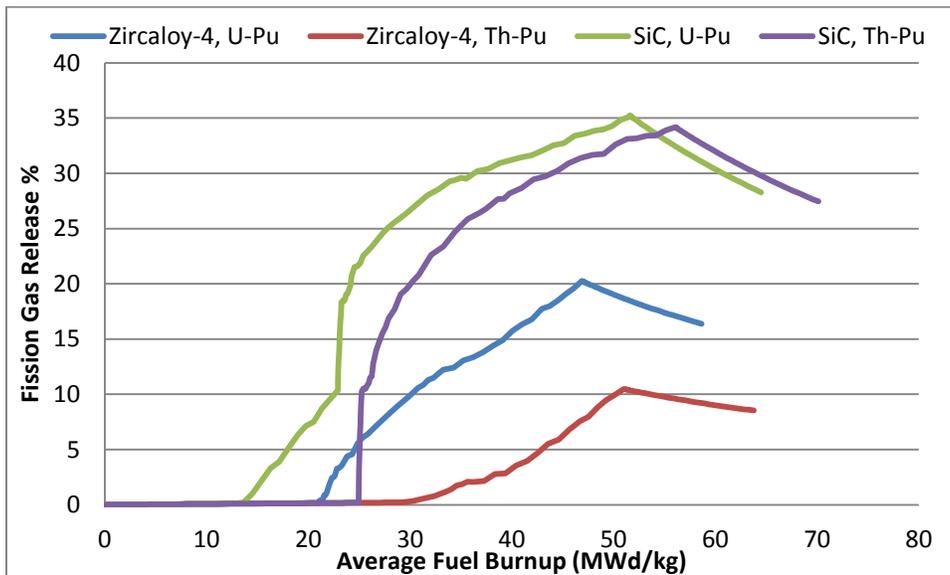


Figure 24: Comparison of FGR for simulated rods

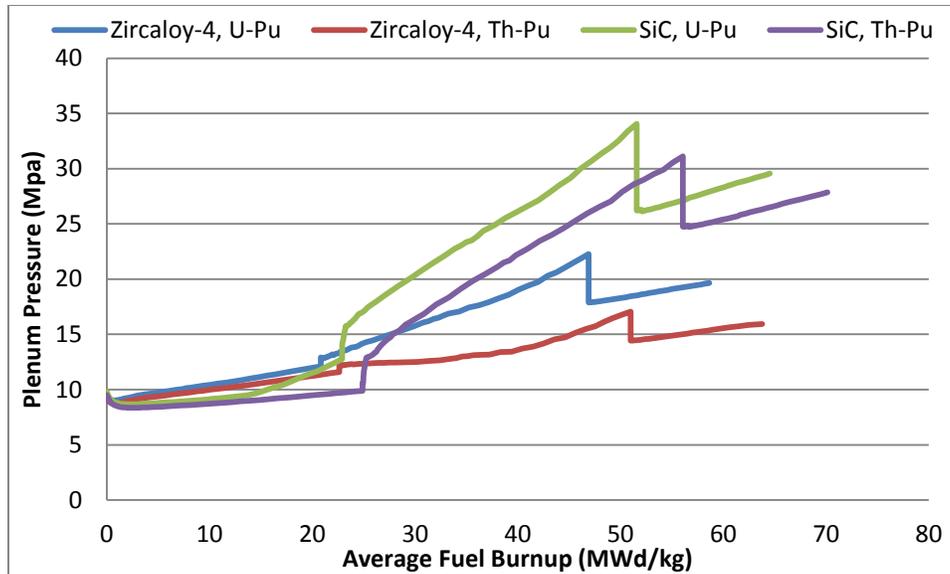


Figure 25: Comparison of plenum pressure for simulated rods

The results of this study were compared to the results obtained using both the standard UO_2 diffusivity model and Long's diffusivity model (Long, 2002) to reveal the impact of the diffusivity model on the fuel's thermomechanical performance. Table 8 presents the comparison, showing that the peak historic fuel temperatures remain relatively unaffected by the diffusivity model. Because the differences between the models only concerns thorium-based rods, the non-thorium rods are neglected in Table 8. While the new diffusivity model gives similar results as the original UO_2 diffusivity model (because at high temperatures the new model is identical to the UO_2 model), Long's diffusivity model gives significantly lower FGR. The results are also shown graphically in Figure 26, Figure 27, and Figure 27.

Table 8: Comparison of results between different diffusivity models

	Zr-4, Th-Pu			SiC, Th-Pu		
	FGR %	Peak T (K)	EOL Plenum Pressure (MPa)	FGR %	Peak T (K)	EOL Plenum Pressure (MPa)
New Model	8.5	1654	15.9	27.5	2061	27.9
UO_2 Model	9.4	1655	16.4	27.3	2058	27.8
Long's Model	2.1	1652	12.4	14.6	1997	20.1

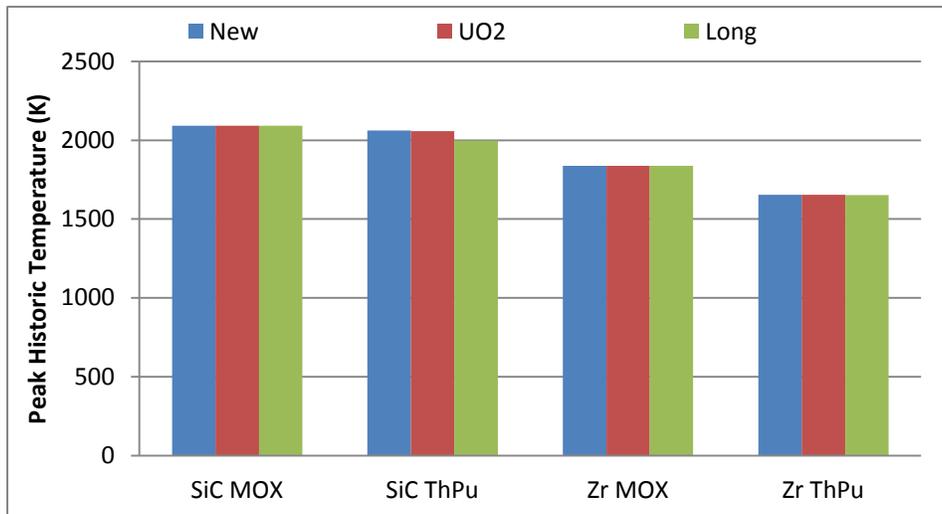


Figure 26: Temperature comparison between diffusivity models

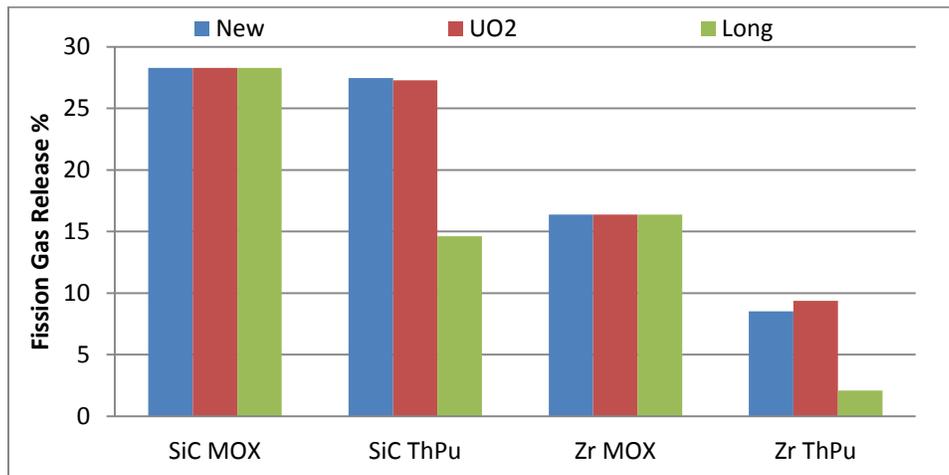


Figure 27: FGR comparison between diffusivity models

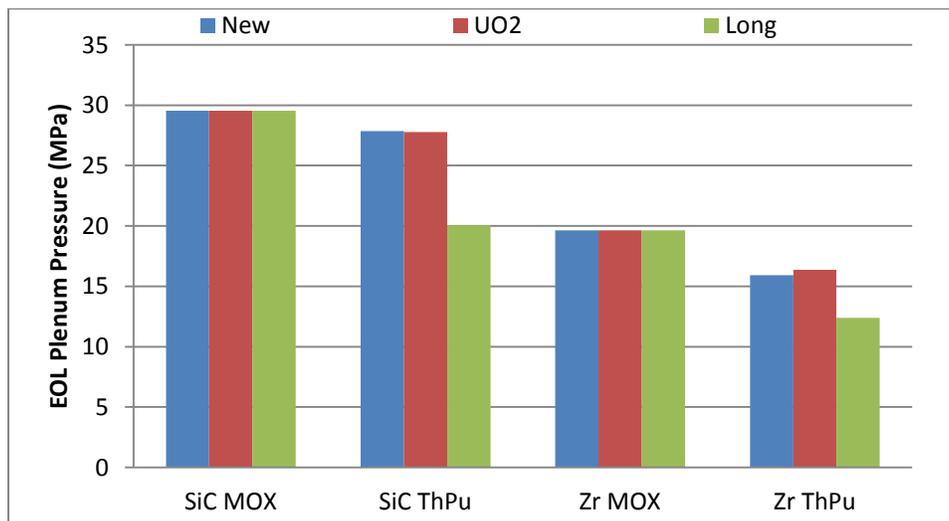


Figure 28: EOL plenum pressure comparison between diffusivity models

3. Silicon Carbide Cladding

3.1. Uses of Silicon Carbide

Although SiC has seen significant use as an abrasive due to its high hardness, it has also been used in high-temperature and corrosive environments. With a melting temperature of 2730°C and no significant degradation in mechanical strength up to 1500°C (Snead, et al., 2007), SiC has excellent thermomechanical properties that make it a subject of interest for high-temperature mechanical applications. The excellent corrosion resistance observed of SiC is attributable to strong covalent bonding and the development of a protective silica layer when exposed to an oxidizing atmosphere.

SiC composite materials have been demonstrated to have significant potential for use in high-temperature aerospace and gas-turbine applications. SiC composites have been explored for use as thermal structures of spacecraft such as with Hermes European space shuttle program (Christin, 2002) which culminated in prototyping C/SiC CMC (carbon fiber reinforced SiC matrix composite) components (Naslain, 2005). The SiC would be used for the reentry and ascent phases of the mission where the temperatures would be expected to reach 1600°C with oxidizing atmosphere and cyclical loading. Snecma Moteurs investigated the use of SiC as a cryogenically-cooled aerospike ramp with long-life and high reusability (Christin, 2002). Furthermore, C/SiC CMC technology has been demonstrated for use as exhaust flap components of afterburning jet engines. Testing of C/SiC CMC for use as outer exhaust flaps showed reliable performance at 700°C and led to the implementation of C/SiC CMC for use in the Snecma M88-2 engine outer exhaust flaps (Christin, 2002). Tests of SiC/SiC CMC have shown promising performance at 1100°C as the inner exhaust flaps for afterburning jet engines, although refined manufacturing techniques are required to improve component reliability (Christin, 2002). SiC/SiC CMC combustors have been tested in three different Solar Turbine Centaur 50s power plant gas turbines with an accumulation of 24,000 hours at 1250°C without failure (Lee, et al., 2003).

SiC has also seen use as the pressure boundary for TRISO fuel particles used in gas-cooled reactors. Such use has demonstrated the applicability of SiC in a nuclear environment and the SiC has shown good reliability at high temperatures and under irradiation. Furthermore, SiC/SiC CMC is being investigated for use as a structural material in fusion reactors. SiC exhibits extremely low radioactivity after 14 MeV neutron irradiation, performs at high temperatures allowing for high thermal efficiency, and has a thermal conductivity high enough to transfer heat loads but low enough to also perform as an insulator (Raffay, et al., 2001).

3.2. Previous Silicon Carbide LWR Cladding Research

SiC has already been used extensively in TRISO fuel particles in high temperature reactors and it therefore has already proven to be an effective material in a nuclear environment. However, the TRISO particles implemented SiC as one component in a multi-layered architecture involving pyrolytic carbon and porous carbon layers, and the SiC was not directly exposed to the coolant in TRISO-fueled reactors. A schematic of the TRISO fuel particle is presented in Figure 29. Because of the layered structure of the TRISO fuel particle, its use of SiC is not entirely representative of the use of SiC in LWR cladding.

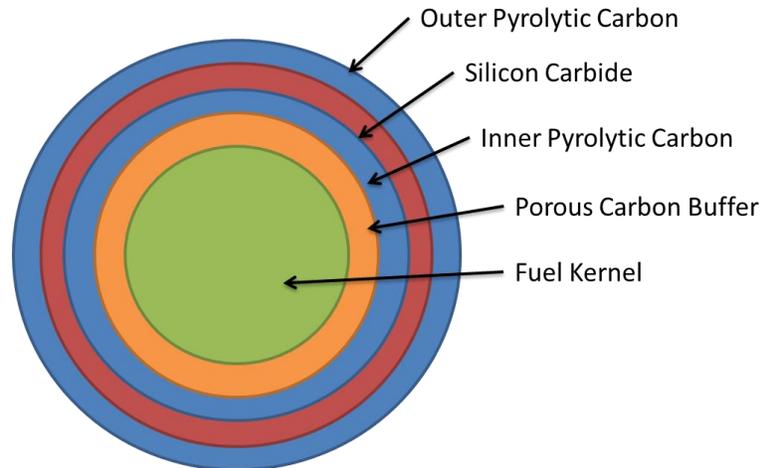


Figure 29: Schematic of TRISO fuel particle

Because SiC offers numerous benefits for nuclear fuel performance it has been investigated as an LWR cladding material. However, SiC has never been used commercially in LWR conditions, so studies have been performed to determine SiC performance in LWRs.

Carpenter (Carpenter, 2010) showed that SiC cladding will likely be usable at burnups beyond 100 MWd/kgU although the maximum burnup for SiC will be limited by aqueous corrosion. Furthermore, Carpenter showed that SiC cladding can be made much stronger by careful manufacturing and by eliminating impurities from the SiC, with the CVD process producing the best results. SiC cladding was able to resist higher internal pressures than Zircaloy cladding and the fiber composite layer was able to arrest crack growth and prevent catastrophic failure of the cladding upon failure of the monolith. Stempien (Stempien, 2011) studied samples similar to Carpenter's and found that the irradiated samples exhibited reduced strength compared to non-irradiated samples.

Lee (Lee Y. , McKrell, Yue, & Kazimi, 2013) investigated the high-temperature steam oxidation behavior of SiC monolith cladding samples and discovered that SiC oxidizes differently than Zircaloy and is far more oxidation resistant. When SiC samples were oxidized, a weight loss was observed due to the volatilization of the oxide, resulting in a thin oxide layer on the SiC samples. In Zircaloy, a weight gain was observed due to the capture of oxygen and the accumulation of a stable oxide layer. Therefore, a strong dependence on both oxidation steam temperature and flow rates was characterized for the oxidation of SiC. Lee also demonstrated that SiC monolith experienced 1,000 times slower oxidation than Zirconium.

Ben-Belgacem (Ben-Belgacem, Richet, Terrani, Katoh, & Snead, 2014) developed a framework for thermomechanical analysis of in-pile SiC/SiC CMC cladding in LWR conditions that showed the SiC cladding behaves very differently from metallic cladding. The absence of creep coupled with a large temperature-gradient-driven irradiation swelling strain gradient resulted in large stresses across the cladding thickness at modest neutron doses of only 1 dpa. This behavior is markedly different from the negligible or absent swelling strains associated with metallic cladding (Ben-Belgacem, Richet, Terrani, Katoh, & Snead, 2014). The study showed that the enhanced swelling strain of SiC cladding could

increase the pellet-cladding gap and result in high fuel temperatures and higher fission gas release. The plenum pressure should be lower than the coolant pressure to allow for thinner cladding, which would lower the probability of axial failure and minimize the probability of azimuthal failure. By designing the fuel to have lower end-of-life (EOL) pressure, the EOL failure risk can be minimized.

3.3. Manufacturing of Silicon Carbide Cladding

3.3.1. Monolith SiC

Monolithic SiC can be produced by a number of means, but the CVD process enables the easiest application of a thin uniform SiC coating. CVD reduces processing steps and allows for continuous manufacturing at the expense of high temperature and gaseous purity of the CVD vapors (Carpenter, 2010). CVD SiC also has superior microstructure because it is highly stoichiometric, crystalline, and has minimal impurities, resulting in superior performance at high temperatures and irradiation resistance (Snead, et al., 2007). CVD SiC is formed when gases such as methyltrichlorosilane and hydrogen or silane and propane contact a heated surface and result in deposition of SiC (Carpenter, 2010), where the thickness of the SiC layer is determined by the elapsed time of the process. The monolithic SiC (mSiC) layer of the samples investigated in this work was fabricated via CVD.

3.3.2. SiC/SiC Composites

The key to radiation performance of SiC/SiC composites is the stability of the fibers under irradiation (Fenici, Rebelo, Jones, Kohyama, & Snead, 1998). Among the most ubiquitous SiC fibers are commercial Nicalon fibers, which are produced by a polymer preceramic process described by Yajima (Yajima, Hayashi, & Omori, 1979). The Nicalon process involves first generating fibers by low temperature melt-spinning of polycarbosilane, followed by stabilization of the spun fibers by high-temperature air curing and finally ceramization at 1300°C. The SiC fibers produced by the Nicalon process have seen extensive use due to a combination of low price, good mechanical properties, and weavability (Snead, Osborne, & More, 1995). However, the primary downside of the Nicalon process is the excess oxygen produced by the air curing step, which results in irradiation-induced mechanical degradation (Snead, Osborne, & More, 1995) and poor performance above 1300°C (Ishikawa, 1994). The elimination of oxygen from the fibers minimizes the irradiation effects and yields significantly more radiation-resistant SiC composites (Snead, Osborne, & More, 1995). To reduce the oxygen content in the Nicalon fibers, the Hi-Nicalon process was developed, which replaces the air-curing step with electron beam irradiation in an oxygen-free atmosphere, allowing for a fiber oxygen content of approximately 0.4 wt.%, compared to the 11.2 wt.% content of Nicalon fibers (Ishikawa, 1994). The Nicalon and Hi-Nicalon fiber production processes as illustrated by Ishikawa are shown in Figure 30, and the typical properties of Nicalon and Hi-Nicalon fibers are presented in Table 9.

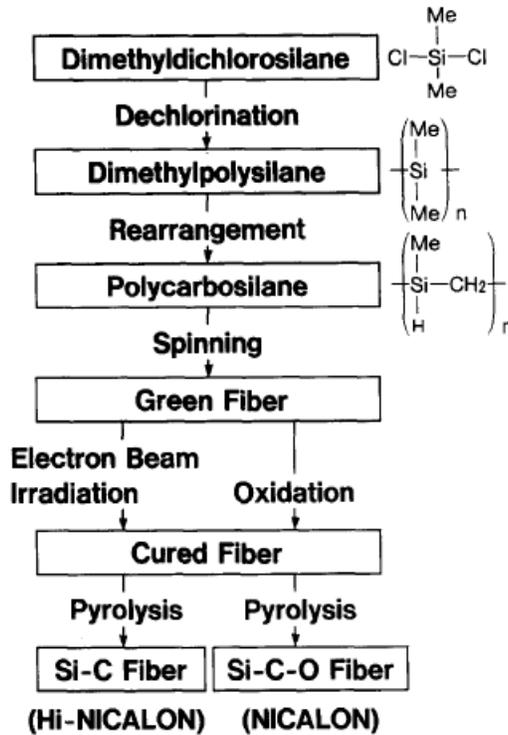


Figure 30: Production of Hi-Nicalon fibers (Ishikawa, 1994)

Despite the advantages of the Hi-Nicalon process over the Nicalon process, the Hi-Nicalon fibers still have poor high-temperature steam oxidation and creep performance due to micro-crystallinity and excess carbon (Ichikawa, 2000). To improve creep and oxidation of the Hi-Nicalon fiber, the Hi-Nicalon type S fiber was developed which has stoichiometric SiC composition and high crystallinity (Ichikawa, 2000). The Hi-Nicalon type S process involves a modified Hi-Nicalon process that includes a C/Si ratio of 1.05 and high-temperature pyrolyzing in special conditions to promote crystal growth while maintaining strength (Takeda, Sakamoto, Saeki, & Ichikawa, 1996). The resulting Hi-Nicalon type S fiber has an oxygen content of 0.2 wt.%, an elastic modulus of 420 GPa, and a tensile strength of 2.6 GPa (Takeda, Sakamoto, Saeki, & Ichikawa, 1996). The Hi-Nicalon type S fibers are used in the accident-tolerant SiC cladding investigated in this work due to their superior high-temperature performance when compared to other SiC fiber options. Typical properties Hi-Nicalon type S fibers are given in Table 9.

Table 9: Properties of SiC fibers (Takeda, Sakamoto, Saeki, & Ichikawa, 1996)

	Nicalon	Hi-Nicalon	Hi-Nicalon type S
Fiber Diameter	14 μm	14 μm	12 μm
Filaments per Yarn	500	500	500
Tensile Strength	3 GPa	2.8 GPa	2.6 GPa
Tensile Modulus	200 GPa	270 GPa	420 GPa
Elongation	1.4 %	1.0 %	0.6 %
Density	2.55 g/cm ³	2.74 g/cm ³	3.10 g/cm ³
Oxygen wt. %	11.7 %	0.5 %	0.2 %

The SiC fibers are then used in the manufacture of 2D or 3D preforms with the desired geometry of the final product. The fibers of the preform can be woven in a textile with a desired weave pattern (architecture), and once the preform is fabricated, the matrix is subsequently filled in (as discussed below).

The optimization of the interface between the fiber and matrix for SiC/SiC ceramic composites is highly important for improving toughness (Naslain, 2005). To achieve optimal interfacing between the fiber and matrix, a thin layer of interfacial material is coated on the fiber, known as the interphase. The interphase deflects matrix cracks, permits fiber pullout during matrix fracture, and allows for ductility between fiber and matrix (Igawa, et al., 2005). The interphase is generally applied by the decomposition of a carbon precursor coating (such as propylene) on the fiber surface (Igawa, et al., 2005).

Although there are numerous methods for fabricating the matrix, the samples investigated in this work consist of a matrix fabricated via chemical vapor infiltration (CVI). The CVI process involves first infiltrating the CMC region with carbon precursors such as propylene, which are subsequently decomposed into carbon, followed by a reaction to convert the carbon into SiC via a gas such as methyltrichlorosilane (Igawa, et al., 2005). There are two main techniques for performing CVI. The first technique is the isobaric/isothermal CVI, which produces SiC with good microstructure and limited fiber degradation and is the easiest CVI technique and most adaptable to industrial manufacturing (Naslain, 2005). The second technique is the forced flow/thermal gradient CVI method, which is the best techniques for creating a matrix with a high-purity, stoichiometric, crystalline β -SiC with low thermal stress (Igawa, et al., 2005), although it requires fixturing to create the gradients and is more difficult to perform industrially (Naslain, 2005). Regardless of which method is performed, CVI inevitably leads to a matrix with poor homogeneity and high porosity (Igawa, et al., 2005) (Naslain, 2005). The analysis performed on the samples in Section 5.3 demonstrates that the samples studied in this work suffer from significant matrix porosity, with the highest porosity observed at approximately 10%. Because Snead noted that the elastic modulus of SiC decreases with increasing porosity (Snead, et al., 2007), the porosity of the CMC matrix for the samples investigated in this work likely reduces the elastic modulus of the matrix below the 460 MPa of fully dense SiC.

3.3.3. Endplug

SiC cladding samples are fabricated with an endplug instead of an endcap because it permits the use of already-existing fuel rod dimensions. The method used for producing the endplugs is described by Khalifa (Khalifa H. E., Deck, Gutierrez, Jacobsen, & Back, 2015) and involves using a transient eutectic phase (TEP) approach with a precursor consisting of SiC, Al_2O_3 , Y_2O_3 , and SiO_2 nanopowders. The high surface area of the nanopowders allow for fast densification when used under pressure at high temperatures (above 1500°C), and the TEP process allows for good control over the final shape of the endplugs (Khalifa H. E., Deck, Gutierrez, Jacobsen, & Back, 2015). The endplug design used in the samples investigated in this work is a scarf endplug with an angle of approximately 7.5° . Khalifa's work showed that the scarf design has higher strength and more predictable failure modes when compared to other endplug designs, although the scarf design had unacceptable gas leakage through the joint.

The endplug joining method used in the close-ended samples investigated in this work consisted of a hybrid preceramic polymer, CVI approach according to a patented technique (Khalifa, Deck, & Back, 2013). The polycarbosilane-based preceramic polymer slurry is used to coat the joining surfaces and undergoes a 3-step process for forming the basis for the endplug joint. The preceramic slurry is first cured at low-temperature, then pyrolyzed, and finally heat-treated above 1300°C to refine the microstructure (Khalifa H. E., Deck, Gutierrez, Jacobsen, & Back, 2015). The resultant joint is then subjected to CVI for densification. The joint material formed with this method consists of high-purity β -SiC with uniform grain size and purity similar to that of the fibers and is expected to preserve its mechanical performance at temperatures above 1000°C (Khalifa H. E., Deck, Gutierrez, Jacobsen, & Back, 2015). The joint length of approximately 10 mm allows for sufficient strength to withstand the plenum pressure at EOL conditions.

3.4. Silicon Carbide Cladding Options

There are three primary designs that have been investigated for SiC cladding: the monolith, three-layer, and two-layer designs. The monolith design consists only of a monolith tube as the cladding, and although it shows excellent corrosion resistance, it suffers from brittle and catastrophic failure. The monolith has low fracture toughness and is effectively unable to arrest cracks. The failure behavior observed in monolith tubing does not maintain coolable fuel geometry and would result in fuel spillage from the fuel rod upon cladding failure, as can be observed in Figure 31.

To prevent the brittle and catastrophic failure of the monolith cladding, multilayer composite cladding was developed. With multilayer cladding, the corrosion resistance of monolith SiC is combined with the improved mechanical behavior of the CMC to create a cladding that has good high-temperature corrosion performance while maintaining failure characteristics compatible with nuclear accident scenarios. The failure behavior of multilayer composite cladding can be observed in Figure 31. From the figure, it can be noted that, whereas the monolith tubing failure results in shattering of the cladding, the failure of the multilayer composite has much less fragmentation and remains relatively intact.

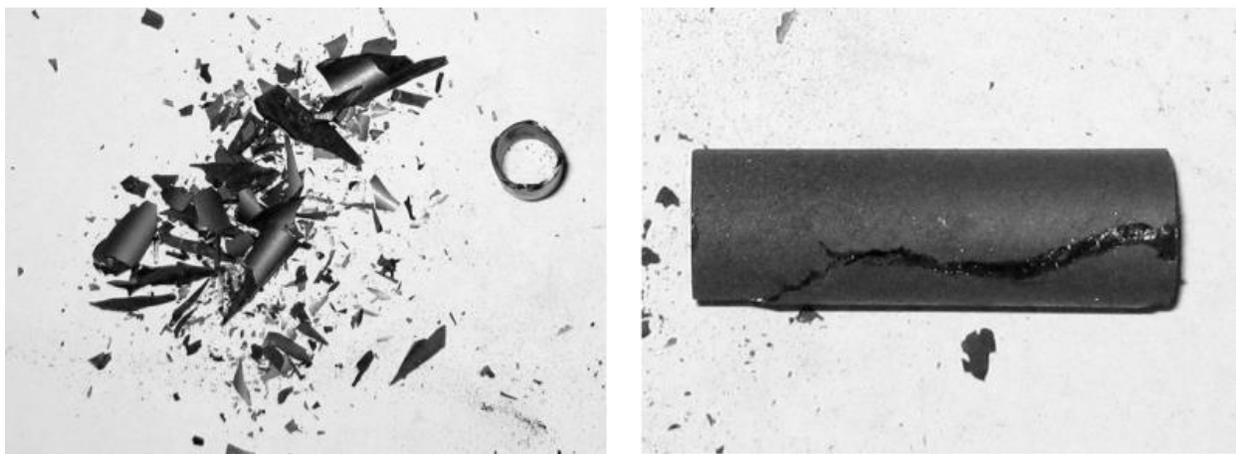


Figure 31: Comparison of failure behavior for monolith (left) and multilayer composite (right) tubing (Carpenter, 2010)

The design of multilayer cladding is dictated by consideration for corrosion resistance, improved mechanical properties, and the retention of fission gases. The first of these concerns, corrosion

resistance, arises from the observed susceptibility of the CMC to oxidation (Eaton & Linsey, 2002). To resolve this issue, the environmental barrier coating (EBC) approach was developed which protects the CMC using a coating (such as mSiC) on the exposed CMC surfaces. The second concern, improved mechanical properties, is achieved by maximizing the CMC's volumetric fraction in the samples because with more CMC the samples will be dominated more by the CMC mechanical behavior and less by the mSiC mechanical behavior. The third concern, fission gas retention, results from the CMC's permeability to gases due to the inherent as-manufactured void structure (Bloom, 1998). Therefore, to prevent release of fission gases into the reactor environment, mSiC is required to maintain hermeticity of the cladding.

Two approaches have been taken to addressing the design concerns for multilayer cladding. The first approach is the three-layer design, which uses an inner mSiC layer for fission gas retention, a middle CMC layer for mechanical performance, and an outer mSiC EBC to protect the CMC from corrosion. The second approach is the two-layer design, which uses an inner or outer CMC layer for mechanical performance and an outer or inner mSiC layer to retain fission gases and prevent corrosion of the CMC. Cross-sectional SEM views of the two-layer and three-layer designs are shown in Figure 32. It should be noted that the large voids observed in the figure exist because of the inability of the manufacturing techniques to completely fill the matrix within the CMC. Such voids are currently unavoidable and will likely be present in reactor-grade cladding.

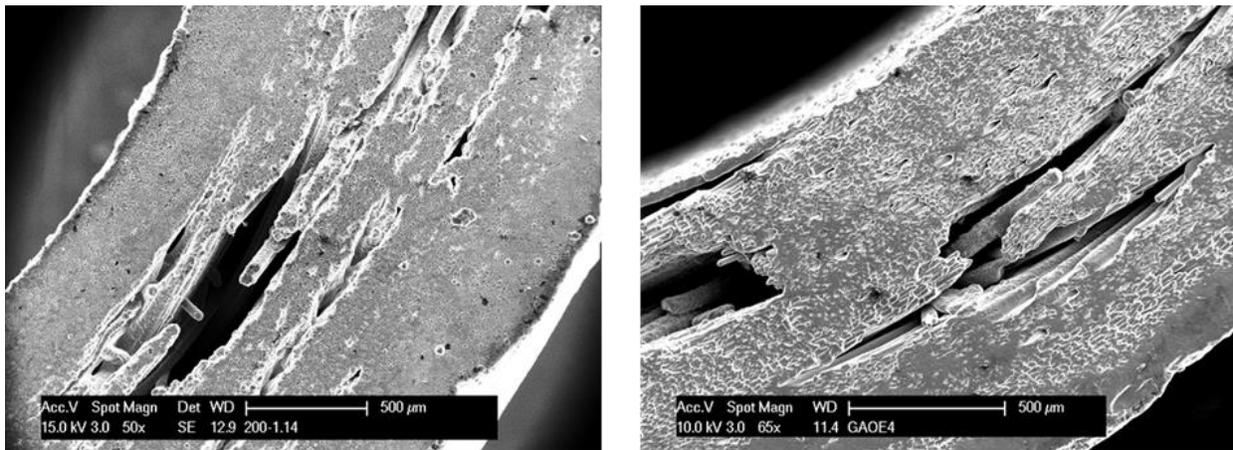


Figure 32: Cross-sectional SEM views of three-layer (left) and two-layer (right) samples

Stone (Stone, et al., 2015) performed analysis of multilayer cladding designs to determine the best design to reduce failure probability in the cladding. Among the options investigated in the work were a design with an inner mSiC layer and an outer CMC layer and a design with an inner CMC layer and an outer mSiC layer. The work showed that the stresses in the SiC resulting from temperature-dependent irradiation swelling are much larger than the stresses resulting from temperature and pressure differentials across the sample and, because the swelling stresses remain after shutdown, the peak stresses in the cladding occur during shutdown conditions. By analyzing the stress states in the different cladding designs, Stone discovered that the largest tensile stresses in the sample occur at the inside surface of the cladding. This large tensile stress suggests that the mSiC should be placed on the outside surface of the sample and that an inner CMC layer would be able to pseudo-plastically deform to

accommodate some of the swelling stress. Furthermore, the outer mSiC would be under a compressive load, and because of the deformation of the CMC, more of the tensile load during shutdown could be transferred to the outer mSiC without posing a significant risk of failure (Stone, et al., 2015). Stone concluded that an inner monolith/outer CMC design has a high failure probability, whereas the inner CMC/outer monolith design has a low failure probability of 5.28×10^{-5} for the lifetime of one cladding tube in typical LWR conditions.

Based on Stone's analysis, the two-layer design with an inner CMC layer and an outer mSiC layer appears to be the optimal design for multilayer SiC composite cladding. Accordingly, the samples investigated in this work are all two-layer inner CMC/outer monolith designs.

4. Experimental Methodology

4.1. Overview of Specimens

The samples investigated in this work were designed and provided by GA using Hi-Nicalon type S fibers manufactured by Nippon Carbon Co.

This work investigates the mechanical performance and corrosion characteristics of three different architectures of two-layer SiC composites. All samples were manufactured according to the processes outlined in Section 3.3, with the CMC layer manufactured using Hi-Nicalon type S fibers with a pyrolytic carbon interphase and CVI matrix, and the mSiC layer manufactured using CVD. The first architecture investigated is denoted GAOE (General Atomics Open-Ended) and consists of six open-ended cladding samples tested for hoop strength. The other two architectures investigated are denoted GACE-A and GACE-B (General Atomics Close-Ended) and consist of respectively three and five samples, each with one closed end and one open end. The closed end of the GACE samples consists of a 7.5° scarf endplug sealed by GA using the method discussed in Section 3.3.3. The GACE samples are all investigated for endplug joint strength; no hoop strength testing was performed on any GACE samples.

All samples investigated consist of two-layer designs, with an inner CMC layer and an outer EBC layer. The three architectures differed in the weave structure of the CMC layer and overall geometry (diameter and wall thickness). Table 10 presents the overview of architecture and geometry of the samples investigated in this work and Figure 33 illustrates the terminology used in describing the samples, and Figure 34 depicts the three different architectures investigated in this work.

Table 10: Overview of architecture and geometry of samples

General Architecture							Dimensions			
	Global	CMC layer					Geometry		Layer Ratio	
	Structure	Weave Pattern	Helicoidal Pitch	Interlace Angle	Inter-Tow Distance	Tow Width	OD	ID	CMC	EBC
GAOE	Two-Layer Open-Ended	Herringbone (Plain weave)	15 mm	120°	1.47 mm	1.2 mm	10.8 mm	9.4 mm	0.83	0.17
GACE A	Two-Layer Close-Ended	Three Tows	30 mm	100°	1.80 mm	1.2 mm	10.5 mm	7.8 mm	0.83	0.17
GACE B	Two-Layer Close-Ended	Herringbone (Plain weave)	6 mm	150°	1.22 mm	1.2 mm	10.4 mm	7.8 mm	0.83	0.17

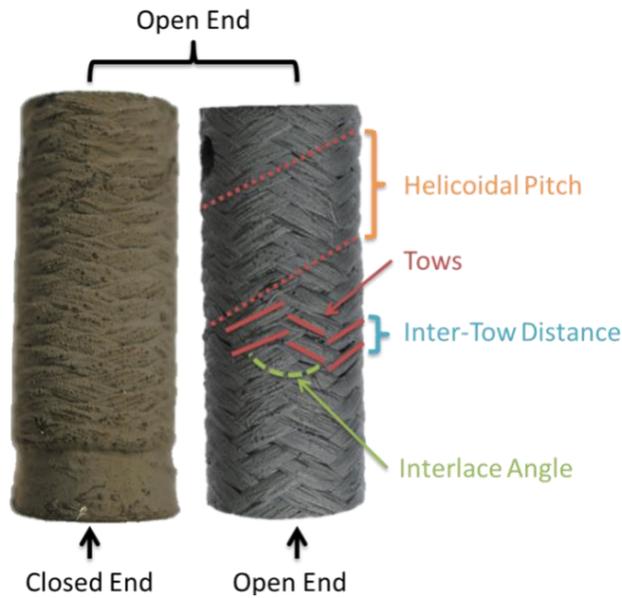


Figure 33: Graphic of sample architectural and geometric terminology



Figure 34: Overview of the three architectures investigated

The two-layer samples consist mostly of the CMC layer, with a thin mSiC EBC on the exterior surface. The CMC layer accounts for approximately 83% of the total wall thickness of the samples, with the EBC accounting for the remaining 17%; thus, the samples are almost entirely CMC. Figure 35 shows a cross-sectional SEM view illustrating the two-layer structure.

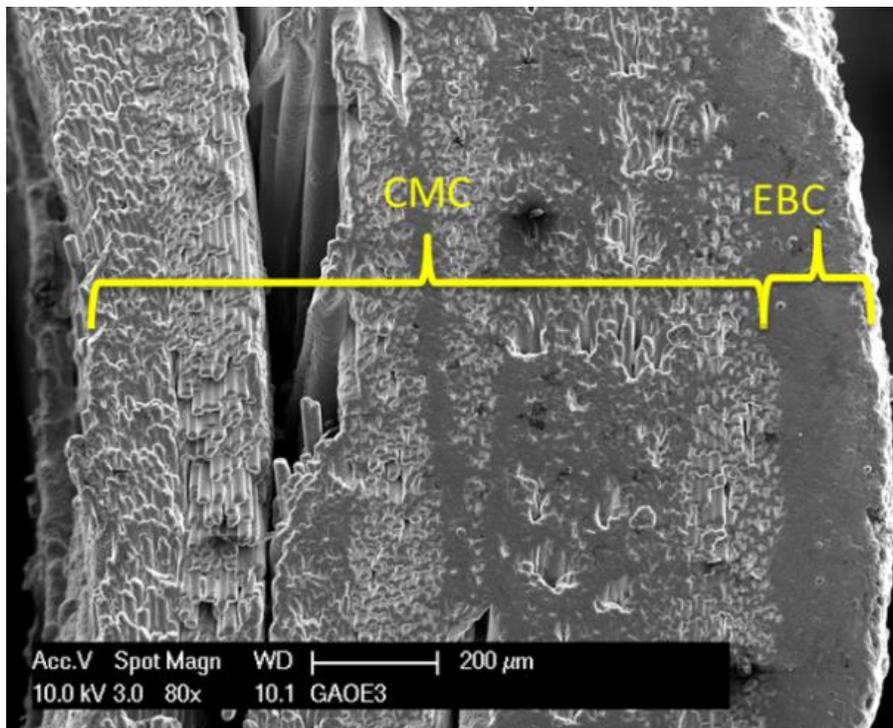


Figure 35: Cross-sectional SEM view showing two-layer architecture

4.1.1. Open-Ended Specimens

The open-ended samples investigated in this work were provided by GA and consist of six two-layer samples. Each sample was approximately 25 mm tall and had two diametrically-opposed circular penetrations at the top of the sample to assist with suspension in the oxidation and thermal-shock facilities. A typical GAOE sample, with the circular penetrations, is shown in Figure 36. Within the GAOE series, one sample was analyzed as-received, two samples were analyzed after thermal shock, two samples were analyzed after 48 hour oxidation, and one sample was analyzed after 24 hour oxidation. The test matrix for the GAOE samples is shown in Table 11.

Table 11: Test matrix for GAOE samples

Sample	Testing	Test Conditions
GAOE 1	Oxidation	24 hours, 6 g/min, 1400°C
GAOE 2	As-Received	As-Received
GAOE 3	Oxidation	48 hours, 6 g/min, 1400°C
GAOE 4	Oxidation	48 hours, 6 g/min, 1400°C
GAOE 5	Thermal Shock	1200°C into 100°C water
GAOE 6	Thermal Shock	1200°C into 90°C water

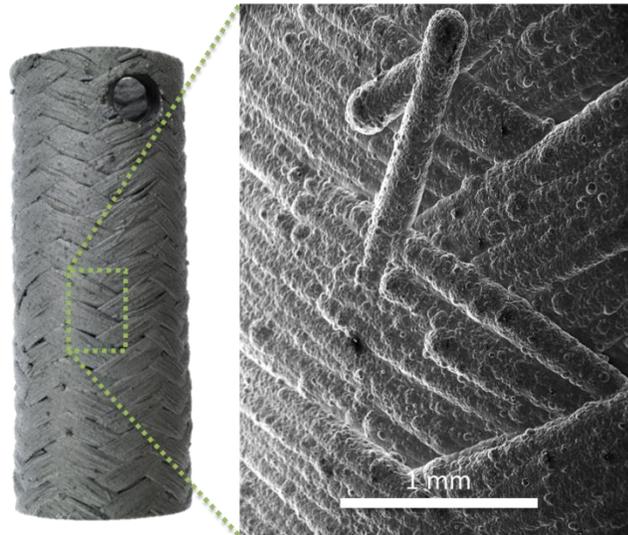


Figure 36: Typical GAOE sample and SEM close-up

4.1.2. Close-Ended Specimens

The close-ended samples investigated in this work were provided by GA and consist of a total of 8 two-layer samples in two unique CMC architectures (two-tow and three-tow designs). The first architecture is denoted GACE-A and consists of a three-tow CMC, while the second architecture is denoted GACE-B and consists of a two-tow CMC. Three samples were tested in the GACE-A series and four samples were tested in the GACE-B series. One sample in the GACE-B series was not tested due to a defective endplug joint as revealed by XCT analysis (discussed in Section 5.4.3). Within the GACE-A series, one sample was analyzed as-received, one sample was analyzed after thermal shock, and one sample was analyzed after 48 hour oxidation. The lack of any duplicability within the GACE-A series is due to the extremely limited number of samples available and the number of tests required to be performed on the series (three

samples were provided, and three unique tests were expected). Within the GACE-B series, one sample was analyzed as-received, two samples were analyzed after thermal shock, and one sample was analyzed after oxidation. Figure 37 shows typical GACE samples and Table 12 presents the test matrix for the GACE samples.

Table 12: Test matrix of GACE-A and GACE-B samples

	Sample	Testing	Test Conditions
GACE-A	GACE 1	Thermal Shock	1200°C into 100°C water
	GACE 2	As-Received	As-Received
	GACE 3	Oxidation	48 hours, 6 g/min, 1400°C
GACE-B	GACE 4	Oxidation	48 hours, 6 g/min, 1400°C
	GACE 5	Thermal Shock	1200°C into 100°C water
	GACE 6	As-Received	As-Received
	GACE 7*	-	-
	GACE 8	Thermal Shock	1200°C into 100°C water

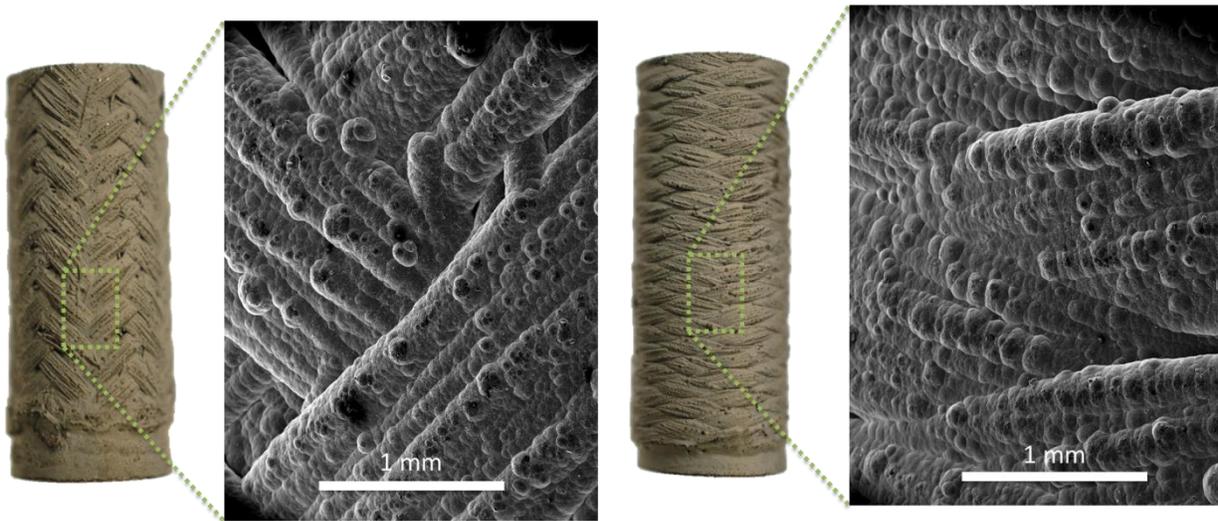


Figure 37: Typical GACE-A sample (left) and GACE-B sample (right) with SEM close-ups

4.2. Strength Test Facilities

Two strength testing facilities were implemented to perform mechanical evaluation of the samples. One facility was used to perform internal pressurization tests on the open-ended samples to evaluate the hoop strength of the tubular part of SiC cladding. Strain gages were implemented on the external surface of the samples during pressurization testing to allow for determination of the stress-strain response.

A different strength test facility was used to evaluate the mechanical strength of the endplug joint. The joint test facility performed uniaxial loading of the endplug following GA procedures (Khalifa H. E., Deck, Gutierrez, Jacobsen, & Back, 2015) and was intended to determine the peak pressure required for endplug joint failure (termed “burst strength”).

* No testing was performed due to defective endplug joint

4.2.1. Pressurization Test Facility

4.2.1.1. Pressurization Test Facility Overview

The facility used to perform internal pressurization tests of the samples consisted of an Instron 8501 load frame equipped with a 100 kN load cell with $\pm 0.5\%$ accuracy. The pressurization test consists of the internal pressurization of the tubular cladding samples at ambient temperature. A polyurethane plug, whose volume matches the internal volume of the sample being tested, is placed inside the sample and is axially compressed on one end by a piston while the other end rests on a platen. As the plug is compressed, it wants to expand radially, thus exerting internal pressure on the sample. A simplified schematic of the facility is illustrated in Figure 38. Previous research has shown that the expanding plug test gives an easy and accurate way of conducting internal pressurization tests (Carter, 2006). Furthermore, Lee used the expanding plug test in his work on SiC (Lee Y. , McKrell, Yue, & Kazimi, 2013). The internal pressure resulting from the compressive loading of the plug is determined by starting with the general Hooke's Law equation for axial strain in the plug:

$$\epsilon_x = \frac{1}{E_p} [\sigma_x - \nu_p(\sigma_r + \sigma_\theta)]$$

Where ϵ_x , E_p , σ_x , σ_r , σ_θ , and ν_p are respectively the plug axial strain, plug elastic modulus, plug axial stress, plug radial stress, plug circumferential stress, and plug Poisson ratio. The load from the load frame is used to apply an axial stress on the plug. For the expanding plug test, the plug radial and circumferential stresses are equal (Carter, 2006). Furthermore the internal pressure of the sample, P_i , is equal to the radial stress of the plug at the plug's outer surface. For an incompressible linear elastic material such as polyurethane $\nu_p = 0.5$. Substituting these values yields:

$$P_i = E_p \epsilon_{x,charging} - \sigma_x$$

During testing, an initial charging load is needed to load the plug until the plug fills the interior volume of the sample as reflected by the $E_p \epsilon_{x,charging}$ term. Afterwards, further load contribution due to plug axial strain is minimal. Thus, by using the load frame to apply an axial stress on the plug the internal pressure of the sample can be determined.

Although the samples investigated in this work are composed of two layers, with an inner CMC layer and an outer EBC layer, because the CMC layer composes over 80% of the wall thickness, the entire sample was assumed to be a homogenous material. Therefore, the geometry of the samples was simplified to a single homogenous layer, and therefore the stress of the samples during the pressurization tests was determined using the thick-wall cylinder stress equation:

$$\sigma_{hoop} = \frac{p_i r_i^2 - p_o r_o^2}{r_o^2 - r_i^2} - \frac{r_i^2 r_o^2 (p_o - p_i)}{r^2 (r_o^2 - r_i^2)}$$

With no external pressure, the equation becomes:

$$\sigma_{hoop} = \frac{p_i r_i^2}{r_o^2 - r_i^2} + \frac{r_i^2 r_o^2 p_i}{r^2 (r_o^2 - r_i^2)}$$

Because the strain gages were applied to the external surface of the sample, the stress at the OD is used for the construction of the stress-strain curves. The OD stress is:

$$\sigma_{hoop_{OD}} = \frac{2p_i r_i^2}{r_o^2 - r_i^2}$$

However, the maximum stress achieved during testing occurs in the internal surface of the sample, so the stress at the ID is used for determination of the peak failure stress of the sample:

$$\sigma_{hoop_{ID}} = \frac{p_i (r_o^2 + r_i^2)}{r_o^2 - r_i^2}$$

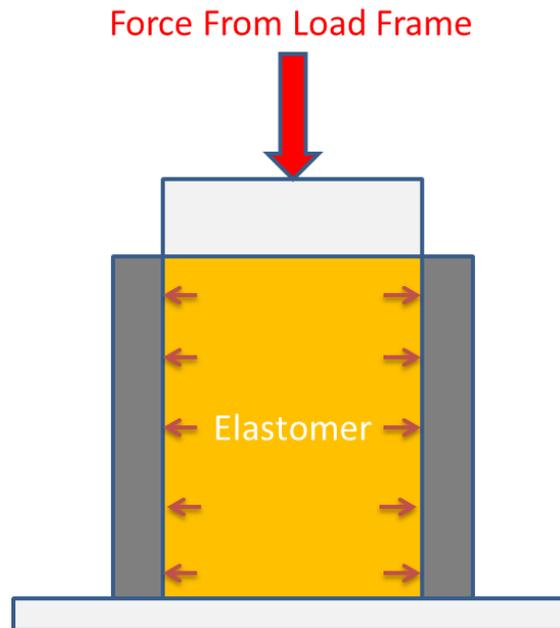


Figure 38: Schematic of the internal pressurization test facility

To obtain the stress-strain behavior of the samples, 1000 Ω strain gages* were implemented on the external surface of the samples. An image of the strain gage (containing two independent gages) is shown in Figure 39. The active area of the strain gages was aligned with the circumferential (hoop) direction of the samples to determine the hoop strain. By synchronizing the strain gage measurements with the load measurements, the stress-strain states for each measurement could be obtained.

* Omega SGD-2/1000-DY13 dual parallel 2 mm grid, +/- 0.5% resistance accuracy, +/- 1% gage factor accuracy

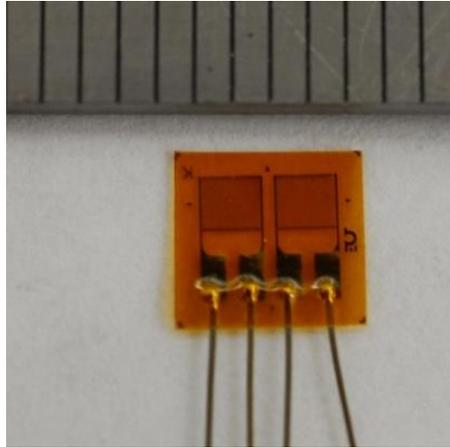


Figure 39: Photograph of strain gage (ruler increments 1/16 inch)

The strain gages were implemented in a Wheatstone bridge circuit, whereby two strain gages were applied to the sample and formed two legs of the bridge. The other two legs of the bridge were formed using resistors with a constant value of $1000\ \Omega$, equal to the strain gage nominal resistance. Thus, a half-bridge setup was utilized, as shown in Figure 40. The strain gage resistance is given as:

$$R_g = R_{g0} * GF * (1 + \epsilon)$$

Where ϵ is the strain, GF is the gage factor, and R_{g0} is the nominal gage resistance. Using this equation, the bridge voltage for the half bridge can be determined as:

$$\frac{V_{bridge}}{V_{ex}} = \frac{GF * \epsilon}{2 + GF * \epsilon}$$

Where V_{bridge} is the bridge output voltage (equal to $V_+ - V_-$ in Figure 40 below) and V_{ex} is the bridge excitation voltage. The strains experienced by the samples were small, and therefore the bridge voltage is small. Consequently, the bridge voltage signal was amplified prior to being recorded by the DAS.

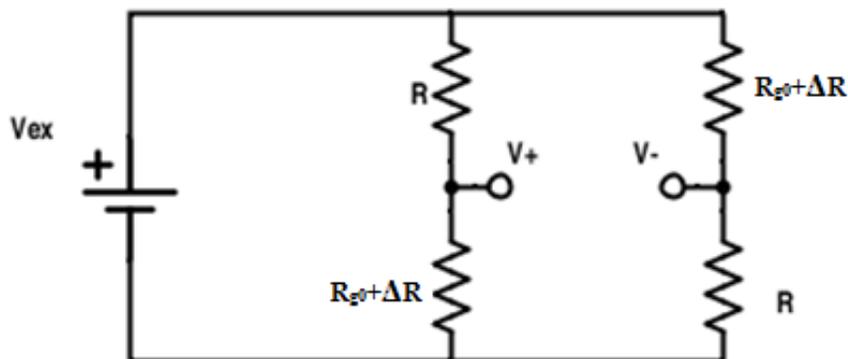


Figure 40: Diagram of half-bridge used for strain gage measurement

Amplification of the bridge voltage signal was performed using an instrumentation amplifier* with an external resistor for gain adjustment. The amplified signal was then recorded by the Agilent 34980A

* AD620 instrumentation amplifier

data acquisition system (DAS). The bridge was excited by 18 VDC supplied by two 9 VDC batteries in series. Batteries were chosen over a DC power because they could provide a compact, low-noise strain measurement setup. Because the voltage supplied by the batteries was not precisely constant, the bridge excitation voltage was recorded by the DAS during each bridge voltage measurement. With the DAS recording the bridge excitation voltage and the bridge output voltage, and with the known gage factor for the strain gages, the strain could be calculated using the half-bridge equation above.

The strain gages were applied to the surfaces of the samples using epoxy* specific to transducer-quality strain gage implementation. The gage application process involved first filling the texture of the samples where the strain gage was to be applied. Multiple layers of epoxy were deposited on the region until the texture was completely filled. Afterwards, the epoxy was sanded until it was smooth with the sample surface. The same epoxy was used to glue the strain gages to the now-smooth surface. A custom gluing jig was utilized to apply the appropriate pressure to the strain gage during curing. The jig consisted of a split shaft collar with silicone rubber tubing segments to evenly distribute the clamping pressure to the strain gage. Screws were used to adjust spring pressure on the clamp, and the appropriate spring deflection was calculated from the recommended clamping pressure for transducer-quality results. Figure 42 shows the curing jig utilized for strain gage application.



Figure 41: Strain gage curing jig with brass sample

4.2.1.2. *Pressurization Test Validation*

The strain gage implementation was validated by performing compressive tests of metallic rods with strain gages implemented. Such tests would compress solid metal rods, and strain gages would be implemented to measure either axial strain or hoop strain. With the axial strain gage measurements, the elastic modulus of the metal could be determined, and from the hoop strain gage measurements the Poisson's ratio of the metal could be determined. The measurements would be compared to the expected values for the metals, and the results would be used to determine the validity of the strain measurements. During the tests, it was discovered that there was poor contact between the load frame and the metal rods resulting in uneven stress distributions within the rods. To resolve this issue, annealed copper pads were placed above and below the rod to allow for even stress distribution within the rod. The basic setup is illustrated in Figure 42.

* Omega TT300 2-part epoxy

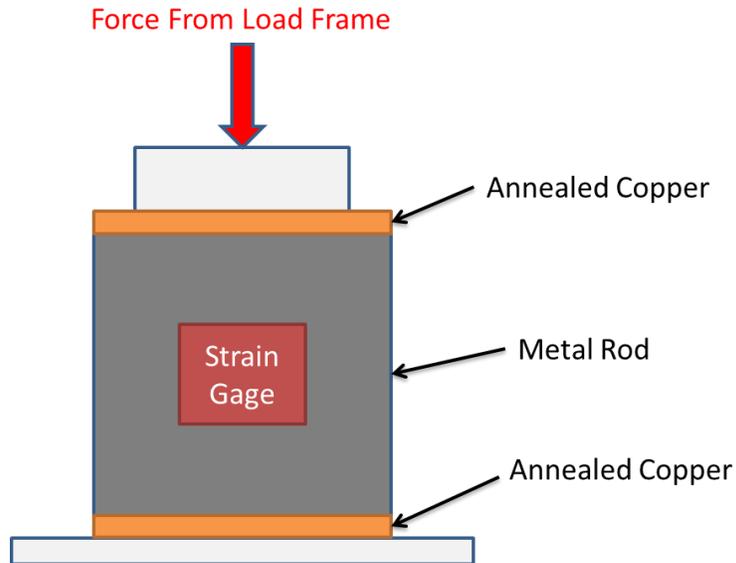


Figure 42: Strain gage validation setup

The strain gages were observed to be able to accurately measure both the elastic modulus and the Poisson's ratio for the specimens tested. Four tests were conducted to validate the strain measurements: two axial strain tests (to measure the elastic modulus) and two hoop strain tests (to measure the Poisson's ratio). Table 13 presents the results of the strain gage validation, and Figure 43 presents the comparison between the observed and expected stress-strain behavior for both axial and hoop tests for 18-8 stainless steel specimens. It should be noted that in Figure 43 the measured stress-strain behavior deviates from the expected behavior at low axial stress due to the copper pressure pads not making full contact between the specimen and the load frame. However, in the figure the behavior at high axial stresses corresponds well with the expected data. Because the measured quantities matched the expected quantities, the strain gage implementation was considered validated.

Table 13: Strain gage validation results

Test	Material	Expected Quantity	Measured Quantity
Axial 1	18-8 SS	E = 193-210 GPa	E = 197 GPa
Axial 2			E = 205 GPa
Hoop 1		v = 0.29	v = 0.28
Hoop 2			v ≈ 0.29

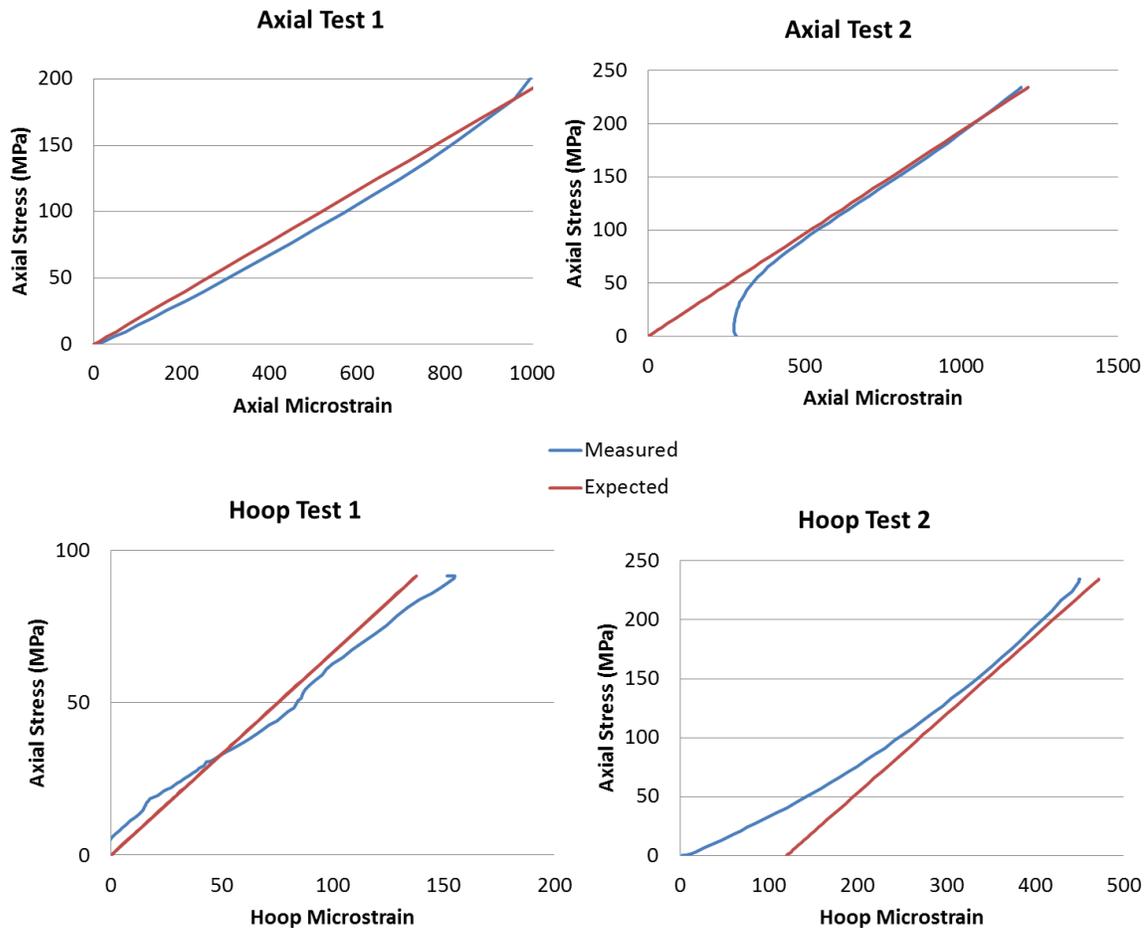


Figure 43: Strain gage validation data

After validation of the strain gage implementation, the expanding plug internal pressurization test was validated by performing pressurization tests of metallic tubes with strain gages employed and measuring the elastic moduli of the metals. During initial validation attempts, it was observed that the measured Young's modulus was consistently higher than the expected Young's modulus, signifying that the stress calculations were overestimating the true stress of the sample. To resolve the discrepancy, lubrication was employed at the mating surface between the plug and the ID of the specimens. Multiple lubricants were attempted, and Zinc Stearate was determined to be the lubricant that was most effective and easiest to apply. Thus, the pressurization test procedures incorporated the use of Zinc Stearate lubrication for all pressurization tests. Four tests were conducted to validate the pressurization test: three pressurization tests on brass tubing were performed and one pressurization test on steel tubing was performed. After the tests, the load measurements were used to calculate stress (using the thick wall cylinder stress equation) and the strain data coupled with the stress data allowed for the construction of a stress-strain curve for the pressurization test. From the stress-strain curve, the elastic modulus of the material being tested was measured and compared against the expected data. The validation results of the pressurization test are presented in Table 14 and the data is presented in Figure 44. Although the measured elastic moduli for the brass tests were slightly higher than the expected, this appears to be attributable to transient conditions during loading, as can be observed at low strains for

all three brass tests, as well as transients at high stresses, as can be observed in the Brass 2 test. Overall, the non-transient portions of the stress-strain behavior obtained for the brass and for the steel closely matched the expected behavior, and therefore the pressurization test was considered validated.

Table 14: Pressurization test validation results

Test	Material	Expected Quantity	Measured Quantity
Brass 1	260 Brass	$E \approx 110 \text{ GPa}$	$E = 126 \text{ GPa}$
Brass 2			$E = 124 \text{ GPa}$
Brass 3			$E = 118 \text{ GPa}$
Steel 1	4130 Steel	$E = 190\text{--}210 \text{ GPa}$	$E = 214 \text{ GPa}$

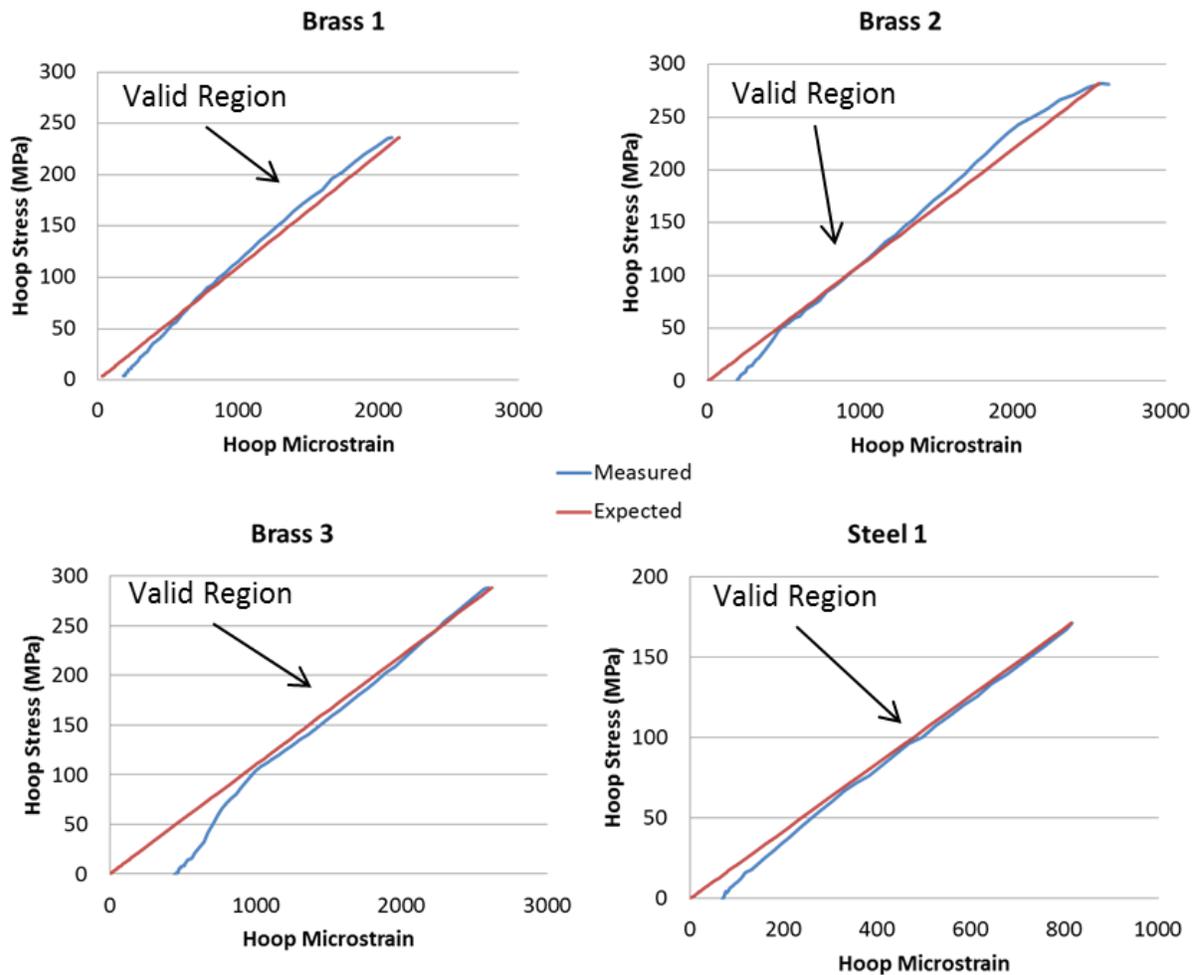


Figure 44: Pressurization test validation data

After validation, the pressurization test facility was used to test the hoop strength of the GAOE samples. Strain gages were applied to the OD surface of each GAOE sample and the stress-strain response was acquired. Figure 45 shows a photograph of the pressurization testing of a GAOE sample. In the figure, the rod can be observed at the top of the sample and the strings supporting the weight of the strain gage excitation wires can be observed wrapped around the bottom of the sample. The four excitation wires (two for each grid of the dual-grid strain gage) can also be seen exiting the right of the figure.

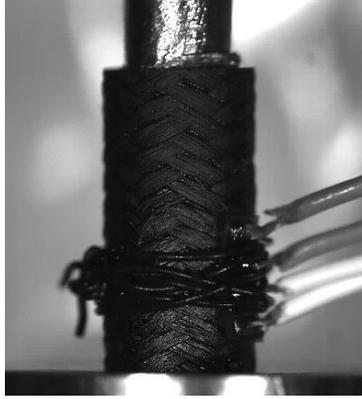


Figure 45: Photograph of GAOE sample undergoing pressurization test

4.2.1.3. Pressurization Test Uncertainty

During pressurization testing, there were several sources of error in the measured strength and stress-strain behavior of the samples. Most importantly, there was significant uncertainty in the friction forces between the plug and the tube. Although validation testing showed that the use of zinc stearate reduced the friction, the validation testing was performed on smooth-walled tubes, whereas the SiC cladding samples have a texture interior, likely leading to more friction and thereby reducing the stresses within the tube. However, end effects on the tubes resulted in stress concentrations at the tube ends, leading to increased tube stress and preferential tube failure at the tube ends. One further source of uncertainty was the accuracy of the load cell ($\pm 0.5\%$).

There were also sources of error in the strain measurements. Three primary sources of error were uncertainty in the gage factor ($\pm 1\%$), uncertainty in the nominal resistance of the gage ($\pm 0.5\%$), and uncertainty in the gain-setting resistor used with the instrumentation amplifier ($\pm 0.5\%$). Overall, these three sources of uncertainty resulted in strain measurement uncertainty of approximately 2%. However, additional uncertainty in the effectiveness of the strain gage application and alignment resulted in further uncertainty about the accuracy of the strain measurements that was not quantified in this analysis.

Although several sources of error were identified, it was difficult to quantify their influence on the measured quantities. Such analysis would require mechanical modeling of the expanding plug test to evaluate the stress distribution in the tube resulting from end effects and the enhanced friction caused by the textured interior tube surface. Quantification of the uncertainty in the pressurization test was outside the scope of this work and should be a topic for future work.

4.2.2. Joint Strength Test Facility

4.2.2.1. Joint Strength Test Facility Overview

The endplug joint test methodology was developed by GA (Khalifa H. E., Deck, Gutierrez, Jacobsen, & Back, 2015). Several components used to perform strength testing of the endplug joint were provided by GA, and the facility allowed for uniaxial loading of the endplug in the GACE samples. During the testing procedure, a fixture supported the samples and a pushrod was used to transmit force to the endplug. An Instron 8501 load frame equipped with a 100 kN load cell located in the H. H. Uhlig corrosion

laboratory was used to apply the force to the pushrod, and the load versus pushrod displacement was acquired during the test.

Figure 46 shows a diagrammatic representation of the endplug joint testing facility. The support fixture for the samples consisted of a support block with a mating interface for collets holding the specimen. The collets holding the specimen consisted of split conical collets attached to the sample using high-strength adhesive* and were designed by GA to prevent damage to the tubular part of the specimen during joint strength testing. During testing, the specimen-collet assembly was mated with the support fixture such that the axis of the specimen was coaxial with the loading axis of the load frame. The mating surface between the collets and the support block was coated with Teflon to assist with axial alignment. Furthermore, a grafoil disk was placed at the interface between the pushrod and the endplug to evenly distribute the load.

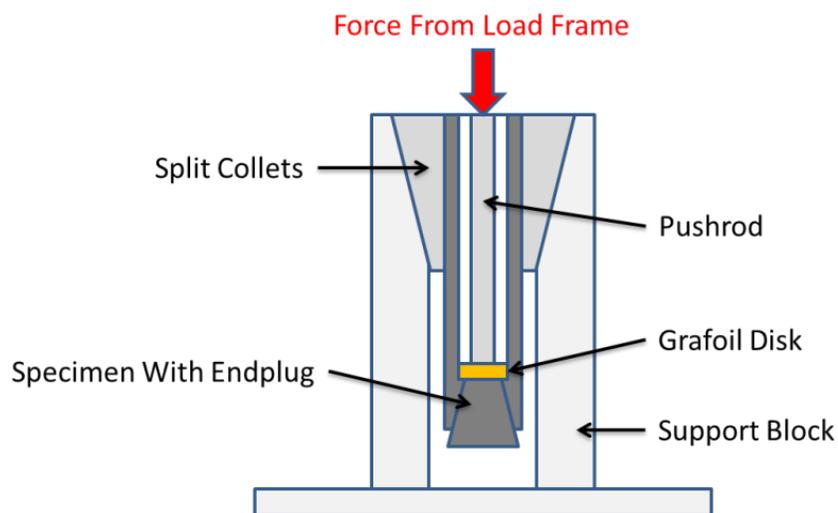


Figure 46: Endplug joint strength test facility

Validity of the joint strength test was determined by observing the failure mechanism during the test. During an ideal joint strength test, failure should be observed entirely in the joint with no fracture of the tube. However, fracture in the tube is permissible if it occurs in the endplug region of the specimen. If the failure occurs entirely in the tube away from the endplug region then the test is considered an invalid joint strength test. If the test is considered valid, then the burst strength of the sample is determined by the equation (where r_i is the inside radius of the tube):

$$\text{Burst Strength} = \frac{\text{Peak Load}}{\pi r_i^2}$$

4.2.2.2. Joint Strength Test Validation

The endplug joint strength testing facility was validated by performing tests on five dummy samples provided by GA. Both the tube and the endplug of the dummy samples were composed of mSiC, and the endplug joint of the dummy samples was composed of epoxy. The dummy samples were tested

* United Resin Corporation Tuffbond Epoxy

following the burst testing procedures, and the failure mode of the dummy samples was used to determine the validity of the joint strength testing. The joint strength testing of four out of the five dummy samples was valid. The invalidity of the one test is attributable to excess epoxy at the top of the endplug, resulting in stress concentration that caused failure in the tube above the endplug region. The results of the joint strength testing of the dummy samples are presented in Table 15.

Table 15: Results of joint strength testing with dummy samples

Sample	Peak load (N)	Nominal burst strength (MPa)	Fracture location	Validity	Comments
Monolith 1	6466	211	Tube at Joint	Valid	-
Monolith 2	6254	204	Joint	Valid	-
Monolith 3	1688	-	Tube	Invalid	Pushrod-tube interference
Monolith 4	6023	196	Tube at Joint	Valid	-
Monolith 5	5529	180	Joint	Valid	-

Figure 47 presents photographs showing the different failure characteristics of the valid dummy tests. Although variance was observed in the fracture location among the valid tests, all valid tests exhibited similar burst strengths which matched the burst strengths observed by GA during their validation testing. Therefore, the valid tests were all an indication of the true strength of the endplug joint for the dummy samples. Because four of the tests were valid, and because the invalid test was attributable to a manufacturing flaw, the endplug joint strength testing facility was considered validated.

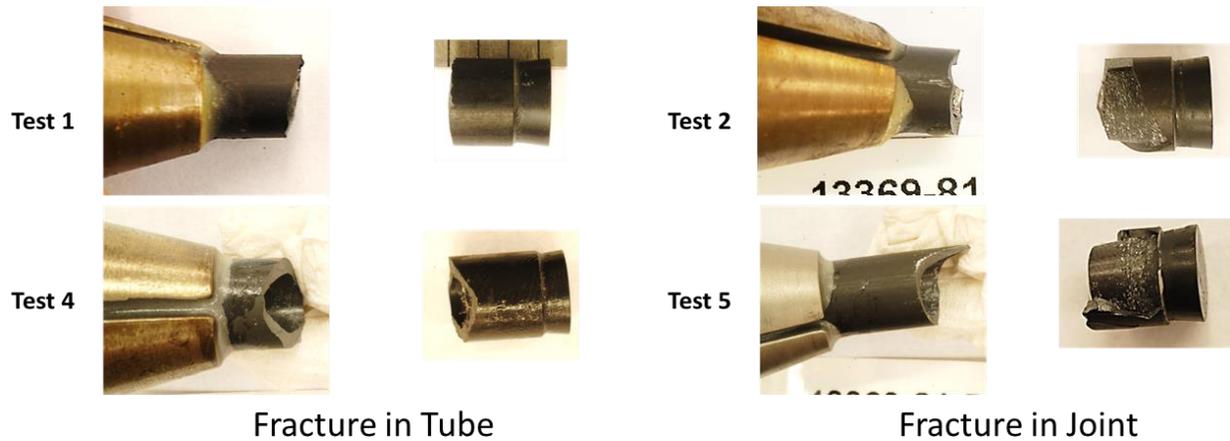


Figure 47: Failure characteristics of valid dummy tests

4.2.2.3. Joint Strength Test Uncertainty

Sources of uncertainty were identified in the endplug pushout test. One important source of uncertainty is the likely presence of bending moments in the tube, which would lead to failure not entirely representative of what would be observed during service. Furthermore, bending moments would increase the stress in the tubing, thereby lowering the effective burst strength of the specimens. Another source of uncertainty is the stress concentration due to the presence of the collet. A stress concentration is likely introduced by the collet at the location where the collet meets the tube and, because of the shortness of the samples investigated, the collet-induced stress concentration was close to the endplug joint region. Therefore, it is possible that the collet resulted in increased stress in the endplug joint region and consequently lowered the effective burst strength of the specimens. However,

the uncertainties in the joint strength test were not quantified in this work, as the mechanical modeling such analysis would require was beyond the scope of this work. The only uncertainty that was quantified for this study was that of the load cell used in the joint strength testing, which had a $\pm 0.5\%$ accuracy.

4.3. Thermal Shock Facility

The facility used to perform the thermal shock analysis of the samples consisted of a quartz tube rising from a pool of atmospheric-pressure water to a heater capable of 1500°C . The heater was controlled manually using a DC power supply, and heater temperature measurement was performed using a k-type thermocouple. The sample was suspended in the heater region using an alumina rod which was attached to a pneumatic actuator. The quench water was maintained at the desired temperature using a thermocouple and a hotplate with PID control. The entire quenching process was recorded using a high-speed video camera. A diagrammatic representation of the thermal-shock facility is shown in Figure 48.

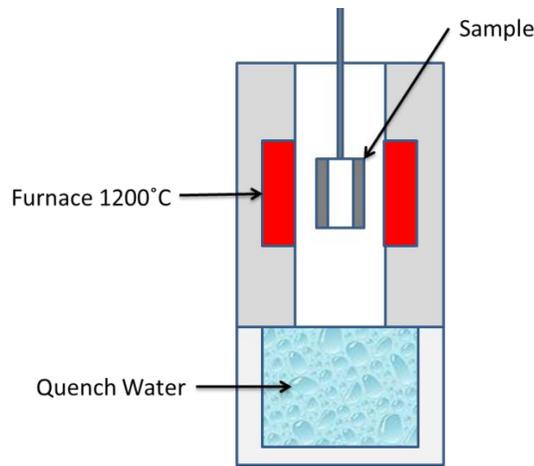


Figure 48: Diagram of thermal-shock facility

The thermal-shock conditions investigated in this work consisted of quenching the sample from 1200°C into either 90°C or 100°C atmospheric-pressure water. Therefore, the heater was set to 1200°C and the sample was suspended in the heater for 10 minutes prior to quenching to ensure that the sample achieved steady-state temperature with the heater. Afterwards, the actuator was used to plunge the sample into the pool of water. For the GAOE samples, the quenching water was 100°C for GAOE 5 and 90°C for GAOE 6. The 90°C water was intended to impose harsher quenching conditions on the sample and investigate the influence of water temperature on the test results. However, all GACE thermal shock samples were quenched at 100°C . Table 16 presents the test matrix for the thermal-shock samples.

Table 16: Test matrix for thermal-shock samples

Sample	Test Conditions
GAOE 5	Quench 1200°C to 100° water
GAOE 6	Quench 1200°C to 90°C water
GACE 1 (A)	Quench 1200°C to 100° water
GACE 5 (B)	Quench 1200°C to 100° water
GACE 8 (B)	Quench 1200°C to 100° water

The time between when the sample left the heater and when the sample began to enter the quench water was approximately 500 milliseconds. The time between when the sample began to enter the quench water and when it was fully submerged was 50 milliseconds. To determine the temperature drop of the sample during its transit from the heater to the quench water, numerous tests were performed using dummy samples with thermocouples attached. The dummy samples underwent quench testing identical to that of the actual test samples, and the thermocouples were used to measure the surface temperature of the dummy samples as they were driven from the heater to the water. The testing showed consistently that the surface temperature of the samples (with an initial temperature of 1200°C) was 1110°C upon entering the quench water. The temperature of the SiC during the transition from the heater to the quench water can also be approximated analytically by assuming only radiative heat transfer:

$$mC(T_0 - T_f) = \frac{\int_{T_f}^{T_0} \epsilon \sigma A T^4 dT}{T_0 - T_f} \Delta t$$

Where m , C , T_f , T_0 , ϵ , σ , A , and Δt are respectively the mass, heat capacity, final temperature, initial temperature, emissivity, Stefan-Boltzmann constant, external surface area, and transition time for the SiC sample. By using typical properties for CVD SiC ($C = 640 \text{ J/kgK}$, $\epsilon = 0.96$) (Rohm and Haas Company, 2008), a transition time of 500 milliseconds, and an initial temperature of 1200°C, the final temperature of the SiC is calculated to be 1140°C. This analytical result is likely higher than the experimental result due to the neglect of convective heat transfer and uncertainty in the transition time. Nevertheless, the analytical result agrees well with the experimental results, and therefore the actual test sample surface temperature was likely approximately 1110°C upon entering the quench water.

4.4.Oxidation Facility

The facility used to perform high-temperature steam oxidation tests of the samples consisted of a sealed pool of boiling water feeding steam inside a quartz tube (19 mm ID) through a succession of heaters with the ultimate steam temperature reaching 1400°C. The steam then passed across the sample, with the steam flow rate, sample oxidation time, and oxidation temperature predetermined based on the testing criteria. Thermocouples measured the temperature of the heating stages and the temperature of the steam flowing across the sample. The furnaces at each heating stage had closed-loop temperature control and the steam generator was powered by a DC power supply, thus allowing for accurate control of the steam flow rate. This facility was built specifically for this investigation but is similar to that used by Lee to measure oxidation behavior of previous SiC samples (Lee Y. , McKrell, Yue, & Kazimi, 2013).

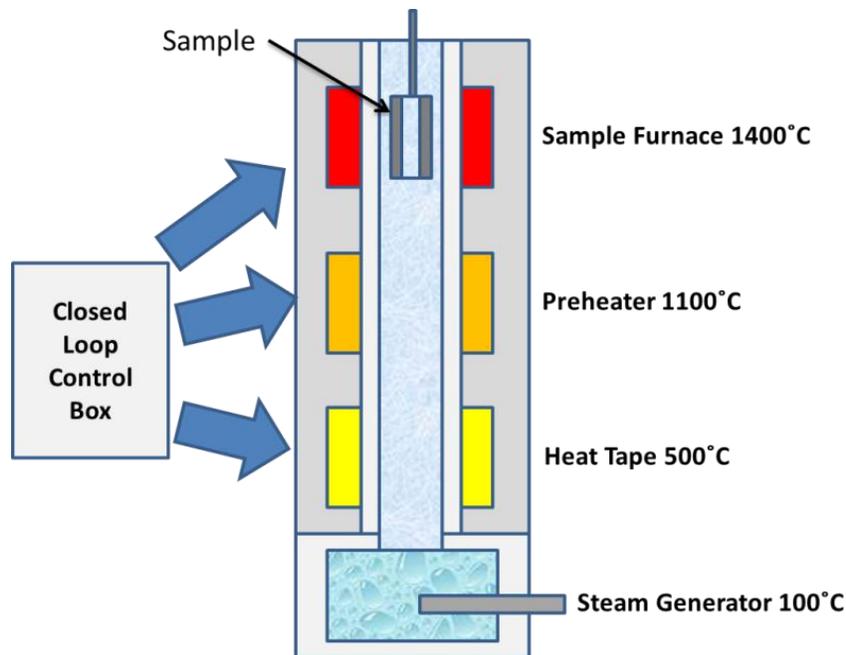


Figure 49: Diagrammatic representation of the high-temperature steam oxidation facility

Testing was performed by suspending the sample in the high-temperature sample furnace as the steam was passed across the sample surface. The sample was positioned vertically in the center of the quartz tube and steam was allowed to pass across both the inner and outer surfaces for all samples. Although the close-ended samples had their plug facing the steam flow, steam could enter from the top open end of the sample. After the oxidation test the sample was removed and allowed to air-cool.

Oxidation conditions were intended to approximate the long-term accident conditions in a typical PWR, although the peak oxidation temperature was limited by the capabilities of the experimental facility. Following Lee's work (Lee Y. , McKrell, Yue, & Kazimi, 2013), the 1400°C oxidation temperature was based on the limits of the oxidation facility and the results of Figure 50. Furthermore, the steam flow rate and facility geometry were based on Lee's analysis of subchannel oxidation conditions in a typical PWR (Lee Y. , McKrell, Yue, & Kazimi, 2013).

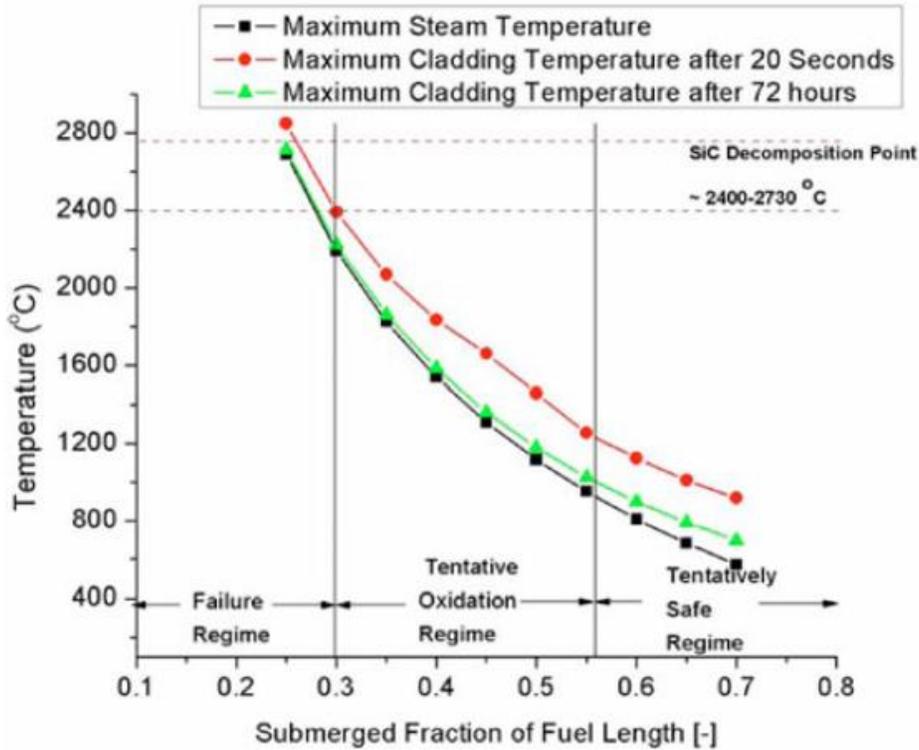


Figure 50: Oxidation regime for SiC (Lee Y. , McKrell, Yue, & Kazimi, 2013)

The oxidation conditions investigated in this work involved oxidizing the sample at 1400°C for either 24 hours or 48 hours with a steam flow rate of 6 g/min. All oxidation occurred at atmospheric pressure. To achieve the desired oxidation temperature, the heating stages were set according to Figure 49. The oxidation time for all samples except GAOE 1 was 48 hours; a less-harsh 24 hour oxidation time was chosen for GAOE 1 to investigate the evolution of the effects of oxidation. Table 17 presents the oxidation test matrix for all samples.

Table 17: Oxidation test matrix for all samples

Sample	Test Conditions
GAOE 1	Oxidation 24 hour, 1400°C, 6 g/min
GAOE 3	Oxidation 48 hour, 1400°C, 6 g/min
GAOE 4	Oxidation 48 hour, 1400°C, 6 g/min
GACE 3 (A)	Oxidation 48 hour, 1400°C, 6 g/min
GACE 4 (B)	Oxidation 48 hour, 1400°C, 6 g/min

5. XCT Analysis of Cladding Specimens

5.1. Motivation

Large voids have been observed to be present in the SiC/SiC CMC cladding specimens. The voids exist due to the inability of the CVI to entirely fill all inter-tow regions and consequently the voids concentrate at interfaces between tows, although small voids are also present in the inter-fiber matrix due to the inability of the CVI to completely fill all inter-fiber regions (Naslain, 2005). Voids can be problematic because they reduce the heat transfer capabilities of the CMC and because they can provide pathways for oxidation to penetrate axially in the CMC layer. Therefore, it is important to characterize the void distribution and morphology and relate void properties to sample architecture. In this manner, the voids can be better understood and potential oxidation pathways within the CMC can be identified.

5.2. Void Analysis Methodology

Void characterization was performed using XCT image analysis. First, XCT scans of all samples were taken as-received to obtain stacks of cross-sectional images of the samples. Then, image processing was performed to convert the grayscale XCT images into binary images. Finally, image processing of the binary images was performed to quantify the void ratio and characterize the void dimensions in the samples. Additionally, void analysis was performed on the joint region for the GACE samples to quantify the voiding of the joining material.

5.2.1. Void Analysis Facility

XCT scans were taken by a GE Healthcare eXplore CT-120 XCT scanner located in the Koch Institute for Integrative Cancer Research at MIT. The scans were taken with a voxel resolution and axial resolution of 50.3 μm and produced stacks of cross-sectional images of each sample. The images consisted of grayscale values representing the amount of x-ray interaction at each voxel, with higher values corresponding to increased x-ray interaction. Thus, “full” voxels appeared bright, and “empty” voxels appeared dark, although the exact value of each voxel was on a continuum of grayscale values. Representative pre-processed XCT images are presented in Figure 51.

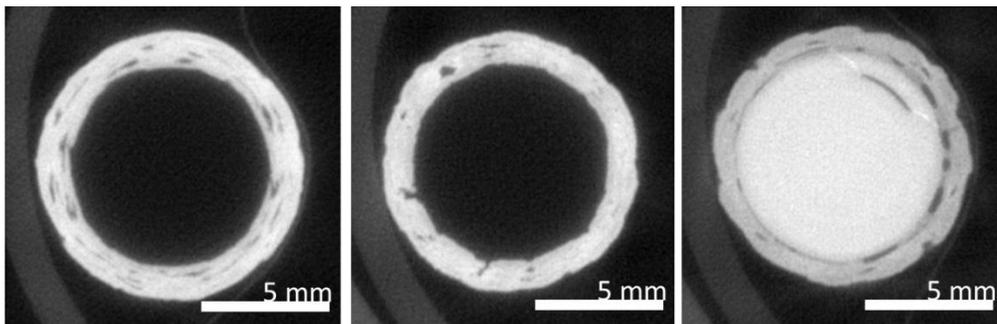


Figure 51: XCT images of typical GAOE sample (left), GACE-A sample (middle), and endplug region (right)

5.2.2. Image Processing

After the XCT images were obtained, processing was required to convert the grayscale images into binary images, in which a voxel is either full or empty. After the images were converted to binary, algorithms were created to quantify the void ratio and characterize the void morphology. Void ratio

reflects the ratio of empty voxels to total voxels within the sample's walls. Similarly, joint void ratio reflects the ratio of empty voxels to total voxels within only the joint material. The void axial height represents the total uninterrupted axial distance capable of being travelled inside a single void.

The first step in image processing was the conversion of the grayscale XCT images into binary images. Two algorithm options were explored to accurately convert the grayscale images into binary images: a simple threshold method and a combined threshold/moving average method. The simple threshold method consisted of applying a threshold to the grayscale image, below which a voxel is considered empty and above which the voxel is considered full. The typical threshold for most samples varied between 1700 and 1900, although the best value depended on the sample. However, it was discovered that the threshold alone was not accurate at characterizing small details of the voids. Therefore, a moving average method was combined with the threshold method to faithfully reproduce the details of the voids.

The moving average method consisted of scanning rows in the grayscale image and tracking the moving average and moving variance of the voxels. Each voxel is compared to a conservative threshold and the difference between the current voxel and the moving average is compared to the moving variance. If the voxel is below the threshold for empty voxels, then the voxel is considered empty; if the voxel is above the threshold for full voxels, then the voxel is considered full. Otherwise, if the difference between the voxel and the moving average is larger than a specified fraction of the variance, then the voxel is considered potentially different from the previous voxel. In such a circumstance, if the previous voxel is full and the current voxel has a higher value, or if the previous voxel is empty and the current voxel has a lower value, then no change is implemented. Otherwise, the current voxel is set to be the opposite of the previous voxel, and the moving average and moving variance are restarted.

The values of the thresholds and the variance fraction were determined by visually comparing the processed image with the original and choosing the values that give the most faithful reproduction of the grayscale image. Figure 52 shows a comparison between the original grayscale image obtained from XCT with the binary images after threshold processing and moving average processing. From the figure, it can be observed that the moving average processing more faithfully reproduces the fine details of the voids.



Figure 52: Comparison of original grayscale image (left) with threshold processed (middle) and moving average processed (right) Boolean images

5.2.2.1. Void Fraction Analysis

After the binary images were obtained, each image was analyzed to determine the void fraction within the thickness of the sample. The algorithm began by scanning left-to-right until it encountered a full voxel, and that full voxel was considered to be the leftmost boundary of the sample's thickness. Then, the algorithm began in the middle of the sample and scanned right-to-left until it encountered a full voxel, and that full voxel was considered to be the rightmost boundary of the sample's thickness. The process was repeated for the right half of the sample, and a total of four boundaries were obtained. After the boundaries were obtained, the algorithm scanned the row only between the boundaries and tallied the total number of voxels and the total number of empty voxels within the sample's thickness. The void fraction was determined by dividing the total number of void voxels by the total number of voxels within the thickness, and the axial variation of the void fraction was obtained by recording the void fraction for each image slice. The mean void fraction for the entire sample's CMC was obtained by averaging the void fraction over all image slices in the sample (excluding those that contained the endplug). The variance of the void fraction was determined by analyzing the axial variance of the void fraction for each image slice. A flowchart for the void fraction algorithm is presented in Figure 53.



Figure 53: Void fraction algorithm flowchart

5.2.2.2. Endplug Joint Void Analysis

Furthermore, it was desired to measure the void fraction of the joint material bonding the endplug to the tubing for the GACE samples. Therefore, an algorithm was implemented which only scanned the void fraction within user-defined concentric circles delineating the joint region. The algorithm allowed the user to construct two circles representing the innermost and outermost boundaries of the joint region. The algorithm then scanned the void fraction only between the two circles in a manner similar to the CMC void fraction algorithm described above. The bounding circles were user-defined to allow for accurate border definition without overlapping either the endplug or the CMC regions. However, because the user manually defined the scan area for the endplug joint region, only five image slices were analyzed for each sample, and the analysis was repeated three times for each sample. However, because the joint voids were observed to be of substantial axial length, the five slices were representative of the axial void profile of the endplug joint. Figure 54 shows the user-defined scanning boundaries for a joint region, whereby the full voxels within the scan region are white and the empty voxels are gray. Voxels outside the scan area in the figure are also gray. Joint void fraction analysis allowed for the comparison of endplug joints between the different GACE samples prior to mechanical testing. A flowchart for the endplug joint void fraction algorithm is presented in Figure 55.

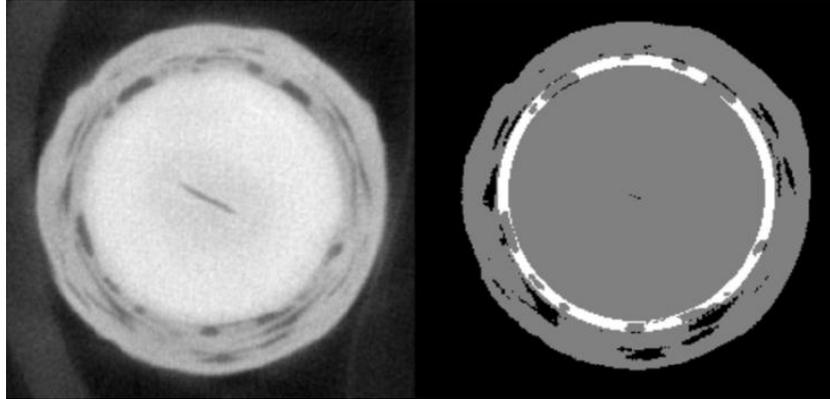


Figure 54: Original grayscale image (left) and joint scan region with joint voids (right)



Figure 55: Endplug joint void fraction algorithm flowchart

5.2.2.3. *Sample Density*

It was also desired to measure the density of the volume considered to be full to evaluate the presence of voids smaller than the resolution of the XCT. The density of the “full” volume was determined by counting the number of full voxels in each image slice of the sample. Because each voxel is a 50.3 μm cube, counting the total number of “full” voxels in the sample allowed for the total “full” volume to be determined. The samples were also weighed, and thus the density could be determined. The density values obtained through XCT analysis were compared to the theoretical density of SiC to determine the void fraction in the “full” volume of the sample. This algorithm showed sensitivity to the grayscale-Boolean image conversion, and thus a range of reasonable values was obtained for the sample’s true full volume density. Figure 56 presents a flowchart of the algorithm used to determine the density of the filled volume of the sample.



Figure 56: Sample density algorithm flowchart

5.2.2.4. *Void Height Analysis*

Finally, an algorithm was implemented to measure the axial height of voids in the samples. The algorithm allowed the user to pick voids, and the algorithm then searched to find the axial limits of the voids. The searching process imitated the motion of a gas particle in the void which experienced randomized lateral movement but biased axial movement (only upwards or only downwards), and by tracking the paths of numerous particles, the axial limits of the void were obtained. By comparing the

uppermost and bottommost axial limits of a specified void, the total height of the void was obtained. By performing such analysis for numerous independent voids that do not exit the sample, a histogram could be generated that illustrates the distribution of void axial heights within each sample. Although the analysis did not suggest complete axial percolation of the voids throughout the sample, the analysis was limited by the resolution of the XCT scanner, and thus void pathways smaller than 50.3 μm were not accounted for. Therefore, the true axial extent of the voids is likely higher than that determined through this analysis. The flowchart for the algorithm for finding the void height distributions is shown in Figure 57.

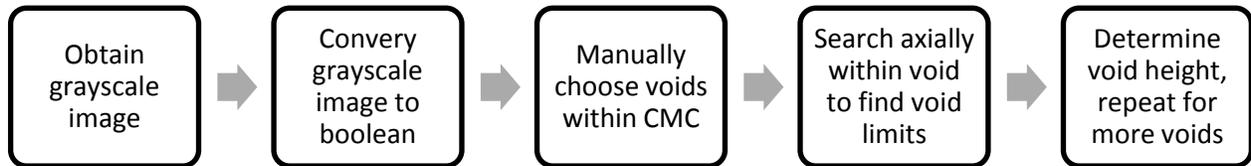


Figure 57: Void height algorithm flowchart

5.3.Void Analysis of CMC

Because the majority of the sample thickness is CMC, the entire sample is assumed to be CMC for the void analysis. Therefore, the presence of the EBC is ignored in the determination of the CMC void fraction and density.

Except for GAOE 1, the GAOE samples already experienced corrosion testing and strength testing prior to XCT analysis. Therefore, in this analysis it is assumed that the corrosion testing did not affect the void behavior in the samples. However, some GAOE samples still had strain gages on the external surface during XCT analysis which caused signal distortion and prevented accurate determination of the sample's volume, thereby preventing accurate determination of sample density. However, the algorithm for void fraction determination was not sensitive to the signal distortions caused by the strain gages and thus the strain gages did not significantly affect the void fraction data. An example of the image distortion due to the strain gage is shown in Figure 58.

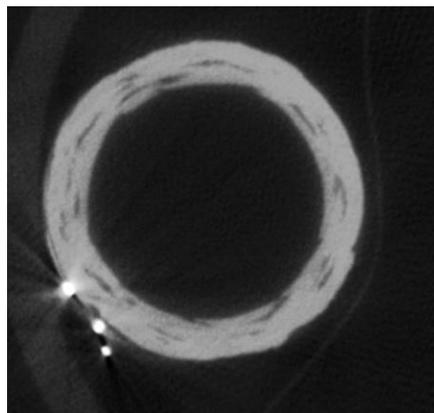


Figure 58: XCT image distortion due to strain gage on bottom left

Finally, the presence of the endplugs prevented determination of the weight of the CMC-only region for the GACE samples, and consequently the density of the CMC in the GACE samples was not obtained.

Table 18 presents the different XCT analysis tests performed on each sample, and identifies the reasons why certain XCT analysis was not performed on certain samples.

Table 18: Table showing XCT analysis test matrix with reasons for omitted tests

Sample	CMC Void Fraction	CMC Density	Joint Void Fraction	Void Height
GAOE 1	✓	✓	No Joint	✓
GAOE 2	✓	Strain Gage	No Joint	✓
GAOE 3	✓	✓	No Joint	✓
GAOE 4	✓	✓	No Joint	✓
GAOE 5	✓	Strain Gage	No Joint	✓
GAOE 6	✓	Strain Gage	No Joint	✓
GACE 1	✓	Endplug	✓	✓
GACE 2	✓	Endplug	✓	✓
GACE 3	✓	Endplug	✓	✓
GACE 4	✓	Endplug	✓	✓
GACE 5	✓	Endplug	✓	✓
GACE 6	✓	Endplug	✓	✓
GACE 7	✓	Endplug	✓	✓
GACE 8	✓	Endplug	✓	✓

5.3.1. CMC Void Data

Void fraction analysis was performed on all samples, and from the analysis the axial variation in void fraction was obtained. However, because the GAOE samples had already been strength tested (except GAOE 1), the failed CMC regions were eliminated from the void fraction analysis and only the intact CMC regions were considered. The resulting axial variation of void fraction for each GAOE sample is presented in Figure 59. From the figure, it can be observed that all GAOE samples had similar void fractions, and the period of the axial fluctuations of void fraction roughly correspond to the 1.47 mm axial inter-tow distance of the GAOE series. The CMC void fractions varied from 2% to 10%, corresponding well with the 6-7% (Abdul-Aziz, Ghosn, Baaklini, & Bhatt, 2003) and 10% (Bloom, 1998) porosity values obtained in a previous studies but somewhat higher than the 0.03% void fraction determined by Puglia (Puglia, Sheikh, & Hayhurst, 2004).

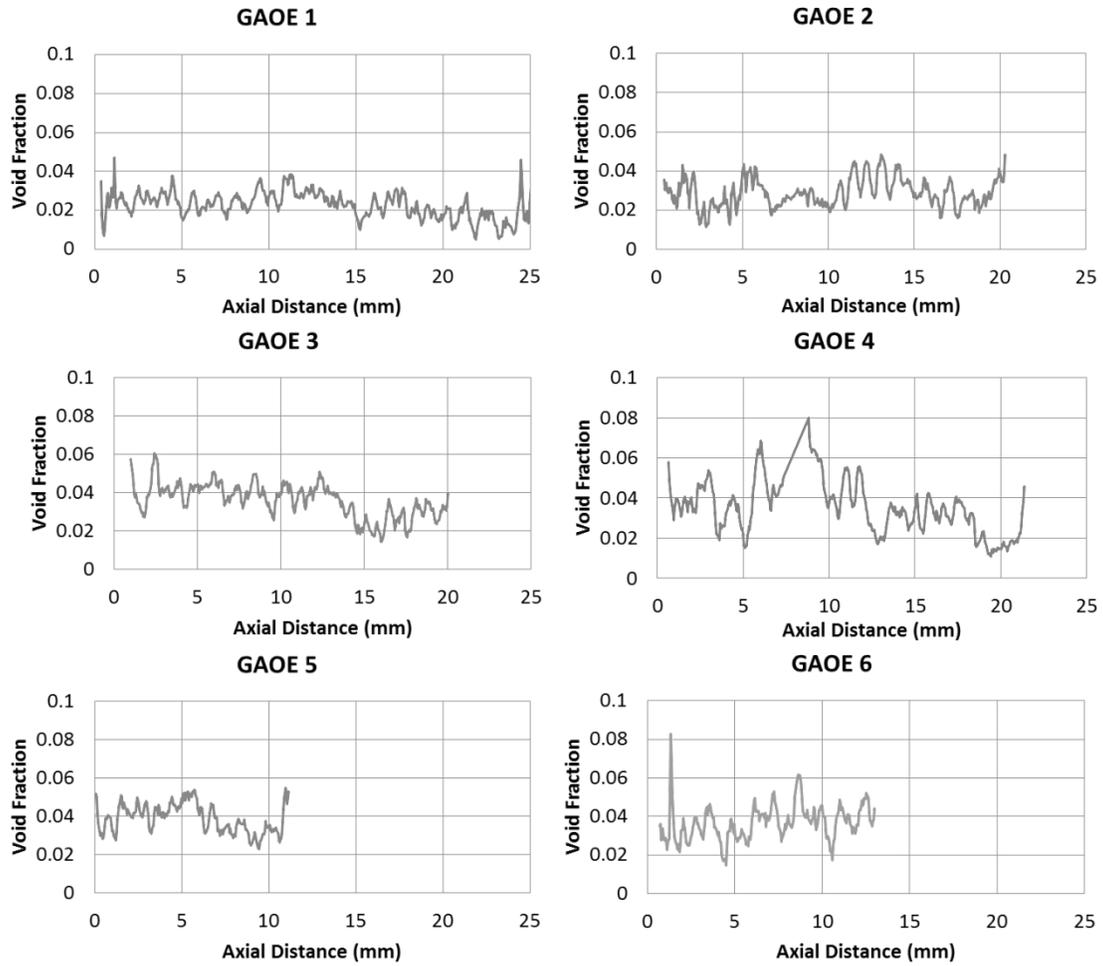


Figure 59: Axial variation of void fraction for GAOE series

For the GACE samples, the endplug influences the void fraction in axial slices containing the endplug because it appears as a large non-void region. Therefore, the CMC void fraction of the GACE samples was calculated only above the endplug joint (which comprised approximately the first 10 mm). Figure 60 presents the axial variation of the void fraction for the GACE-A series, and Figure 61 presents the axial variation of the void fraction for the GACE-B series. From the figures, it can be noted that most of the samples within a series have similar void fractions, although the GACE-B series exhibited more spread in void fraction among its samples. Also, the period of the axial fluctuations of void fraction roughly correspond to the axial inter-tow distance of 1.8 mm and 1.2 mm for GACE-A and GACE-B respectively.

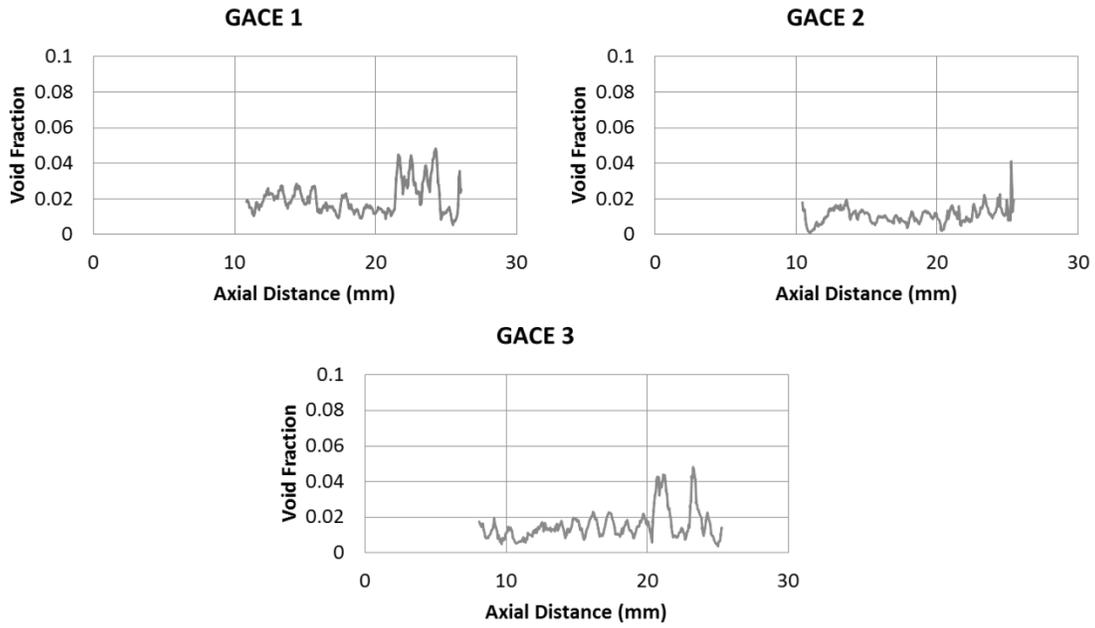


Figure 60: Axial variation of void fraction for GACE-A series

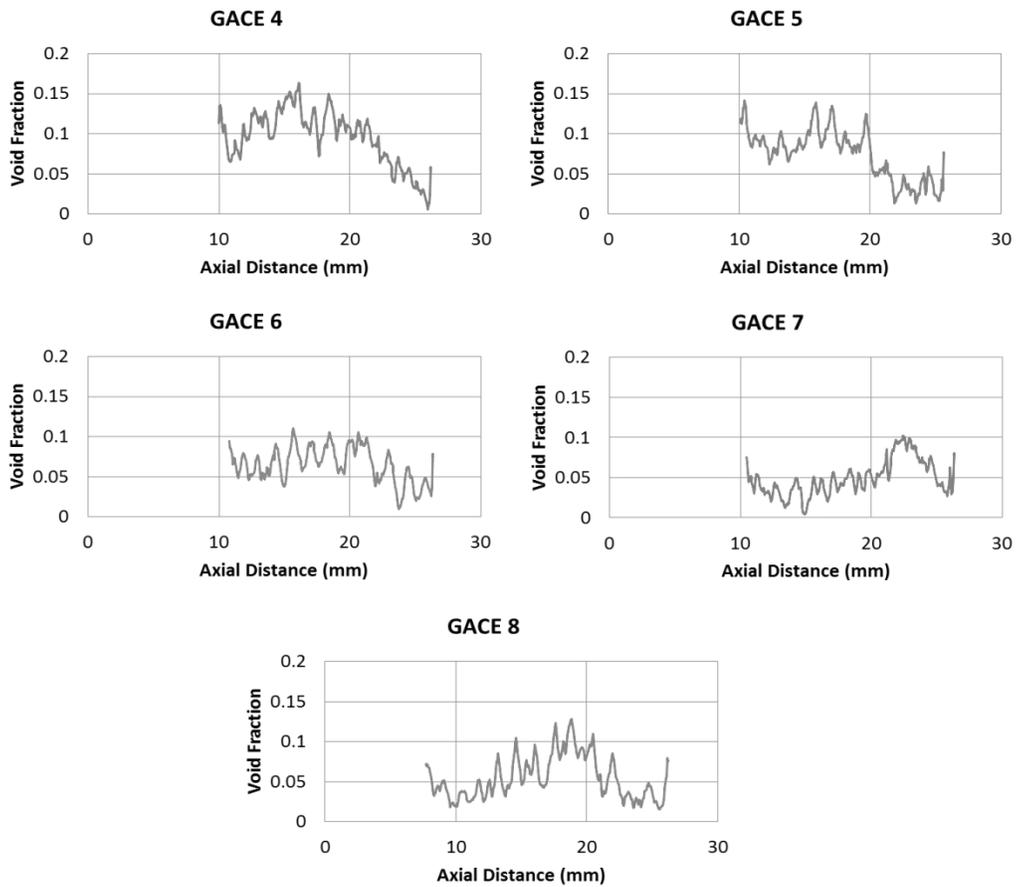


Figure 61: Axial variation of void fraction for GACE-B series

The resulting average and standard deviation of the CMC void fraction for all samples is reported in Table 19.

Analysis of the density of the “full” regions of the CMC layer was performed on samples GAOE 1, GAOE 3, and GAOE 4. The analysis revealed that the density of the CMC layer for those samples is at least 96% theoretical density and can potentially be 100% theoretical density. This relatively low micro-porosity corresponds well with previous work which estimated an inter-fiber micro-porosity of 0.03% (Puglia, Sheikh, & Hayhurst, 2004). The values for CMC solid region density are reported in Table 19.

Analysis of the void heights was performed by measuring the height of approximately 15 voids within the samples. The number of voids available for analysis was limited because, to avoid bias, the voids were chosen to be independent (non-intersecting) and not allowed to exit the sample. Histograms were constructed for each series reflecting the distribution of void axial heights. The histogram for the GAOE series is reported in Figure 62, the histogram for the GACE-A series is reported in Figure 63, and the histogram for the GACE-B series is reported in Figure 64. From the histograms, it can be observed that the distribution of void heights followed a roughly lognormal distribution and that the shape of the void height distribution differed between each series. However, the histograms also exhibited slightly bimodal behavior which indicates the interconnectedness of some voids within the samples.

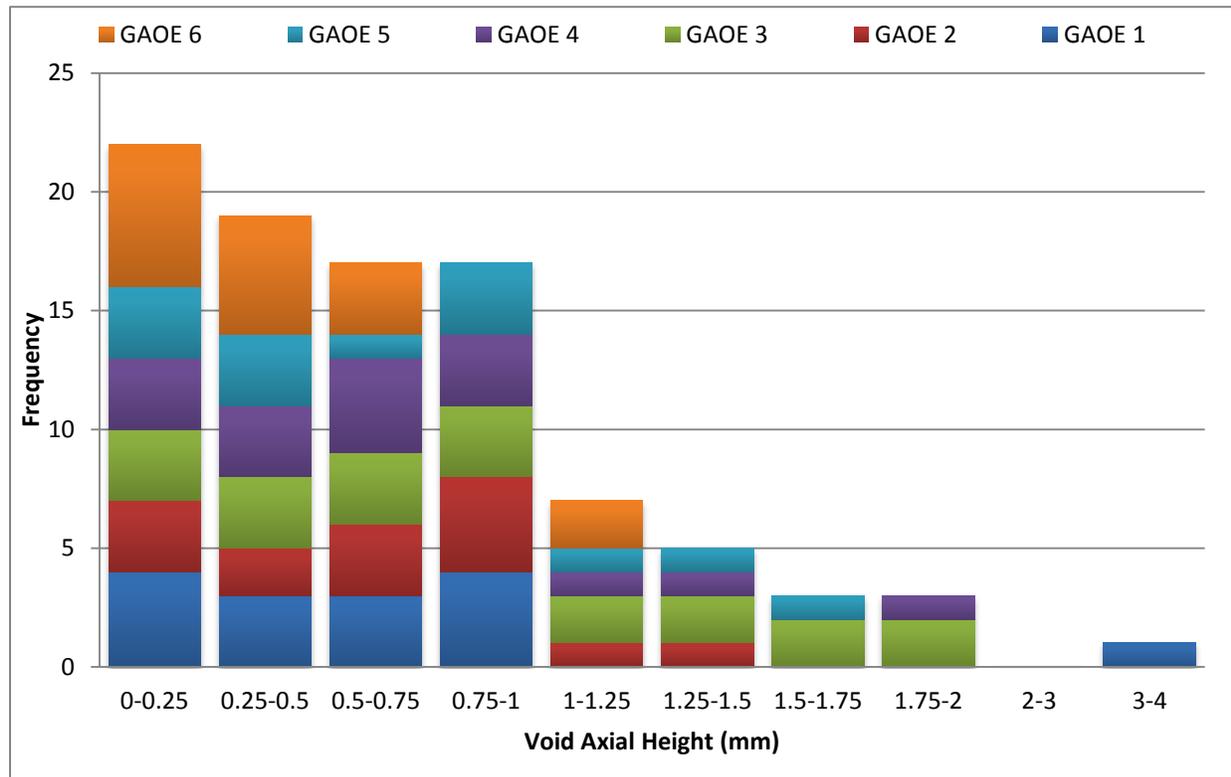


Figure 62: Histogram of void heights for GAOE series

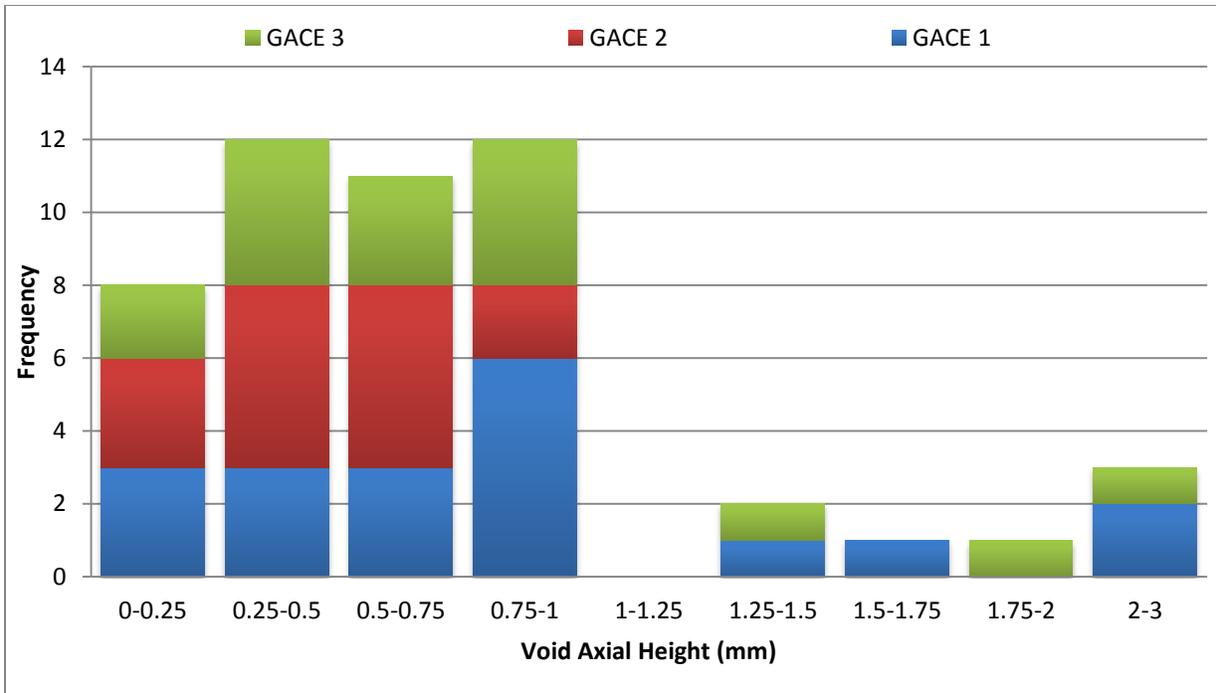


Figure 63: Histogram of void heights for GACE-A series

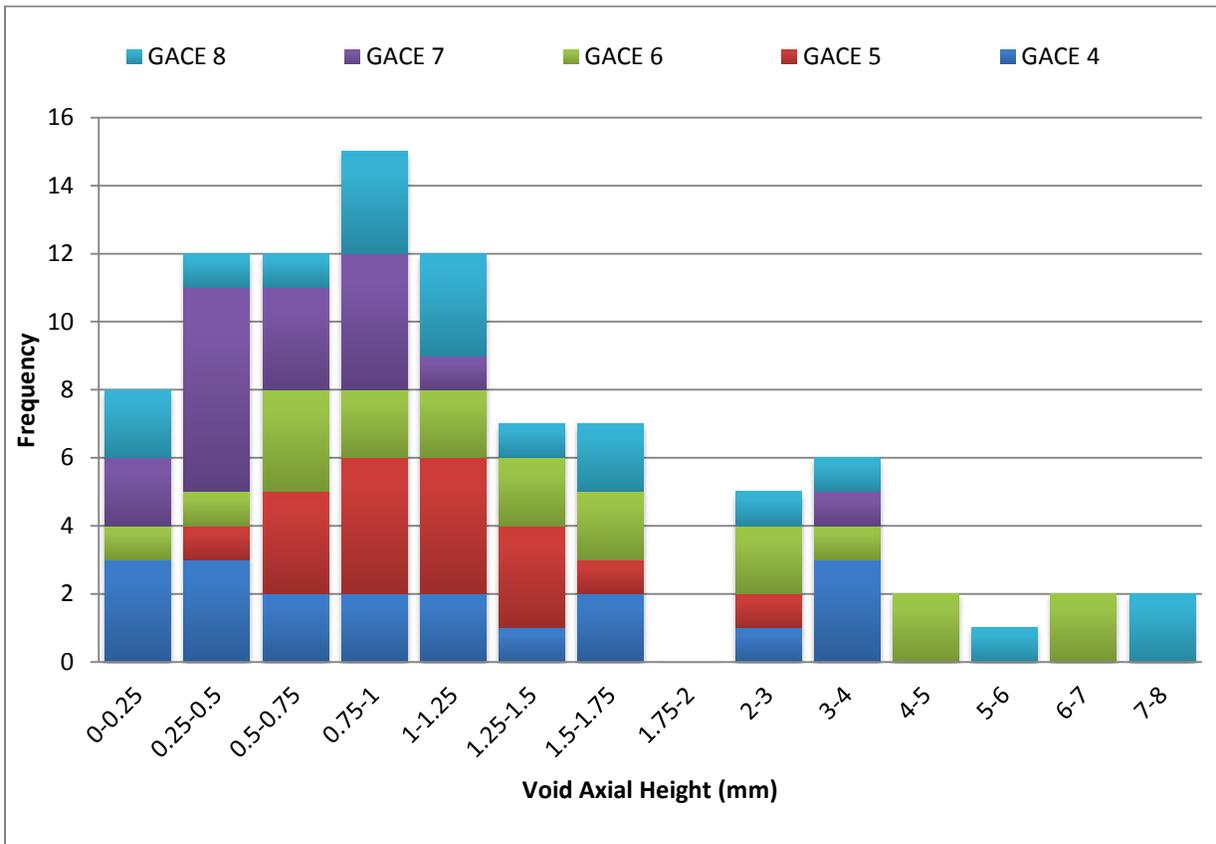


Figure 64: Histogram of void heights for GACE-B series

Table 19: Results of CMC XCT analysis for all samples

	Sample	CMC Void Percentage	Solid Theoretical Density Percentage	Void Height
GAOE	GAOE 1	4.1 ± 1.0 %	96.2 to 100 %	0.7 ± 0.9 mm
	GAOE 2	3.7 ± 0.9 %	-	0.6 ± 0.4 mm
	GAOE 3	4.6 ± 1.0 %	95.7 to 100 %	0.9 ± 0.6 mm
	GAOE 4	4.2 ± 1.3 %	96.6 to 100 %	0.7 ± 0.5 mm
	GAOE 5	3.8 ± 0.7 %	-	0.7 ± 0.5 mm
	GAOE 6	4.4 ± 1.0 %	-	0.4 ± 0.3 mm
GACE-A	GACE 1	2.8 ± 0.8 %	-	0.9 ± 0.7 mm
	GACE 2	1.9 ± 0.7 %	-	0.5 ± 0.2 mm
	GACE 3	2.3 ± 1.0 %	-	0.9 ± 0.7 mm
GACE-B	GACE 4	9.6 ± 1.9 %	-	1.3 ± 1.1 mm
	GACE 5	8.2 ± 1.6 %	-	1.1 ± 0.5 mm
	GACE 6	8.8 ± 2.7 %	-	2.1 ± 1.9 mm
	GACE 7	8.1 ± 3.0 %	-	0.7 ± 0.7 mm
	GACE 8	9.2 ± 3.5 %	-	2.1 ± 2.3 mm

5.3.2. CMC Void Discussion

XCT analysis of the void fraction and void height in the CMC layer allowed for the average void fraction and void height for each series to be determined. From the analysis it can be observed that each series had a unique void percentage and void morphology. Thus, the XCT analysis suggests that the sample architecture influences the properties of the voids in the CMC. The average CMC macro-void fraction for each series is presented in Table 20.

Table 20: Results of CMC XCT analysis for all series

Series	Architecture	Interlace Angle	Mean CMC Macro-Void Percentage	Mean CMC Void Height
GAOE	Two-Tow	120°	4.1 ± 0.3 %	0.7 ± 0.2 mm
GACE-A	Three-Tow	100°	2.3 ± 0.5 %	0.8 ± 0.2 mm
GACE-B	Two-Tow	150°	8.8 ± 0.6 %	1.5 ± 0.6 mm

From the XCT scans, it was observed that the void morphology was dependent on the architecture of the samples. Figure 65 shows a comparison between the sample architecture and the void morphology for the different series. The interlace angle between tows strongly influenced void morphology: the higher interlace angle of the GACE-B series with respect to the GAOE series led to voids that visibly appeared more circumferentially-elongated and the GACE-B series had a higher void fraction. In contrast, the GACE-A series had the shallowest interlace angle, and the XCT scans revealed that the CMC voids were visibly smaller in the circumferential direction than those of the GAOE and GACE-B series. Furthermore, the GACE-A series exhibited the smallest CMC void fraction of all series. Figure 66 demonstrates the apparent dependence of CMC void fraction on tow interlace angle. The correspondence between void fraction and interlace angle that was observed during XCT analysis suggests that the high interlace angles interfere with the CVI process used to fill the inter-tow regions, thus resulting in numerous large voids.

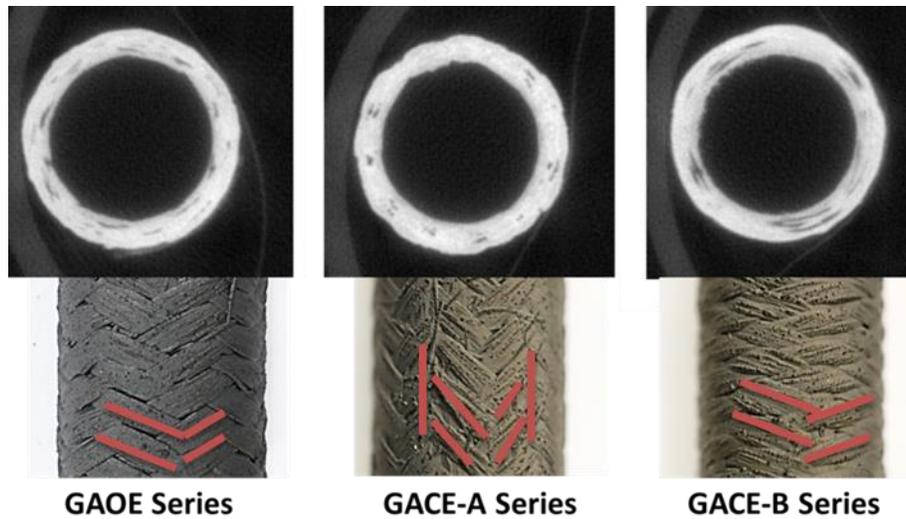


Figure 65: Comparison of void morphology and sample architecture

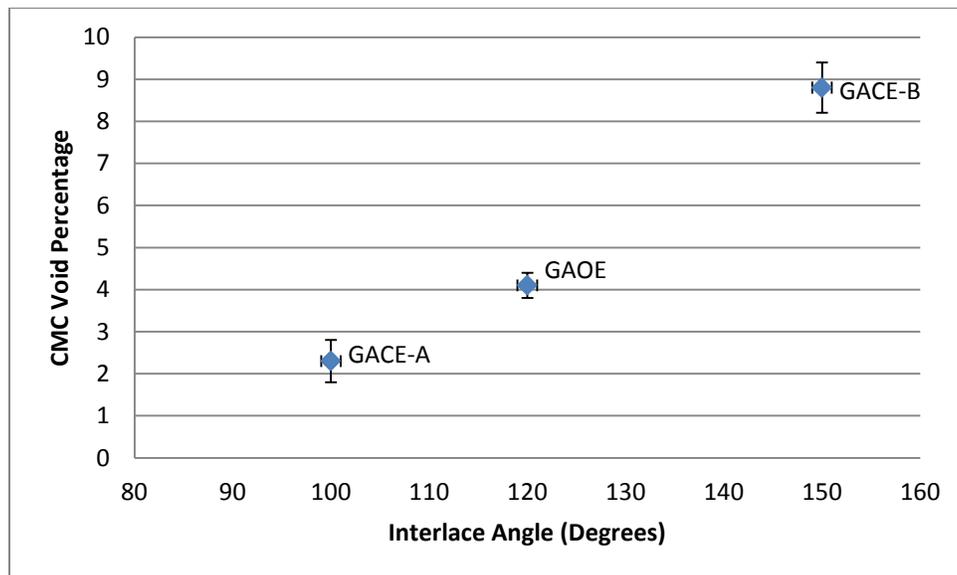


Figure 66: Observed dependence of CMC void fraction on interlace angle

The void morphology's dependence on architecture and the macro-void concentration at the tow intersections is possibly attributable to the tows shielding the tow intersections from full CVI, thus resulting in macro-voids at tow intersections. However, it is also possible that the preforms have an inherently higher porosity prior to CVI, leading to higher post-CVI porosity. All of the CMC void measurements have high uncertainty due to the uncertainty in the voids smaller than the 50.3 μm resolution of the XCT data. The values discussed above principally reflect the large macro-voids present in the intra-tow regions of the CMC.

The void height was observed to have less predictable dependence on sample architecture than the void fraction. Although series GAOE and GACE-A displayed similar average void heights, the series differed in tow design, interlace angle, and average void fraction. Additionally, the GACE-A series had axial tows but did not display a higher average void height than the GAOE series, which did not have axial tows.

However, the GACE-B series exhibited both the largest average void height and the largest void fraction, thus suggesting that a higher void fraction promotes axially longer voids.

The distributions of void heights obtained by the XCT analysis displayed bimodal behavior for series GACE-A and GACE-B (Figure 63 and Figure 64 above), with most voids clustering in two distinct regions. Such data suggests that the larger voids are composed of a series of interconnected smaller voids, with the height of any individual void in the network enhanced by connection to voids above and below. Thus, the solitary voids are represented by the first peak in the void height distribution, and the void networks are represented by the second peak in the void height distribution.

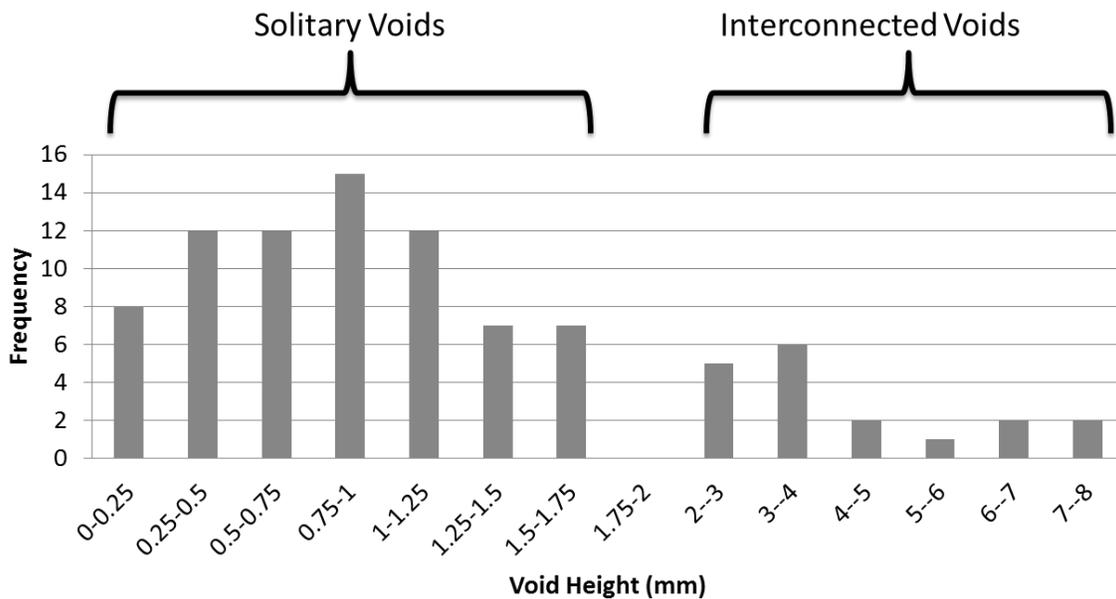


Figure 67: Bimodal void height distribution for GACE-B series

5.3.3. CMC Void Implications

Voids within the CMC can be problematic for thermomechanical and corrosion performance of the CMC. One important implication of the CMC voids is their introduction of stress concentrators in the CMC, leading to the voids being likely failure initiation sites. Abdul-Aziz (Abdul-Aziz, Ghosn, Baaklini, & Bhatt, 2003) investigated the influence of porosity on stress distribution in a CMC and discovered that a porosity of approximately 10% resulted in stresses 20% to 40% higher than the nominal applied stress at the void locations. Furthermore, higher porosity resulted in higher stresses at the voids.

In addition to weakening the CMC, internal CMC voids obstruct radial heat flow through the CMC layer and reduce overall heat transfer through the CMC (Puglia, Sheikh, & Hayhurst, 2005) (Fenici, Rebelo, Jones, Kohyama, & Snead, 1998). Figure 68 shows results from Fenici illustrating how the thermal conductivity decreases with increasing porosity. Furthermore, the voids could potentially weaken the CMC due to inadequate buildup of inter-tow matrix (Abdul-Aziz, Ghosn, Baaklini, & Bhatt, 2003).

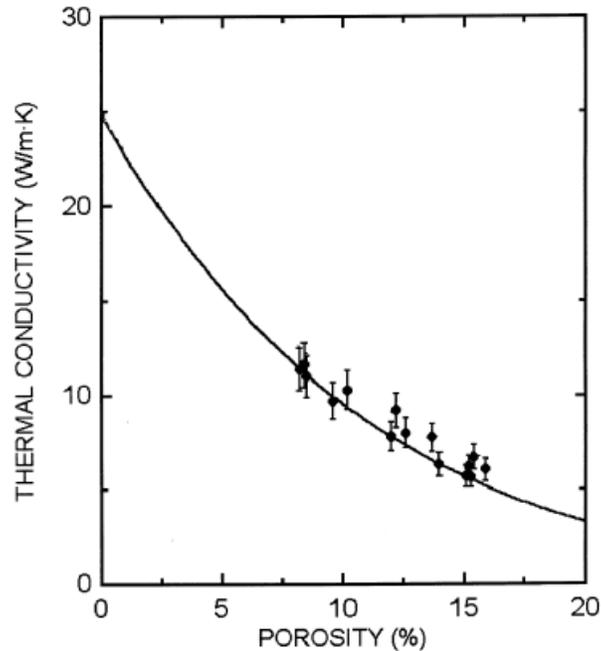


Figure 68: Thermal conductivity for 2-D Nicalon CG/SiC composites (Fenici, Rebelo, Jones, Kohyama, & Snead, 1998)

However, the voids also have the potential to reduce the corrosion performance of the CMC during high-temperature steam oxidation. Bloom noted that the CMC voids make the CMC structure permeable to gasses (Bloom, 1998). Because the voids allow unobstructed axial travel through the interior of the CMC, the voids could potentially allow for the percolation of oxidative steam through the interior of the samples during the high-temperature steam oxidation tests performed in this work. Therefore, minimizing CMC void fraction would reduce the pathways available for interior oxidation of the CMC.

During normal reactor use, both ends of the cladding would be sealed with an endplug and no corrosive agents would directly contact the CMC without first penetrating the EBC. However, the samples investigated in this work consist of either one or two open ends which allow for direct contact between the corrosive agents and the CMC at the cut surface. Although the cut surfaces were CVD sealed by GA prior to the corrosion tests, the CVD sealing was not successful at blocking access to the voids as revealed by SEM and XCT imaging. Figure 69 shows a cross-sectional SEM view of the cut surface of a GAOE sample. From the figure, multiple entrances to the CMC void network can be observed at the cut surface, thus providing the oxidative steam with access to the CMC void network. Furthermore, because the XCT analysis was limited to 50.3 μm resolution, it is possible that the void networks within the CMC were more interconnected than believed due to sub-50.3 μm pathways that the XCT would not be able to resolve. In such a scenario, it would be possible for the oxidative gasses to penetrate much further into the CMC than the void height analysis suggests. Therefore, during the high-temperature steam oxidation tests the steam could potentially enter the voids at the cut surfaces and penetrate into the void network within the CMC, thus oxidizing the CMC from within and bypassing the EBC. However, the limited resolution of the XCT analysis did not necessarily prove that the void structure of the CMC facilitates such percolation.

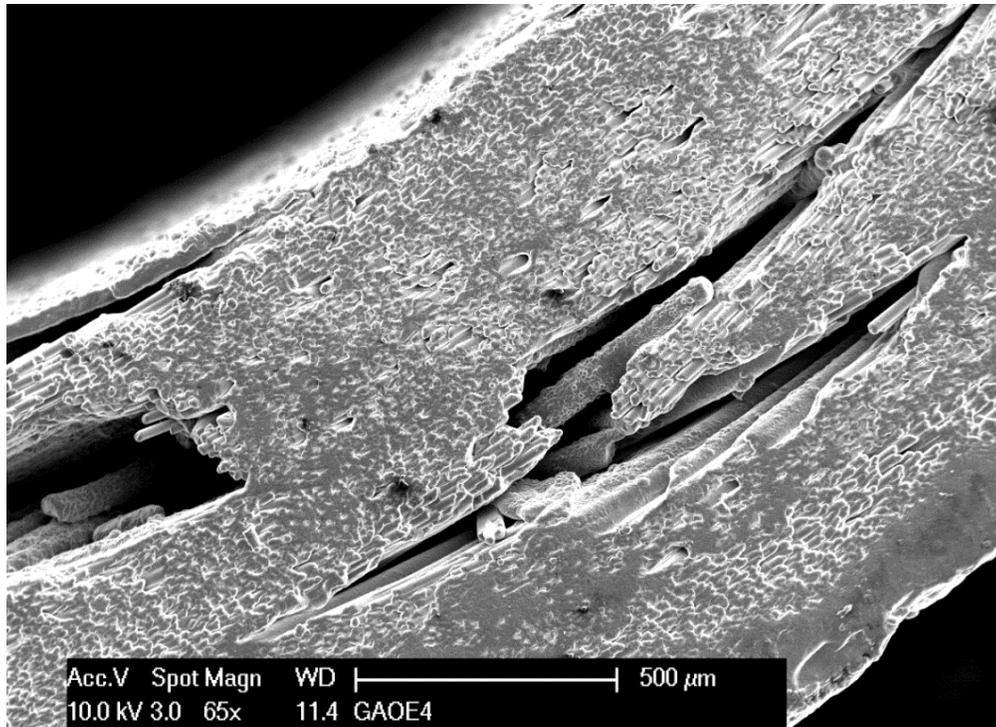


Figure 69: SEM cross-sectional view of GAOE 4 showing entrances to the CMC void network at the cut surfaces

5.4.Void Analysis of Endplug Joint

5.4.1. Endplug Joint Void Data

Analysis of the joint region for the GACE samples revealed varying joint void percentages and joint thicknesses among the samples. Furthermore, the analysis revealed axial variation of the endplug joint characteristics. The axial variation of the endplug joint void fraction is presented in Figure 70, and the axial distribution of the endplug joint thickness is presented in Figure 71. Table 21.

Table 21 presents the endplug joint characteristics for the GACE samples. In the table, the uncertainty in the characteristics of the endplug joint reflects the axial variation observed in the joint. It is also noteworthy that the accuracy of the joint thickness was limited by the resolution of the XCT scans. Because the XCT resolution was a 50.3 μm voxel size, joint thickness measurements were limited to approximations. The results were obtained by repeating the endplug analysis three times for each sample and averaging the results. Only one set of processed images was analyzed, with the processing parameters (such as threshold) chosen to give the most visibly-faithful reproduction of the original sample.

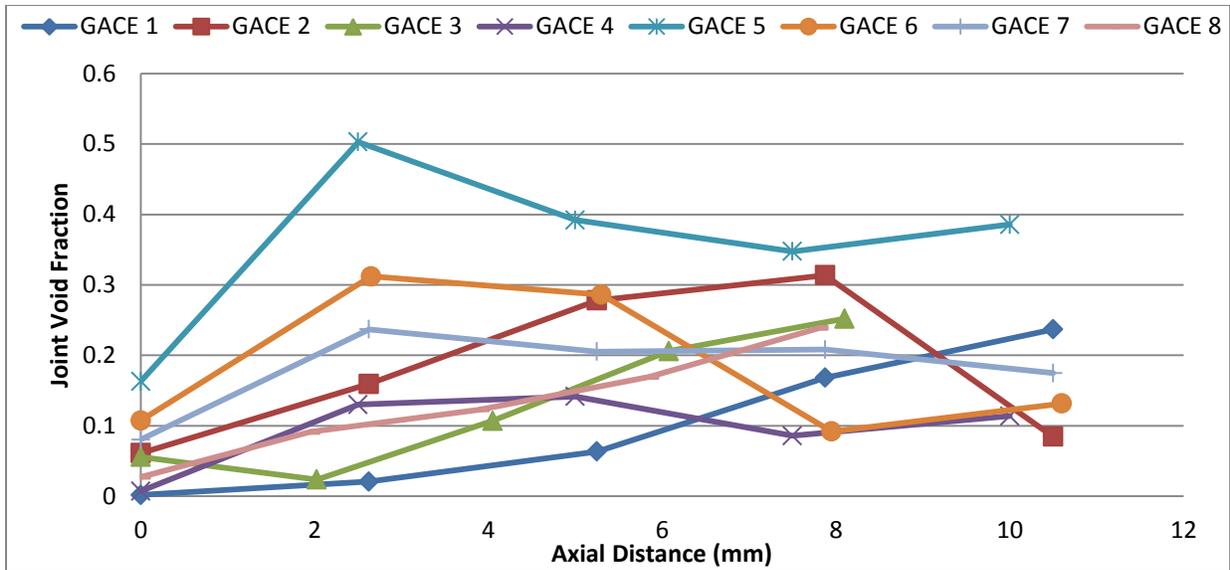


Figure 70: Axial distribution of joint void fraction for GACE samples

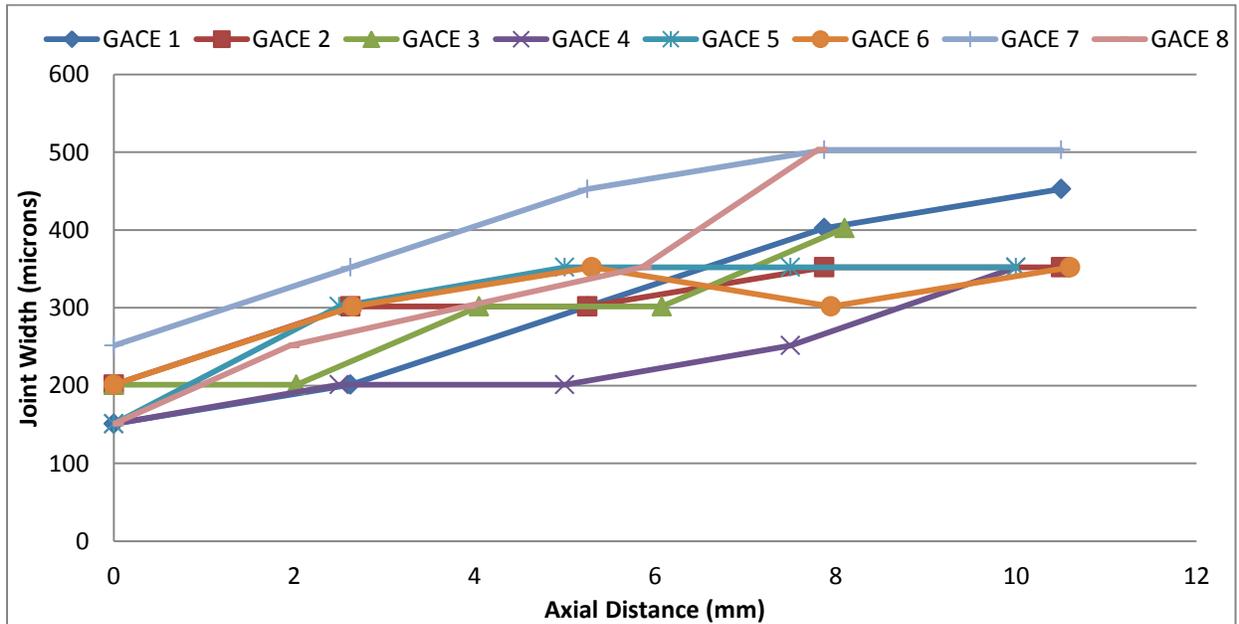


Figure 71: Axial distribution of joint thickness for GACE samples

From Figure 71, it can be observed that the joint width tended to increase with axial distance within the sample. This is likely due to the manufacturing process of the endplug joint, and despite the trend observed in Figure 71, no such trend is observed in Figure 70, suggesting that the CVI process was not significantly affected by the variation in joint width. Indeed, the joint void fraction did not show clear trends with axial distance, although the void fraction was lowest at an axial distance of zero. Additionally, XCT analysis revealed variance in the endplug joint length between samples. Overall, the endplug joint region had far higher void fraction than the CMC region and displayed far more axial and intra-series variance in its characteristics than did the CMC region. All characteristics of the endplug joint region are reported in Table 21.

Table 21: Results of endplug XCT analysis for GACE samples

	Sample	Joint Void Percentage	Joint Thickness	Joint Length
GACE-A	GACE 1	12 ± 3.4 %	315 ± 160 μm	10.5 mm
	GACE 2	19 ± 8.7 %	282 ± 114 μm	10.5 mm
	GACE 3	13 ± 1.8 %	275 ± 125 μm	10.0 mm
GACE-B	GACE 4	9.3 ± 2.3 %	292 ± 159 μm	10.0 mm
	GACE 5	34 ± 4.5 %	350 ± 160 μm	10.0 mm
	GACE 6	18 ± 2.0 %	346 ± 156 μm	10.6 mm
	GACE 7	19 ± 2.2 %	392 ± 179 μm	10.5 mm
	GACE 8	12 ± 4.1 %	302 ± 147 μm	7.8 mm

5.4.2. Endplug Joint Void Discussion

Variance in the joint void fraction among the GACE samples was observed, and it was determined that the joint suffers from higher void fraction than the CMC layer. The highest void fraction observed in the endplug region corresponded to GACE 5 with an average joint void fraction of 34%, and the lowest void fraction observed was for GACE 4 with an average of 9.3%. The voids in the joints were observed to be distributed heterogeneously, and large azimuthal regions of several joints, including the joint of GACE 5, consisted only of void. Figure 72 shows a comparison between the joint with the highest void fraction and the joint with the lowest void fraction. From the figure, it can also be observed that the voids for GACE 5 are clustered and heterogeneously distributed in the joint.

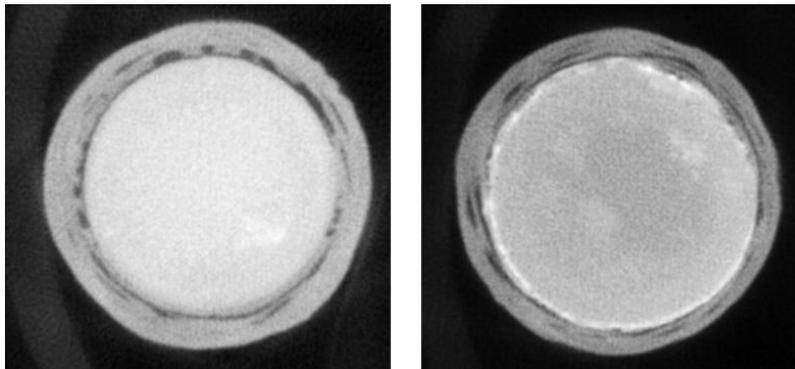


Figure 72: Comparison of joint voids for GACE 5 (left) and GACE 4 (right)

Variance in joint thickness was also observed among the GACE samples. The largest average joint thickness observed corresponded to GACE 7 at approximately 400 μm, and the smallest joint thickness observed was for GACE 3 at approximately 280 μm. However, the endplug for GACE 7 was observed not to be concentric with the tube section of the sample: the endplug was off-center, and thus the sample had the largest variance for joint thickness. Figure 73 shows a comparison between the joint for GACE 7 and the joint for GACE 3. From the figure, the off-center nature of the endplug for GACE 7 can be observed. Furthermore, a concentration of large voids can be observed at the location of widest joint for GACE 7. Because of the off-center joint for GACE 7, the void fraction measurements for GACE 7 are likely smaller than the true void fraction of the joint because the void fraction algorithm assumes concentric endplug and tube. Overall, the variation in joint thickness and void fraction is considered when comparing burst strengths among the different GACE samples.

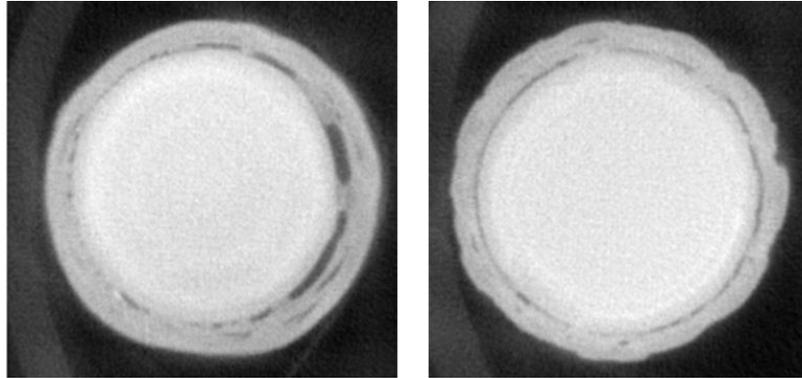


Figure 73: Comparison of joint thickness for GACE 7 (left) and GACE 3 (right)

Finally, the axial length of the joint region was observed to vary among the different samples. The longest joint occurred for GACE 6 at 10.6 mm, and the shortest joint occurred for GACE 8 at 7.8 mm. Figure 74 shows a comparison between the endplug joint lengths for GACE 8 and GACE 6. From the figure, it can be observed that the joint axial length of GACE 6 is significantly larger than for GACE 8. The different joint lengths observed among the samples were considered when comparing sample burst strengths among the different GACE samples.

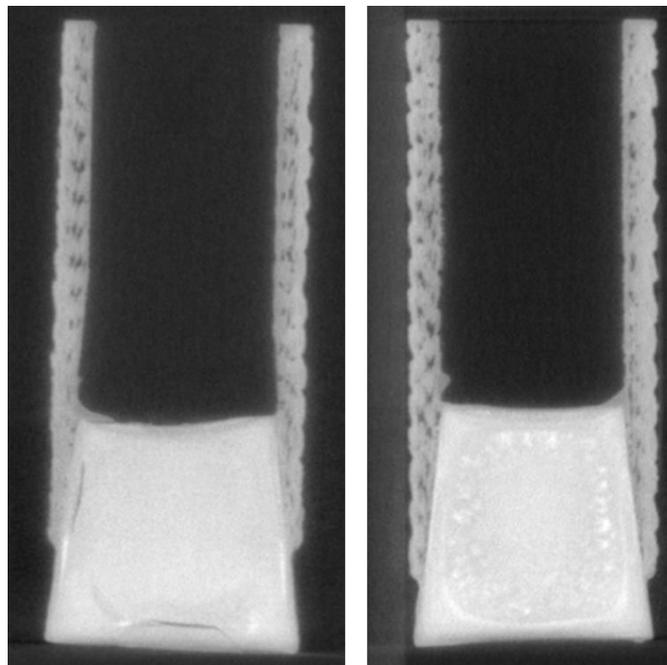


Figure 74: Comparison of joint length for GACE 8 (left) and GACE 6 (right)

5.4.3. Endplug Joint Void Implications

The variation of the joint void fraction, joint thickness, and joint length among the different GACE samples suggests that the as-received mechanical performance of the endplug joint would vary among the samples. Therefore, during analysis of the effect of corrosion testing on mechanical strength, some variance among the samples due to endplug joint variation must be allowed. Furthermore, the XCT analysis allows for qualitative prediction of the relative strengths of the different GACE samples. By

assuming that the strength of the joint is dependent on void fraction, joint thickness, and joint length, then samples GACE 5 and GACE 7 were predicted to have significantly lower strength than the other GACE samples. This hypothesis was confirmed when sample GACE 5 was tested and failed at a significantly lower strength than GACE 8 which experienced identical testing conditions (see Section 6.2.3 below). As a result of the significantly reduced strength of GACE 5, it was decided not to test GACE 7 due to the defects observed in its joint.

The analysis of the endplug joint suggests that further development is needed of the endplug joining methodology. Excessive variation was observed in the endplug joint characteristics among the different GACE samples. Although the endplug joints of several samples were observed to have few flaws (such as GACE 3 and GACE 4), other samples exhibited joints with numerous large voids and gaps in the joining material (such as with GACE 5 and GACE 7). Furthermore, although most samples exhibited joint lengths of 10 mm, sample GACE 8 had a joint length of only 7.8 mm. For nuclear applications, such variation observed in only eight samples is unacceptable, and therefore the joining techniques will need to be refined to provide more consistency among the endplug joints.

Finally, the voids in the endplug joint can potentially provide pathways for internal oxidation of the endplug joint. Because the GACE samples were open on one end, during oxidation testing the steam could potentially enter through the top of the sample and enter the endplug joint voids of the sample. Once the steam is exposed to the joint voids, it could potentially percolate throughout the the joint and oxidize it from within, similar to the aforementioned possible oxidation mechanism of the CMC. Larger joint voids could promote more severe internal oxidation, thus exacerbating an already weak joint. During normal operating conditions, it is unlikely that the steam could enter the joint region at the endplug-sealed end because that end is hermetically sealed. However, if the hermeticity of the endplug joint was compromised, the joint voids could facilitate severe internal oxidation of the endplug joint. Therefore, the elimination of joint voids could increase both the joint performance and the joint corrosion resistance.

5.5.Conclusion

XCT analysis was performed on all the samples investigated in this work. Image processing algorithms were developed to analyze the XCT data and determine the CMC void characteristics and endplug joint characteristics.

The analysis revealed the presence of voids in the CMC layer and in the endplug joint region. The fraction of voids and the void morphology were observed to be dependent on the sample architecture, with a higher interlace angle corresponding to a higher void fraction possibly due to either shielding during CVI or a higher number of tow-tow intersections (where the voids are clustered). Overall, the CMC void fraction ranged from 4% to 9%, and the average void height in the CMC ranged from 0.7 mm to 1.5 mm. Analysis of the CMC “full” region revealed near-theoretical density, suggesting minimal micro-voids in the CMC.

Significant variation in the characteristics of the endplug joint was observed among the different samples, with the joint void fraction ranging from 9% to 35%, the joint thickness ranging from 250 μm to

400 μm , and the joint height ranging from 7.8 mm to 10.6 mm. Furthermore, samples GACE 5 and GACE 7 were identified as having joints far inferior to the other samples. Such analysis of the endplug joint suggests that some scatter attributable to the variance in joint characteristics will be observed in the joint strengths. Therefore, some allowance must be made for the variation in joint properties during evaluation of the impact of corrosion testing on the joint strength.

The XCT analysis can allow for very rough prediction of the relative strengths of the endplug joints for the GACE samples. By assuming that the joint strength scales linearly with joint length, and inversely with joint void fraction, the relative joint strengths can be very roughly approximated. However, because it is believed that the joint void fraction in GACE 7 was much higher than calculated due to the non-concentricity of the endplug and the tube, the true void fraction for GACE 7 was assumed to be 50% higher than measured (void fraction of approximately 30%, similar to GACE 5). The results of such analysis are presented in Figure 75. The analysis is very approximate due to large uncertainties in the true joint void fraction and uncertainty in the influence of void fraction on joint strength. A comparison between the predicted joint strength and the measured joint strength is presented in Figure 153 of Section 8.1 below.

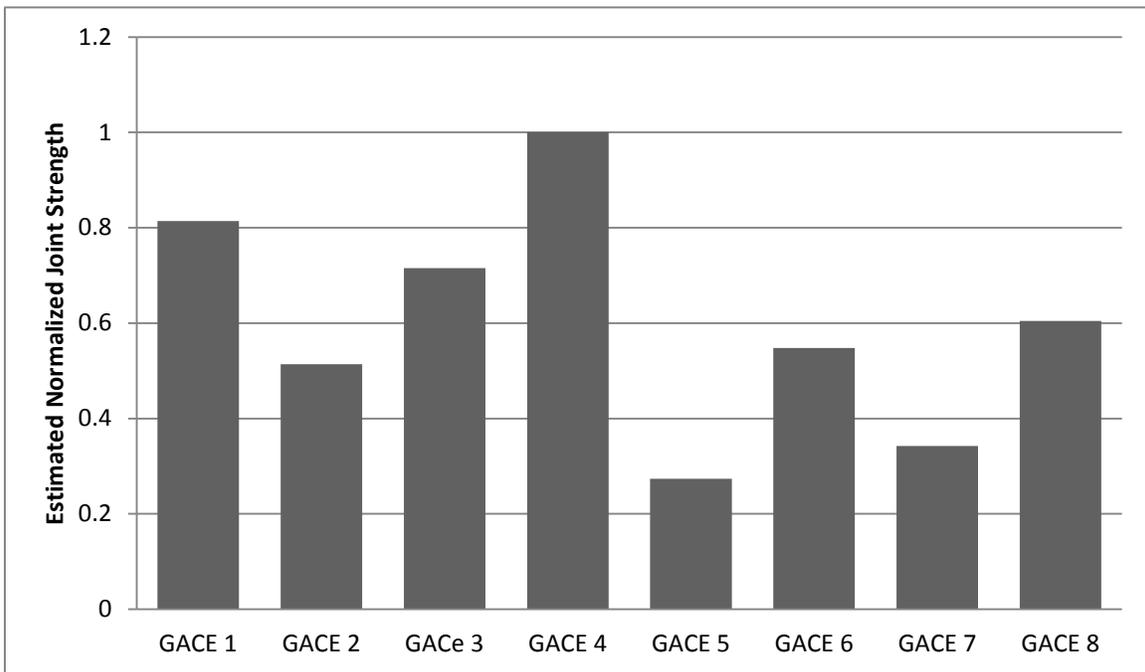


Figure 75: Approximated relative joint strengths of GACE samples from XCT analysis

6. Experimental Results

6.1. Analysis of SiC Cladding Mechanical Performance As-Received

6.1.1. Motivation

It was desired to establish the baseline mechanical characteristics of the as-received samples in each series to obtain control data for comparison against the post-test data. Additionally, it was important to characterize the as-received samples to allow for assessment of SiC cladding during normal reactor conditions. Evaluation of the failure hoop stress also allows for assessment of the peak fuel rod internal pressure at end of life (EOL) conditions.

Investigation into the microstructural behavior of the CMC layer can be performed through analysis of the mechanical response of the samples to external loading. The different stress-strain response regimes observed in the samples can be correlated with microstructural events within the CMC and can allow for insight into the evolution of the flaws within the CMC microstructure due to external loading.

6.1.2. Hoop Testing of As-Received Open-Ended Samples

One sample in the GAOE series underwent pressurization testing to determine the as-received failure hoop strength and stress-strain characteristics. By establishing as-received data, the performance of the GAOE series prior to LOCA testing can be evaluated. Additionally, the control sample provides baseline data for comparison to the test specimens. Finally, the as-received stress-strain behavior allows for insight into the composite behavior of the as-received GAOE series and identification of the microstructural flaw evolution of the CMC during destructive pressurization.

Using the stress equations outlined above in Section 4.2.1, the stress-strain behavior and the yield and failure hoop stresses were obtained. Yielding was observed at an internal pressure of 44 MPa, corresponding to an ID yield stress of 304 MPa. Sample failure occurred at an internal pressure of 86 MPa, corresponding to an ID failure hoop stress of 581 MPa. Figure 76 presents the stress-strain behavior for GAOE 2 and Table 22 presents the strength testing results for GAOE 2.

Three distinct loading regimes were observed in the stress-strain behavior for GAOE 2 and are discussed further in Section 7.1. First, the sample was loaded elastically and was characterized by a steep slope. Next, the sample yielded and large jumps in strain were observed. Finally, the sample exhibited pseudo-ductility and was significantly strained up to sample failure.

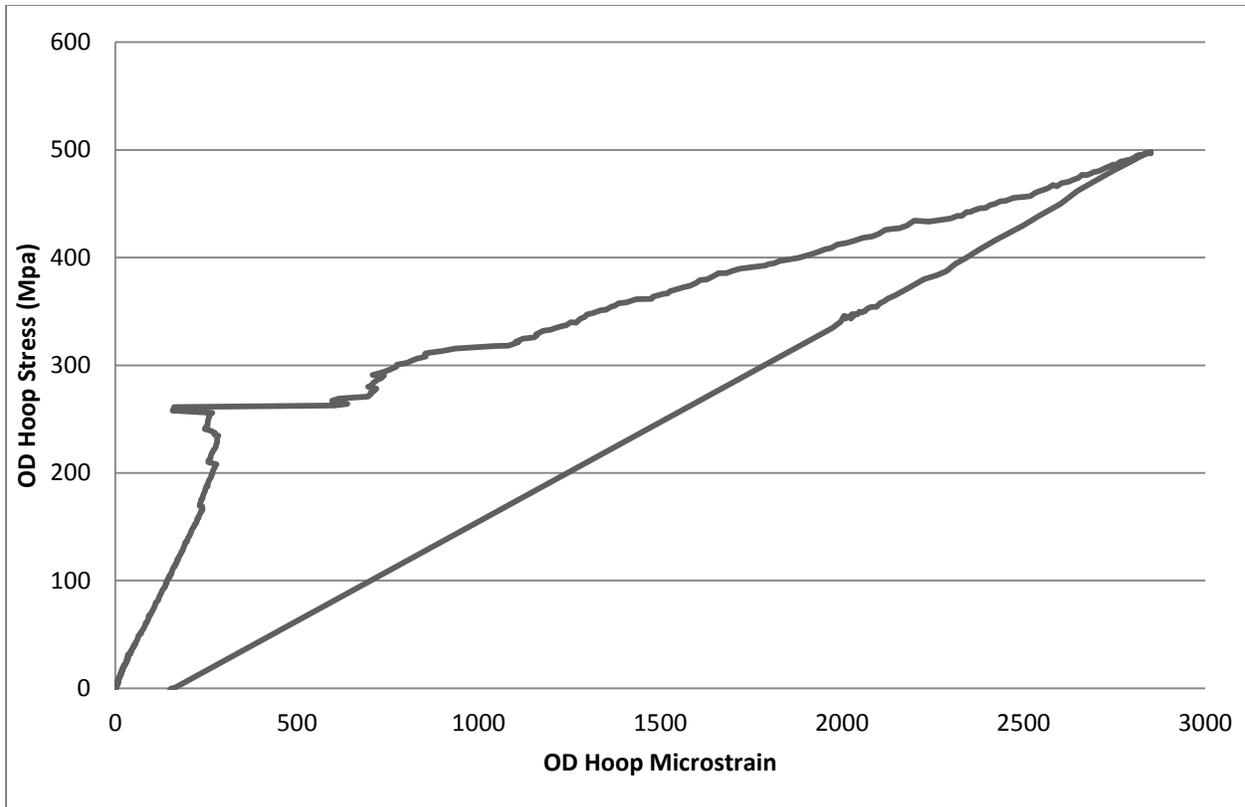


Figure 76: Stress-strain behavior for GAOE 2

Table 22: Strength test results for GAOE 2

	GAOE 2 As-Received*
Yield Hoop Stress ID	304 MPa
Yield Internal Pressure	44 MPa
Failure Hoop Stress ID	581 MPa
Failure Internal Pressure	83 MPa
Failure Strain	0.285 ± 0.006 %

6.1.3. Joint Testing of As-Received Close-Ended Samples

One sample in the GACE-A series and one sample in the GACE-B series underwent joint strength testing as-received to determine the as-received failure joint strength. By establishing as-received data, the performance of the GACE-A and GACE-B series prior to LOCA conditions can be evaluated. Additionally, the control sample in each series provides baseline data for comparison to the corrosion test specimens. Furthermore, comparison between the GACE-A and GACE-B as-received samples can indicate whether the architecture of the samples influences the as-received joint strength.

One joint strength test was performed on GACE 2 and one test was performed on GACE 6. Both tests performed uniaxial loading of the endplug until failure following the joint strength testing procedures outlined in Section 4.2.2. For both tests, failure was observed in the joint region signifying valid results.

* Uncertainty due to mechanical setup was not quantified, see Section 4.2.1.3

After testing, the burst strength was calculated to determine approximate internal pressure required to result in endplug joint failure.

The peak loads observed for as-received samples was 1621 N for the GACE-A sample and 1428 N for the GACE-B sample. The burst strength calculated for the sample was 37.1 MPa for the GACE-A sample and 32.3 MPa for the GACE-B sample. Besides the different burst strengths, both samples exhibited similar pushrod load versus displacement behavior, as shown in Figure 77. The results for the joint strength testing are presented in Table 23.

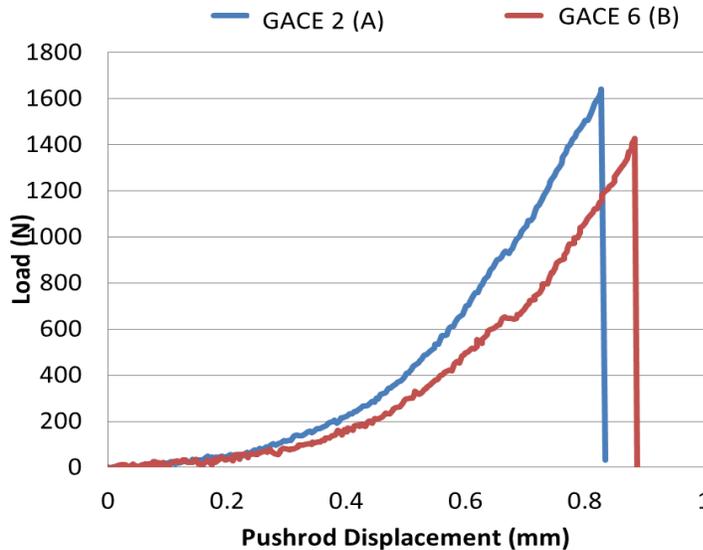


Figure 77: Pushrod load versus displacement curves for as-received GACE samples

Table 23: Joint strength test results for as-received GACE samples

	GACE 2 (A) As-Received*	GACE 6 (B) As-Received*
Peak Load	1641 ± 8 N	1428 ± 7 N
Burst Strength	37.1 ± 0.2 MPa	32.3 ± 0.2 MPa

6.1.4. Failure Observations

Observing the failure characteristics of the samples tested as-received can allow for determination of the typical failure characteristics expected of SiC cladding during normal reactor operating conditions. The GAOE as-received sample failure resulted in the detachment of large sections of the CMC and partially exposed the interior of the sample, although the sample still maintained a somewhat coolable geometry. Failure of the GACE samples was characterized by the complete separation of the endplug from the tubing.

6.1.4.1. Open-Ended Samples

Failure for the GAOE as-received sample was characterized by the detachment of pieces of the CMC and partial opening of the sample, although the failure crack did not travel the axial length of the sample and instead was only approximately 10 mm long. The sample did not fail catastrophically and instead only

* Uncertainty due to mechanical setup was not quantified, see Section 4.2.2.3

failed at one angular location. Portions of the EBC detached from the exterior surface of the sample and exposed the underlying CMC layer. Figure 78 shows a cross-sectional view of GAOE 2 after pressurization testing, showing how the sample opened and ejected a fragment of the CMC. Figure 79 shows a lateral view of GAOE 2 after pressurization testing.



Figure 78: Cross-sectional view of GAOE 2 and fragment after pressurization testing



Figure 79: GAOE 2 sample before (left) and after (right) pressurization testing

Although the GAOE sample failure exposed some of the interior of the sample, because the failure was localized and did not fully penetrate the axial length of the sample a coolable geometry was maintained. However, because the failure was characterized by the detachment of pieces of the EBC and fragments of the CMC, the failure characteristics observed for the GAOE sample pose a risk for clogging the coolant channels in the core. However, it should be noted that an open end will not be present in service (because the fuel rods are closed on both ends), and therefore the presence of the open end likely influenced the observed failure characteristics.

6.1.4.2. Close-Ended Samples

GACE sample failure primarily occurred in the endplug joint, with limited fracture of the tubing in the endplug region. After the joint failed, the endplug completely detached from the sample intact. The remaining tubular section of the cladding was intact and did not fragment during endplug joint failure. Thus, if the endplug joint failed in a reactor, the freed endplug could get caught in the coolant flow and would risk clogging the coolant channels in the core, but the remaining tubing would still be structurally intact and coolable.



Figure 80: Endplug post-pushout characteristics for GACE 2 (A, left) and GACE 6 (B, right)

The failure characteristics of the endplug joint were observed to correlate with the joint voids identified through XCT analysis. Locations with a high concentration of joint voids tended to result in tube fracture

at the joint location. Although GACE 6 did not exhibit any tube fracture, GACE 2 tube fracture correlated well with the concentrations of joint voids, as shown in Figure 81. In the figure, the red line corresponds to locations of tube fracture where after failure the tubing remained attached to the endplug and was severed from the rest of the cladding. The large voids in the figure are several hundreds of microns in axial height.

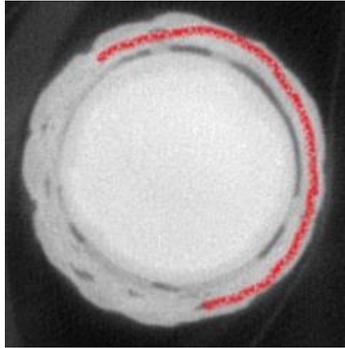


Figure 81: XCT analysis of GACE 2 showing location of tube fracture (red line)

6.2. Analysis of SiC Cladding Performance after Thermal-Shock

6.2.1. Motivation

The thermal-shock experiments were intended to simulate the fuel conditions associated with the restoration of coolant flow following a LOCA. During the reflood event, the fuel rods are exposed to saturated or slightly subcooled water at gauge pressure less than one atmosphere and experience severe thermal stresses. The thermal shock testing investigated in this work is intended to ensure that the SiC cladding can withstand the reflood and evaluate the mechanical properties of the cladding post-reflood.

The mechanical characteristics of the post-thermal-shock samples in each series were obtained to compare with the control data for determination of the impact of thermal shock on mechanical properties. Additionally, it was important to characterize the thermal-shock samples to allow for assessment of SiC cladding survivability during a reflood event. Evaluation of the failure hoop stress also allows for assessment of the peak fuel rod plenum pressure allowed following a reflood.

Investigation into the failure behavior of the CMC layer was performed through analysis of the stress-strain behavior of the thermal-shock samples. The mechanical behavior of the thermal-shock samples was compared to the behavior of the as-received samples to evaluate the influence of thermal-shock on the samples. Furthermore, SEM analysis of the microstructure was performed to investigate the failure mechanisms of the thermal-shock samples.

6.2.2. Hoop Testing of Thermal-Shock Open-Ended Samples

The two samples in the GAOE series underwent pressurization testing after thermal-shock testing to determine the failure hoop strength and stress-strain characteristics after thermal-shock. The internal pressurization facility and procedures outlined above in Section 4.2.1 were used for the hoop testing of

the post-thermal-shock samples. The samples investigated for post-thermal-shock behavior were samples GAOE 5 and GAOE 6.

The performance of the GAOE samples after thermal-shock can be compared to the as-received data to evaluate the effect of thermal shock on the mechanical behavior of the samples. The post-thermal-shock stress-strain behavior allows for insight into the composite behavior of the GAOE series after thermal-shock and allows for assessment of microstructural changes in the samples attributable to the thermal shock.

Internal pressurization tests were performed on samples GAOE 5 and GAOE 6 which loaded the samples until complete failure. Using the stress equations outlined above in Section 4.2.1, the stress-strain behavior and the yield and failure hoop stresses were obtained. Overall, the post-thermal-shock samples exhibited similar mechanical behavior to the as-received sample. Whereas the as-received sample GAOE 2 experienced a peak internal pressure of 83 MPa and a failure stress of 581 MPa, GAOE 5 and GAOE 6 experienced peak internal pressures of 86 MPa and 73 MPa respectively, corresponding to failure hoop strengths of 572 MPa and 492 MPa respectively. Although the thermal-shock samples experienced slightly lower failure strengths, the shock appeared to have little influence on the mechanical behavior of the samples. Figure 82 presents the stress-strain behavior comparison between the thermal-shock samples and the as-received sample for the GAOE series. The mechanical results of the thermal-shock testing are compared to the results for the as-received sample in Table 24.

The stress-strain behavior of the thermal-shock samples was very similar to that of the as-received sample, indicating that the thermal shock has little impact on the mechanical response to loading for the GAOE series. Furthermore, the three characteristic loading regimes observed for the as-received sample (as detailed in Section 7.1.1) were also observed for the thermal-shock samples.

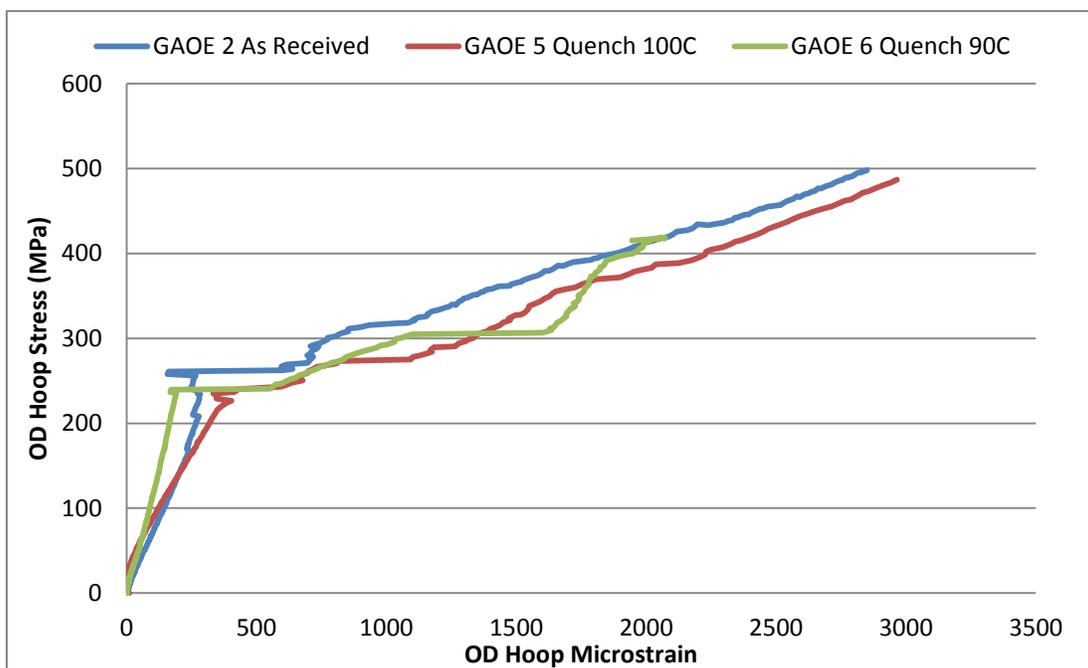


Figure 82: Stress-strain comparison between thermal-shock and as-received GAOE samples

Table 24: Strength test results for thermal-shock and as-received GAOE samples

	GAOE 2 As-Received*	GAOE 5 Quench 100°C*	GAOE 6 Quench 90°C*
Yield Hoop Stress ID	304 MPa	283 MPa	282 MPa
Yield Internal Pressure	44 MPa	40 MPa	41 MPa
Failure Hoop Stress ID	581 MPa	572 MPa	492 MPa
Failure Internal Pressure	83 MPa	86 MPa	73 MPa
Failure Strain	0.285 ± 0.006 %	0.297 ± 0.006 %	0.205 ± 0.004 %

6.2.3. Joint Testing of Thermal-Shock Close-Ended Samples

One sample in the GACE-A series and two samples in the GACE-B series underwent joint strength testing after thermal-shock to determine the influence of thermal-shock on failure joint strength. By comparing the thermal-shock results to the as-received results, the performance of the GACE-A and GACE-B series during reflood conditions can be evaluated. Furthermore, comparison between the GACE-A and GACE-B thermal-shock samples can indicate whether the architecture of the samples influences the tolerance to thermal-shock.

Joint strength tests were performed on samples GACE 1 (A), GACE 5 (B), and GACE 8 (B) which loaded the endplugs until complete pushout. Using the equation outlined above in Section 4.2.2, the burst strength of the endplug joint can be obtained. Overall, the post-thermal-shock sample in the GACE-A series did not exhibit significant mechanical degradation attributable to the thermal-shock. In the GACE-A series, the as-received sample GACE 2 experienced burst strength of 37.1 MPa and the thermal-shock sample GACE 1 experienced burst strength of 34.2 MPa. Figure 83 presents the pushrod load versus displacement comparison between the thermal-shock samples and the as-received sample for the GACE-A series, and Table 25 compares the thermal-shock and as-received results for the GACE-A series.

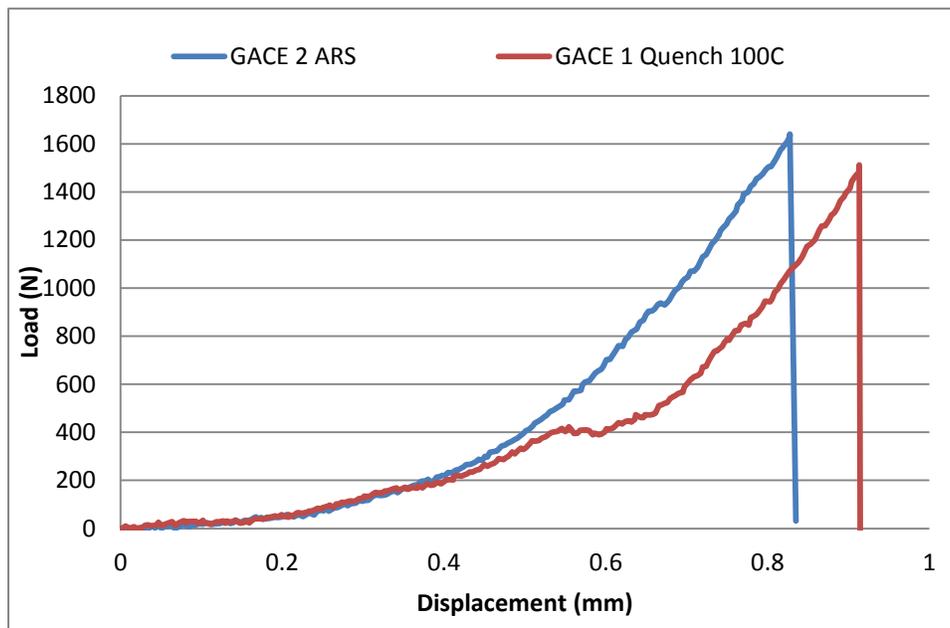


Figure 83: Pushrod load versus displacement comparison between thermal-shock and as-received GACE-A samples

* Uncertainty due to mechanical setup was not quantified, see Section 4.2.1.3

Table 25: Pushout test results for thermal-shock and as-received GACE-A samples

	GACE 2 As-Received*	GACE 1 Quench 100C*
Peak Load	1641 ± 8 N	1513 ± 8 N
Burst Strength	37.1 ± 0.2 MPa	34.2 ± 0.2 MPa

In contrast to the GACE-A series, the post-thermal-shock samples in the GACE-B series exhibited significantly degraded mechanical behavior when compared to the as-received samples. In the GACE-B series, the as-received sample GACE 6 showed burst strength of 32.3 MPa while the thermal-shock samples GACE 5 and GACE 8 only showed burst strengths of 7.2 MPa and 14 MPa respectively. Although some allowance must be made for variation in joint strengths, as discussed in Section 5.4, the thermal-shock appeared to have significant influence on the mechanical behavior of the joints for the GACE-B series. Figure 84 presents the pushrod load versus displacement comparison between the thermal-shock and as-received samples for the GACE-B series, and Table 26 compares the thermal-shock and as-received results for the GACE-B series.

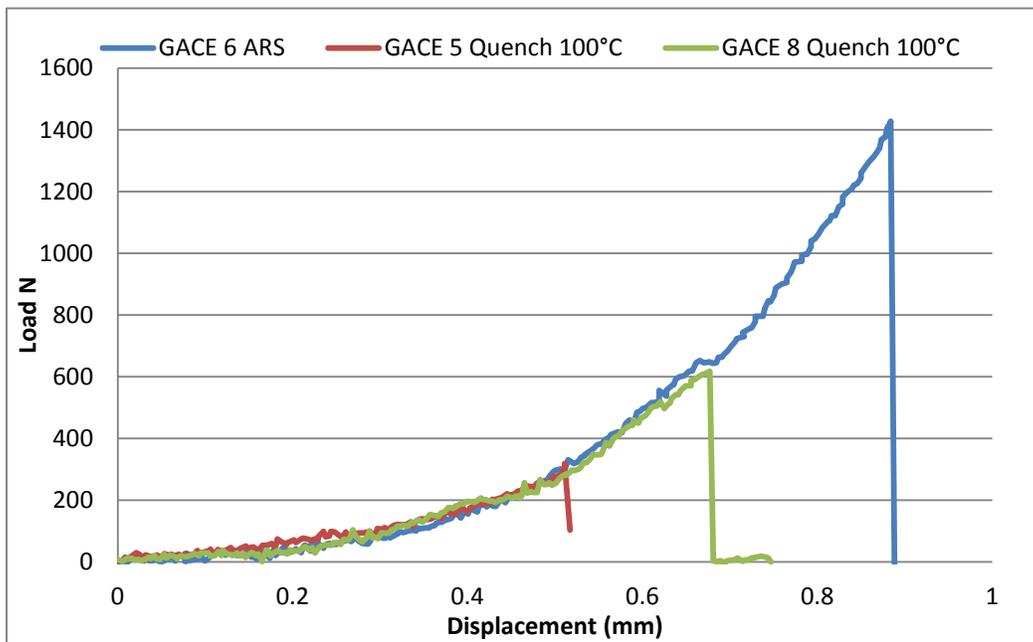


Figure 84: Pushrod load versus displacement comparison between thermal-shock and as-received GACE-B samples

Table 26: Pushout test results for thermal-shock and as-received GACE-B samples

	GACE 6 As-Received*	GACE 5 Quench 100C*	GACE 8 Quench 100C*
Peak Load	1428 ± 7 N	318 ± 2 N	617 ± 3 N
Burst Strength	32.3 ± 0.2 MPa	7.2 ± 0.03 MPa	14 ± 0.1 MPa

6.2.4. Failure Observations

Observing the failure characteristics of the samples tested after thermal-shock can allow for determination of the typical failure characteristics expected of SiC cladding after a reflow event. The GAOE thermal-shock sample failure characteristics were very similar to the as-received failure characteristics, with opening of the tubing and exposure of portions of the interior, although a coolable

* Uncertainty due to mechanical setup was not quantified, see Section 4.2.2.3

geometry was maintained. Similarly, GACE failure characteristics were similar for thermal-shock and as-received samples except for GACE 5. Failure of the GACE samples was characterized by the complete separation of the endplug from the tubing.

6.2.4.1. Open-Ended Samples

Failure for the GAOE thermal-shock samples was characterized by partial opening of the sample with partial detachment of sections of the CMC, although the failure crack did not travel the axial length of the sample and instead was only approximately 10 mm long. The cracks terminated by following the contours of the CMC weave structure. The sample did not fail catastrophically and instead only failed at one angular location. Portions of the EBC detached from the exterior surface of the sample and exposed the underlying CMC layer. Figure 85 shows a lateral view of the thermal-shock samples after pressurization testing. Figure 86 presents a cross-sectional view of the thermal-shock samples after pressurization testing, showing how the samples opened.



Figure 85: Lateral view of failure characteristics of GAOE 5 (left) and GAOE 6 (right)



Figure 86: Cross-sectional view of the failure characteristics for GAOE 5 (left) and GAOE 6 (right)

Although the GAOE thermal-shock sample failure exposed some of the interior of the sample, because the failure was localized and did not fully penetrate the axial length of the sample a coolable geometry was maintained. However, because the failure was characterized by the detachment of pieces of the EBC, the failure characteristics observed for the GAOE thermal-shock samples pose a risk for clogging the coolant channels in the core. Unlike the failure of the as-received GAOE sample, no large pieces of the CMC detached from the thermal-shock GAOE samples, although the sections of CMC at the failure location partially detached from the tube body.

6.2.4.2. Close-Ended Samples

GACE sample failure primarily occurred in the endplug joint, with limited fracture of the tubing in the endplug region (with the exception of GACE 5, attributable to the inferior endplug joint). After the joint failed, the endplug completely detached from the sample intact. The remaining tubular section of the cladding was intact and did not fragment during endplug joint failure, although the endplug carried some of the tubing with it after detachment. Thus, if the endplug joint failed in a reactor, the freed endplug could get caught in the coolant flow and would risk clogging the coolant channels in the core, although the remaining tubing would still be structurally intact and coolable. Figure 87 shows images of the endplug joints after pushout testing, revealing the failure characteristics observed in the endplug region.



Figure 87: Endplug failure characteristics for GACE 1 (left), GACE 5 (middle), and GACE 8 (right)

Variation was observed in the failure behavior of the endplug joint among the thermal-shock samples. The endplug for GACE 5 detached carrying most of the tubing, whereas the endplug for GACE 8 detached carrying only the tubing from the end of the tube. The endplug for GACE 1 also carried some tubing after detachment. As observed for the as-received endplug failure discussed in Section 7.1, the tubing fracture is correlated with the void joints. The failure of the endplug for GACE 5 was unique because it was accompanied by complete tubing fracture, which is likely attributable to the high void fraction of the GACE 5 endplug joint. The tubing fracture locations after pushout testing were compared to the XCT images showing the locations of the joint voids, and it was found that the tubing fracture locations corresponded with joint regions of high void fraction. Figure 88 shows the correspondence between the locations of tube fracture in the thermal-shock samples and the joint voids observed during XCT analysis. In the figure, the red line represents where the sections of tubing fractured from the tube body and remained attached to the endplug after pushout.

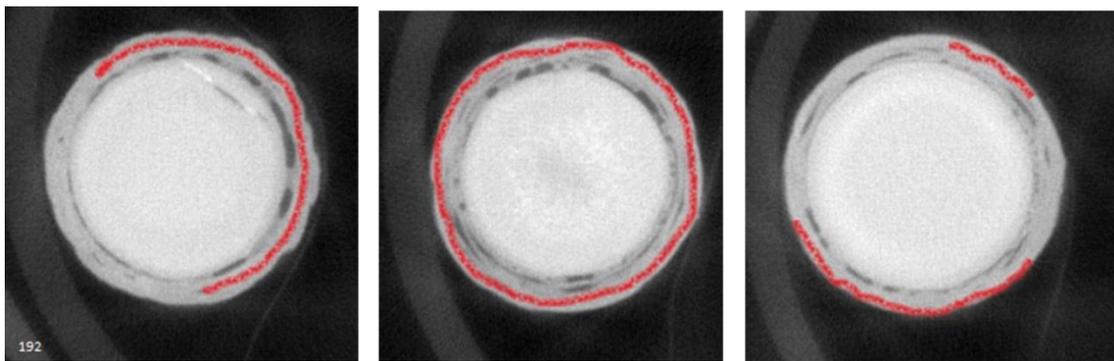


Figure 88: XCT analysis of GACE 1 (left), GACE 5 (middle), and GACE 8 (right) showing location of tube fracture (red line)

6.3. Analysis of SiC Cladding Performance after Steam Oxidation

6.3.1. Motivation

SiC has exceptional resistance to oxidation at high temperature due to the formation of a protective silica (SiO₂) layer, which limits oxidation by requiring diffusion of oxidant through the oxide (Costello & Tressler, 1986). However, previous studies have determined that high-temperature processes can weaken SiC and lead to mechanical degradation. Heat treatment above 1200°C weakens SiC fibers due to CO evaporation (Mah, et al., 1984) and grain growth (Mah, et al., 1984) (Clark, Prack, Haider, & Sawyer, 1987), and Zdaniewski (Zdaniewski & Kirchner, 1987) showed that high-temperature steam oxidation below 1100°C increases the fracture toughness of SiC due to flaw tip blunting, but at higher temperatures the fracture toughness decreases due to increased crystallinity of the silicate phase. Furthermore, Easler (Easler, Bradt, & Tressler, 1981) showed that at an oxidation temperature of 1370°C, fracture toughness decreases for oxidation times longer than one hour due to the introduction of flaws and general degradation of the exposed surface and grain boundaries. To protect the fibers against corrosion, the environmental barrier coating approach has been implemented and has shown substantial improvement in oxidation performance of SiC composites (Eaton & Linsey, 2002).

The oxidation experiments were intended to simulate the fuel conditions associated with the steam oxidation of exposed fuel rods during a LOCA. During the fuel rod oxidation event, the fuel rods become exposed because of coolant boiling and are oxidized by the high-temperature steam. The oxidation testing investigated in this work is intended to evaluate the resilience of the SiC cladding to oxidation and evaluate the mechanical properties of the cladding post-oxidation.

The mechanical characteristics of the post-oxidation samples in each series were obtained to compare with the control data for determination of the impact of oxidation on mechanical properties. Additionally, it was important to characterize the oxidized samples to allow for assessment of SiC cladding survivability during a high-temperature steam oxidation event. Evaluation of the failure hoop stress also allows for assessment of the peak fuel rod plenum pressure allowed following a high-temperature steam oxidation.

Investigation into the microstructural behavior of the CMC layer was performed through analysis of the stress-strain behavior of the oxidized samples. The mechanical behavior of the thermal-shock samples can be compared to the behavior of the as-received samples to evaluate the influence of thermal-shock on the samples. Furthermore, SEM analysis of the oxidized samples was performed to investigate the microstructural effects of oxidation and evaluate the failure characteristics of the oxidized samples.

6.3.2. Oxidation Data

The sample weight was taken both before and after high-temperature steam oxidation to better understand the oxidation mechanisms of the samples. Although it was difficult to ensure that the weight change measurements were not corrupted by the detachment of pieces of the sample during oxidation, the samples were visually inspected and underwent SEM inspection post-oxidation to identify if any portions of the sample had flaked off. None of the samples showed any signs of detachment after inspection. However, because the weight change measurement for GAOE 4 was inconsistent with the

measurements for the other samples, it was concluded that the weight change measurement of GAOE 4 was corrupted by the detachment of pieces of the sample.

The weight change observed in SiC during high-temperature steam oxidation is determined by a balance of weight gain due to the deposition of oxide on the sample and weight loss due to the volatilization of the oxide (Opila & Hann, 1997). Initially, the SiC is oxidized by the O₂ and results in silica (SiO₂) deposition on the exposed surfaces of the SiC. The silica forms a protective layer that helps prevent further oxidation of the underlying SiC and adds mass to the sample. However, moisture can convert the silica layer into Si(OH), which can then be volatilized by the high-temperature steam, resulting in mass removal from the sample. Therefore, the samples weight change is determined by the rate of silica deposition versus the rate of Si(OH) volatilization (Opila & Hann, Paralinear Oxidation Kinetics of CVD SiC in Water Vapor, 1997).

Consequently, the high-temperature steam oxidation of the SiC cladding samples investigated in this work could result in either a weight change or a weight loss depending on the flow conditions. The weight change of SiC samples discussed in this work is normalized to the surface area of the samples, and is reported as the normalized weight change:

$$\Delta w_{norm} = \frac{\Delta w_{absolute}}{SA}$$

Where Δw_{norm} is the normalized weight change during oxidation, $\Delta w_{absolute}$ is the absolute weight change during oxidation, and SA is the sample's surface area exposed to the steam (the sample is simplified to having smooth surfaces). For 48 hour oxidation conditions similar to those investigated in this work, Lee (Lee, McKrell, & Kazimi, 2014) observed a normalized weight change of -4.6 mg/cm² on monolith SiC samples. The weight loss that Lee observed indicates that the volatilization of the silica outpaces the deposition of the silica, resulting in net volatilization of the sample. The results of the weight analysis performed on the oxidized samples investigated in this work are presented in Table 27.

Table 27: Oxidation weight change measurements for all series

Sample	Oxidation Test Conditions	Normalized Weight Change
GAOE 1	24 hour, 1400°C, 6.1 g/min	+0.29 ± 0.002 mg/cm ²
GAOE 3	48 hour, 1400°C, 6.1 g/min	+0.66 ± 0.005 mg/cm ²
GAOE 4	48 hour, 1400°C, 6.1 g/min	-0.13 ± 0.001 mg/cm ²
GACE 3 (A)	48 hour, 1400°C, 6.1 g/min	+0.00 ± 0.001 mg/cm ²
GACE 4 (B)	48 hour, 1400°C, 6.0 g/min	+0.01 ± 0.001 mg/cm ²

From the analysis of the weight change during oxidation, a weight gain was observed for GAOE 1 and GAOE 3, a weight loss was observed for GAOE 4, and no appreciable weight change was observed for GACE 3 and GACE 4. The weight gain observed in GAOE 1 and GAOE 3 indicates that the silica deposition occurred faster than the volatilization. Because the oxidation conditions for GAOE 3 was identical to the conditions for GAOE 4, it is believed that the weight loss observed in GAOE 4 was caused by the detachment of a piece of the sample during oxidation and the weight loss consequently does not reflect the oxidation kinetics of GAOE 4. The weight gain observed in the GAOE samples is likely attributable to the internal voids in the CMC layer, which allow for the buildup of silica and protect against excess

moisture required for silica volatilization. All in all, the net weight gain observed in the GAOE samples suggests buildup of silica in the CMC voids. Because Lee (Lee, McKrell, & Kazimi, 2014) investigated monolith SiC samples without internal voids, Lee's oxidation mechanics were inherently different than those investigated in this work and resulted in a net weight loss during oxidation.

Whereas the GAOE samples experienced a weight gain during oxidation, both GACE samples experienced no appreciable weight change. The negligible weight change observed for the GACE samples is attributable to the presence of the endplug and endplug sealing process. The endplug entirely blocks steam from entering the CMC on the endplug side of the sample, and the sealing process resulted in significant SiC deposition on the cut surfaces opposite the endplug. As a result, both entrances to the CMC (top and bottom cut surfaces) were protected against steam penetration and the CMC voids were consequently less oxidized when compared to the CMC voids of the GAOE samples. Figure 89 shows a comparison of the cross-sectional views for the open-end of typical GACE and GAOE samples, showing that the GACE sample has a better-sealed cross-section than the GAOE sample thereby protecting the CMC voids from significant oxidation. Because of the enhanced protection of the CMC in the GACE samples, significantly less silica buildup occurred in the CMC voids and the GACE samples experienced far less weight gain than the GAOE samples. Overall, the near-zero weight change for the GACE samples suggests that the scant silica deposition in the CMC voids balanced the silica volatilization on the external surfaces.



Figure 89: Comparison of as-received cross-section for GACE 4 (left) and GAOE 4 (right)

6.3.3. Hoop Testing Evaluation

Three samples in the GAOE series underwent pressurization testing after oxidation testing to determine the failure hoop strength and stress-strain characteristics after high-temperature steam oxidation. The internal pressurization facility and procedures outlined above in Section 4.2.1 was used for the hoop testing of the post-thermal-shock samples. The samples investigated for post-oxidation behavior were samples GAOE 1, GAOE 3, and GAOE 4. Sample GAOE 1 was oxidized for 24 hours, and samples GAOE 3 and GAOE 4 were oxidized for 48 hours.

The performance of the GAOE samples after oxidation can be compared to the as-received data to evaluate the effect of oxidation on the mechanical behavior of the samples. The post-oxidation stress-strain behavior allows for insight into the composite behavior of the GAOE series after oxidation and

allows for assessment of how the microstructural changes outlined in Section 7.2.3 influence the mechanical behavior of the samples.

Internal pressurization tests were performed on samples GAOE 1, GAOE 3, and GAOE 4 which loaded the samples until complete failure. Using the stress equations outlined above in Section 4.2.1, the stress-strain behavior and the yield and failure hoop stresses were obtained. Overall, the post-oxidation samples exhibited different mechanical behavior than the as-received sample. Whereas the as-received sample GAOE 2 experienced a peak internal pressure of 83 MPa and a failure stress of 581 MPa, the 48 hour oxidized samples GAOE 3 and GAOE 4 experienced peak internal pressures of 30 MPa and 39 MPa respectively, corresponding to failure hoop strengths of 203 MPa and 262 MPa respectively. The 24 hour oxidized sample GAOE 1 experienced a peak pressure of 71 MPa and a failure stress of 475 MPa. The substantially reduced failure strengths of the oxidized samples indicate that the high-temperature steam oxidation has a profound impact on the mechanical properties of the samples. Figure 90 presents the stress-strain behavior comparison between the oxidized samples and the as-received sample for the GAOE series. The mechanical results of the oxidation strength testing are compared to the results for the as-received sample in Table 28.

The stress-strain behavior of the oxidized samples was very different from that of the as-received sample. The 48 hour oxidized samples did not exhibit any pseudo-ductility and failed in a brittle non-frangible manner. The 24 hour oxidized sample exhibited pseudo-ductility but nevertheless displayed inferior mechanical performance to the as-received sample. The severely reduced failure strength of the 48 hour oxidized samples is attributable to the lack of pseudo-ductility in the samples: the 48 hour samples fail immediately upon reaching the yield stress. Ultimately, oxidation resulted in a significant degradation of mechanical properties for the samples.

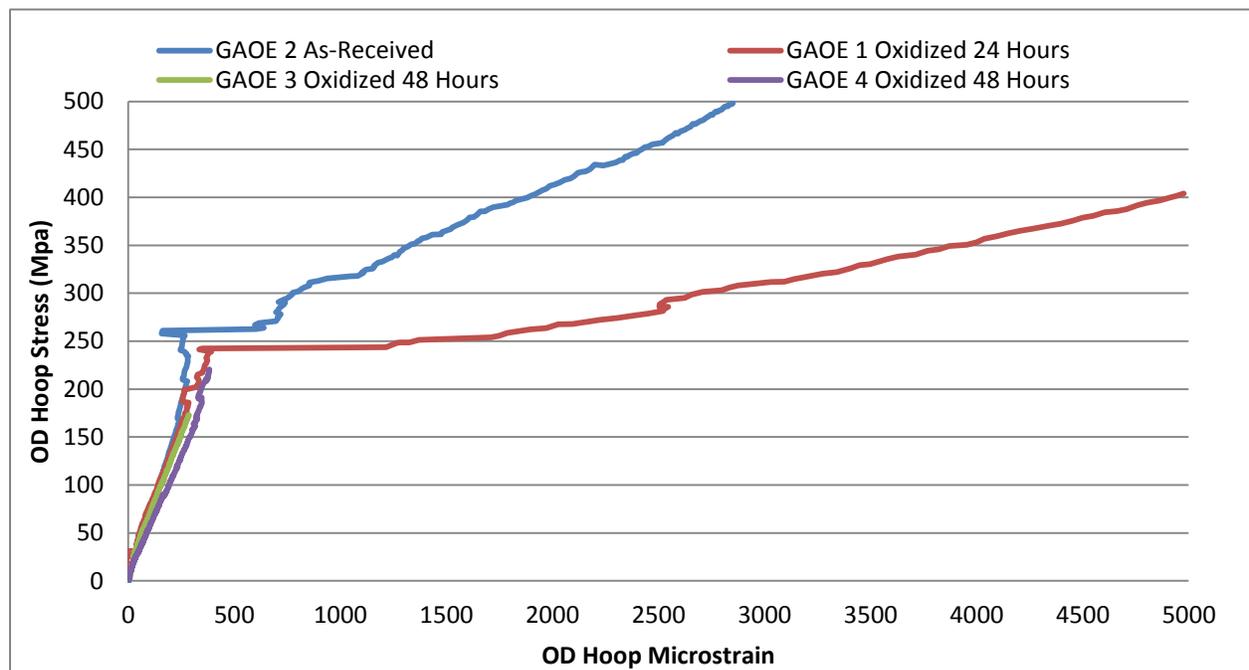


Figure 90: Stress-strain comparison between oxidized and as-received GAOE samples

Table 28: Strength test results for the oxidized and as-received GAOE samples

	GAOE 2 As-Received*	GAOE 1 Oxidation 24 Hour*	GAOE 3 Oxidation 48 Hour*	GAOE 4 Oxidation 48 Hour*
Yield Hoop Stress ID	304 MPa	285 MPa	No Yielding	No Yielding
Yield Internal Pressure	44 MPa	42 MPa	No Yielding	No Yielding
Failure Hoop Stress ID	581 MPa	475 MPa	203 MPa	262 MPa
Failure Internal Pressure	83 MPa	71 MPa	30 MPa	39 MPa
Failure Strain	0.285 ± 0.006%	0.498 ± 0.01%	0.029 ± 0.001%	0.038 ± 0.001 %

Because the normalized weight change for the samples during oxidation reflects the amount of oxidation, the weight change can be compared to the failure stress of the samples to observe whether the mechanical degradation corresponds with the extent of oxidation in the samples. From Figure 91 it can be observed that the weight change and the failure stress are inversely related, whereby higher weight gain lowers the failure stress. It should be noted that the weight loss observed for sample GAOE 4 was ignored for this comparison as it is believed that the measured weight loss was erroneous.

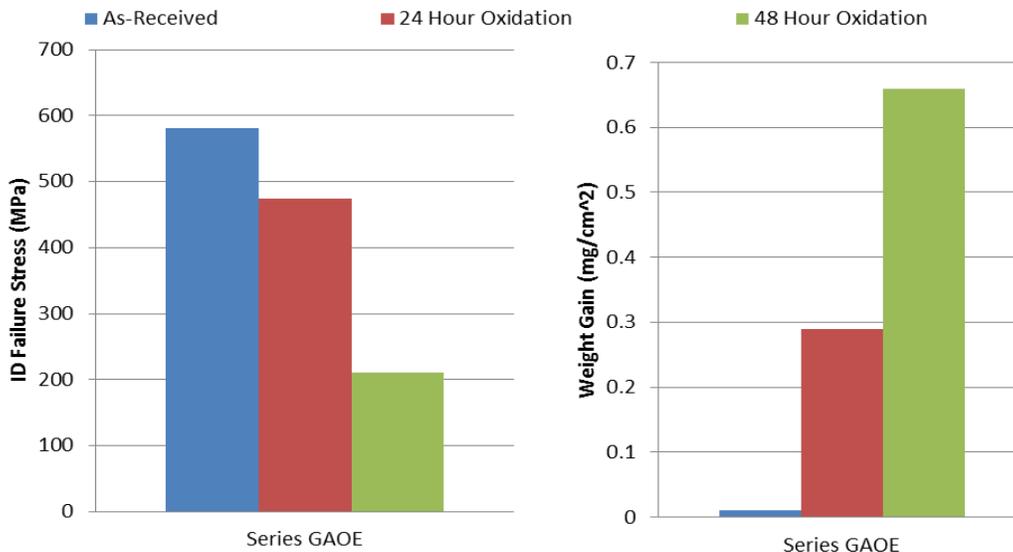


Figure 91: Comparison of weight change and failure stress for oxidized GAOE samples

6.3.4. Joint Testing Evaluation

One sample in the GACE-A series and one sample in the GACE-B series underwent joint strength testing after high-temperature steam oxidation to determine the influence of oxidation on failure joint strength. By comparing the oxidation results to the as-received results, the performance of the GACE-A and GACE-B series during oxidation conditions can be evaluated. Furthermore, comparison between the GACE-A and GACE-B oxidized samples can indicate whether the architecture of the samples influences the tolerance to oxidation.

* Uncertainty due to mechanical setup not quantified, see Section 4.2.1.3

Joint strength tests were performed on samples GACE 3 (A) and GACE 4 (B) which loaded the endplugs until complete pushout. Using the equation outlined above in Section 4.2.2, the burst strength of the endplug joint was obtained. Overall, the post-oxidation sample in the GACE-A series did not exhibit significant mechanical degradation attributable to the oxidation: the as-received sample GACE 2 experienced burst strength of 37.1 MPa and the oxidized sample GACE 3 experienced burst strength of 33.7 MPa. Figure 92 presents the pushrod load versus displacement comparison between the oxidized sample and the as-received sample for the GACE-A series, and Table 29 compares the oxidized and as-received results for the GACE-A series.

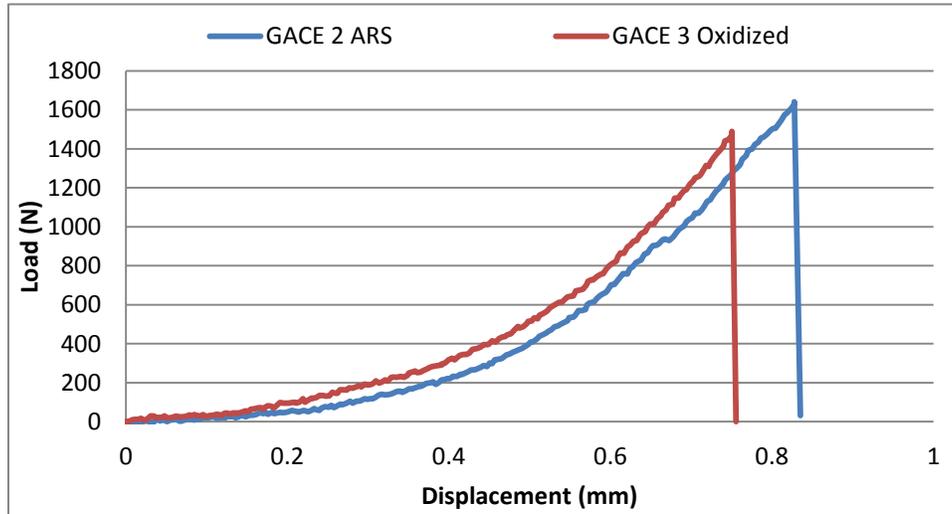


Figure 92: Pushrod load versus displacement comparison between oxidized and as-received GACE-A samples

Table 29: Pushout test results for oxidized and as-received GACE-A samples

	GACE 2 As-Received	GACE 3 Oxidized
Peak Load	1641 ± 8 N	1490 ± 7 N
Burst Strength	37.1 ± 0.2 MPa	33.7 ± 0.2 MPa

In contrast to the GACE-A series, the post-oxidation sample in the GACE-B series exhibits somewhat degraded mechanical behavior when compared to the as-received sample. In the GACE-B series, the as-received sample GACE 6 showed burst strength of 32.3 MPa while the oxidized sample GACE 4 showed burst strength of 22 MPa. Although some allowance must be made for variation in joint strengths as discussed in Section 5.4, the oxidation appeared to reduce the mechanical performance of the joint for the GACE-B series. Figure 93 presents the pushrod load versus displacement comparison between the oxidized and as-received samples for the GACE-B series, and Table 30 compares the oxidized and as-received results for the GACE-B series.

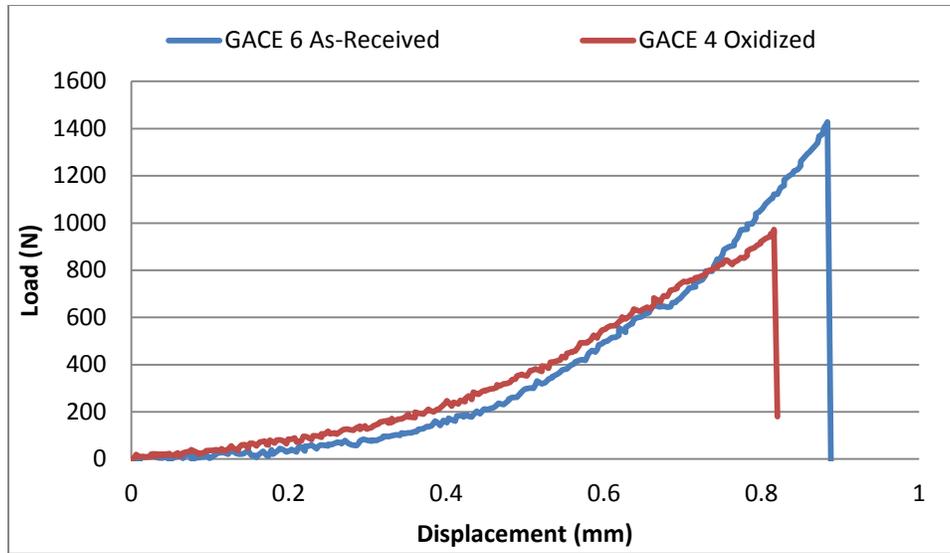


Figure 93: Pushrod load versus displacement comparison of oxidized and as-received GACE-B samples

Table 30: Pushout test results for oxidized and as-received GACE-B samples

	GACE 6 As-Received	GACE 4 Oxidized
Peak Load	1423 ± 7 N	972 ± 5 N
Burst Strength	32.3 ± 0.2 MPa	22.0 ± 0.1 MPa

6.3.5. Failure Observations

Observing the failure characteristics of the oxidized samples allows for determination of the typical failure characteristics expected of SiC cladding after the high-temperature steam oxidation associated with a LOCA. The GAOE oxidized sample failure characteristics were different from those observed for the as-received sample, with a smaller tube opening and less exposure of the interior. A coolable geometry was maintained after testing of the oxidized samples. GACE failure characteristics were different for oxidized and as-received samples. Although failure for the oxidized samples was still characterized by the complete separation of the endplug from the tubing, the morphology of the failure location was different, with failure occurring more significantly in the CMC when compared to the failure of the as-received samples.

6.3.5.1. Open-Ended Samples

Failure for the GAOE oxidized samples was characterized by minimal opening of the sample and no detachment of sections of the CMC. Furthermore, the failure crack did not travel the axial length of the sample and instead was only approximately 10 mm long. The crack was axially straight but followed the contours of the CMC upon termination. The low failure strain associated with the 48 hour oxidation samples resulted in minimal exposure of the CMC and no detachment of EBC fragments. In contrast, the high failure strain of the 24 hour oxidized sample resulted in significant detachment of EBC fragments and exposed significant portions of the underlying CMC at the failure location. Figure 94 shows lateral views of the oxidized samples after pressurization testing and Figure 95 presents a cross-sectional view of the oxidized samples after pressurization testing, showing how the samples opened very little.



Figure 94: Lateral photographs of GAOE 3 (left), GAOE 4 (middle), and GAOE 1 (right) after testing



Figure 95: Cross-sectional photographs of GAOE 3 (left), GAOE 4 (middle), and GAOE 1 (right) after testing

Because the GAOE oxidized sample failure did not expose significant amounts of the interior of the samples and did not fully penetrate the axial length of the samples a coolable geometry was maintained. Furthermore, because the failure was not characterized by the detachment of significant pieces of the EBC (except for GAOE 1), the failure characteristics observed for the GAOE oxidized samples do not pose a strong risk for clogging the coolant channels in the core upon failure. Unlike the failure of the as-received and thermal-shock GAOE samples, no large pieces of the CMC detached from the oxidized samples and there is minimal release of EBC fragments upon failure.

6.3.5.2. Close-Ended Samples

GACE oxidized sample failure occurred in the endplug joint for GACE 3 and within the CMC layer for GACE 4. After failure the endplug completely detached from the sample intact and the remaining tubular section of the cladding was intact and did not significantly fragment during failure. Thus, if the endplug joint failed in a reactor, the freed endplug could get caught in the coolant flow and would risk clogging the coolant channels in the core, although the remaining tubing would still be structurally intact and coolable. Figure 96 shows images of the endplug joints after pushout testing, revealing the failure characteristics observed in the endplug region. From the figure, it can be observed that the endplug surface for GACE 4 is coated with CM whereas the endplug lapped surface for GACE 3 is exposed with no CMC coating.



Figure 96: Endplug failure characteristics for GACE 3 (A, left) and GACE 4 (B, right)

The CMC coating observed on the endplug surface for GACE 4 shows that failure occurred within the CMC and not within the endplug joint. Because the GACE 4 architecture does not have axial tows, the CMC is inherently weaker to axial stresses. The oxidation weakened the CMC to such an extent that the CMC failed prior to joint failure. Figure 97 shows the failed CMC surfaces in the tube and in the endplug, showing how approximately half of the CMC carried with the endplug and half remained attached to the tube.



Figure 97: Photographs of the failed CMC surface in the tube (left) and on the endplug (right) for GACE 4

Because GACE 4 failure occurred in the CMC, the joint voids did not influence the failure characteristics of the sample. However, the failure of GACE 3 occurred in the endplug joint and was accompanied by some fracture of the tubing. As observed for the as-received endplug failure discussed in Section 6.1.4 and for the thermal-shock endplug failure discussed in Section 6.2.4, the tubing fracture is correlated with the void joints. The tubing fracture locations after pushout testing of GACE 3 were compared to the XCT images showing the locations of the joint voids, and it was found that the tubing fracture locations corresponded with joint regions of large voids. Figure 98 shows the correspondence between the locations of tube fracture in GACE 3 and the joint voids observed during XCT analysis. In the figure, the red line represents where the sections of tubing fractured from the tube body and remained attached to the endplug after pushout.

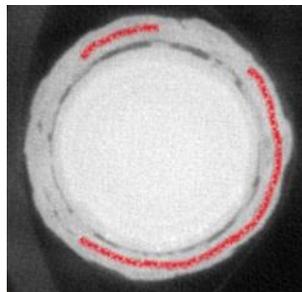


Figure 98: XCT analysis of GACE 3 showing location of tube fracture (red line)

6.4. Summary of Results

6.4.1. As-Received Results

Two facilities were implemented to evaluate the mechanical characteristics of the as-received samples. The samples tested as-received were GAOE 2, GACE 2, and GACE 6. Analysis of the as-received samples indicated that the SiC composite cladding can withstand normal reactor operating conditions. The peak pressure that the tubing can withstand is approximately 80 MPa, corresponding to a peak hoop stress of approximately 570 MPa. Similarly, the peak pressure that the endplug can handle was above 30 MPa. The GAOE series exhibited pseudo-ductility, and failure of the tubing resulted in some fragmentation of the CMC and EBC, although the tubing was largely intact after failure. Failure of the endplug resulted in complete separation of the endplug from the tubing. Overall, failure of the samples would pose a risk for clogging the coolant channels in the core due to the detachment of fragments.

6.4.2. Thermal-Shock Results

A thermal-shock facility was implemented to simulate the reflood event during a LOCA in order to evaluate the thermal-shock resistance of the cladding specimens. The internal pressurization and joint strength testing facilities were then used to evaluate the mechanical performance of the post-thermal-shock samples, which was compared to the performance of the as-received samples to evaluate the influence of thermal-shock on the mechanical performance.

Analysis of the thermal-shock samples indicated that the SiC composite cladding is resistant to thermal-shock in LOCA conditions, displaying minimal changes in performance attributable to the thermal-shock. The peak pressure that the tubing can withstand after thermal-shock is approximately 75 MPa, corresponding to a peak hoop stress of approximately 480 MPa. The GAOE series exhibited pseudo-ductility, as supported by stress-strain analysis and SEM analysis post-testing. Failure of the tubing resulted in some fragmentation of the CMC and EBC, although the tubing was largely intact after failure.

However, variance was observed in the results of the thermal-shock testing for the endplug joints. The GACE-A series exhibited resistance to thermal-shock, with a post-thermal-shock burst strength of 34 MPa. In contrast, the GACE-B series exhibited more significantly degraded mechanical performance, with a post-thermal-shock burst strength of 7 MPa and 14 MPa for the two samples tested, although the 7 MPa burst strength for GACE 5 is attributable to the inferior endplug joint as determined by the XCT analysis in Section 5.4. Failure of the endplug resulted in complete separation of the endplug from the tubing. Overall, failure of the samples would pose a risk for clogging the coolant channels in the core due to the detachment of small fragments of EBC and CMC.

The reduced performance of the GACE-B series may be attributable to its different architecture compared to the GACE-A series. The GACE-B architecture consisted of a two-tow design with a high interlace angle. In contrast, the GACE-A series had a three-tow design with a lower interlace angle. Thus, the CMC of the GACE-A series was expected to be axially stronger than the CMC of the GACE-B series.

Figure 99 presents a comparison of the as-received and thermal-shock failure burst pressures. A slight decrease in mechanical performance attributable to the thermal-shock was observed for the GAOE and GACE-A series, but a significant decrease was observed for the GACE-B series.

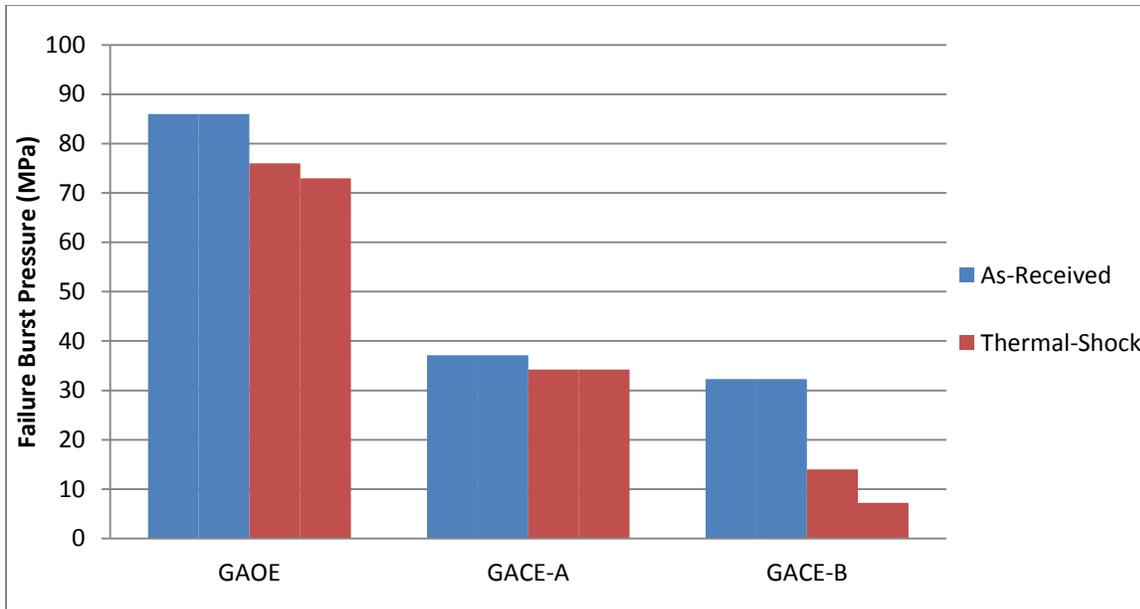


Figure 99: Comparison of as-received and thermal-shock results for all series

6.4.3. High-Temperature Steam Oxidation Results

An oxidation facility was constructed and implemented to simulate the high-temperature steam oxidation that could occur during a LOCA. The oxidation testing was performed in order to evaluate the post-oxidation performance of the cladding specimens. The internal pressurization and joint strength testing facilities were used to evaluate the mechanical performance of the post-oxidation samples, which was compared to the performance of the as-received samples to evaluate the influence of oxidation on the mechanical performance.

Analysis of the oxidized samples indicated that the SiC composite cladding is strongly affected by the high-temperature steam oxidation, displaying significant changes in performance attributable to the oxidation. The peak pressure that the tubing can withstand after 48 hour oxidation is approximately 35 MPa, corresponding to a peak hoop stress of approximately 230 MPa. The 48 hour oxidized samples did not exhibit pseudo-ductility and instead failed in a brittle non-frangible manner. Because of the low strain at failure, failure of the tubing did not result in significant CMC fragmentation or EBC detachment and the tubing was largely intact after failure. The 24 hour oxidized samples exhibited improved performance over the 48 hour oxidized samples, although the performance was still inferior to the as-received sample. The 24 hour oxidized sample experienced a failure pressure of 71 MPa and a corresponding failure hoop stress of 475 MPa. The 24 hour oxidized sample exhibited pseudo-ductility albeit with a shallower pseudo-ductile slope than the as-received sample.

Variance was observed in the results of the thermal-shock testing for the endplug joints. The GACE-A series exhibited improved resistance to oxidation, with post-oxidation burst strength of 33.7 MPa. However, the GACE-B series exhibited more significantly degraded mechanical performance after oxidation, with post-oxidation burst strength of only 22 MPa. The XCT analysis in Section 5.4 suggested that the endplug joints for the oxidized samples were likely of similar strength to the joints for the as-received samples. Therefore, because the endplug joints were of similar strength, the degraded

mechanical performance is attributable to the oxidation. Failure of the endplug resulted in complete separation of the endplug from the tubing. Overall, failure of the samples would not pose as large a risk for clogging the coolant channels as the as-received failure due to less detachment of CMC/EBC fragments, although the detached endplug would still risk blocking coolant channels.

The reduced performance of the GACE-B series may be attributable to its different architecture compared to the GACE-A series. Because of the GACE-B series two-tow architecture, it was expected to have an axially-weaker CMC than the three-tow GACE-A series. Furthermore, the GACE-B series exhibited a higher void fraction than the GACE-A series, thus facilitating easier diffusion of the high-temperature steam through the CMC void network. Because failure of the endplug for the oxidized GACE-B series occurred in the CMC at the endplug region (and not in the actual joint), the inferior endplug strength of the post-oxidized GACE-B sample is attributable to the combination of inherent axial CMC weakness and the susceptibility of the GACE-B CMC to enhanced internal oxidation due to increased void fraction.

Figure 100 presents a comparison of the as-received and oxidized failure burst pressures. A significant decrease in mechanical performance attributable to the high-temperature steam oxidation was observed for the GAOE and GACE-B series, whereas The GACE-A series was more tolerant of oxidation conditions.

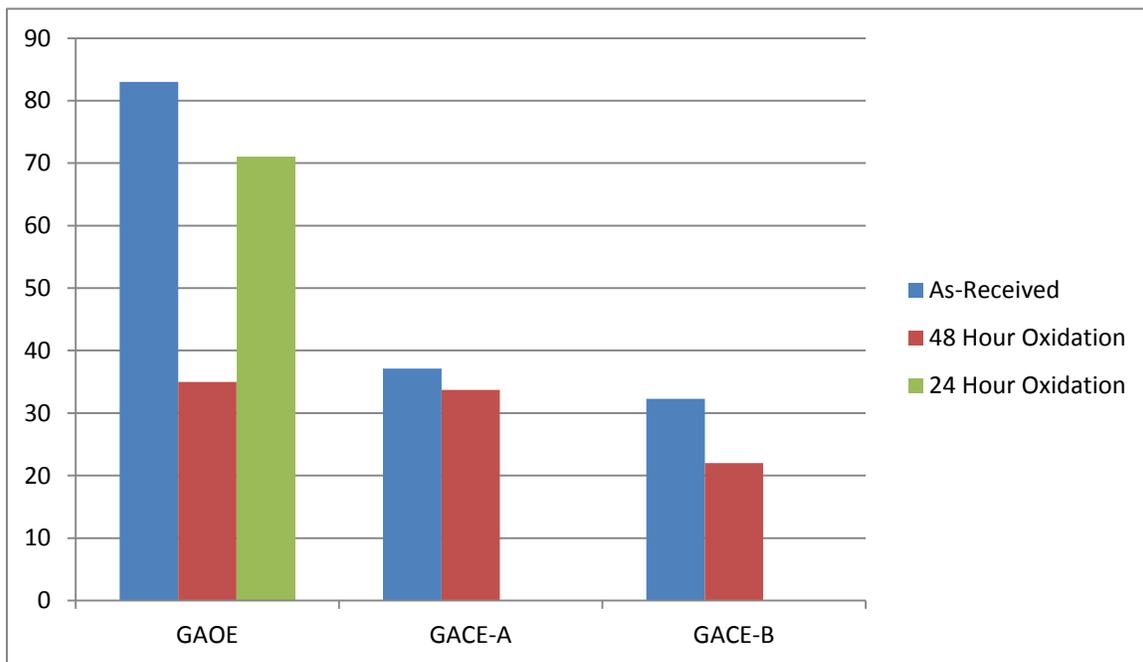


Figure 100: Comparison of as-received and oxidized results for all series

7. Discussion of Results

7.1.As-Received Discussion

7.1.1. Hoop Test

The failure internal pressure observed for the as-received GAOE 2 sample was 83 MPa and the corresponding failure hoop stress was 581 MPa, although hermeticity was likely lost once the sample began yielding. The failure internal pressure for the GAOE 2 sample was significantly higher than the typical LWR end-of-life (EOL) plenum pressure of approximately 15.5 MPa (Khalifa H. E., Deck, Gutierrez, Jacobsen, & Back, 2015). Therefore, the GAOE series can safely handle the pressures expected during normal LWR conditions with a wide safety margin. Furthermore, the failure hoop stress of 581 MPa allows for the cladding to be thin while still safely resisting the LWR EOL conditions, thus helping to reduce fuel temperatures. Overall, the hoop strength testing revealed that the GAOE series is strong enough to withstand normal LWR operation.

The stress-strain behavior obtained for the GAOE 2 sample during the pressurization testing allows for insight to be gained into the microstructural flaw evolution of the CMC layer during testing and failure. As stated previously, several distinct loading regimes were observed in the stress-strain curve for GAOE 2. Each regime corresponds to a unique phase in microstructure flaw development in the CMC region of the specimen as described in previous work (Lamon, 2014). These regimes, labeled on Figure 101, are:

- I. Bulk elastic domain
- II. Inter-tow matrix fragmentation domain
- III. Intra-tow matrix fragmentation domain
- IV. Fiber elastic domain

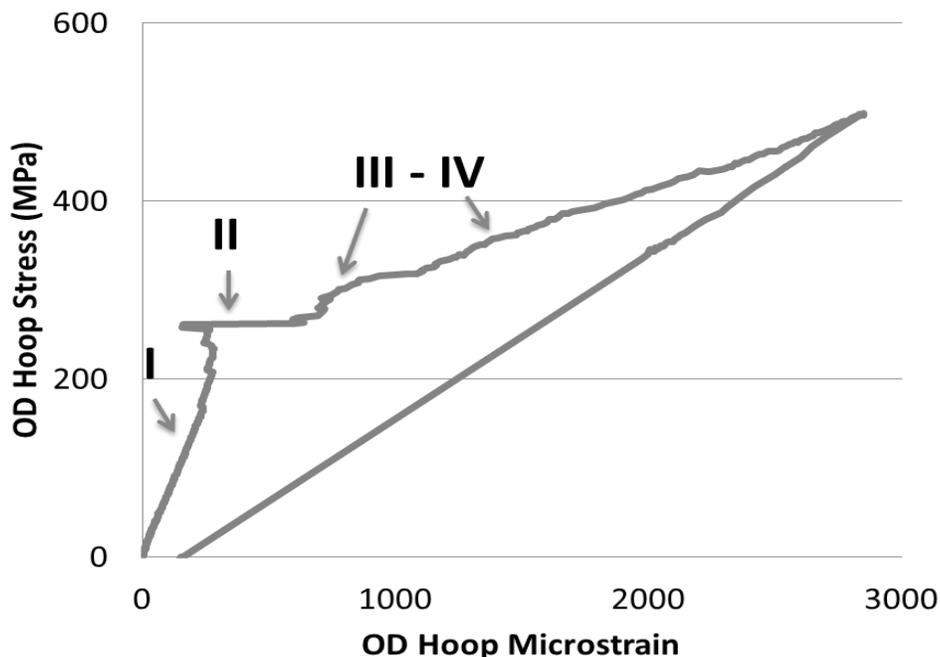


Figure 101: Unique regimes of stress-strain behavior for GAOE 2

The first regime is the bulk elastic domain (Region I) and occurs when all material within the sample is elastically loaded with no cracking. This region is reversible and exhibits a steep slope that terminates with localized yielding of the sample. The bulk elastic domain transitions to inter-tow matrix fragmentation domain when the loading curve exhibits slight decreases in strain which correspond to localized inter-tow matrix fragmentation without bulk fragmentation. The localized fragmentation allows the liberated tows to reorder, thus relieving strain at locations without fragmentation. However, once the stress surpasses the yield point, the bulk inter-tow matrix fragments and all the tows are freed, thus resulting in a sudden large increase in strain (Region II).

After the inter-tow matrix is destroyed, the load is supported by a combination of the intra-tow matrix and the fibers (Regions III and IV). Because the matrix is much stiffer than the fibers, the matrix disintegrates first (Region III) and the load gradually transitions from predominantly matrix supported to fiber supported (Region IV), although these two loading regimes occur simultaneously during pseudo-ductile behavior. Thus, two regimes characterize the final stress-strain behavior of the CMC: the intra-tow matrix fragmentation domain and the fiber domain. Ultimate sample failure occurs when the entire matrix has fragmented and the fibers are stressed to failure. The evolution of flaws is supported by SEM analysis of the post-test sample. Analysis of the failure location reveals fibers dissociated from the surrounding matrix, suggesting that the matrix disintegrated prior to fiber failure. Figure 102 shows an SEM view of a representative failure location showing that the exposed fibers have been liberated from the matrix, thus suggesting that the matrix fragmented prior to fiber failure. Figure 103 shows an SEM view of the fibers and matrix within a tow, showing a profusion of cracks within the matrix that resulted in matrix fragmentation.



Figure 102: SEM view of failure location for GAOE 2 showing freed fibers

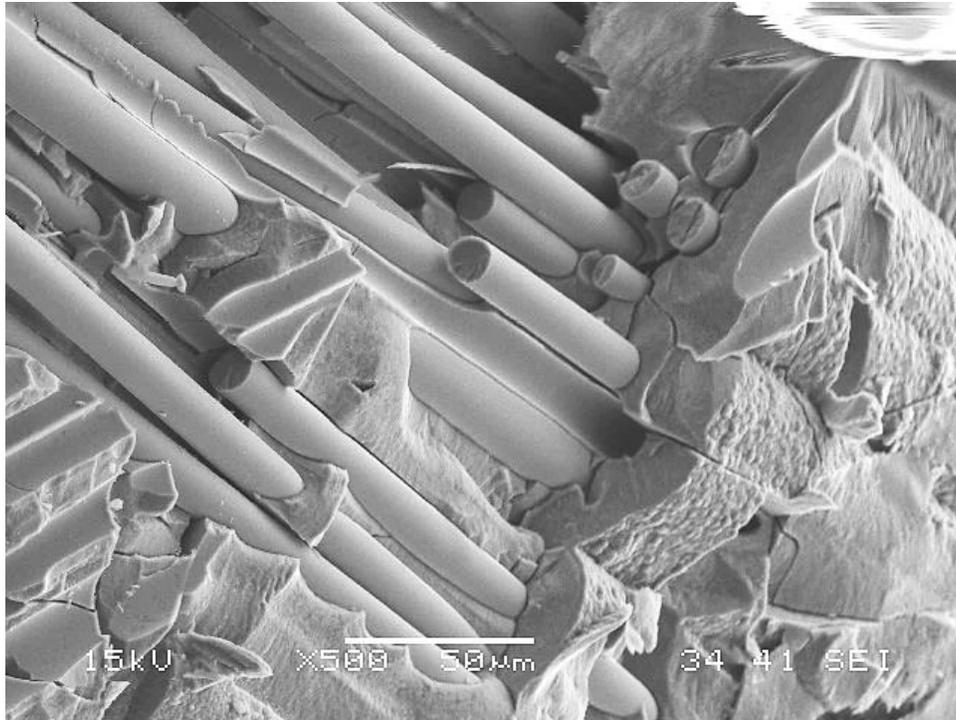


Figure 103: SEM view of fragmented intra-tow matrix for GAOE 2

7.1.2. Joint Test

The failure burst strength for both as-received GACE samples was above 30 MPa. Because the burst strength of the samples was significantly higher than the 15.5 MPa EOL plenum pressure for a typical LWR fuel rod (Khalifa H. E., Deck, Gutierrez, Jacobsen, & Back, 2015), the endplug joints are strong enough to withstand the typical pressures observed during normal LWR operating conditions. However, the failure pressure for the GAOE tubing (approximately 80 MPa) was significantly higher than the failure pressure for the endplug joints, suggesting that the endplug joint is a performance-limiting factor for the strength of the cladding. Indeed, the endplug joint would likely fail before the tubing begins to yield. Therefore, the tubing could be made thinner to reduce the discrepancy between tubing and endplug burst strengths, or the endplug joint should be made stronger.

Both as-received samples exhibited similar endplug joint quality when analyzed by XCT: both samples had joint void fractions of approximately 20%, and both had joint lengths of approximately 10.5 mm. Figure 104 shows a comparison between the endplug joints for the GACE 2 (A) and GACE 6 (B). Despite the similar joints, the sample from the GACE-A series exhibited 15% higher as-received burst strength than the sample from the GACE-B series. This suggests that the sample architecture influences the burst strength of the endplug. Because the GACE-A series has one axial tow and a shallower interlace angle, it would be expected that the CMC layer for GACE-A supports the endplug more than the high interlace angle two tow designs such as GACE-B. Therefore, even though failure occurred in the joint region, the architecture of the samples was observed to have a contribution to the overall burst strength of the endplug joint. However, because only one sample from each series was tested as-received, statistically significant conclusions cannot be obtained.

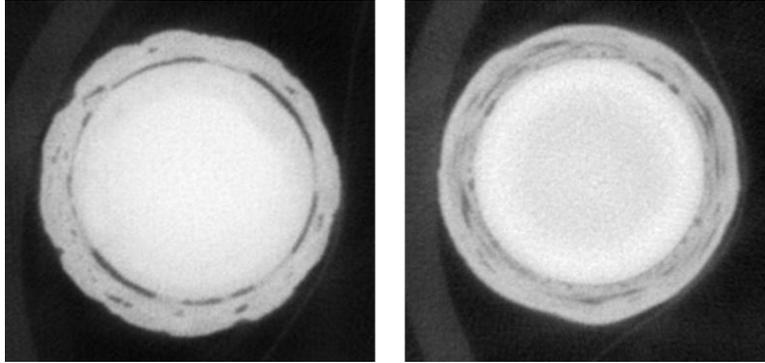


Figure 104: Joint comparison between GACE 2 (A, left) and GACE 6 (B, right)

7.1.3. Microstructural Analysis

SEM analysis was performed on the samples after mechanical testing to gain insight into the microstructural changes in the samples after failure. Analysis of the CMC region after failure revealed extensive matrix fragmentation and exposed fibers. Figure 105 presents an SEM view of the CMC layer after failure, showing a severely fragmented matrix and exposed fibers.

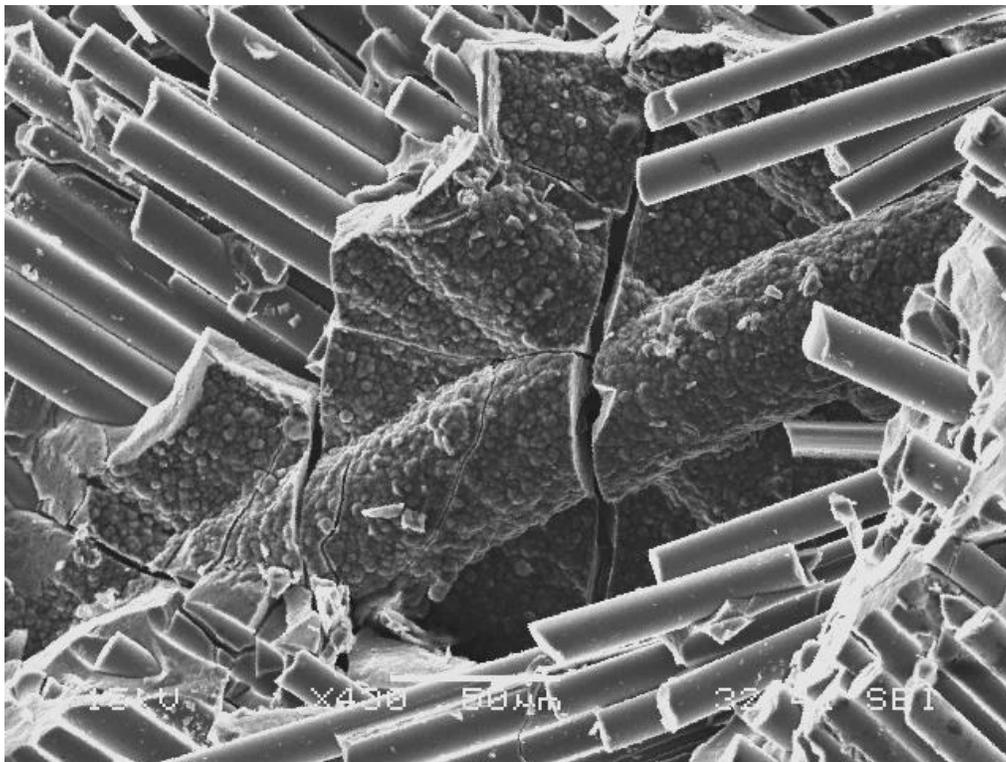


Figure 105: SEM view of CMC region of GAOE sample showing fragmented matrix among exposed fibers

Analysis of the failed locations for the GAOE sample revealed fiber pullout, suggesting that the matrix fragmented prior to fiber failure. Furthermore, the extensive fiber pullout observed indicates that the Carbon interphase between the fibers and the matrix is effective at decoupling the failure of the fibers from the failure of the matrix. Figure 106 and Figure 107 present cross-sectional and lateral SEM views of GAOE 2 showing fiber pullout and evidencing matrix fragmentation prior to fiber failure.

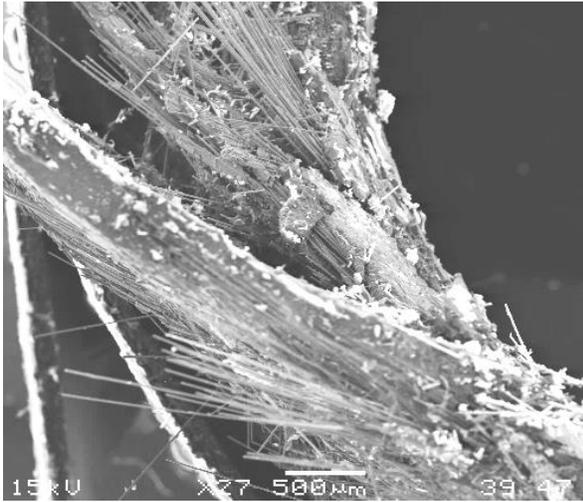


Figure 106: Cross-sectional SEM image of GAOE 2 showing exposed fibers

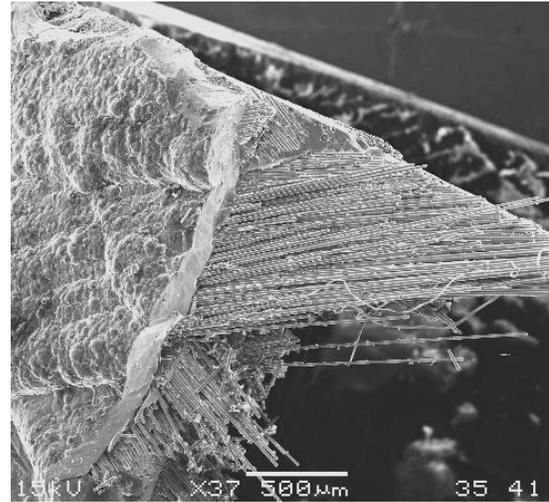


Figure 107: Lateral SEM image of GAOE 2 showing exposed fibers

Cracking in the EBC was also observed via SEM analysis after sample failure. The cracking likely resulted from the large stresses experienced by the EBC after CMC yielding and the cracks propagated during subsequent loading. The strain gage measured a peak strain on the EBC of 0.285%: a strain that the EBC could never achieve without experiencing cracking. Because of the EBC cracking, small flakes of the EBC were observed to detach from the sample after failure. Figure 108 presents a lateral SEM view of the EBC and shows extensive cracking resulting from the mechanical testing of GAOE 2.

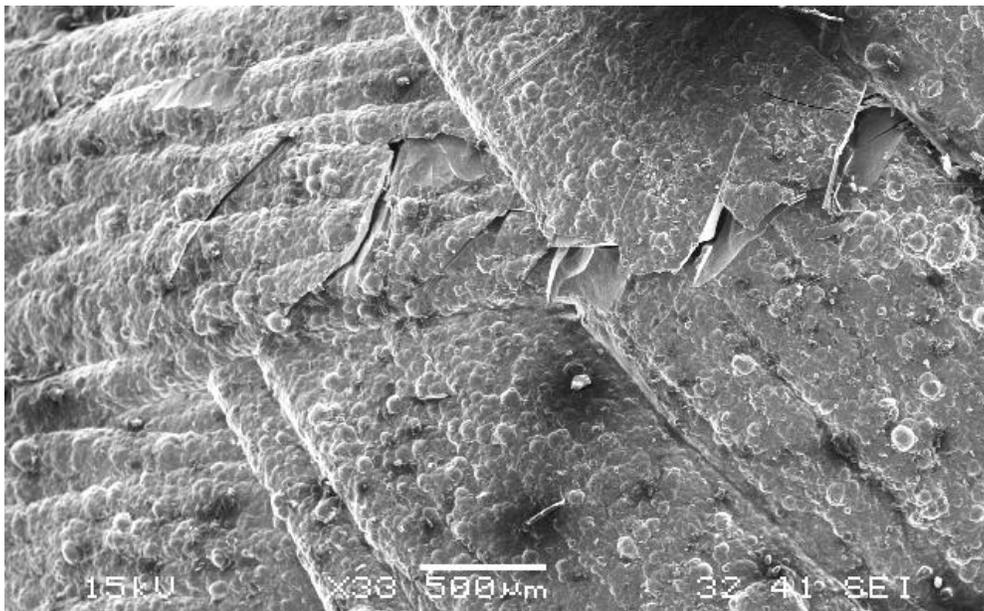


Figure 108: Lateral SEM image of GAOE 2 showing cracked EBC

SEM analysis was also performed on the endplug region of the GACE samples after pushout testing. Analysis of the endplug joint was enabled because some sections of tubing remained attached to the

GACE 2 endplug after pushout, thus allowing for cross-sectional SEM views of the joint. Large voids were observed in the joint connecting the endplug to the tubing, suggesting that the failure location in the tubing was correlated with the joint voids. Figure 109 and Figure 110 show cross-sectional SEM views of the endplug joint for the tubing still attached to the endplug after pushout for GACE 2.

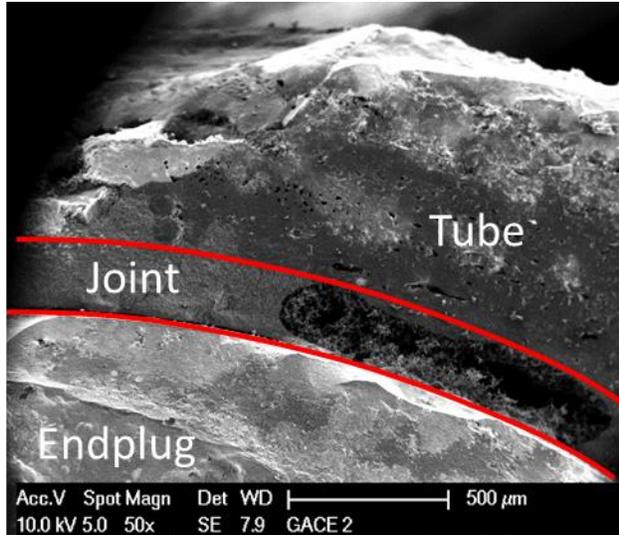


Figure 109: Cross-sectional SEM view of GACE 2 endplug joint showing large void

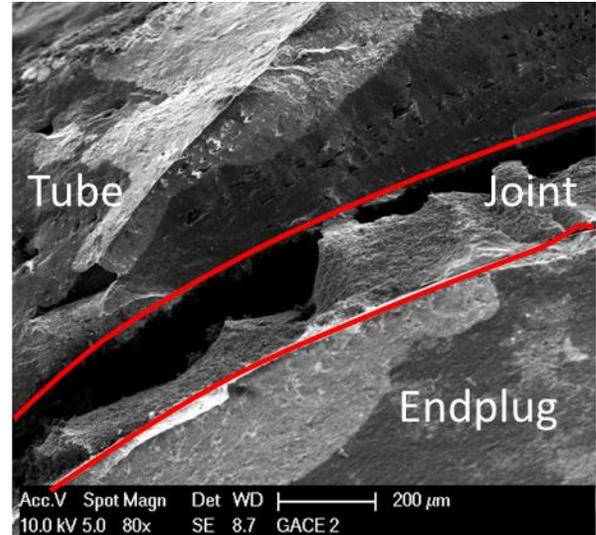


Figure 110: Cross sectional SEM view of GACE 2 endplug joint showing voids

Analysis of the failed CMC layer still attached to the endplug showed no fiber pullout or matrix fragmentation. Instead, the region appeared to shear without showing any characteristics of pseudo-ductility. Figure 111 shows an SEM view of the CMC region still attached to the endplug. From the figure, it can be observed that there is no fiber pullout and the matrix did not fragment. It is uncertain why fiber pullout was not observed for the tube failure at the joint.

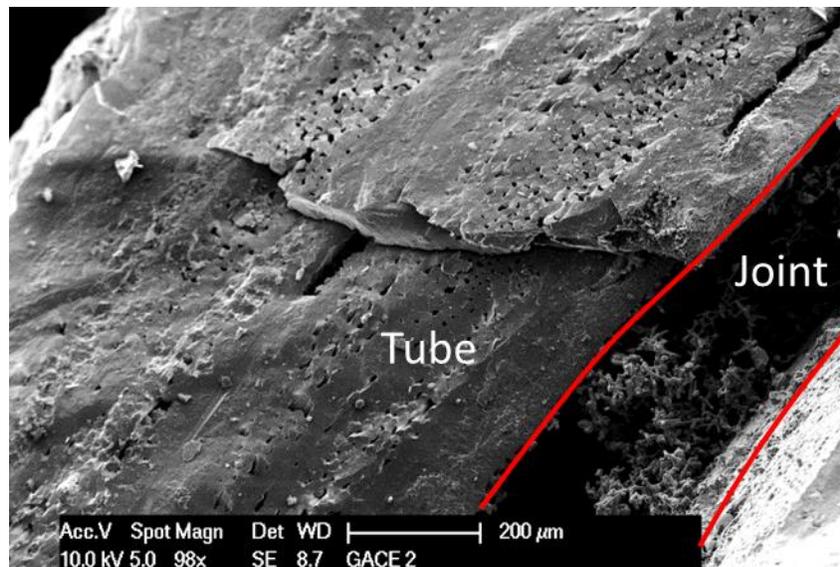


Figure 111: Cross-sectional SEM view of CMC region still attached to endplug

Because none of the joint material remained attached to the endplug for GACE 6 after pushout, SEM analysis of the joint region for GAOE 6 was performed on the inside surface of the tubing. The joint analysis revealed the presence of voids in the joint material, although the voids appeared smaller and more evenly dispersed than those in the joint of GACE 2. The failure surface of the endplug joint was smooth, with very little of the joint material or tubing remaining attached to the endplug after pushout. Figure 112 shows a view of the joint material for GACE 6 revealing the voids in the joint and failure surface.

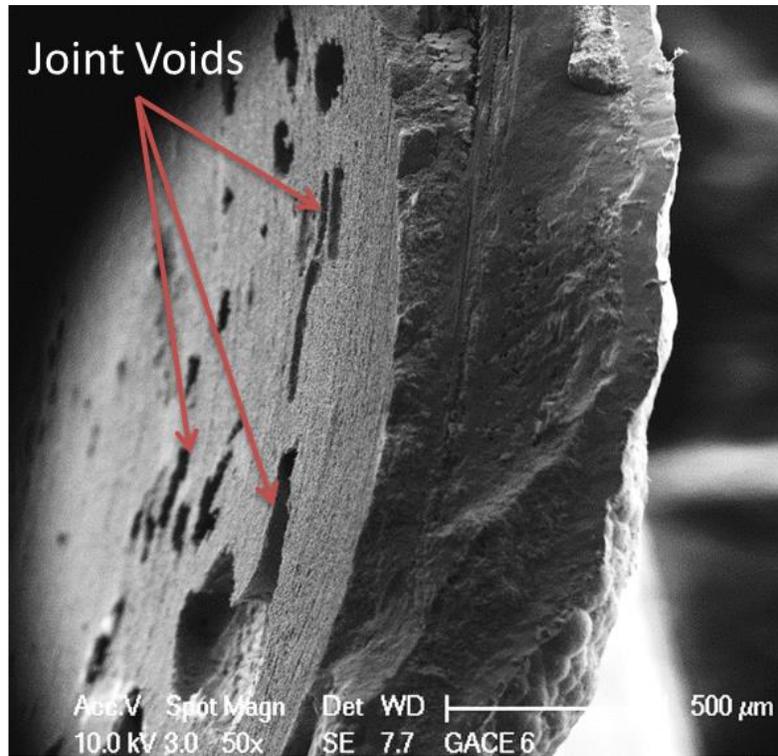


Figure 112: SEM view of joint inside tubing for GAOE 6 showing voids

7.2. Thermal-Shock Discussion

7.2.1. Hoop Test

The stress-strain behavior observed for the thermal-shock samples was similar to the behavior for the as-received sample, indicating that the thermal-shock has little impact on the mechanical behavior of the GAOE series. Because the same loading regimes outlined in Section 7.1.1 were observed in the thermal-shock samples, the thermal shock appeared to have no influence on the microstructural evolution of the sample during strength testing. Because the stress-strain response after yielding is dominated by matrix fragmentation and fiber elastic loading, the similar behavior during this regime between the thermal-shock and as-received samples suggests that the matrix was not significantly weakened by the thermal shock, nor were cracks introduced into the matrix due to thermal shock. Instead, the matrix gradually fragmented in a manner similar to in the as-received sample. This evaluation is supported by SEM analysis performed after the thermal-shock but before mechanical testing. The SEM analysis did not reveal any cracks on the surface of the sample and further suggests

that there is little microstructural change in the samples attributable to the thermal-shock. Figure 113 shows a comparison between lateral SEM views of sample GAOE 5 after thermal-shock and before thermal shock. Figure 114 shows a comparison between cross-sectional SEM views of sample GAOE 6 before and after thermal-shock. From the figures, it can be observed that no cracks developed on the thermal-shock sample, suggesting that the thermal-shock has limited impact on the microstructure of the sample.

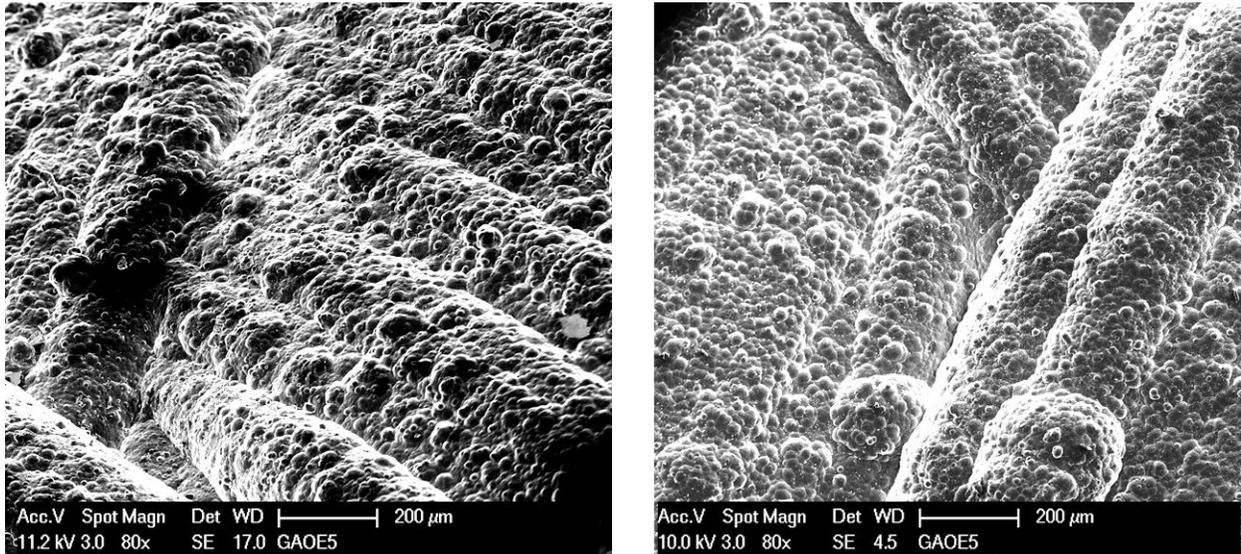


Figure 113: Lateral SEM view comparison of post-thermal-shock sample (left) with as-received sample (right)

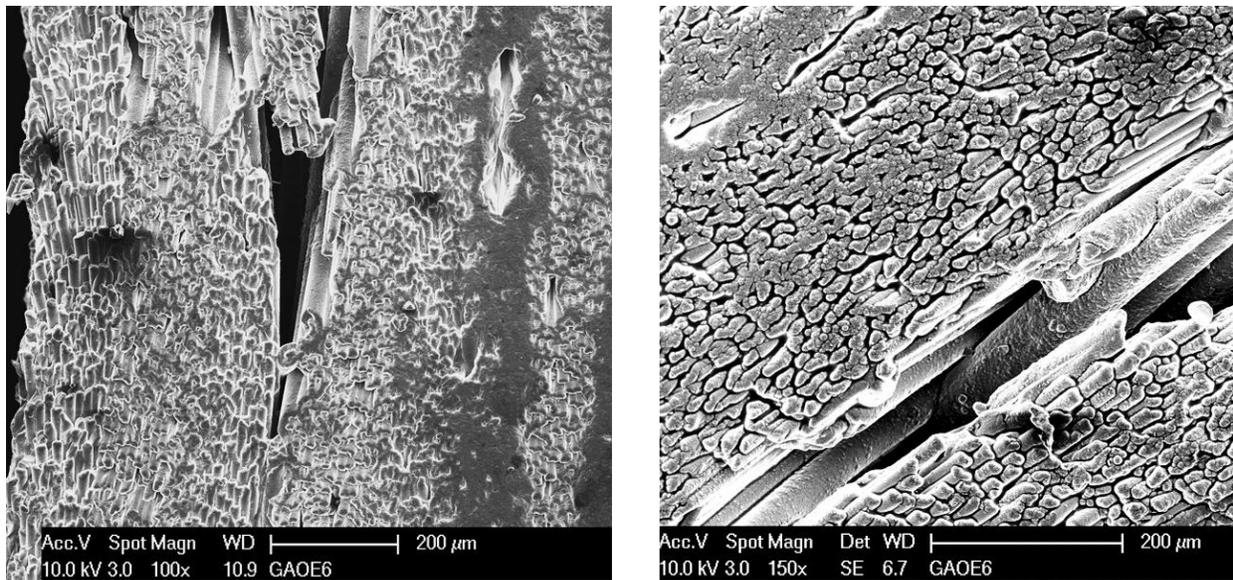


Figure 114: Cross-sectional SEM view comparison of post-thermal-shock sample (left) with as-received sample (right)

The failure behavior observed in the thermal-shock GAOE samples was similar to the behavior of the as-received sample. After failure, many fibers were exposed, suggesting matrix fragmentation prior to fiber failure. The failure characteristics also evidence the pseudo-ductile behavior exhibited by the thermal-

shock samples. Figure 115 shows an SEM view of the failure location for a thermal-shock sample with significant fiber pullout.

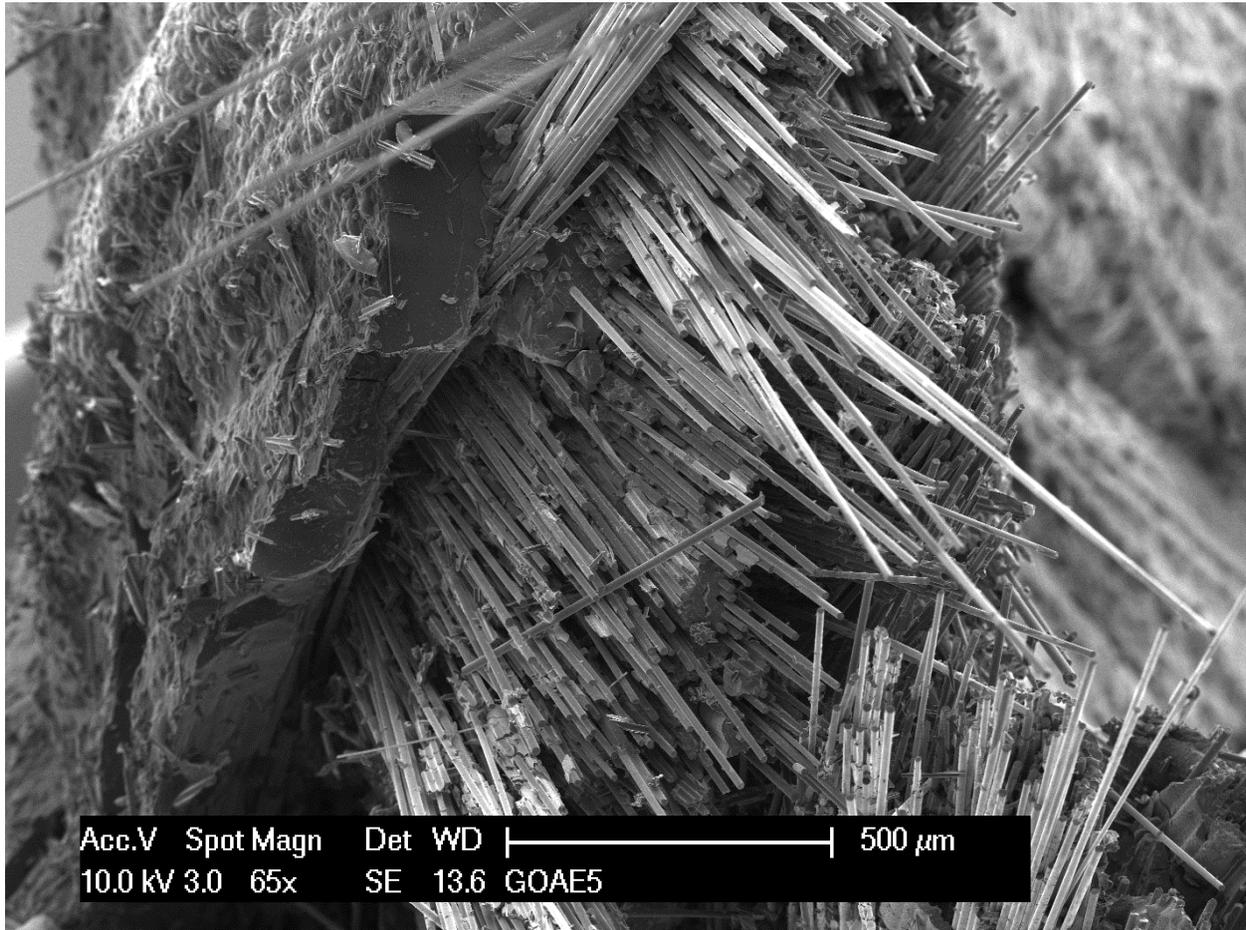


Figure 115: SEM view of failure location in thermal-shock sample showing fiber pullout

During the quenching process of the GAOE samples, film boiling was observed for the majority of the quench. Immediately upon entering the water, the sample experienced film boiling which lasted until a quench front of nucleate boiling progressed upwards and terminated all boiling. The film boiling lasted for approximately 10 seconds, and the nucleate boiling quench front lasted for approximately 2 seconds. The quench front began at the bottom of the sample and progressed axially upwards, and all boiling ceased after the passage of the quench front. The film layer protected the sample by maintaining a high surface temperature and limiting the radial thermal gradient in the sample. The presence of the vapor film insulated the sample from high thermal gradients sufficient to prevent the development of thermal cracking, thereby preserving the as-received properties of the sample.

7.2.2. Joint Test

The results of the joint strength testing for the GACE-A series indicated little mechanical degradation due to the thermal-shock. The thermal-shock sample exhibited burst strength in excess of 30 MPa, showing only an 8% reduction in burst strength when compared to the as-received sample. The results of the void analysis in Section 5.4 suggest that the GACE 1 endplug joint was likely of similar strength to

the joint for GACE 2, showing similar void fractions, joint widths, and joint heights. Figure 116 shows a comparison between the XCT images of the joints for the thermal-shock and as-received samples. Because of the similarity of the joint properties, the joint strength difference between the two samples is likely attributable to the thermal-shock.

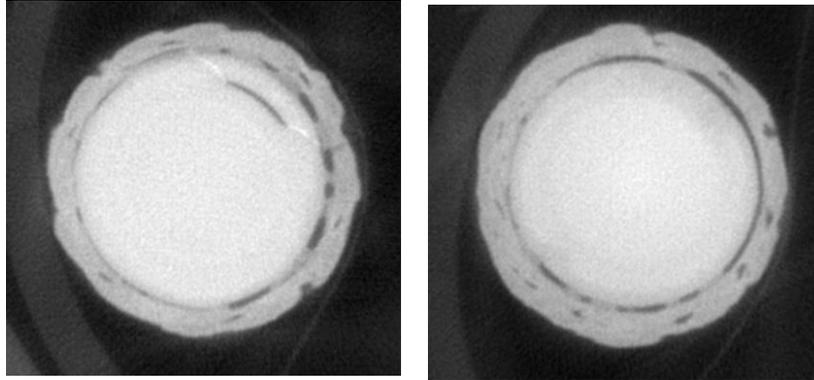


Figure 116: XCT comparison of joints for GACE 1 (left) and GACE 2 (right)

The results of the joint strength testing for the GACE-B series indicated substantial mechanical degradation due to the thermal-shock. The thermal-shock samples exhibited burst strengths of 7.2 MPa and 14 MPa, showing over 50% reduction in burst strength when compared to the as-received sample. The results of the void analysis in Section 5.4 suggest that the endplug joints for both thermal-shock samples were likely of inferior strength to the joint for GACE 6, showing different void fractions and joint heights. The joint for sample GACE 8 was significantly shorter than the joint for GACE 6, at only 7.8 mm compared to 10.6 mm. Furthermore, the joint for sample GACE 5 had a significantly higher void fraction than the joint for GACE 6, at 34% compared to 18%. Figure 74 in Section 5.4.2 above shows a comparison between XCT images of the endplug joint height for GACE 6 and GACE 8, demonstrating that GACE 8 has a significantly shorter endplug joint than GACE 6. Figure 117 shows a comparison of XCT images for GACE 5 and GACE 6 showing the wider and more porous joint of GACE 5. Overall, because both thermal-shock samples exhibited inferior joints to the control sample, some allowance must be made to accommodate the variation in the endplug joints. However, due to the dramatic decrease in mechanical strength of the endplug joint for the GACE-B series, quenching appears to significantly degrade the mechanical performance of the GACE-B endplug joint.

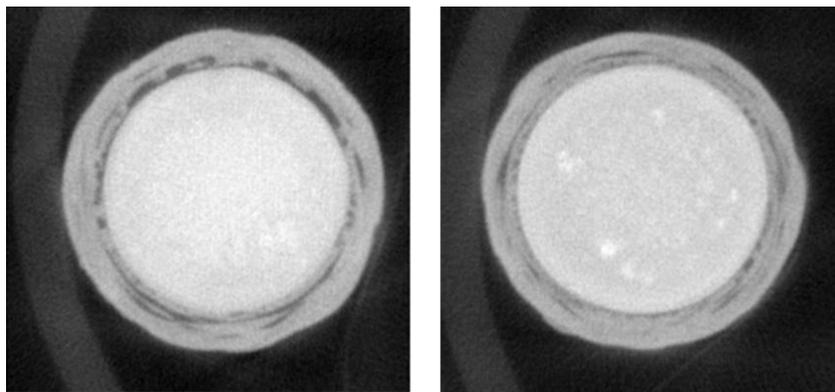


Figure 117: XCT comparison of joints for GACE 5 (left) and GACE 6 (right)

The difference observed in the effect of thermal-shock among the two GACE series, although somewhat attributable to the inferior joints of the GACE-B thermal-shock samples, is likely also attributable to the different architectures of the samples. The GACE-A series was a three-tow weave pattern, with one axial tow and two tows with an interlace angle of 100°. The GACE-B series was a two-tow weave pattern with an interlace angle of 150°. Because the GACE-A tows were more axially inclined, the CMC structure was likely stronger in the axial direction when compared to the GACE-B series. Thus, the improved axial strength of the GACE-A samples observed during thermal-shock testing may be attributable to the architecture of the GACE-A series.

The GACE sample exhibited film boiling similar to the GAOE samples as described in Section 7.2.1 above. However, whereas for the GAOE samples the quench front moved upwards, for the GACE samples the quench front moved downwards. Furthermore, film boiling for the GACE samples lasted approximately 30 seconds in comparison to the 10 second film boiling observed in the GAOE samples. The difference in both quench properties and film boiling duration is attributable to the presence of the endplug. Because of the density of the endplug and its central location away from the quench water, the endplug stored latent heat which was dissipated mostly by boiling on the surfaces of the tubing. Thus, the endplug was the hottest part of the sample during quenching and the endplug's latent heat prolonged film boiling. Furthermore, when the quench front reached the endplug, the latent heat of the endplug sustained nucleate boiling longer than for the open-ended samples: the quench front was observed to slow when it reached the endplug. The prolonged nucleate boiling in the endplug region possibly resulted in a more severe thermal gradient than that observed in the open-ended samples and weakened the joint.

7.2.3. Microstructural Analysis

Microstructural analysis of the thermal-shock samples was performed after mechanical testing to investigate the failure characteristics of the thermal-shock specimens. Analysis of the GAOE thermal-shock samples revealed similar post-testing characteristics as the as-received GAOE samples. Extensive matrix fragmentation and fiber pullout were observed, signifying that the thermal-shock specimens experienced pseudo-ductility and a gradual destruction of the matrix during testing. Figure 118 shows SEM views of the exposed fibers for the thermal-shock GAOE samples, and Figure 119 shows an SEM view of the fragmented matrix for the thermal-shock GAOE samples.

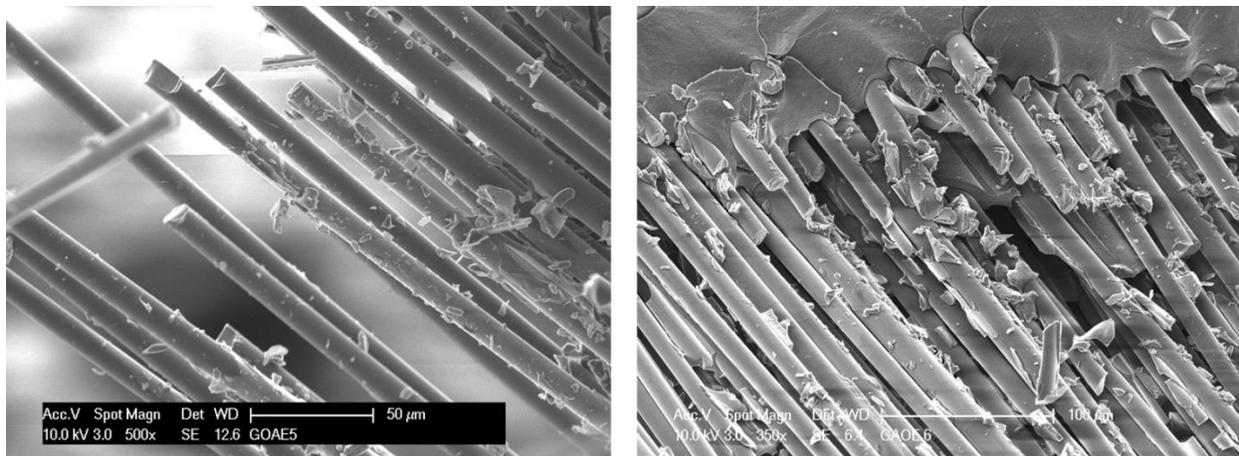


Figure 118: SEM views of failure location for GAOE 5 (left) and GAOE 6 (right) showing exposed fibers

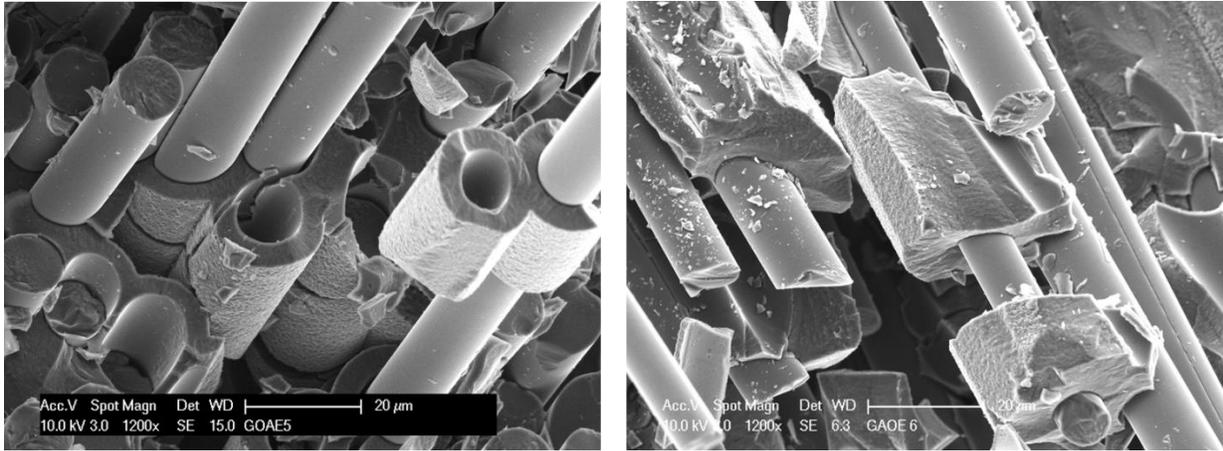


Figure 119: SEM views of failure location for GAOE 5 (left) and GAOE 6 (right) showing fragmented matrix

The failure location of the thermal-shock samples showed fiber pullout resulting in numerous exposed fibers spanning the failure location. Some fibers were observed to extend over 1 mm beyond the matrix, suggesting that the carbon interphase was effective at decoupling the matrix failure from the fiber failure. Because the thermal-shock post-testing failure microstructure was similar to the as-received failure microstructure, thermal-shock appears to have negligible impact on the microstructure of the samples. Figure 120 shows an SEM view of the failure location of GAOE 5 and Figure 121 shows a cross-sectional view of the failure location for GAOE 6. Both figures show fiber pullout resulting in naked fibers extending over 1 mm out of the matrix.

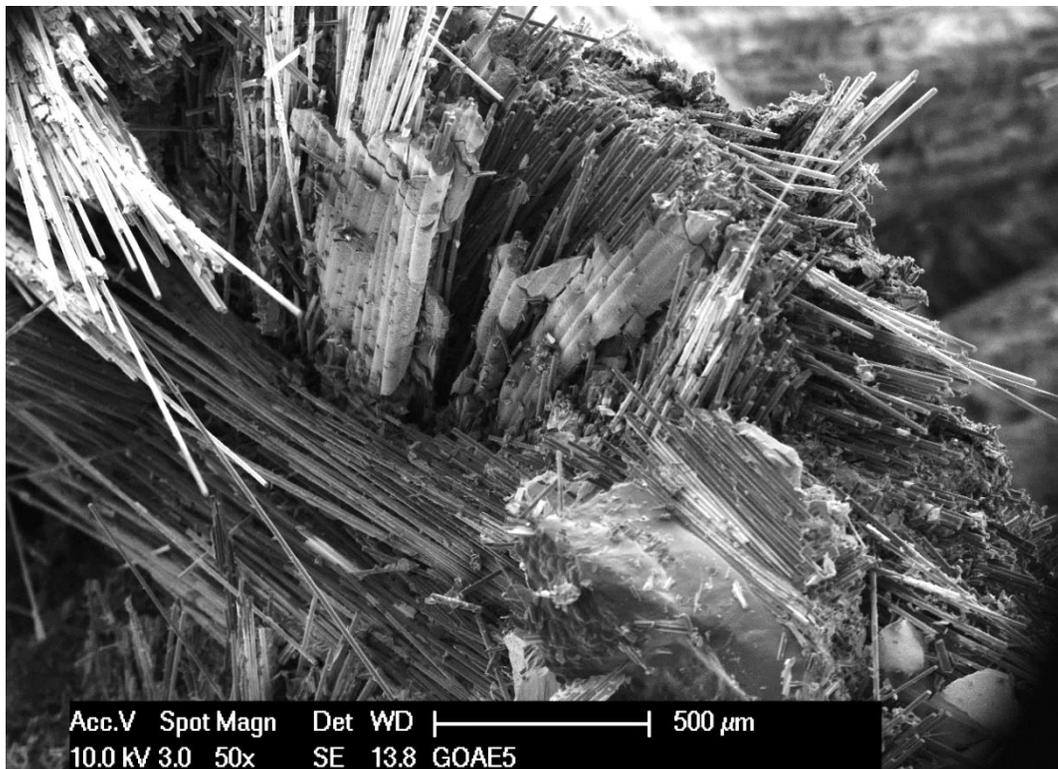


Figure 120: Lateral SEM view of failure location for GAOE 5

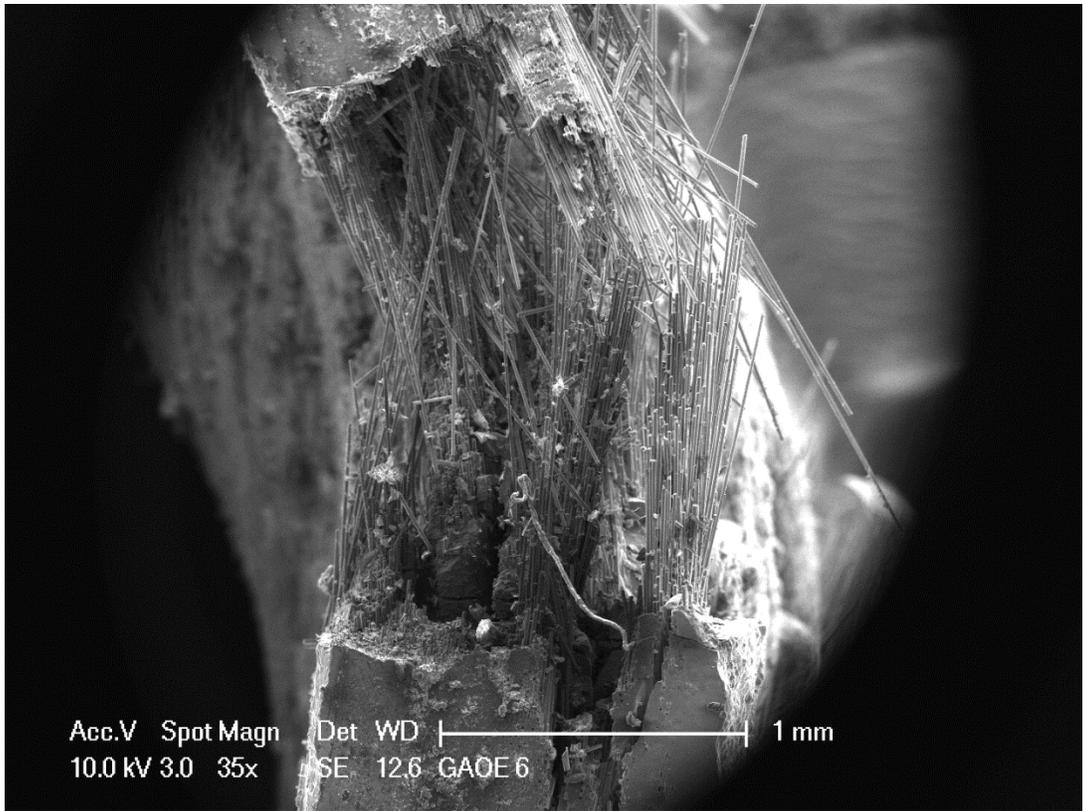


Figure 121: Cross-sectional SEM view of failure location for GAOE 6

Analysis of the failure location for the endplug joint revealed that the failure behavior for the thermal-shock samples was similar to the behavior of the as-received samples. Large voids in the joint were observed at the failure location, suggesting that the voids weakened the joint and precipitated the failure of the joint. Figure 122 and Figure 123 show cross-sectional SEM views of the endplug joint with voids observed in the joint material.

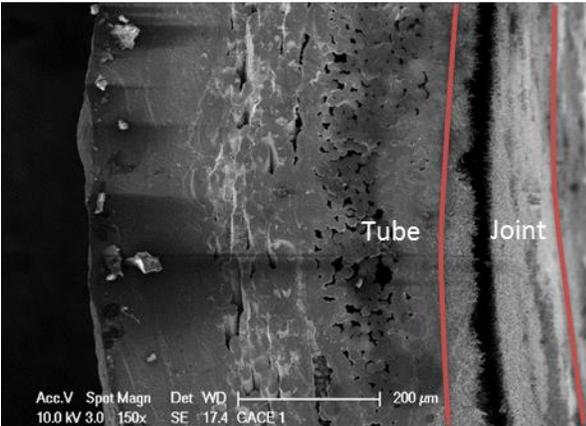


Figure 122: Cross-sectional SEM view of endplug joint for GACE 1 showing void

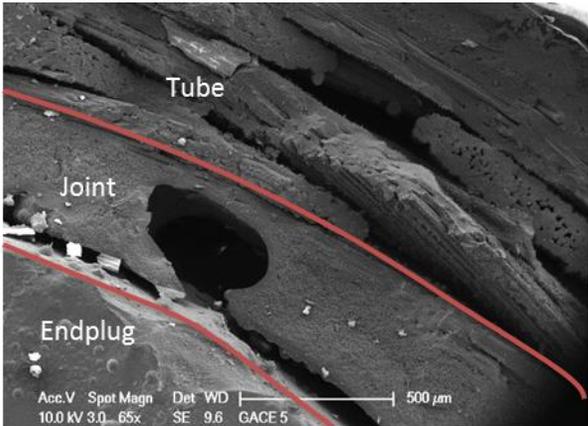


Figure 123: Cross-sectional SEM view of endplug joint for GACE 5 showing void

Analysis of the CMC region that remained attached to the endplug after pushout revealed that the CMC experienced no fiber pullout or matrix fragmentation prior to failure. This suggests that the CMC attached to the endplug did not experience pseudo-ductility before it separated from the main tube body. Figure 124 shows an SEM view of the CMC layer still attached to the endplug post-pushout. From the figure, it can be observed that there was no fiber pullout and the failure surface is smooth and the matrix is still intact.

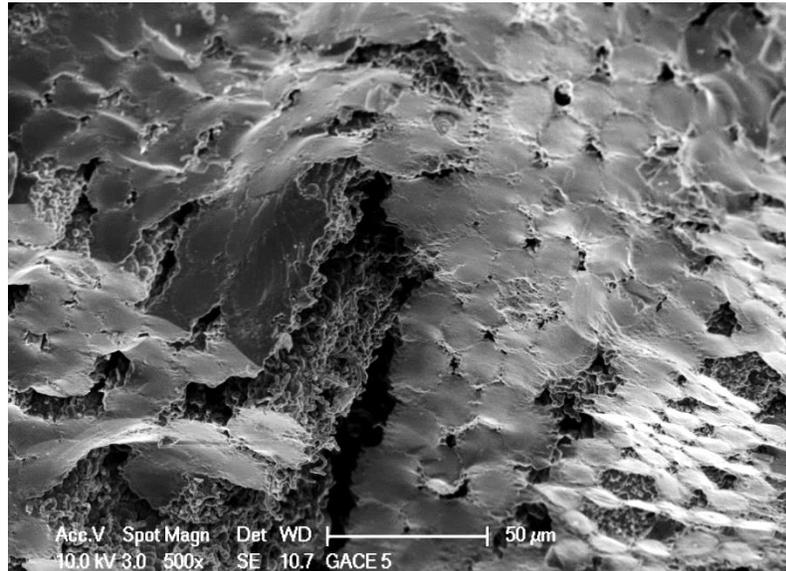


Figure 124: Cross-sectional SEM view of CMC remaining attached to endplug for GACE 5

7.3. Oxidation Discussion

The oxidation kinetics of the samples was analyzed by observing the weight change in the samples during oxidation. The weight change reflects the dominant oxidation mechanisms active during the high-temperature steam oxidation testing, and thus by analyzing the weight change the oxidation kinetics can be better understood. Furthermore, SEM analysis of the samples after oxidation was performed to observe the oxide behavior and locations of severe oxidation. Additionally, EDS analysis allowed for the determination of the elemental composition of the oxide.

7.3.1. Oxidation Microstructural Analysis

Ceramographic analysis of the oxidized samples was performed to investigate the oxidation mechanisms and penetration depth in the samples. Non-destructive investigation was performed on the samples' lateral and cross-sectional surfaces after oxidation to characterize the oxide structure. After mechanical testing, oxidized samples were destructively investigated to determine the oxidation penetration characteristics within the CMC layer. The destructive investigation consisted of sectioning the samples and performing SEM and EDS analysis to identify the presence of the oxide within the CMC voids.

The non-destructive investigation of the samples after oxidation revealed an oxide coating on the lateral surface of the sample which resulted in darkened surfaces exhibiting some thin-film interference patterning, as shown in Figure 125. SEM analysis of the oxide coating revealed numerous oxide

morphologies, including smooth, faceted, and textured oxide coatings. Additionally, some regions of the oxide coating were cracked.



Figure 125: Comparison of a GAOE sample before (left) and after (right) oxidation

SEM analysis of the oxidized lateral surfaces showed that the oxide coating often was smooth, and EDS analysis confirmed that the coating was composed of silica (SiO_2). The smooth coating observed in this work is similar to the oxide coatings observed in previous investigations (Opila, 1999). Opila's work used XRD analysis to show that the smooth silica coating observed in 1200°C oxidation was amorphous with slight cristobalite XRD peaks (Opila, 1999) although Opila observed that the amorphous oxide was not present for 1400° oxidation. Figure 125 shows a comparison of lateral views of a GAOE sample as-received and after oxidation. Table 31 presents the results for the EDS analysis of the post-oxidation view in Figure 126. The silica coating deadened the rough features of the EBC, resulting in a much smoother surface with fewer of the characteristic bumps observed in the as-received lateral surfaces.

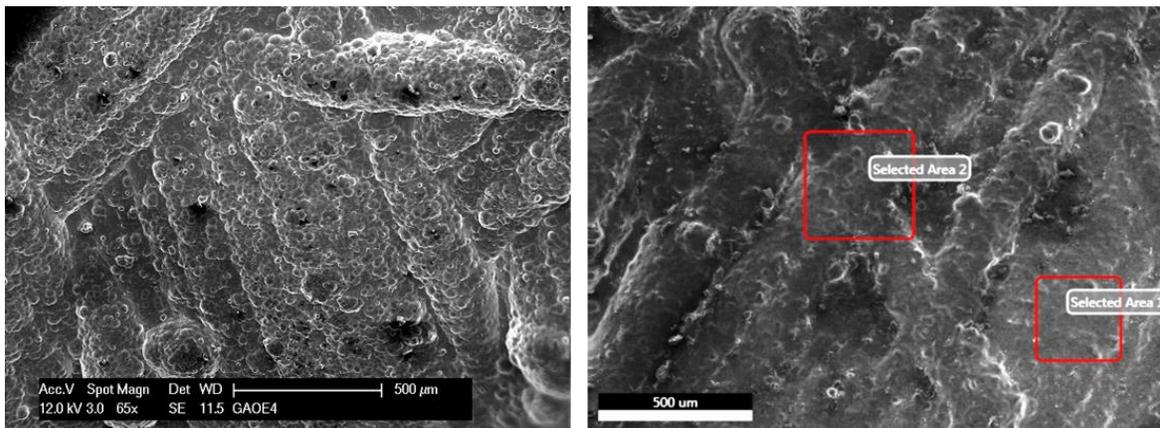


Figure 126: Lateral SEM view of GAOE 4 before (left) and after (right) oxidation

Table 31: EDS results for lateral view of GAOE 4

	Silicon		Carbon		Oxygen	
	Atom Percent	Error	Atom Percent	Error	Atom Percent	Error
Area 1	38 %	3 %	0 %	-	62 %	6 %
Area 2	29 %	3 %	20 %	12 %	51 %	7 %

Faceted, crystalline oxide morphology was also observed on the oxidized samples. In this morphology, the oxide assumed a blocky crystalline structure as shown in Figure 127. This morphology is likely similar to the crystalline oxide morphology observed for 1400°C oxidation in previous work, such as Opila (Opila, 1999) and Costello (Costello & Tressler, 1986). Figure 128 shows the crystalline structure Costello observed for 1400°C oxidation, which Costello presumed to be mullite. Opila observed that the crystalline oxide morphology was not present below 1300°C oxidation temperature (Opila, 1999). Oxidation diffusion through the crystalline silica phase is significantly slower than through the amorphous silica phase, signifying that the crystalline phase offers better protection to the underlying SiC (Costello & Tressler, 1986). EDS results of Figure 127 confirmed that the faceted structure was silica, as shown in Table 32.

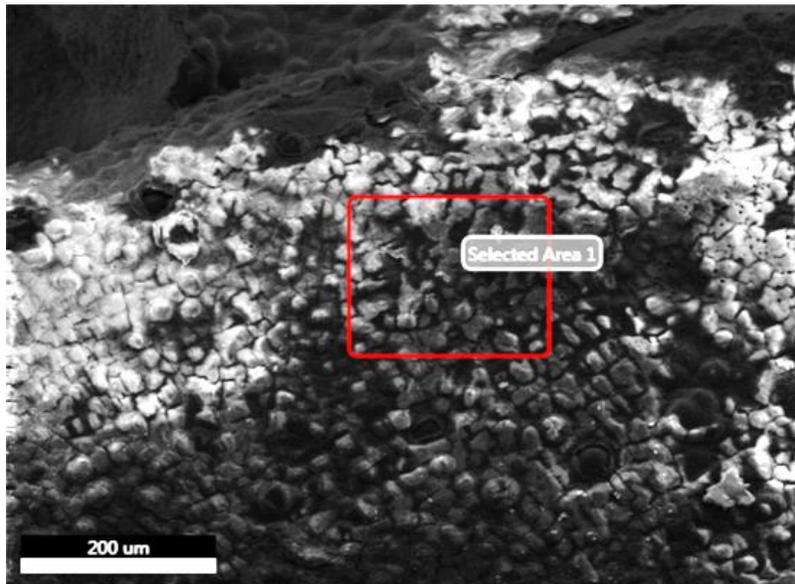


Figure 127: Cross-sectional SEM view of GACE 3 endplug showing faceted oxide morphology

Table 32: EDS results for cross-sectional view of GACE 3 endplug

	Silicon		Carbon		Oxygen	
	Atom Percent	Error	Atom Percent	Error	Atom Percent	Error
Area 1	30 %	4 %	0 %	-	70 %	6 %

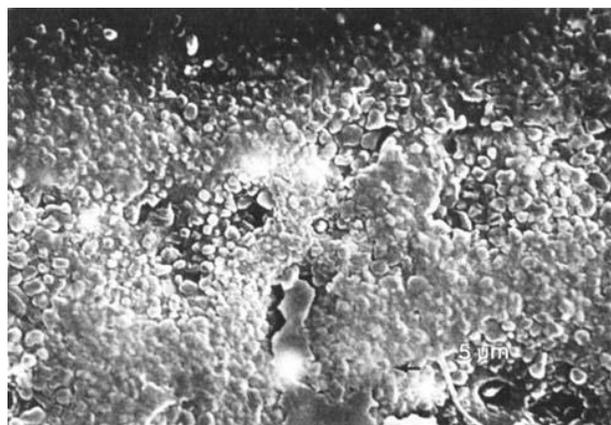


Figure 128: Crystalline silica morphology (Costello & Tressler, 1986)

The oxide coating was also observed to produce textured features on the surfaces of the samples that occurred alongside the smooth silica morphology. These texture regions are similar to the bubbly silica regions observed in previous work (Opila, 1999) although Opila noticed that the bubbles were not present for 1400°C oxidation. Opila observed that the bubble density increased with increasing H₂O concentration (Opila, 1999), corresponding well with this work which observed high bubble density using 100% H₂O. Figure 129 shows an SEM view of the smooth and textured morphologies, and Table 33 presents the EDS analysis of Figure 129 proving that the oxide in both the smooth and textured regions is silica (SiO₂). Figure 131 shows the smooth and textured silica morphologies occurring together. The texture of the silica was composed of chimney-like structures, as observed in Figure 129 and Figure 130.

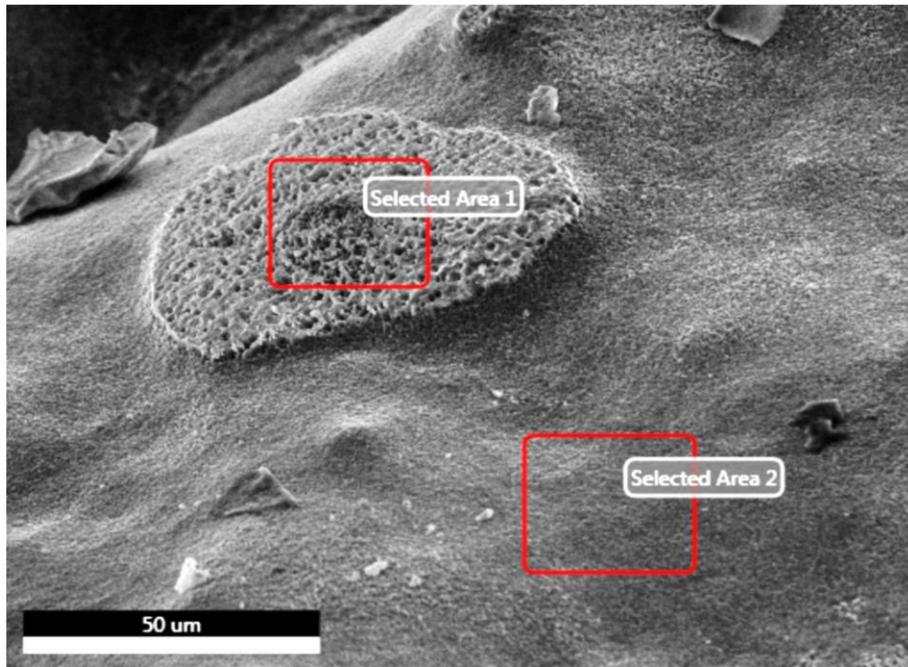


Figure 129: Lateral SEM view of GACE 4 endplug showing textured and smooth oxide

Table 33: EDS results for lateral view of GACE 4 endplug

	Silicon		Carbon		Oxygen	
	Atom Percent	Error	Atom Percent	Error	Atom Percent	Error
Area 1	40 %	4 %	0 %	-	60 %	7 %
Area 2	39 %	4 %	0 %	-	61 %	7 %

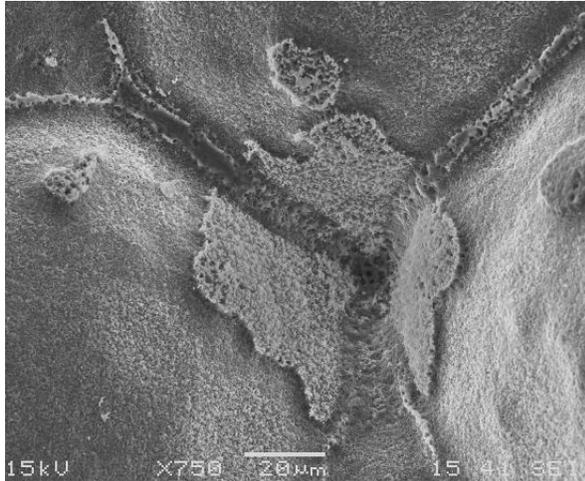


Figure 130: Lateral SEM view of GACE 3 showing textured oxide morphology

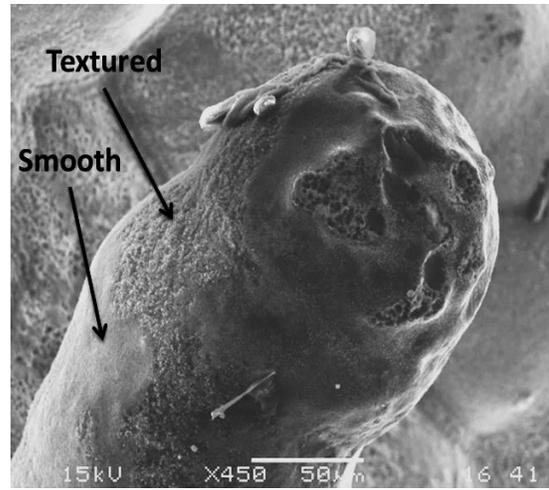


Figure 131: Lateral SEM view of GACE 3 showing smooth and textured oxide

Some lateral surfaces exhibited cracked oxide coatings, suggesting that the thermal-stresses resulting from cooling the sample to room temperature after high-temperature steam oxidation were severe enough to fracture the silica. A previous study found that cristobalite formations caused silica cracking due to thermal contraction (Clark, Prack, Haider, & Sawyer, 1987). Figure 132 and Figure 133 show how the oxide coating has a profusion of cracks on the lateral surface of GACE 4. Some surfaces exhibited such severe fragmentation of the silica that a plate-like structure was formed, with the plates delineated by cracks in the silica (Figure 134). The formation of the plate-structure also resulted in the detachment of some silica plates, thus exposing the underlying SiC. The plate behavior and plate detachment is shown in Figure 134, and the EDS analysis of the figure, shown in Table 34, proves that the plates are silica while the underlying material is SiC.

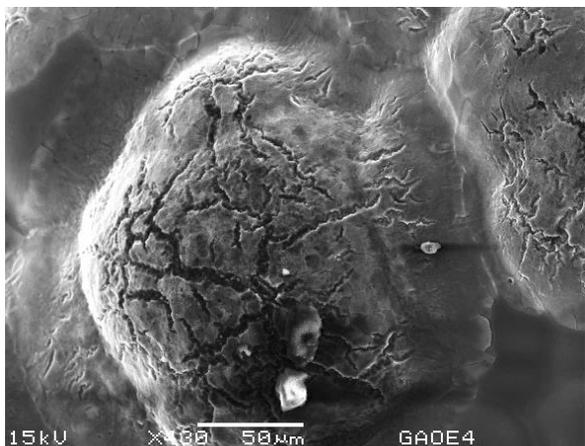


Figure 132: Lateral SEM view of GACE 4 showing cracked oxide coating

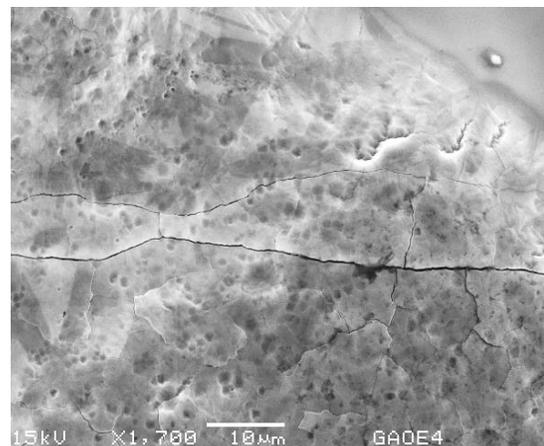


Figure 133: Lateral SEM view of endplug for GACE 4 showing cracks in silica

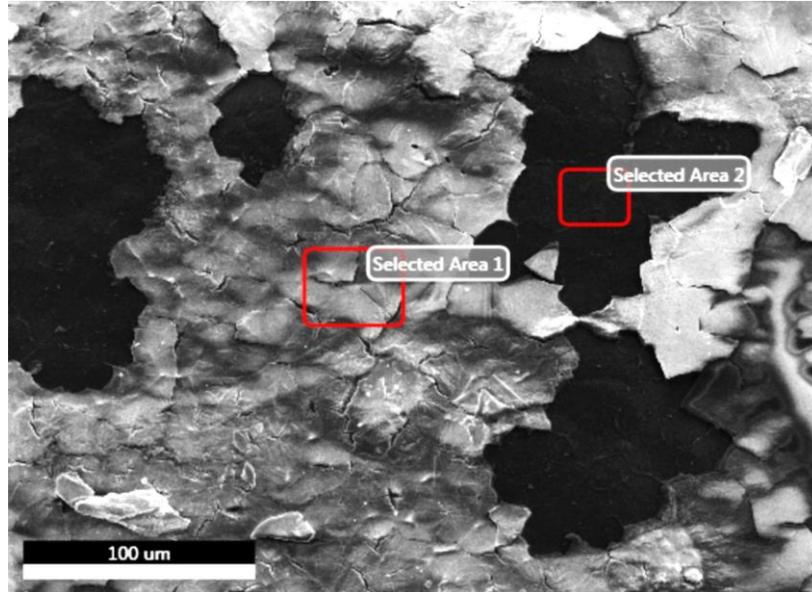


Figure 134: Lateral SEM view of GACE 4 endplug showing silica plate structure

Table 34: EDS results for lateral view of GACE 4 endplug plate structure

	Silicon		Carbon		Oxygen	
	Atom Percent	Error	Atom Percent	Error	Atom Percent	Error
Area 1	35 %	4 %	7 %	22 %	58 %	7 %
Area 2	50 %	3 %	45 %	14 %	5 %	16 %

SEM analysis of the cross-sectional views of the samples revealed the presence of oxide in the CMC voids. Although EDS was unable to be performed on some views due to the recessed location of the oxide in the voids, the morphology of the oxide was similar to the silica morphology observed on the lateral surfaces, and therefore the oxide in the voids was likely silica. Figure 135 shows SEM views of the oxide formation in the CMC voids on the cross-sectional surfaces of the GAOE samples.

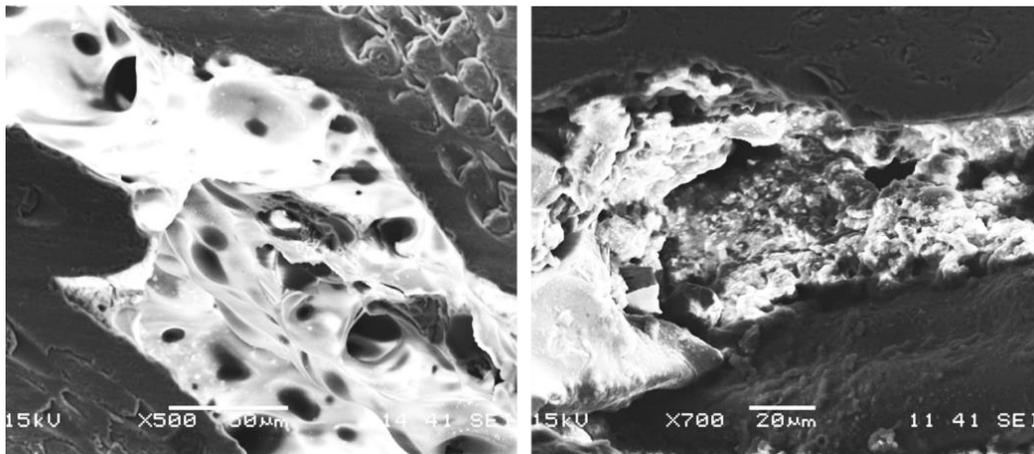


Figure 135: Cross-sectional SEM views of oxidized GAOE 3 (left) and GAOE 4 (right) showing oxide formation in CMC voids

After mechanical testing, destructive investigation on sample GAOE 1 was performed, whereby the sample was sectioned and the oxidation penetration behavior was analyzed. Interior CMC voids several millimeters from the cut surfaces were investigated and silica was observed to fill the voids, as shown in Figure 136 and the corresponding EDS results presented in Table 35.

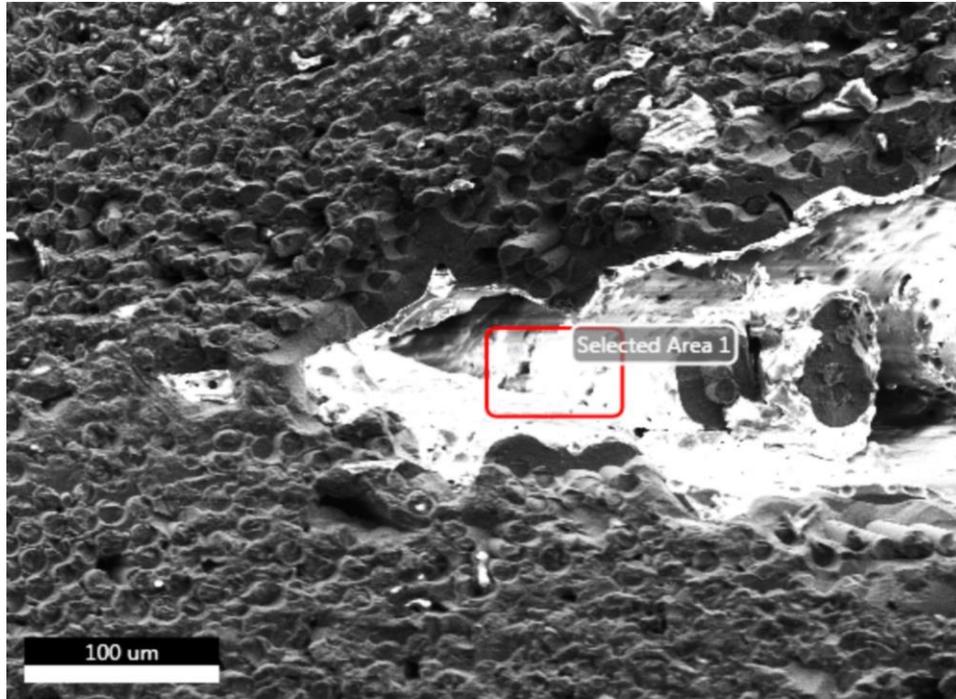


Figure 136: SEM view of silica formation filling GAOE 1 interior CMC void

Table 35: EDS results for GAOE 1 oxidized interior void

	Silicon		Carbon		Oxygen	
	Atom Percent	Error	Atom Percent	Error	Atom Percent	Error
Area 1	19 %	4 %	35 %	12 %	46 %	8 %

Analysis was performed to characterize the oxidation penetration into the SiC. EDS analysis was performed on sectioned surfaces exposing interior CMC voids, and it was discovered that the oxidation has negligible penetration through the SiC and only results in oxide deposits on the exposed surfaces. Figure 137 shows an SEM view of an oxidized interior void in GAOE 1, and the corresponding EDS analysis in Table 36 shows that there was no oxidation penetration into the SiC surrounding the void. Instead, the oxidation was localized to the void itself and did not affect the surrounding CMC.

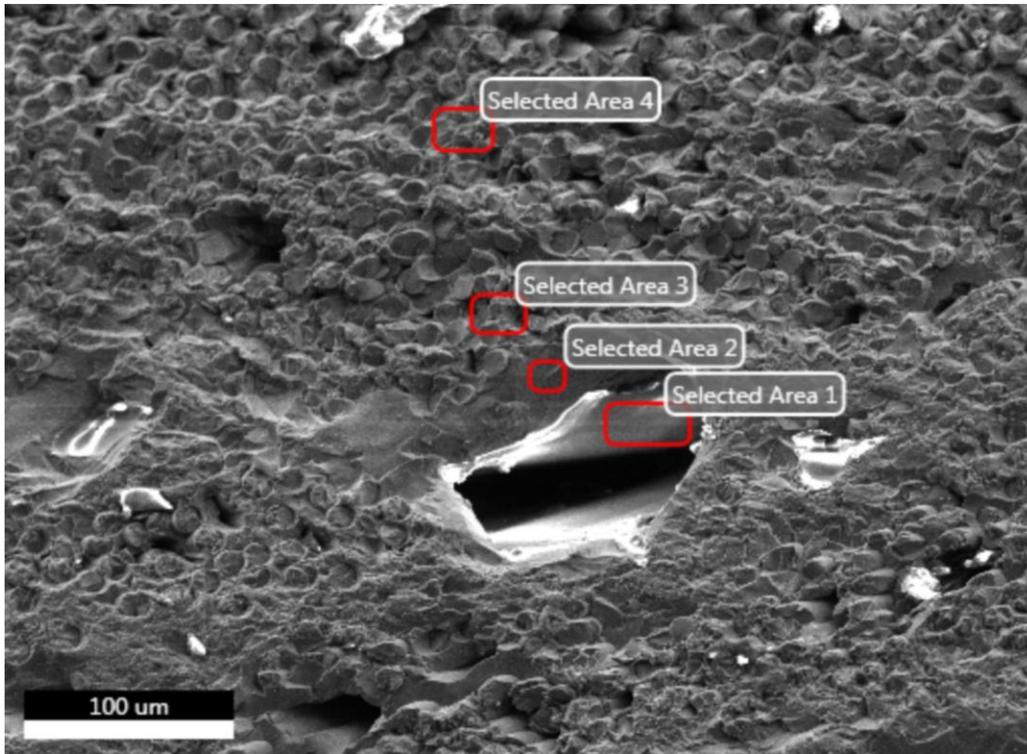


Figure 137: SEM view investigating oxidation penetration at GAOE 1 interior CMC void

Table 36: EDS results for oxidation penetration behavior in GAOE 1

	Silicon		Carbon		Oxygen	
	Atom Percent	Error	Atom Percent	Error	Atom Percent	Error
Area 1	20 %	9 %	36 %	23 %	44 %	13 %
Area 2	53 %	2 %	47 %	12 %	0 %	-
Area 3	40 %	3 %	60 %	11 %	0 %	-
Area 4	41 %	2 %	59 %	11 %	0 %	-

Sample GAOE 1 was sectioned axially and the cut face was analyzed to evaluate the oxidation penetration from the voids into the surrounding SiC. The analysis revealed that the oxidation did not penetrate radially into the SiC and was localized at the CMC voids. Figure 138 shows the results of the EDS investigation into oxidation penetration, revealing that the oxidation remained localized to the surfaces of the interior voids and did not penetrate radially into the surrounding SiC.

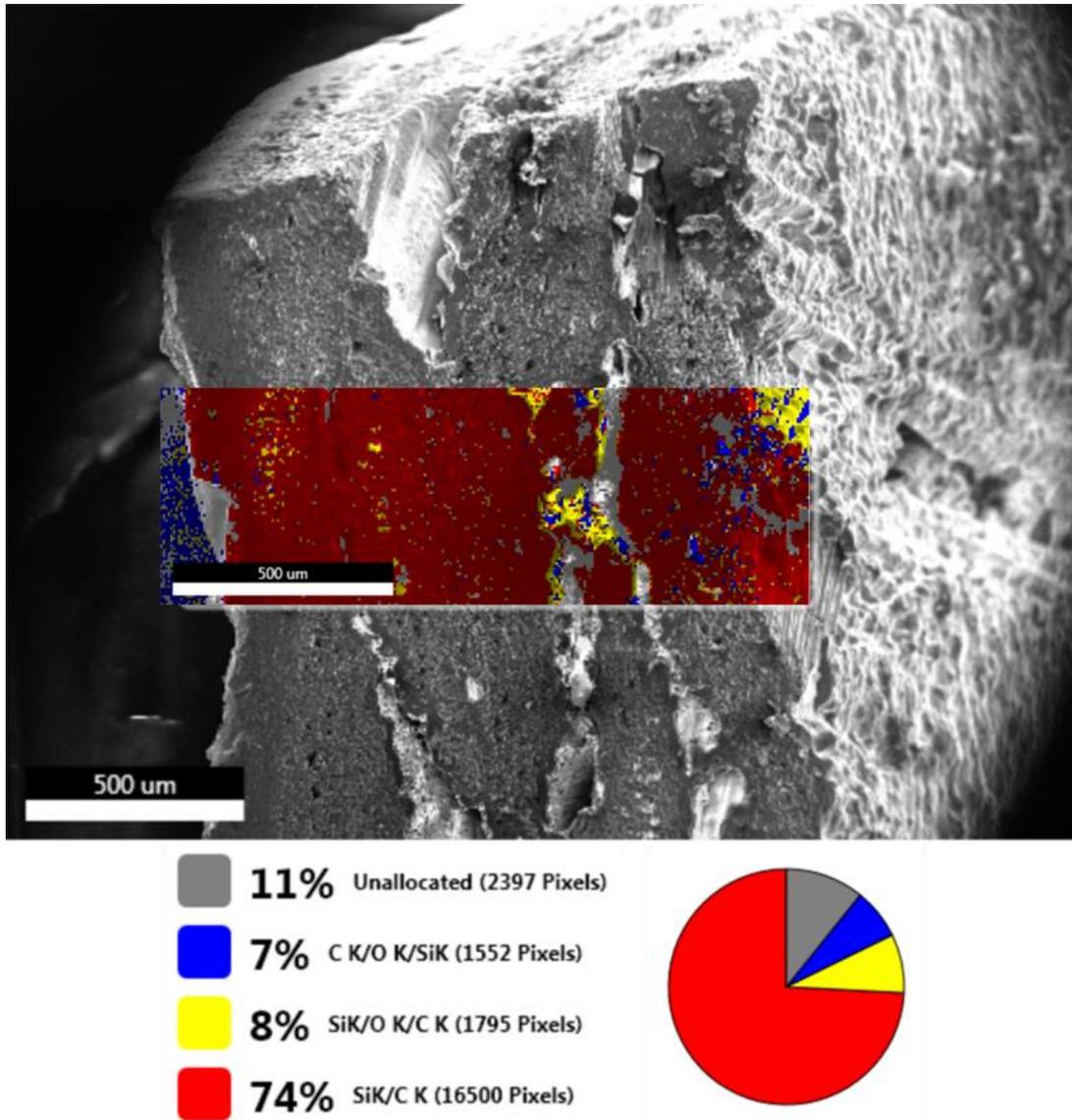


Figure 138: EDS analysis of GAOE 1 oxidation penetration from CMC voids into surrounding SiC

Overall, the SEM and EDS analysis of the oxidized samples revealed that the oxidation was a superficial phenomenon, with oxidation occurring only on the surfaces of the sample exposed to the high-temperature steam. The oxidation was able to fully axially penetrate the interior of the CMC via the void network. Silica was observed coating the interior CMC voids throughout the sample. Although the oxidation was able to penetrate axially into the CMC, the oxidation was unable to penetrate radially into the sample. The SiC surrounding the oxidized voids was not oxidized and showed no traces of Oxygen.

Previous studies have shown that oxidation can also attack the interior of the CMC by oxidizing the interphase between the fibers and the matrix. Such oxidation would bind the fibers with the matrix and prevent fiber pullout, resulting in the embrittlement of the CMC. The microstructural analysis performed in this work did not focus on the interphase, and so it is unknown to what extent the carbon interphase was oxidized for the samples investigated in this work.

7.3.2. Hoop Test

The stress-strain behavior observed for the oxidized samples was different from that of the as-received samples, suggesting that the oxidation significantly impacts the mechanical properties of the samples. As discussed in Section 7.3.1, the oxidation was not observed to penetrate significantly into the SiC and instead remained on the exposed surfaces of the samples. However, the oxidation was able to penetrate axially into the CMC region via the void network. Therefore, the accumulation of silica on the exterior surfaces of the sample and in the inner voids of the CMC is likely responsible for the observed degradation in mechanical properties. It is unknown to what extent the carbon interphase was oxidized for the samples investigated in this work.

Previous work has shown that high-temperature steam oxidation of SiC can weaken the SiC through the introduction of surface-based defects (Moorhead, 1989). Thus, despite the lack of observed oxidation penetration into the mSiC of the CMC, it is nevertheless possible that the silica weakened the mSiC through the introduction of the surface defects on the CMC void surfaces. Such defects could form a basis for a potential crack network between the CMC voids, whereby the cracks could more easily travel between tows, from one void-based surface defect to another. Such cracking behavior could result in more dramatic tow reordering because the cracks allow for easier liberation of tows from one another. Thus, when the yield point is achieved the inter-tow matrix of the oxidized samples fragments more dramatically and results in looser tows than in the as-received sample. Furthermore, the intra-tow matrix could be weakened by the surface defects and would result in inferior pseudo-ductility.

The oxidation weakening mechanics outlined above are supported by the stress-strain behavior observed in the samples. The stress-strain behavior of the 24 hour oxidized sample GAOE 1 shows a much larger jump in strain immediately after yielding when compared to the as-received sample. The 24 hour oxidized sample strain jumps almost 1000 microstrain upon yielding compared to the jump of about 500 microstrain for the as-received sample. Because these jumps in strain correspond to the inter-tow matrix fragmentation regime (as discussed in Section 7.1.1), the larger jump experienced by the 24 hour oxidized sample suggests more severe inter-tow matrix cracking when compared to the as-received sample. However, the stress-strain behavior for GAOE 1 also suggests that the intra-tow matrix is weakened by the 24 hour oxidation because the pseudo-ductile slope of GAOE 1 is shallower than that of the as-received sample. The pseudo-ductile slope is determined by the rate of matrix fragmentation versus stress: a weaker matrix cracks more easily and therefore an incremental increase in stress results in more strain due to more matrix cracking. Overall, the stress-strain behavior for GAOE 1 suggests that both the inter-tow and the intra-tow matrix are weakened by the 24 hour oxidation.

Figure 139 shows a stress-strain comparison of the 24 hour oxidized sample and the as-received sample, showing the stress-strain regimes important for the analysis of oxidation results. Specifically, the figure illustrates the pseudo-ductile slopes and the inter-tow matrix fragmentation strain jumps. Both properties are affected by the silica in the CMC voids and ultimately determine the post-oxidation mechanical behavior.

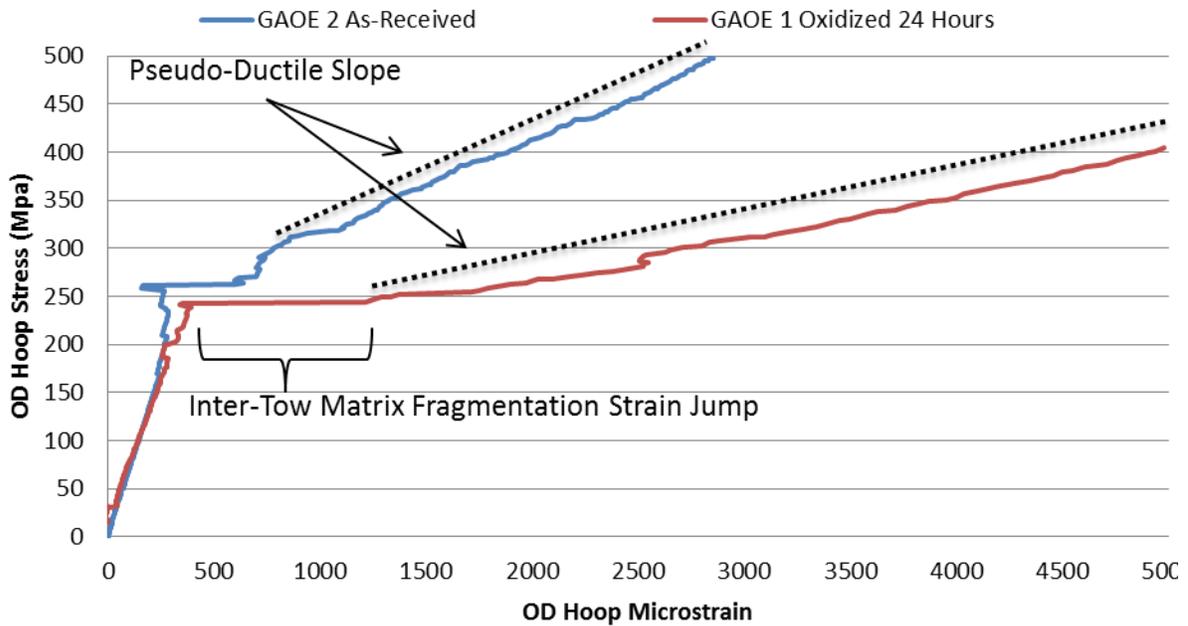


Figure 139: Illustration of stress-strain regimes important for oxidation behavior

The 48 hour samples did not exhibit any pseudo-ductility and instead failed in a brittle non-frangible manner upon nearing the yield point observed in the as-received sample. The lack of any pseudo-ductility observed in the 48 hour oxidized samples is likely attributable to the advanced weakening of the inter-tow and intra-two matrix. As discussed for the 24 hour oxidation sample, the oxidation likely weakens the inter-tow matrix and results in larger inter-tow matrix fragmentation strain jumps. Additionally, the oxidation likely weakens the intra-tow matrix and results in a shallower pseudo-ductile slope. Therefore, with sufficient oxidation time, it is possible that either the pseudo-ductile slope will approach zero, or the inter-tow matrix fragmentation strain jump will become too large for the sample to handle. In either case, as soon as the yield point is achieved the sample would fail in a brittle manner with no observed pseudo-ductility. Such behavior is the likely reason why the 48 hour oxidized samples failed with no pseudo-ductility. Figure 140 shows an illustration of the possible evolution of brittle failure for oxidized samples. In the figure, a combination of a larger inter-matrix fragmentation strain jump and near-zero pseudo-ductile slope result in the apparent brittle failure of GAOE 4. The dashed line in the figure represents what the pseudo-ductile regime for GAOE 4 might look like: because the regime is near-horizontal, the sample essentially fails immediately upon yielding.

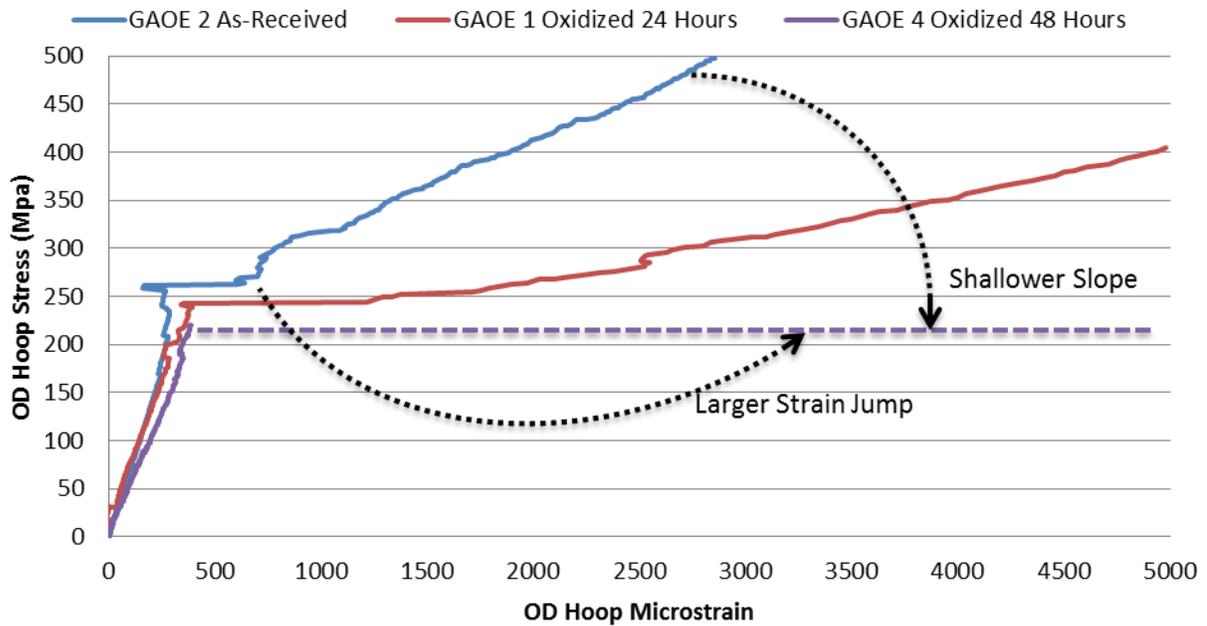


Figure 140: Illustration of evolution of brittle failure for oxidized samples

7.3.3. Joint Test

The results of the joint strength testing for the GACE-A series indicated little mechanical degradation due to the oxidation. The oxidized sample exhibited burst strength in excess of 30 MPa, showing a 9% reduction in burst strength when compared to the as-received sample. The results of the void analysis in Section 5.4 suggest that the GACE 3 endplug joint was likely of similar strength to the joint for GACE 2. The joints exhibited similar void fractions, joint widths, and joint heights. Figure 141 shows a comparison between the XCT images of the joints for the oxidized and as-received samples, showing similar joint properties. Because of the similar joints for GACE 2 and GACE 3, the joint strength difference between the two samples is likely attributable to the high-temperature steam oxidation.

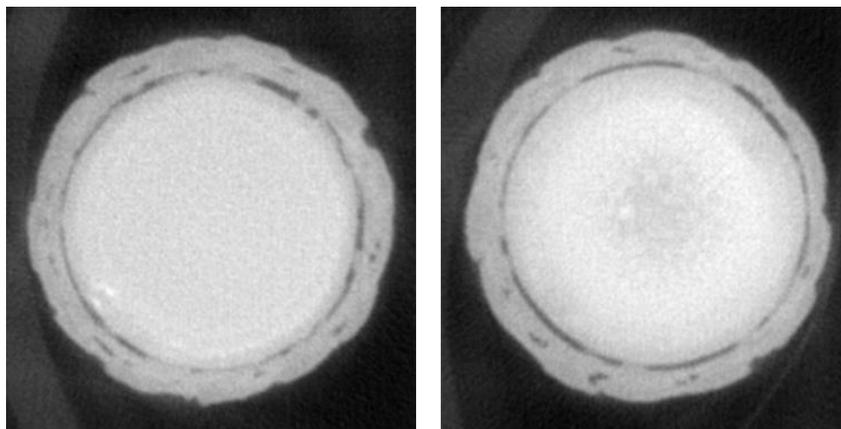


Figure 141: Comparison of XCT images for GACE 3 (left) and GACE 2 (right)

The results of the joint strength testing for the GACE-B series indicated significant mechanical degradation due to the oxidation. The oxidized sample exhibited burst strength of 22 MPa, showing a 32% reduction in strength when compared to the as-received sample. The results of the void analysis in

Section 5.4 suggest that the endplug joint for the oxidized sample was likely stronger than the joint for the as-received sample, showing a smaller void fractions and joint width. The joint for sample GACE 4 had a void fraction of 9% compared to the GACE 6 void fraction of 18%. Furthermore, the joint for GACE 4 had an average width of 300 μm in comparison to the GACE 6 joint width of 350 μm . Figure 142 shows a comparison of XCT images for GACE 4 and GACE 6 showing the slightly wider and more porous joint of GACE 6. Overall, because the oxidized sample exhibited a similar or superior joint to the control sample but nonetheless had degraded mechanical performance, the high-temperature steam oxidation appears to significantly degrade the mechanical performance of the GACE-B endplug joint.

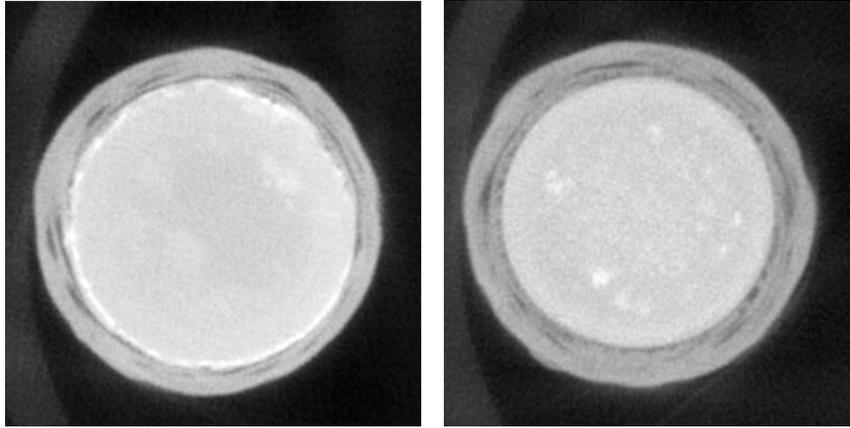


Figure 142: Comparison of XCT images for GACE 4 (left) and GACE 6 (right)

As discussed in Section 6.3.5.2, failure of the endplug for the GACE-B series occurred within the CMC layer whereas failure for the GACE-A series occurred within the joint region. Because of the different failure mechanisms between the two samples, the CMC of the GACE-B series was likely weakened by the oxidation more than the CMC of the GACE-A series, resulting in CMC failure for the GACE-B series.

The difference observed in the effect of oxidation among the two GACE series is likely attributable to the different architectures of the samples. As discussed in Section 7.2.2, because the GACE-A tows were more axially inclined, the CMC structure was likely stronger in the axial direction when compared to the GACE-B series. Thus, the improved axial strength of the GACE-A CMC observed during oxidation testing may be partly attributable to the architecture of the GACE-A series. However, the different void structure between the two series also likely influenced the effect of oxidation between the two GACE series. As discussed in Section 5.3, the GACE-B series has a higher void fraction in the CMC when compared to the GACE-A series. Therefore, the enhanced oxidation pathways within the CMC of the GACE-B series probably allowed for improved diffusion of the high-temperature steam throughout the CMC region. Therefore, the higher void fraction of the GACE-B series likely facilitated faster oxidation of the CMC when compared to the GACE-A series and weakened the CMC more substantially.

This conclusion is supported by SEM and EDS analysis of the failure location for the oxidized GACE samples. Figure 143 shows SEM post-pushout views of the CMC region for both GACE 3 and GACE 4 samples. In the figure, it can be observed that the CMC voids of GACE 4 are severely oxidized (identifiable as the white coating on the void surfaces) whereas the GACE 3 voids have little noticeable

oxidation. The figure suggests that the CMC of GACE 4 was weakened by the oxidation more than the CMC of GACE 3, resulting in the low burst strength for the post-oxidized GACE 4. Furthermore, SEM and EDS analysis of the lateral view of the endplug post-pushout for GACE 4 revealed that the CMC still attached to the endplug was severely oxidized. Figure 144 shows a view of the fibers still attached to the endplug post-pushout, and Table 37 shows the corresponding EDS analysis revealing that the fibers were coated in silica (SiO_2).

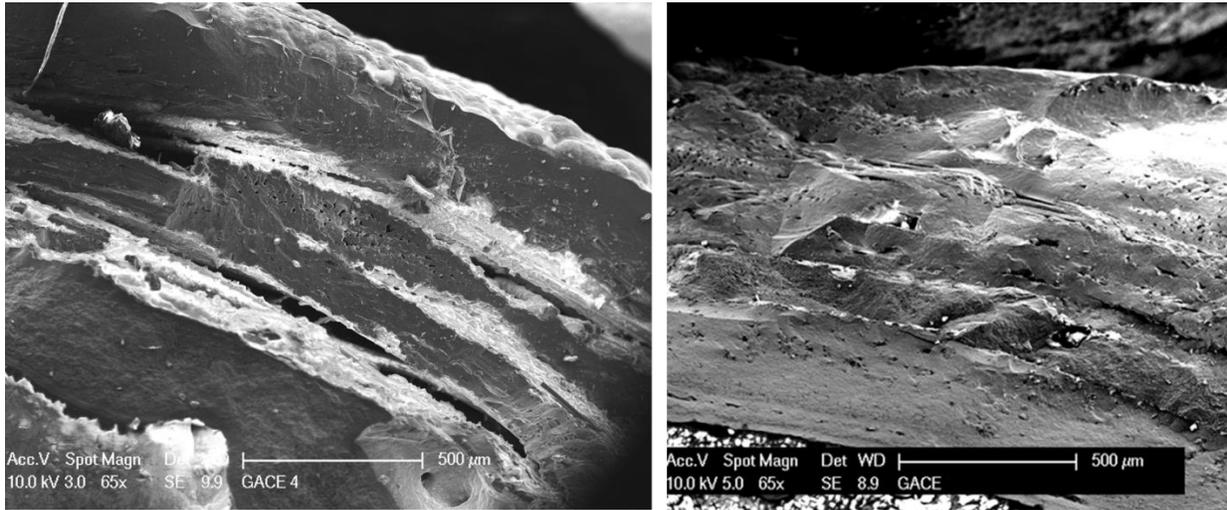


Figure 143: Cross-sectional post-pushout SEM views of GACE 4 (left) and GACE 3 (right)

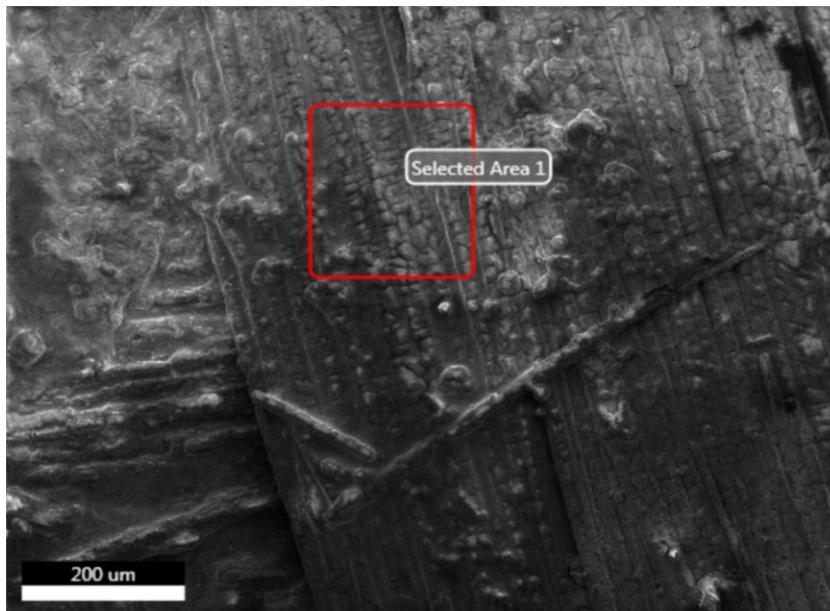


Figure 144: Lateral SEM view of endplug joint region post-pushout for GACE 4

Table 37: EDS results for lateral post-pushout GACE 4 endplug

	Silicon		Carbon		Oxygen	
	Atom Percent	Error	Atom Percent	Error	Atom Percent	Error
Area 1	33 %	4 %	7 %	27 %	60 %	7 %

Overall, the different effects of the high-temperature steam oxidation on the two GACE series are attributable to the different architectures of the two series. The GACE-A series was a three-tow design, with a smaller interlace angle and an axial tow, whereas the GACE-B series was a two-tow design with a higher interlace angle. Because of the different weave patterns, the GACE-A series inherently has higher axial strength than the GACE-B series. Furthermore, because the GACE-B series has a higher CMC void fraction than the GACE-A series, oxidation within the CMC region was enhanced, resulting in more severe weakening of the GACE-B CMC region. Due to the weakening of the CMC, the failure of the endplug for the GACE-B series was accompanied by failure within the CMC (as evidenced by the remains of CMC on the endplug post-pushout), whereas the failure of the endplug for the GACE-A series had far less CMC failure.

7.3.4. Microstructural Analysis

Microstructural analysis of the oxidized samples was performed after mechanical testing to investigate the failure characteristics of the oxidized specimens. Analysis of the GAOE 48 hour oxidized samples revealed different failure characteristics from the as-received GAOE samples. For the 48 hour oxidized samples, very little matrix fragmentation and fiber pullout was observed, supporting the observation that no pseudo-ductility occurred with the 48 hour oxidized samples. Figure 145 shows SEM views of the failure location for the 48 hour oxidized samples, showing far less fiber pullout when compared to the as-received failure in Figure 107. Additionally, the figure demonstrates that the failure crack was far smaller than the crack observed in the as-received samples. Figure 146 shows SEM cross-sectional SEM views of the failure location revealing almost no fiber pullout when compared to the as-received failure in Figure 106.

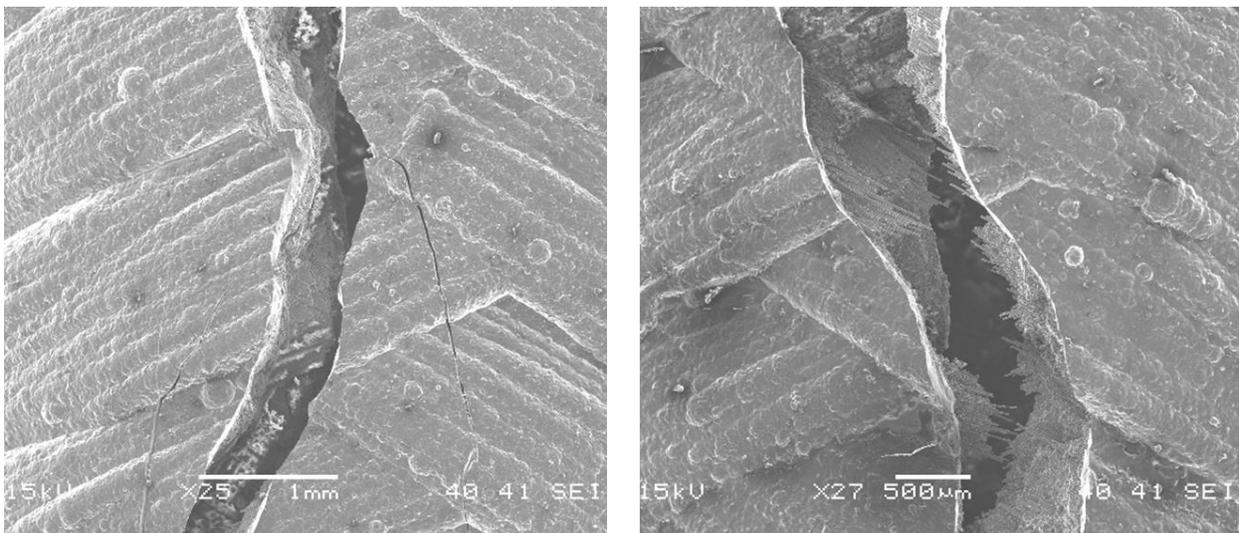


Figure 145: Lateral SEM view of failure location for GAOE 3 (left) and GAOE 4 (right)

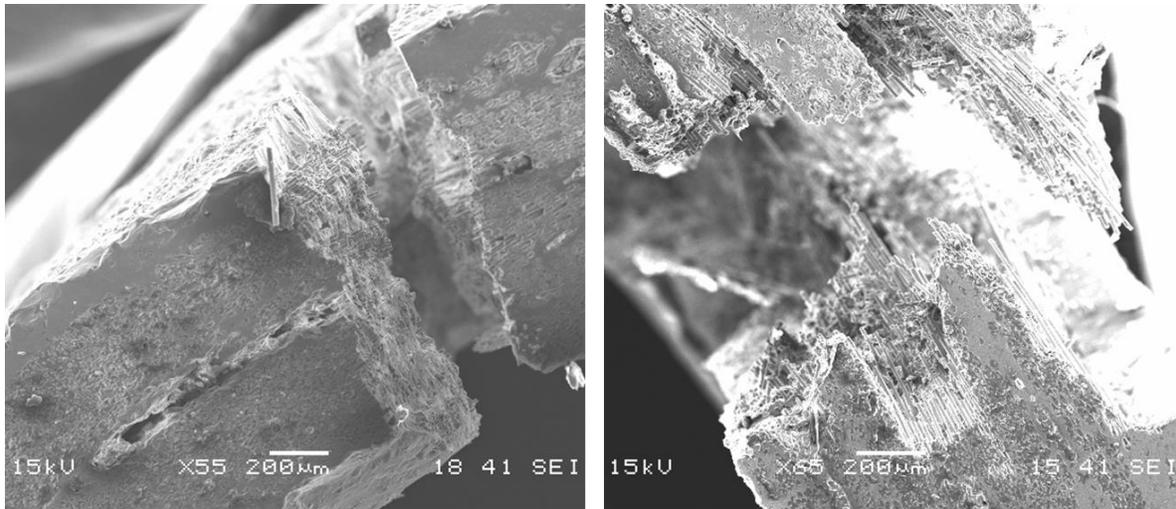


Figure 146: Cross-sectional SEM view of failure location for GAOE 3 (left) and GAOE 4 (right)

Sample GAOE 4 exhibited more fiber pullout than GAOE 3 although both samples failed in a brittle non-frangible fashion. Figure 147 shows an SEM view of GAOE 4 displaying some fiber pullout in the failure location. Although some fiber pullout was observed for GAOE 4, the sample nevertheless exhibited no pseudo-ductility.

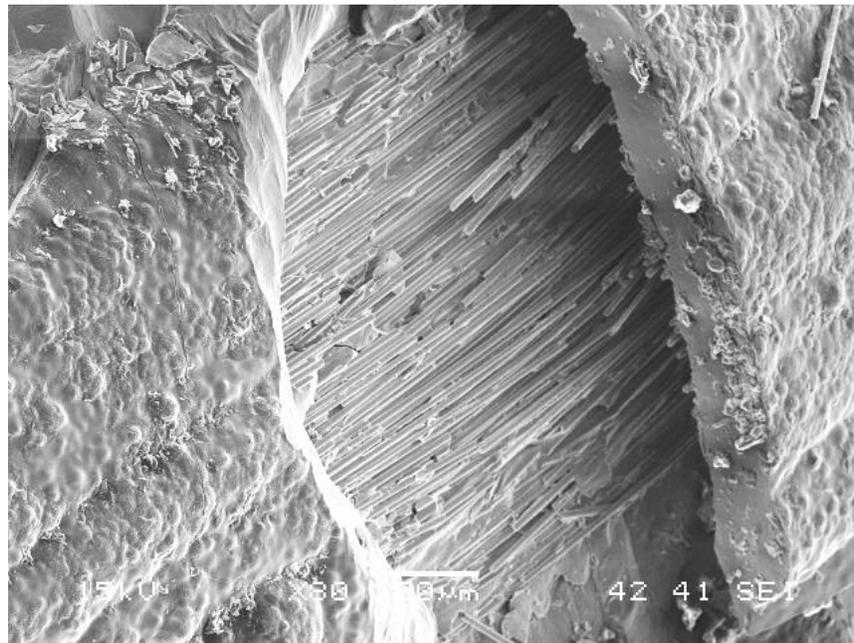


Figure 147: Lateral SEM view of fiber pullout observed in GAOE 4

Analysis of the failure location for the 24 hour oxidized sample revealed similar failure characteristics to the as-received sample. The 24 hour oxidized sample exhibited substantial fiber pullout and matrix fragmentation. The failure characteristics for the 24 hour oxidized sample were expected to be similar to the as-received sample because it exhibited pseudo-ductility and the stress-strain behavior displayed all the regimes observed in the as-received behavior. Figure 148 shows the fiber pullout observed in the failure location for the 24 hour oxidized sample.

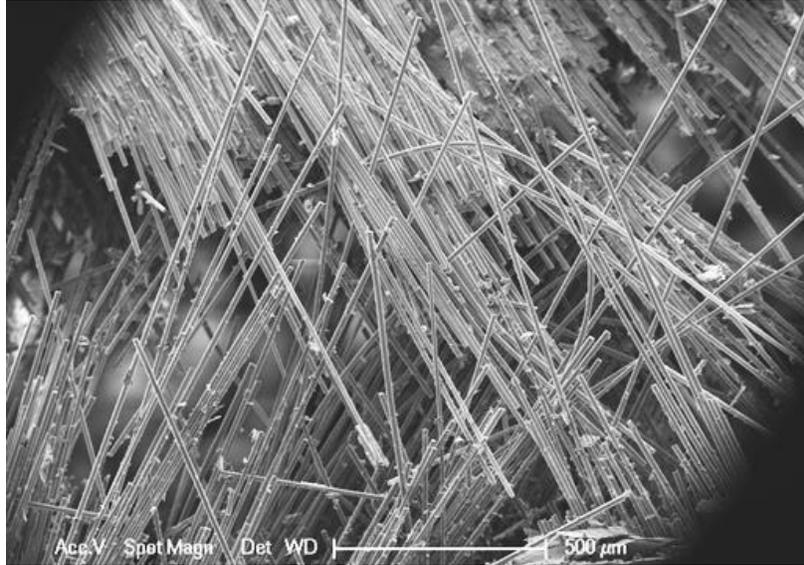


Figure 148: Lateral SEM view of failure location for GAOE 1

SEM analysis of the failure location for the GACE samples revealed that the joint and the CMC were oxidized. Silica was observed on the upper surface of the endplug (Figure 149 and Table 38), within the joint voids (Figure 150 and Table 39), and in the CMC voids in the joint region (Figure 143). The EDS results of the endplug joint oxidation in Figure 150 revealed no oxidation penetration from the joint voids into the CMC. Rather, the CMC oxidation in Figure 143 likely occurred due to penetration of the high-temperature steam through the CMC void network as discussed in Section 7.2.3. The presence of the silica in the joint voids and endplug surfaces indicates that the high-temperature steam entered the sample through the open-end and oxidized the joint from within, as shown in the left half of Figure 149.

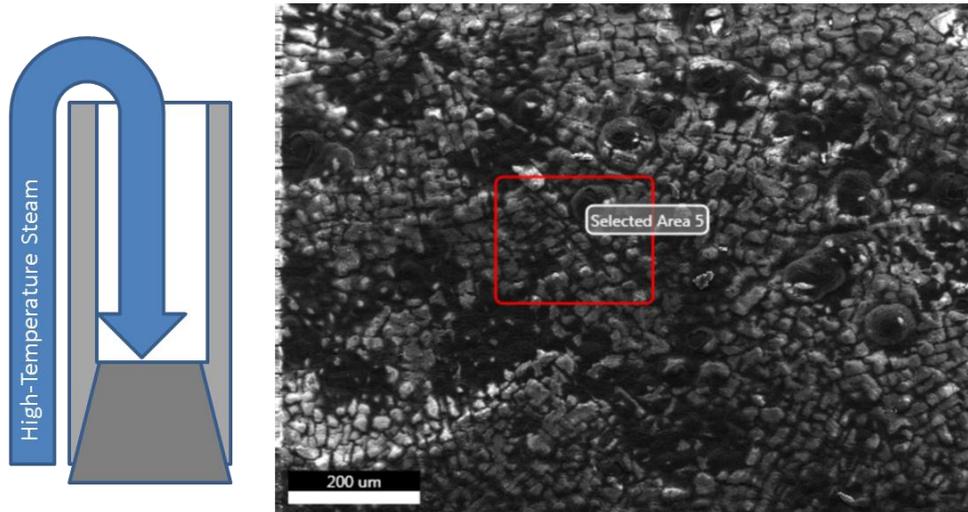


Figure 149: Steam flow path (left) and SEM view of top surface of GACE 3 endplug (right)

Table 38: EDS results for cross-sectional view of top surface of GACE 3 endplug

	Silicon		Carbon		Oxygen	
	Atom Percent	Error	Atom Percent	Error	Atom Percent	Error
Area 5	27 %	4 %	0 %	-	73 %	6 %

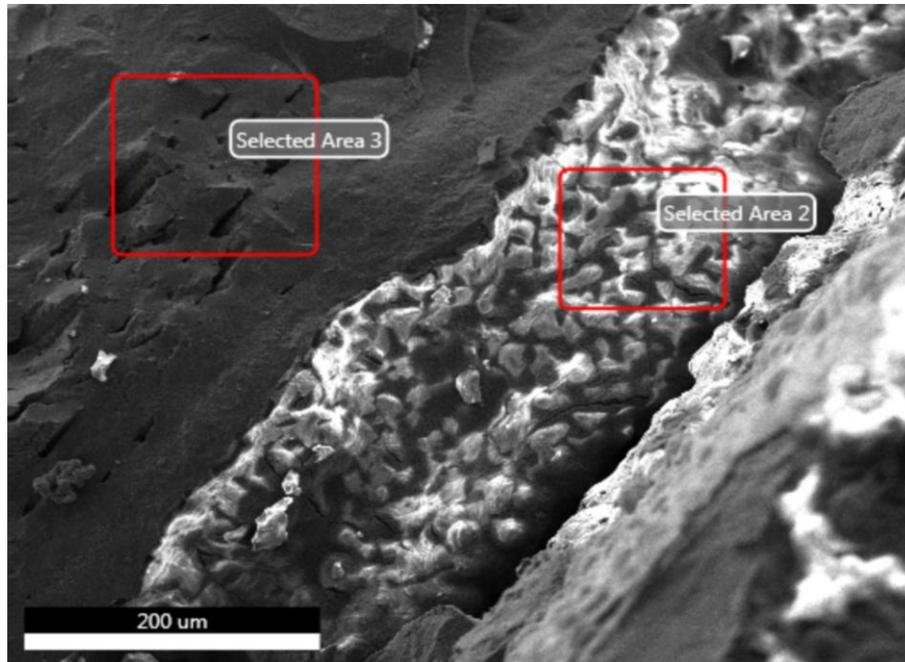


Figure 150: Cross-sectional SEM view of endplug joint (Area 2) and CMC (Area 3) for GACE 3

Table 39: EDS results for view of endplug joint and CMC for GACE 3

	Silicon		Carbon		Oxygen	
	Atom Percent	Error	Atom Percent	Error	Atom Percent	Error
Area 1	71 %	6 %	0 %	-	29 %	4 %
Area 2	47 %	3 %	53 %	11 %	0 %	-

The thorough oxidation of the CMC resulted in CMC axial failure during strength testing of GACE 4. This is supported by the previous analysis of Figure 144, which demonstrates that the lateral surface of the GACE 4 post-pushout endplug was coated in heavily oxidized CMC remains. Although the lateral surface of the post-pushout GACE 3 endplug did not display CMC remains similar to those observed on GACE 4, it nevertheless had a silica coating on the lapped surface of the endplug joint. Figure 151 shows an SEM view of the lateral lapped surface of the endplug joint region, and Table 40 shows the results of EDS analysis, indicating that the surface is coated in silica (SiO_2). In the figure, silica is observed in both areas despite the observed discoloration.

View of Lapped Surface

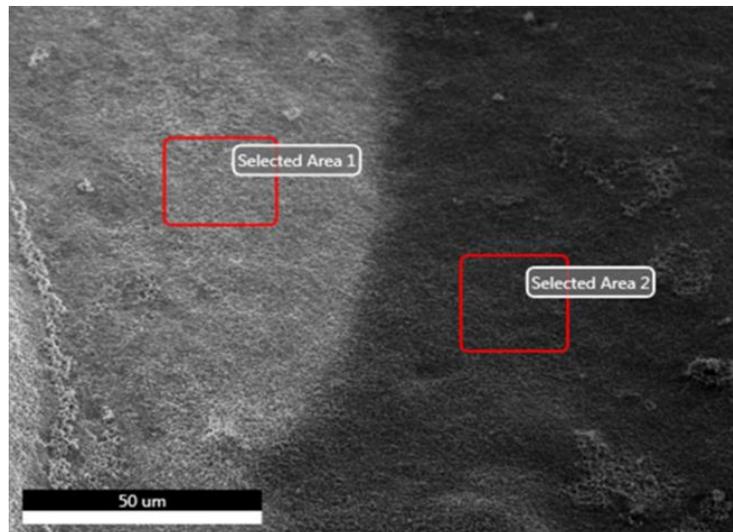
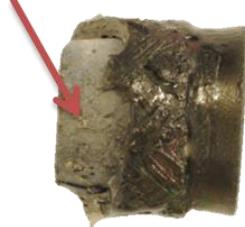


Figure 151: Lateral SEM view of endplug lapped surface for GACE 3

Table 40: EDS results for endplug lapped surface of GACE 3

	Silicon		Carbon		Oxygen	
	Atom Percent	Error	Atom Percent	Error	Atom Percent	Error
Area 1	37 %	5 %	0 %	-	63 %	7 %
Area 2	36 %	4 %	0 %	-	64 %	7 %

Overall, microstructural analysis revealed that the oxidation was not limited to the exterior surfaces of the samples, and instead was able to penetrate through the CMC void networks and oxidized the interior of the CMC. The high-temperature steam was able to enter the void network through the cut surfaces of the open-ends of the samples. The close-ended samples also revealed that the high-temperature steam was able to penetrate into the endplug joint region through the endplug joint void network and oxidized the surface of the endplug joint.

Failure of the 48 hour oxidized samples was brittle and non-frangible. Fiber pullout was not observed and the failure location was far less opened than in the as-received samples. In contrast, the 24 hour oxidized sample exhibited significant fiber pullout and matrix fragmentation, displaying failure characteristics similar to those observed in the as-received sample.

Although the steam was able to penetrate axially through void networks, it was unable to deeply penetrate from the voids into the surrounding SiC. Therefore, oxidation was observed to be a surface-based phenomenon with little penetration into the bulk material. SEM and EDS analysis showed that oxidation was unable to penetrate from CMC voids into surrounding matrix, and similarly was unable to penetrate from endplug joint voids into surrounding CMC. Nevertheless, oxidation of the exterior surfaces and the internal voids resulted in significant mechanical degradation of the samples, leading to brittle non-frangible behavior for the tubing and reduced burst strength for the endplug.

8. Conclusions and Recommendations for Future Work

8.1. Summary of Results

Table 41 presents the results of the testing for all samples and Figure 152 shows a graphical comparison of the burst pressures for all samples. It can be observed that the tubing has a burst pressure approximately double that of the endplug joint. Furthermore, it can be observed that the oxidation has a significant impact on the strength of the tubing but a minimal impact on the strength of the endplug joint. Finally, although thermal-shock had a negligible impact on the GAOE and GACE-A series burst pressures, it caused a severe reduction in burst pressure for the GACE-B series.

Table 41: Summary of results for all samples

	Sample	Test	Tubing Burst Pressure	Endplug Burst Pressure	Failure Stress	Failure Strain	
GAOE	GAOE 1	Oxidation, 24 Hours	71 MPa	-	475 MPa	0.498 %	
	GAOE 2	As-Received	83 MPa	-	581 MPa	0.285 %	
	GAOE 3	Oxidation, 48 Hours	30 MPa	-	203 MPa	0.029 %	
	GAOE 4	Oxidation, 48 Hours	39 MPa	-	262 MPa	0.038 %	
	GAOE 5	Thermal-Shock, 100°C	86 MPa	-	572 MPa	0.297 %	
	GAOE 6	Thermal-Shock, 90°C	73 MPa	-	492 MPa	0.195 %	
GACE-A	GACE 1	Thermal-Shock, 100°C	-	34.2 MPa	-	-	
	GACE 2	As-Received	-	37.1 MPa	-	-	
	GACE 3	Oxidation, 48 Hours	-	33.7 MPa	-	-	
GACE-B	GACE 4	Oxidation, 48 Hours	-	22 MPa	-	-	
	GACE 5	Thermal-Shock, 100°C	-	7.2 MPa	-	-	
	GACE 6	As-Received	-	32.3 MPa	-	-	
	GACE 7	No Testing					
	GACE 8	Thermal-Shock, 100°C	-	14 MPa	-	-	

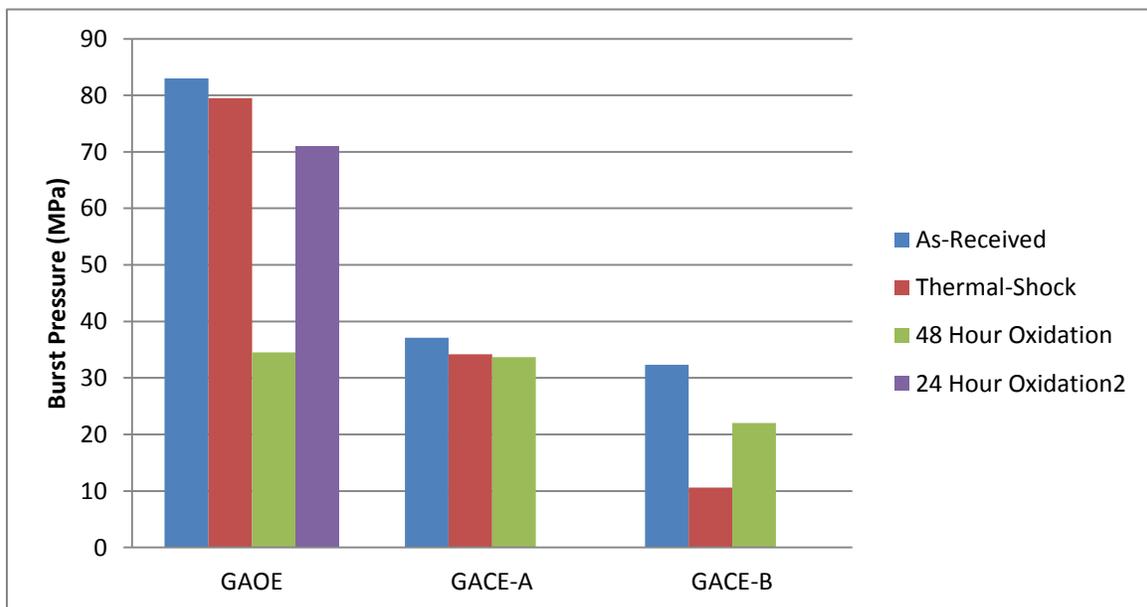


Figure 152: Comparison of results for all samples

The measured burst strength of the GACE endplug joints was also compared to the approximated relative strengths of the endplug joints, as discussed in Section 5.5. The comparison is presented in Figure 153 and shows that, although the predicted joint strength accurately anticipated a lower joint strength for GACE 8 (with a low joint length) and GACE 5 (with a very high void fraction), the predictions were not very accurate for GACE 2 and GACE 6 (with void fractions of approximately 18%). This suggests that the joint void fraction may not have a significant influence on joint strength in the 10%-20% range, but void fraction has a significant impact in the 30% range (as seen with GACE 5).

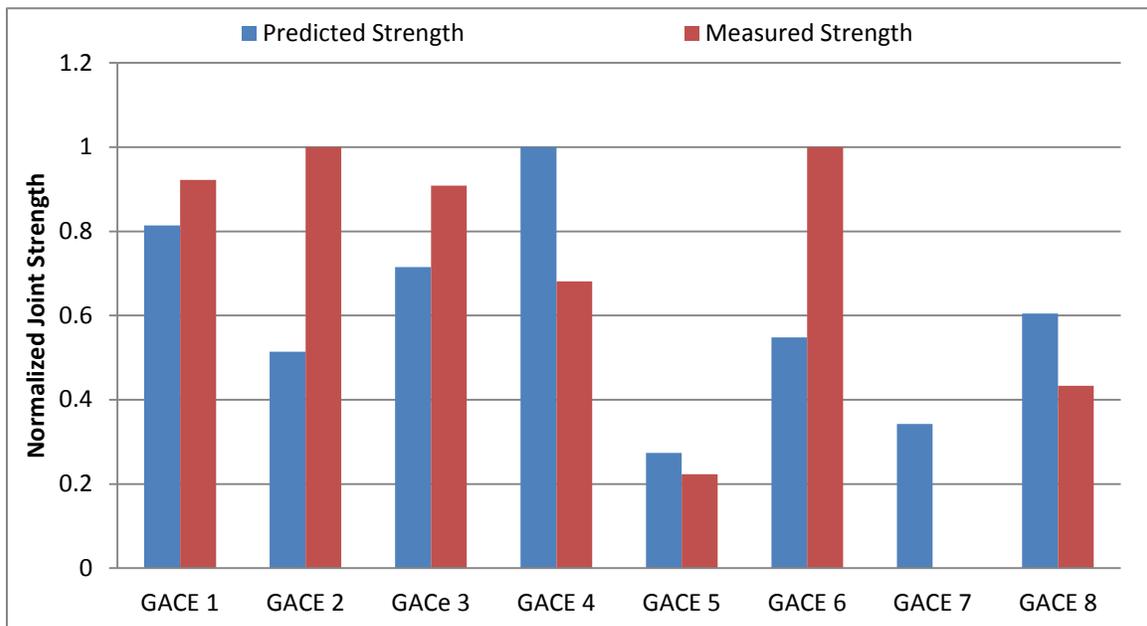


Figure 153: Comparison of approximated and measured joint strengths for GACE samples

8.2. Conclusions of As-Received Testing

Testing of the as-received GAOE sample revealed that the tube is able to withstand internal pressures far in excess of what is typical for normal reactor conditions. The maximum internal pressure that the as-received tubing can handle was 83 MPa and the maximum hoop stress was 581 MPa. This indicates that the as-received tubing can safely withstand the typical EOL plenum pressure of 15.5 MPa (Khalifa H. E., Deck, Gutierrez, Jacobsen, & Back, 2015). Furthermore, the as-received tubing exhibited pseudo-ductility, resulting in a failure strain of approximately 0.3%.

Failure of the as-received GAOE sample was non-frangible and was characterized by the partial opening of the sample. The failure crack did not span the entire axial distance of the sample and was dissipated into the weave contours of the CMC. The localized failure permitted much of the tubing to remain intact and preserved a coolable geometry for the fuel. After sample failure, extensive fiber pullout and matrix fragmentation was observed. The failure characteristics observed in the as-received sample indicate that the matrix fragmented prior to failure of the fibers and suggests that the carbon interphase was effective at decoupling the matrix failure from the fiber failure.

XCT analysis performed on all GAOE samples as-received indicated a CMC macro-void fraction of 4% with an average void height of 0.7 mm. Similar analysis performed on the GACE-A samples as-received

indicated a CMC macro-void fraction of 2% with an average void height of 0.8 mm. However, the exact CMC void fraction is influenced by the voids smaller than the 50.3 μm XCT resolution. The analysis for the GACE-B series revealed that the GACE-B architecture had the highest void fraction and the tallest voids, with an average void fraction of 9% and an average void height of 1.5 mm. Typical CMC macro-voids for all architectures were approximately 100-300 μm wide. Overall, the sample architecture appeared to correlate with the void fraction: a higher interlace angle resulted in a higher void fraction. However, analysis of the dependence of void height on sample architecture was less conclusive. Analysis aimed at quantifying the porosity of the non-void regions of CMC revealed that those regions are near 100% theoretical density. The sensitivity of the algorithm used to measure the porosity of the non-void regions disallowed for the determination of a precise porosity, but the porosity of the non-void CMC regions was determined to be less than 5% for the three samples analyzed.

Table 42 presents a summary of the as-received data obtained for the tube section of the cladding for all series. Because strength testing of the tubing for the GACE samples was not performed, the tube burst pressure and failure stress for as-received GACE-A and GACE-B are not known.

Table 42: Summary of as-received properties for all series

Series	Architecture	Interlace Angle	Tube Burst Pressure	Tube Failure Stress	CMC Average Void Fraction	CMC Average Void Height
GAOE	Two-Tow	120°	83 MPa	581 MPa	4.1 %	0.7 mm
GACE-A	Three-Tow	100°	Not Measured	Not Measured	2.3 %	0.8 mm
GACE-B	Two-Tow	150°	Not Measured	Not Measured	8.8 %	1.5 mm

Testing of the as-received GACE endplugs showed that the endplug joint fails at a lower internal pressure than the tubing of the GAOE series: the internal pressure at failure for the GACE-A and GACE-B series were 37.1 MPa and 32.3 MPa respectively. The increased burst strength of the GACE-A series may be attributable to the CMC architecture: with a three-tow design and a lower interlace angle, the GACE-A series CMC is axially stronger than the two-tow high interlace design of the GACE-B series. However, variance in the as-manufactured joint strengths may also be partly responsible for the higher burst strength of the as-received GACE-A sample.

XCT analysis performed on the GACE endplug joints revealed significant variance among the endplug joints between the GACE samples. The joint void fraction ranged from 9% to 34%, the endplug joint thickness ranged from roughly 200 μm to 400 μm , and the endplug joint heights ranged from 7.8 mm to 10.6 mm. However, the majority of endplug joints exhibited a void fraction of about 15%, a joint thickness of about 350 μm , and a joint height of about 10 mm. Because of the variance in joint properties among the different samples, the as-received endplug joint strengths would be expected to vary considerably. Indeed, because the endplug joints for samples GACE 5 and GACE 7 were determined to be of exceptionally poor quality when compared to the other endplug joints, were those samples tested as-received they would likely experience burst pressures significantly lower than those obtained during the testing of GACE 2 and GACE 6. Thus, the XCT analysis strongly suggests that there is significant variance in the as-received endplug burst strengths among the samples, and the endplug joint porosity correlated well with the inferior burst strength of several samples (such as for GACE 5).

Table 43 presents the results of the analysis of the GACE endplug joints. In the table, the endplug burst pressure reflects the performance of GACE 2 (A) and GACE 6 (B). However, the joint void fraction, width, and height are values determined by XCT analysis of all samples within the architecture.

Table 43: As-received GACE endplug joint properties

Series	Endplug Burst Pressure	Joint Void Fraction	Joint Width	Joint Height
GACE-A	37.1 MPa	12-19 %	250-350 μm	10.0-10.5 mm
GACE-B	32.3 MPa	9-34 %	250-400 μm	7.8-10.6 mm

8.3. Conclusions of Thermal-Shock Testing

Testing of the post-thermal-shock GAOE tubing revealed that the tube is resistant to quenching from 1200°C into atmospheric-pressure water at 90°C and 100°C. The maximum internal pressure for post-quench GAOE 5 was 86 MPa corresponding to a maximum hoop stress of 572 MPa. The maximum pressure and stress for post-quench GAOE 4 was 73 MPa and 492 MPa respectively. Furthermore, the post-thermal-shock tubing exhibited pseudo-ductility resulting in a failure strain of approximately 0.3%. Because failure pressure and stress-strain behavior was very similar between the as-received and post-thermal-shock tubing, the thermal-shock appears to have limited impact on the performance of the GAOE tubing. Table 44 presents the results for the thermal-shock testing of the GAOE series.

Failure of the post-quench GAOE tubing was very similar to the failure of the as-received tubing, characterized by non-frangible failure accompanied by the partial opening of the sample. The failure crack did not span the entire axial distance of the tube and was instead dissipated into the weave contours of the CMC. The localized failure allowed much of the tubing to remain intact and preserved a coolable geometry for the fuel. Similar microstructural failure characteristics were observed in the post-quench samples as were observed in the as-received samples, including fiber pullout and matrix fragmentation. These observations suggest that the thermal-shock had limited effect on the microstructure of the samples; during testing the microstructural evolution of the post-quench samples was similar to that of the as-received samples.

Testing of the post-thermal-shock endplug joints showed different behavior between the GACE-A and GACE-B series. The burst-pressures for GACE 1 (A), GACE 5 (B), and GACE 8 (B) post-thermal-shock samples were 34.2 MPa, 14 MPa, and 7.2 MPa respectively. Whereas the GACE-A series proved to be resistant to thermal-shock with a negligible decrease in burst strength for the thermal-shock sample, the GACE-B thermal-shock samples showed severely degraded performance when compared to the as-received GACE-B sample. The GACE-A thermal-shock sample showed an 8% decrease in burst strength after thermal-shock, the GACE-B thermal-shock samples GACE 5 and GACE 8 showed a 77% and a 57% reduction in burst strength respectively. XCT analysis of the endplug joint for GACE 5 revealed the highest void fraction of all GACE samples at 34%, suggesting that the joint for that sample was inherently weaker than the joint of the other samples. Similarly, XCT analysis of the endplug joint for GACE 8 revealed a joint length of 7.8 mm, much shorter than the 10 mm joints observed in the other GACE samples. Therefore, the low burst strength observed for both GACE-B thermal-shock samples is

attributable to the combination of thermal-shock and inferior joint. Table 44 presents the results for the thermal-shock testing of the GACE series.

Given the inferior joints of the thermal-shock GACE-B samples, this work cannot determine whether the thermal-shock influences the mechanical strength of the endplug joints for the GACE-B series. However, the thermal-shock behavior for the GACE-B series could be different from that of the GACE-A series because of the different architecture of the GACE-B series when compared to the GACE-A series. Because the GACE-B series architecture consisted of a two-tow weave with a high interlace angle, the CMC was axially weaker than the CMC of the GACE-A series whose architecture was a three-tow weave with a lower interlace angle. Thus, it is possible that the thermal-shock weakened the GACE-B series more than it did the GACE-A series, but the inferior endplug joints of the samples tested prevent conclusions concerning the influence of thermal-shock on the burst strength of the samples.

Table 44: Summary of post-thermal-shock properties for all series*

Series	Tube Burst Pressure	Tube Failure Stress	Endplug Joint Burst Pressure	Strength Reduction
GAOE	80 MPa	530 MPa	Not Measured	9%
GACE-A	Not Measured	Not Measured	34.2 MPa	8%
GACE-B	Not Measured	Not Measured	10.6 MPa	67%

8.4. Conclusions of High-Temperature Steam Oxidation Testing

Testing of the oxidized GAOE tubing revealed that the tube is weakened and embrittled by 48 hour oxidation at 6 g/min 1400°C steam flow. The maximum internal pressure that the oxidized tubing was observed to handle was approximately 35 MPa corresponding to a maximum hoop stress of approximately 230 MPa. Thus, the oxidized tubing was weakened by more than 50% when compared to the as-received tubing. Furthermore, unlike the as-received tubing, the oxidized tubing did not exhibit pseudo-ductility but still failed in a brittle non-frangible manner, with a failure strain of approximately 0.03%. Because of the mechanical degradation of the oxidized samples, the high-temperature steam oxidation has a significant impact on the performance of the GAOE tubing.

Failure characteristics of the 48 hour oxidized GAOE tubing had similarities and differences to those of the as-received tubing. Similar to the as-received sample, the oxidized samples' failure was non-frangible, although there was less opening of the failure crack in the oxidized samples. The failure crack did not span the entire axial distance of the tube and was instead dissipated into the weave contours of the CMC. The localized failure allowed much of the tubing to remain intact and preserved a coolable geometry for the fuel. However, the oxidized samples showed different microstructural failure characteristics compared to the as-received samples, with much less fiber pullout and matrix fragmentation. The oxidized failure was brittle and did not show the microstructural characteristics of pseudo-ductility. These observations suggest that the oxidation affected the microstructure of the samples, resulting in brittle failure with no pseudo-ductility.

* Properties are the average for all thermal-shock samples tested in each series

The 24 hour oxidized sample showed some mechanical degradation, although the sample performed much better than the 48 hour oxidized samples. The 24 hour oxidized sample had a failure pressure of 71 MPa corresponding to a failure stress of 475 MPa, and the sample exhibited significant pseudo-ductility, although the stress-strain behavior indicated a weakened matrix due to a 50% shallower pseudo-ductile slope. Although the 24 hour oxidation weakened the sample, it did not result in the embrittlement observed after the 48 hour oxidation. The high-temperature steam entered the sample through the cut surfaces and axially penetrated the sample via the CMC void network, leading to internal oxidation of the CMC. The mechanisms of oxidation weakening are further discussed in Section 7.3.2 above. The results of the oxidized specimens are presented in Table 45.

Testing of the oxidized endplug joints showed that the oxidation weakens the endplug joint, although the GACE-A series appeared more resilient than the GACE-B series. The burst-pressure for the GACE-A and GACE-B oxidized samples were 33.7 MPa and 22 MPa respectively. The oxidation for the GACE-A and GACE-B series resulted in a weakening of approximately 9% and 32% respectively. XCT analysis revealed that the endplug joints for the oxidized samples were of similar or superior strength to the endplug joints of the as-received samples. Therefore, the decrease in strength observed in the oxidized samples is likely a result of the oxidation and is not attributable to endplug joint quality. Table 45 presents the results of the testing of the oxidized GACE samples.

The increased mechanical degradation of the endplug joint for the GACE-B series when compared to the GACE-A series is attributable to the different architecture. Because the GACE-B series had a higher CMC void fraction than the GACE-A series, oxidation through the CMC was enhanced for the GACE-B series. Furthermore, because the CMC architecture of the GACE-B series has a higher interlace angle without axial tows, it was axially weaker than the GACE-A CMC. Thus, the oxidation of the GACE-B series weakened the CMC due to enhanced oxidation pathways in the void network, and because the CMC was inherently axially weak, the CMC failed during the endplug pushout testing instead of the joint proper. In contrast, the GACE-A CMC was axially stronger and had fewer oxidation pathways, thereby reducing CMC weakening. The GACE-A oxidized CMC was axially stronger than the endplug joint, and as a result, failure for GACE-A occurred in the joint proper. In summary, because the CMC for GACE-B was axially weaker and more susceptible to oxidation than the CMC for GACE-A, failure for oxidized GACE-B occurred in the CMC whereas failure for oxidized GACE-A occurred in the endplug joint.

Table 45: Summary of post-oxidation properties of all series*

Series	Tube Burst Pressure	Tube Failure Stress	Endplug Joint Burst Pressure	Strength Reduction
GAOE	71 MPa	475 MPa	Not Measured	18%
GACE-A	Not Measured	Not Measured	33.7 MPa	9%
GACE-B	Not Measured	Not Measured	22 MPa	32%

8.5.Recommendations for Future Work

Although this work determined several important conclusions about the LOCA performance of SiC cladding, it also identified several topics for further research.

* Properties are the average for all oxidized samples in tested in each series

1. Statistical study of SiC samples

The conclusions of this work were limited by the small number of samples available for investigation, so a key enhancement to this work would involve the investigation of a larger number of samples sufficient to perform statistical analysis. This is especially important because of the statistical nature of the failure of ceramics. Testing 30 samples within a series for each LOCA condition would allow for definitive conclusions about the results of LOCA conditions on the mechanical performance of the specimens, and testing 30 as-received samples would provide much more concrete data concerning the variance in mechanical properties among SiC cladding specimens. Furthermore, because of the high variance observed in the endplug joint quality among the GACE samples, it is likely that the endplug joint performance will have a wide distribution and it is therefore especially important to test numerous close-ended samples to evaluate their strength distribution. Ultimately, studies of large numbers of cladding specimens will be a necessary step towards the commercialization of SiC cladding.

2. Thermal-shock testing endplug joints with consistent joint properties

The results of the thermal-shock analysis on the endplug joint strength were influenced by the inferior joints of the thermal-shock samples when compared to the as-received sample. XCT analysis showed that both thermal-shock specimens had joints of inferior quality, exhibiting either a higher void fraction or a shorter joint length than the as-received sample's joint. Therefore, the observed weakness of the post-thermal-shock joints was a combination of both poor joint quality and thermal-shock. To properly evaluate the effect of thermal-shock on the joint, all specimens must have similar joint properties, and therefore future research should be performed on samples with consistent joint characteristics. XCT analysis must be performed on the as-received and thermal-shock samples to ensure that the joint quality does not confound the thermal-shock test results.

3. Analysis of high-temperature oxidation of carbon interphase

In this work, the oxidation was observed to penetrate axially in the CMC layer via the void network, and the oxidation was observed to coat the exposed surfaces of the samples. Analysis of oxidation of the surrounding SiC matrix suggested very limited oxidation penetration and supported the hypothesis that the oxidation is primarily a surface-based phenomenon. However, this work did not investigate the oxidation of the carbon interphase between the fibers and the matrix. Previous studies have shown that oxidation of the interphase results in the brittle failure characteristics that were observed for the oxidized samples in this work due to binding of the fibers and the matrix. Therefore, to better characterize the oxidation weakening mechanisms, it is important to perform future investigation into the oxidation of the fiber-matrix interphase. Furthermore, X-ray photoelectron spectroscopy (XPS) should be performed on the interphase to characterize its oxidation behavior and its bonding behavior with the fibers and matrix.

4. High-temperature oxidation testing of tubing with fully sealed cross-sectional faces

The oxidation results suggest that oxidation weakened the CMC by entering at the cross-sectional/cut tube faces and axially penetrating throughout the sample via the CMC void network. SEM analysis

showed significant silica deposition in the CMC voids which potentially weakened the surrounding CMC. Furthermore, SEM and EDS analysis showed that the oxidation has negligible penetration into the matrix and remained localized to the CMC void surfaces and exposed surfaces of the sample. Because actual nuclear cladding is sealed on both ends, the cross-sectional surfaces of the CMC would not be exposed to the high-temperature steam during an oxidation event. The steam would not be able to enter the CMC void network, and therefore internal oxidation of the CMC would not occur by the same mechanism as it did during the oxidation testing performed in this work. Therefore, by fully sealing the cross-sectional surfaces using either more significant CVD or using endplugs, the steam would not be able to enter the CMC void network and thus the oxidation would be more realistic of actual oxidation during LOCA scenarios.

5. Oxidation conditions sensitivity study

All samples investigated in this work except GAOE 1 were oxidized at the same conditions (48 hours, 6 g/min 1400°C steam). However, the 24 hour oxidation of GAOE 1 demonstrated that the oxidation time has a significant impact on the post-oxidation behavior of the sample. Therefore, analysis should be performed on the sensitivity of sample performance to oxidation time to better understand the temporal evolution of oxidation-induced mechanical degradation. Furthermore, as discussed in Section 6.3.2, oxidation kinetics depends on the steam temperature and flow rate. Better understanding of the oxidation kinetics could be achieved by analyzing the effect of oxidation at different temperatures and flow rates.

6. Evaluation of irradiated samples

The performance of composite SiC cladding must be evaluated after irradiation to evaluate swelling, embrittlement, and thermomechanical performance degradation. Furthermore, although the LOCA testing performed in this work was conducted on un-irradiated samples, during actual LOCA scenarios the cladding will likely be irradiated. Therefore, better understanding of the true LOCA performance of SiC cladding would be obtained by testing irradiated specimens. The lower thermal conductivity of neutron-irradiated SiC (Price, 1977) may result in significantly more degradation due to thermal-shock testing than what was observed in this work. The lower thermal conductivity would cause increased thermal stresses which could initiate cracking and possibly compromise the sample.

7. Analysis of thermal conductivity

The XCT analysis performed in this work revealed a network of voids within the CMC layer. These voids could reduce the thermal conductivity of the CMC and increase the thermal gradient in the intra-void material. Analysis of the thermal conductivity of the different architectures would allow for assessment of the thermal stresses expected in the samples. Furthermore, finite element analysis of the thermal gradient in the sample would allow for determination of the effect of CMC voids on the thermal performance of the sample. Because XCT analysis showed different void morphologies and void fractions among the different architectures investigated in this work, it is expected that the different architectures would also exhibit different thermal conductivities.

8. Development of mechanical model for multilayer specimens and evaluation of uncertainty

This work treated the tubing specimens as a single layer thick-wall cylinder. However, analyzing the true stresses in the CMC is much more complicated and requires modeling of the composite structure. Therefore, future work should be performed on evaluating the true stresses observed in the CMC layer by developing a model that accounts for the multilayer composite structure. Such a model could also allow for predictive analysis of the mechanical performance of the different architectures and better determination of whether a two-tow or three-tow weave is more suitable for implementation into actual nuclear cladding. A mechanical model can also allow for the evaluation of the mechanical uncertainties associated with the mechanical testing performed in this work, such as investigating the end effects of the expanding plug test and evaluating the friction between the plug and the textured interior surface of the samples. Additionally, work should be directed towards thermomechanical modelling of 3D reconstructions of the XCT data for SiC cladding.

Works Cited

- Abdul-Aziz, A., Ghosn, L., Baaklini, G., & Bhatt, a. R. (2003). Combined NDE/Finite Element Analysis Technique to Study the Effects of Matrix Porosity on the Behavior of Ceramic Matrix Composites. *NDE for Health Monitoring and Diagnostics*, 144-151.
- Abeles, B. (1963). Lattice Thermal Conductivity of Disordered Semiconductor Alloys at High Temperature. *Physical Review*, 131(5), 1906-1911.
- Andrews, N., Sukjai, Y., Pilat, E., Shirvan, K., & Kazimi, a. M. (2014). *Optimization of Thorium-Based Fuels for Burning Excess Weeapons Plutonium Stockpile*. Cambridge, MA: MIT.
- Basak, U., Sengupta, A., & Ganguly, C. (1989). *Hot hardness and thermal conductivity of ThO₂-PuO₂ and ThO₂-UO₂*.
- Basu, M., Mishra, R., Bharadwaj, S., & Das, D. (2010). Thermodynamic and transport properties of thoria-urania fuel of Advanced Heavy Water Reactor. *Journal of Nuclear Materials*, 403, 204-215.
- Bates, J. (1970). *High-temperature thermal conductivity of round robin uranium dioxide*. Richland, Washington: Battelle-Northwest.
- Belle, J., & Berman, R. (1984). *Thorium dioxide: properties and nuclear applications*. Washington, DC: USDOE Assistant Secretary for Nuclear Energy.
- Ben-Belgacem, M., Richet, V., Terrani, K., Katoh, Y., & Snead, L. (2014). Thermo-mechanical analysis of LWR SiC/SiC composite cladding. *Journal of Nuclear Materials*, 447(1), 125-142.
- Bjork, K., & Kekkonen, L. (2015). Thermal-mechanical performance modeling of thorium-plutonium oxide fuel and comparison with on-line irradiation data. *Journal of Nuclear Materials*, 467, 876-885.
- Bloom, E. (1998). The challenge of developing structural materials for fusion. *Journal of Nuclear Materials*, 258, 7-17.
- Bragg-Sitton, S. (2014). Development of advanced accident-tolerant fuels for commercial LWRs. *Nuclear News*, 83-91.
- Carpenter, D. (2010). *An Assessment of Silicon Carbide as a Cladding for Light Water Reactors*. PhD Thesis.
- Carter, R. (2006). *Compressed Elastomer Method for Internal Pressure Testing*. Aberdeen Proving Ground, MD: Army Research Laboratory.
- Christin, F. (2002). Design, fabrication, and application of thermostructural composites (TSC) like C/C, C/SiC, and SiC/SiC composites. *Advanced engineering materials*, 4(12), 903-912.

- Clark, T., Prack, E., Haider, M. I., & Sawyer, L. (1987). Oxidation of SiC Ceramic Fiber. *Conference on Composites and Advanced Ceramic Materials: Ceramic Engineering and Science Proceedings*, 8(7/8), 717-731.
- Cornell, R. (1968). The growth of fission gas bubbles in irradiated uranium dioxide. *Philosophical Magazine*, 539-554.
- Costello, J., & Tressler, R. (1986). Oxidation kinetics of silicon carbide crystals and ceramics: I, in dry oxygen. *Journal of the American Ceramic Society*, 69(9), 674-681.
- Cozzo, C., Staicu, D., Somers, J., Fernandez, A., & Konings, R. (2011). Thermal diffusivity and conductivity of thorium-plutonium mixed oxides. *Journal of Nuclear Materials*, 416(1), 134-141.
- Davies, D., & Long, G. (1963). *The emission of Xenon-133 from lightly irradiated uranium dioxide spheroids and powders*. Harwell, Berkshire: Atomic Energy Research Establishment.
- Easler, T. E., Bradt, R. C., & Tressler, R. E. (1981). Strength Distributions of SiC Ceramics After Oxidation and Oxidation Under Load. *Journal of the American Ceramic Society*, 64(12), 731-734.
- Eaton, H., & Linsey, G. (2002). Accelerated oxidation of SiC CMC's by water vapor and protection via environmental barrier coating approach. *Journal of the European Ceramic Society*, 22(14), 2741-2747.
- Fenici, P., Rebelo, A. J., Jones, R. H., Kohyama, A., & Snead, L. L. (1998). Current status of SiC/SiC composites R&D. *Journal of Nuclear Materials*, 258, 215-225.
- Forsberg, K., & Massih, A. R. (1985). Fission Gas Release Under Time-Varying Conditions. *Journal of Nuclear Materials*, 127, 141-145.
- Geelhood, K. J., & Luscher, W. G. (2014). *FRAPCON-3.5: A Computer Code for the Calculation of Steady-State, Thermal-Mechanical Behavior of Oxide Fuel Rods for High Burnup*. Richland, WA: Pacific Northwest National Laboratories.
- Goldberg, I., Spahr, G., White, L., Waldman, L., Giovengo, J., Pfennigwerth, P., & Sherman, J. (1978). *Fission gas release from ThO₂ and ThO₂-UO₂ fuels*. Bettis Atomic Power Laboratory.
- IAEA. (2006). *Thermophysical properties database of materials for light water reactors and heavy water reactors, TECDOC-1496*.
- Ichikawa, H. (2000). Recent advances in Nicalon ceramic fibres including Hi-Nicalon type S. *Annales de Chimie Science des Matériaux*, 25(7), 523-528.
- Igawa, N., Taguchi, T., Nozawa, T., Snead, L. L., T., M. J., & Kohyama, A. (2005). Fabrication of SiC fiber reinforced SiC composite by chemical vapor infiltration for excellent mechanical properties. *Journal of Physics and Chemistry of Solids*, 66(2), 551-554.

- Ishikawa, T. (1994). Recent developments of the SiC fiber Nicalon and its composites, including properties of the SiC fiber Hi-Nicalon for ultra-high temperature. *Composites science and technology*, 51(2), 135-144.
- Karam, M., Dimayuga, F., Montin, J., Floyd, M., Dickson, L., & Boczar, P. (2008). *Fission gas release of (Th, Pu) O₂ CANDU fuel*.
- Khalifa, H. E., Deck, C. P., & Back, a. C. (2013). *Patent No. 13/856,919*. United States of America.
- Khalifa, H. E., Deck, C. P., Gutierrez, O., Jacobsen, G. M., & Back, C. A. (2015). Fabrication and characterization of joined silicon carbide cylindrical components for nuclear applications. *Journal of Nuclear Materials*, 457, 227-240.
- Lamon, N. P. (2014). *Ceramic Matrix Composites: Materials, Modeling and Technology*. John Wiley & Sons.
- Lee, K. N., Fox, D. S., Eldridge, J., Zhu, D., Robinson, R. C., Bansal, N. P., & Miller, R. A. (2003). Upper temperature limit of environmental barrier coatings based on mullite and BSAS. *Journal of the American Ceramic Society*, 86(8), 1299-1306.
- Lee, Y., McKrell, T., & Kazimi, M. (2014). *Safety of Light Water Reactor Fuel with Silicon Carbide Cladding*. Cambridge: CANES.
- Lee, Y., McKrell, T., Yue, C., & Kazimi, a. M. (2013). Safety Assessment of SiC Cladding Oxidation Under Loss-Of-Coolant Accident Conditions in Light Water Reactors. *Nuclear Technology*, 183, 210-227.
- Locke, D. H. (1975). Review of experience with water reactor fuels 1968–1973. *Nuclear Engineering and Design*, 33(2), 94-124.
- Lombardi, C., Luzzi, L., Padovani, E., & Vettriano, F. (2008). Thoria and inert matrix fuels for a sustainable nuclear power. *Progress in Nuclear Energy*, 944-953.
- Long, Y. (2002). *Modeling the Performance of High Burnup Thoria and Urania PWR Fuel*. Cambridge, MA: MIT.
- Mah, T., Hecht, N. L., McMullen, D. E., Hoenigan, J. R., Kim, H. M., Katz, A. P., & Lipsitt, H. A. (1984). Thermal Stability of SiC Fibres (Nicalon). *Journal of Material Science*, 19, 1191-1201.
- Matzke, H. (1980). Gas release mechanisms in UO₂ - a critical review. *Radiation Effects*, 53, 219-242.
- Moorhead, H. K. (1989). Effects of Gaseous Corrosion on the Strength of SiC and Si₃N₄. *Ceramic Transactions*, 10, 81-96.
- Murabayashi, M. (1970). *Thermal Conductivity of ThO₂-UO₂ system*. Tokyo University.
- Naik, M. (1992). In R. Agarwala, *Diffusion Processes in Nuclear Materials*. North Holland.

- Naslain, R. R. (2005). SiC-Matrix Composites: Nonbrittle Ceramics for Thermo-Structural Application. *International Journal of Applied Ceramic Technology*, 2(2), 75-84.
- Nuclear Regulatory Commission. (n.d.). *NRC: 10 CFR 50.46 Acceptance criteria for emergency core cooling systems for light-water nuclear power reactors*.
- Ohira, K., & Itagaki, N. (1997). Thermal conductivity measurements of high burnup UO₂ pellets and benchmark calculation of fuel center temperature. *Proceedings of the ANS international topical meeting on LWR fuel performance*, 541-549.
- Opila, E. (1999). Variation of the Oxidation Rate of Silicon Carbide with Water-Vapor Pressure. *Journal of the American Ceramic Society*, 82(3), 625-636.
- Opila, E., & Hann, R. (1997). *Paralinear Oxidation Kinetics of CVD SiC in Water Vapor*. National Aeronautics and Space Administration.
- Page, R. (1976). *Canadian Power Reactor Fuel*. Mississauga: Atomic Energy of Canada Limited.
- Pillai, C., & Raj, P. (2000). Thermal Conductivity of ThO₂ and Th-0.98 U-0.02O₂. *Journal of Nuclear Materials*, 116-119.
- Price, R. J. (1977). Properties of Silicon Carbide for Nuclear Fuel Particle Coatings. *Nuclear Technology*, 35(2), 320-336.
- Puglia, P. D., Sheikh, M. A., & Hayhurst, a. D. (2005). Thermal Transport Property Prediction of a CMC Laminate from Base Materials Properties and Manufacturing Porosities. *Proceedings of the Royal Society of London A: Mathematical, Physical and Engineering Sciences*, 461(2063).
- Puglia, P. D., Sheikh, M., & Hayhurst, a. D. (2004). Classification and Quantification of Initial Porosity in a CMC Laminate. *Composites Part A: Applied Science and Manufacturing*, 35(2), 223-230.
- Raffay, A. R., Jones, R., Aiello, G., Billone, M., Giancarli, L., Golfier, H., . . . Tillack, M. (2001). Design and material issues for high performance SiC f/SiC-based fusion power cores. *Fusion Engineering and Design*, 55(1), 55-95.
- Rohm and Haas Company. (2008). *CVD Silicon Carbide*.
- Ronchi, C., Sheindlin, M., Musella, M., & Hyland, G. (1999). Thermal conductivity of uranium dioxide up to 2900 K from simultaneous measurement of heat capacity and thermal diffusivity. *Journal of Applied Physics*, 85(2), 776-789.
- Ross, S. B., El-Genk, M. S., & Matthews, a. R. (1988). Thermal conductivity correlation for uranium nitride fuel between 10 and 1923 K. *Journal of nuclear materials*, 151(3), 318-326.
- Sarma, K., Fourcade, J., Lee, S.-G., & Solomon, A. A. (2006). New processing methods to produce silicon carbide and beryllium oxide inert matrix and enhanced thermal conductivity oxide fuels. *Journal of Nuclear Materials*, 352(1), 324-333.

- Shiba, K. (1992). In R. Agarwala, *Diffusion Processes in Nuclear Materials* (p. 71). North Holland.
- Snead, L. L., Nozawa, T., Katoh, Y., Byun, T.-S., Kondo, S., & Petti, D. A. (2007). Handbook of SiC Properties for Fuel Performance Modeling. *Journal of Nuclear Materials*, 371, 329-377.
- Snead, L., Osborne, M., & More, K. (1995). Effects of radiation on SiC-based Nicalon fibers. *Journal of Materials Research*, 10(3), 736-747.
- Springer, J., Eldridge, E., Goodyear, M., Wright, T., & Langedrost, J. (1968). *Fabrication, characterization and thermal property measurements of ThO₂-UO₂ fuel materials*. Columbus: Battelle Memorial Institute.
- Stehle, H., Kaden, W., & Manzel, a. R. (1975). External corrosion of cladding in PWRs. *Nuclear Engineering and Design*, 33(2), 155-169.
- Stempien, J. (2011). *Behavior of Triplex Silicon Carbide Fuel Cladding Designs Tested Under Simulated PWR Conditions*. MS Thesis.
- Stone, J., Schleicher, R., Deck, C., Jacobsen, G., Khalifa, H., & Back, C. (2015). Stress analysis and probabilistic assessment of multi-layer SiC-based. *Journal of Nuclear Materials*, 1-16.
- Sukjai, Y. (2014). *Silicon Carbide Performance as Cladding for Advanced Uranium and Thorium Fuels for Light Water Reactors*. Massachusetts Institute of Technology.
- Sunder, S., & Miller, N. H. (1998). XPS and XRD Studies of Corrosion of Uranium Nitride by water. *Journal of Alloys and Compounds*, 271, 568-572.
- Takeda, M., Sakamoto, J., Saeki, A., & Ichikawa. (1996). Mechanical and Structural Analysis of Silicon Carbide Fiber Hi-Nicalon Type S. *Proceedings of the 20th Annual Conference on Composites, Advanced Ceramics, Materials, and Structures-B: Ceramic Engineering and Science Proceedings*, 17(4), 35-42.
- Une, K., Tanabe, I., & Oguma, M. (1987). Effects of additives and the oxygen potential on the fission gas diffusion in UO₂ fuel. *Journal of Nuclear Materials*, 93-99.
- Yajima, S., Hayashi, J., & Omori, a. M. (1979). *Patent No. 4,052,430*. USA.
- Yang, R. C. (2006). Fuel R & D to Improve Fuel Reliability. *Journal of Nuclear Science and Technology*, 43(9), 951-959.
- Zdaniewski, W., & Kirchner, H. (1987). Effect of Grain-Boundary Oxidation on Fracture Toughness of SiC. *Journal of the American Ceramic Society*, 70(8), 548-552.